Università degli Studi di Ferrara

DOCTORAL COURSE IN
"ENGINEERING SCIENCE"

CYCLE 36°

COORDINATOR Prof: Stefano Trillo

A novel 2D dissipative connection for the seismic retrofit of precast RC structures: conceptualization, prototyping, mechanical and numerical study

Scientific/Disciplinary Sector (SDS) ICAR/09

Candidate:
Eleonora Grossi

Supervisors:
Prof. Dr. Alessandra Aprile
Dr. Matteo Zerbin

Co-supervisors:
Prof. Dr. Flavia De Luca
Dr. Raffaele De Risi

Years 2020/2024

Abstract

Precast RC structures are widely used in industrial and commercial buildings. However, precast RC buildings with poor connections have a significant seismic risk caused by a combination of high seismic vulnerability and exposure. The objectives of this thesis are the conceptualization, prototyping, mechanical and numerical definition of a 2D dissipative connection called Bidirectional Rotational Friction Damper (BRFD) for the seismic retrofit of precast RC structures. The conceptualisation study aims to define a simplified analytical BRFD model and evaluate its impact on a structure's behaviour during a seismic event. Results show that introducing the BRFD improves the structural dynamic performance, reducing inter-storey drift and total base shear without damaging the structure. The prototyping study aims to identify proper coupling materials that develop a reliable and steady friction coefficient (COF) for the device by performing Pin-on-Disk (PoD) tests set to simulate its real use conditions. The main findings highlight that the interaction between steel and softer metals improves COF steadiness without significant surface damage. The mechanical study aims to assess the mechanical behaviour of the BRFD by performing two investigations: a preliminary one that focuses on the assessment of the selected friction interfaces, and a bidirectional one that focuses on the assessment of the BRFD and the interaction between its longitudinal and transversal components. The results show the promising bidirectional behaviour of the BRFD, both in terms of hysteresis steadiness and good damping capacity. The numerical study aims to validate the mechanical experimental results with FEM analysis by developing two friction-based numerical models that simulate the BRFD behaviour: a simple model for an easy implementation inside a frame structure, and a more refined model to be used as a Virtual Lab tool and that simulates the BRFD elements. The results highlight that the refined model well reproduces the overall behaviour of the BRFD and the interaction between its longitudinal and transversal components. The present study aims to prolong the service life and mitigate the seismic losses of precast RC structures designed for gravity loads only and located in earthquake-prone areas. This is a particularly sensitive topic that allows the pursuit of goals 11, 12 and 13 of the UN 2030 Agenda for Sustainable Development.

Keywords: Precast RC structure; beam-to-column connection; rotational friction damper; conceptualisation; importance analysis; tribology; Pin-on-Disk; real use simulation; cyclic tests; bidirectional damping; FEM analysis.

Sommario

Le strutture prefabbricate in c.a. e c.a.p. sono spesso adottate per la realizzazione di edifici industriali e commerciali. Tuttavia, strutture prefabbricate con uno scarso grado di connettività possiedono un significativo rischio sismico a causa dell'effetto combinato di elevata vulnerabilità sismica ed esposizione. Gli obiettivi di questa tesi sono la concettualizzazione, prototipazione e definizione meccanica e numerica di una connessione dissipativa 2D, chiamata Bidirectional Rotational Friction Damper (BRFD), che adegua sismicamente le strutture prefabbricate in c.a. e c.a.p. Lo studio di concettualizzazione mira alla definizione di un modello analitico semplificato del BRFD e alla valutazione della sua influenza sul comportamento di una struttura durante un evento sismico. I risultati mostrano che l'introduzione del BRFD migliora la risposta dinamica della struttura, riducendo i drift d'interpiano e il tagliante alla base senza danneggiare la struttura. Lo studio di prototipazione mira alla selezione dell'accoppiamento di materiali più adatto per sviluppare un coefficiente d'attrito (COF) affidabile e stabile per il BRFD attraverso l'esecuzione di test Pin-on-Disk calibrati per simularne le condizioni d'uso reali. I risultati principali evidenziano come l'interazione tra acciaio e un metallo più morbido migliori la stabilità del COF senza danneggiare significativamente le superfici. Lo studio meccanico del BRFD è stato condotto attraverso due campagne sperimentali: una campagna preliminare focalizzata sulla valutazione delle interfacce attritive selezionate, ed una campagna bidirezionale focalizzata sulla valutazione del comportamento meccanico del BRFD e dell'interazione tra la componente longitudinale e trasversale. I risultati mostrano una comportamento promettente del BRFD, sia in termini di stabilità del ciclo d'isteresi, sia in termini di capacità dissipativa. Lo studio numerico mira alla validazione delle prove meccaniche con analisi FEM attraverso lo sviluppo di due modelli numerici che riproducano il comportamento complessivo del BRFD basati sull'attrito: un modello semplificato per una semplice implementazione all'interno di un telaio, ed un modello raffinato per essere usato come Virtual Lab e che riproduca gli elementi del BRFD. I risultati evidenziano come il modello raffinato riproduca fedelmente il comportamento del BRFD e l'interazione tra la componente longitudinale e trasversale. La presente tesi mira al prolungamento della vita utile e alla mitigazione delle perdite dovute al sisma di strutture prefabbricate in c.a. e c.a.p. progettate solo per carichi verticali e situate in aree a rischio sismico. Questo è un argomento particolarmente sensibile che permette di soddisfare gli obiettivi 11, 12 e 13 dell'agenda ONU 2023 per uno sviluppo sostenibile.

Parole chiave: Strutture prefabbricate in c.a. e c.a.p.; connessione trave-colonna; dissipatore attritivo rotazionale; concettualizzazione; analisi d'importanza; tribologia; Pin-on-Disk; simulazione condizione d'uso reale; tests ciclici; dissipazione bidirezionale; analisi FEM.

Publications

List of papers published and submitted related to the present thesis:

1. Grossi E., De Risi R., Zerbin M., De Luca F., Aprile A. "A Novel Bidirectional Friction Damper for Retrofitting of RC Precast Structures: Experimental and Numerical Assessment", *Earthquake Engineering & Structural Dynamics* (in review)

2. Grossi E., Zerbin M., Aprile A., De Risi R., De Luca F., "Conceptual study of an innovative friction damper for the seismic retrofit of precast RC structures with poor connections", *Structures* (in review)

3. Grossi E., De Risi R., Zerbin M., Aprile A., De Luca F. (2024) "Innovative setup and testing methodology of a novel bidirectional rotation friction damper (BRFD)", 18th World Conference on Earthquake Engineering Milan 2024 (accepted for publication)

4. Grossi E., Aprile A., Zerbin M., Livieri P.,"Preliminary Experimental Tests of a Novel Friction Damper for Seismic Retrofit of RC Precast Structures", *Engineering Structures*, 305 (117718)

   DOI: 10.1016/j.engstruct.2024.117718

5. Aprile A., Grossi E., Zerbin M. (2023) "A Novel Friction Damper for Seismic Retrofit of Precast RC Structures with Poor Connections". Lecture Notes in Civil Engineering - International Symposium of the International Federation for Structural Concrete, *fib Symposium 2023*, 349 LNCE, 1384-1394.

   ISSN: 2366-2557, DOI: 10.1007/978-3-031- 32519-9_140

6. Grossi, E.; Baroni, E.; Aprile, A.; Fortini, A.; Zerbin, M.; Merlin, M. (2023) "Tribological Behavior of Structural Steel with Different Surface Finishing and Treatments for a Novel Seismic Damper", *Coatings*, 13 (135).

   DOI: 10.3390/coatings13010135

7. Grossi E., Aprile A., Zerbin M. (2022) “Tribological investigation on metal mating surfaces of a novel friction damper for seismic applications”, *Engineering Structures*, 278 (115473).

   DOI: 10.1016/j.engstruct.2022.115473

Acknowledgements

The present thesis has been carried out at the Engineering Department of the University of Ferrara (Italy) and its preparation and completion would not have been possible without the help, guidance and support of several individuals, which have my most sincere gratitude.

Firstly, I would like to thank my supervisors, Prof. Alessandra Aprile and Dr Matteo Zerbin of the Engineering Department of the University of Ferrara (Italy), for guiding and supporting me during these years. Your expertise has been essential for this work, teaching me how a thorough methodology can lead to meaningful research. Our teamwork proved to be very efficient and I am looking forward to the next steps of our collaboration.

I also warmly thank my co-supervisors, Prof. Flavia De Luca and Dr Raffaele De Risi from the CADE School of the University of Bristol (UK), for helping me during the most difficult part of my work and showing me different research approaches. Your wide expertise is remarkable and inspires me to widen my knowledge and explore more fields. I hope we will carry out more research together.

I would like to thank the Mechanical Engineering colleagues from the Engineering Department of the University of Ferrara (Italy) for helping me through the several stages of this research. Firstly, I thank the Metallurgy Research Group led by Prof. Gianluca Garagnani and, in particular, I thank Dr Annalisa Fortini and Enrico Baroni for helping me to understand friction and wear mechanisms. I also thank Prof. Paolo Livieri for the execution of the mechanical tests in the Structural Integrity Laboratory and his guidance during all the stages of the mechanical design of the device object of this study. Finally, I kindly thank Prof. Raffaella Rizzoni for checking the analytical part of this work: your expertise has been remarkable.

I wish to thank the technical staff of the Heavy & Light Laboratory of the University of Bristol (Bristol) for helping in the setting and execution of my experimental tests. In particular, I thank Steve Harding, Guy Pern and Daniel Muscat: I enjoyed working in the lab with you (literally dirtying my hands), and learning from your expertise. I also warmly thank Dr Yusuf Mahadik for helping tune the actuators in the laboratory: without your help, I would not have performed bi-directional tests.

Several people supported and cheered for me during these years. I thank my friends from Ferrara, Margherita, Silvia, Martina and Michele: always ready for an aperitif and to share the joys and struggles of a PhD student life. I also thank the friends I met in Bristol, Greta, Numan, Shahin and Zhixin, for all the trips, laughs and beers we shared. You're all amazing people and I feel lucky to have you as friends. A special thanks go also to Alison for cheering for me about my work and any time I made a new friend in Bristol: you, Elsa and Theo made me feel at home and you'll always be like my British/South African family.

Federico is a special person I would like to thank. I love how we learned to team up with and for each other, and that you never stopped pushing me to pursue my goals, even if it meant being apart from time to time. Your understanding, patience and kindness helped me a lot, especially during these last months.

The most special thanks go to my family, my parents Lorella and Paolo, and my brother Alessandro. You supported me during all these years and never stopped believing in my capabilities, always ready to cheer me up during the most struggling parts of my work. I will always be grateful to have such a lovely and supportive family.

Table of contents

List of figures

List of tables

Abbreviations

ADAS	Added Damping and Stiffness
BRB	Buckling Restrained Brace
BRFD	Bidirectional Rotational Friction Damper
BS	Brass pins used in the Pin-on-Disk tests
BZ	Bronze pins used in the Pin-on-Disk tests
CF	Coulomb Friction model in Opensees
COF	Coefficient of Friction
DA1	Dissipative area 1
DA2	Dissipative area 2
DA3	Dissipative area 3
DA4	Dissipative area 4
EDD	Energy Dissipation Device
F0	Case study model without BRFDs
F1	Case study model with the elastic properties of the BRFDs
F2	Case study model with the hysteretic properties of the BRFDs
FD	Friction Damper
FSB	Flat Sliding Bearing element in Opensees
FRP	Fibre-Reinforced Polymer
G1	Group 1 tests group in mechanical tests
G2	Group 2 tests group in mechanical tests
G3	Group 3 tests group in mechanical tests
LED	Lead Extrusion Device
M0.8	Milled disk with nominal roughness $Ra = 0.8$ μm used in the Pin-on-Disk tests
M1.6	Milled disk with nominal roughness $Ra = 1.6$ μm used in the Pin-on-Disk tests
M3.2	Milled disk with nominal roughness $Ra = 3.2$ μm used in the Pin-on-Disk tests
M6.3	Milled disk with nominal roughness $Ra = 6.3$ μm used in the Pin-on-Disk tests
MCDM	Multi-Criteria Decision-Making
MLVDF	Multi-Linear Velocity Dependant Friction model in Opensees
NAO	Nonasbestos Organic
NB	BRFD prototype with nickelled steel vs. bronze friction interface
NI	Disk treated with a nickel base coating used in the Pin-on-Disk tests
NLTHA	Nonlinear Time History Analysis
NN	BRFD prototype with nickelled steel vs. nickelled steel friction interface
PEDD	Passive Energy Dissipation Device
PO	Push-Over
PoD	Pin-on-Disk

PT	Post-Tensioned
PVW	Principle of Virtual Works
RC	Reinforced Concrete
RFD	Rotational Friction Damper
RI	Running-in tests group in mechanical tests
SB1	Instrumented stud bolt in correspondence of DA1
SB2	Instrumented stud bolt in correspondence of DA2
SB3	Instrumented stud bolt in correspondence of DA3
SBC	Slotted Bolted Connection
SP1	Shot peened disk with with nominal roughness $Ra = 1.0$ μm used in the Pin-on-Disk tests
SP2	Shot peened disk with with nominal roughness $Ra = 2.0$ μm used in the Pin-on-Disk tests
ST	Steel pins used in the Pin-on-Disk tests
SMRF	Steel Moment Resisting Frame
T0.8	Turned disk with nominal roughness $Ra = 0.8$ μm used in the Pin-on-Disk tests
T1.6	Turned disk with nominal roughness $Ra = 1.6$ μm used in the Pin-on-Disk tests
T3.2	Turned disk with nominal roughness $Ra = 3.2$ μm used in the Pin-on-Disk tests
T6.3	Turned disk with nominal roughness $Ra = 6.3$ μm used in the Pin-on-Disk tests
TC1	Thermocouple in correspondence of DA1
TC2	Thermocouple in correspondence of DA2
TC3	Thermocouple in correspondence of DA3
TMD	Tuned-Mass Damper
VDF	Velocity Dependant Friction model in Opensees
WFD	Web Friction Device
ZN	Disk treated with a zinc base coating used in the Pin-on-Disk tests

List of symbols

a	Transition rate
$a_{l,x}$	Transition rate associated with the overall BRFD linear behaviour computed along the x direction
$a_{l,y}$	Transition rate associated with the overall BRFD linear behaviour computed along the y direction
$a_{r,x}$	Transition rate associated with the rotational mechanism of the friction interface of the BRFD computed along the x direction
$a_{r,y}$	Transition rate associated with the rotational mechanism of the friction interface of the BRFD computed along the y direction
A_w	Area of the wear tracks
A_r	Real contact area
cv	Coefficient of variation
cv_{Fact}	Coefficient of variation of F_{act}
$cv_{Fact,st}$	Coefficient of variation of $F_{act,st}$
cv_{Fp}	Coefficient of variation of F_P
cv_t	Coefficient of variation of t_{tr}
$cv_{wr,d}$	Coefficient of variation of WR_d
$cv_{wr,p}$	Coefficient of variation of WR_p
cv_μ	Coefficient of variation of μ_{st}
d_{max}	Maximum displacement reached in an hysteresis cycle
E	Young's modulus
E_h	Hysteretic energy dissipated by the structure
E_{hd}	Hysteretic energy dissipated by an EDD
E_i	Seismic input energy
E_k	Kinetic energy
E_{PoD}	Energy dissipated during Pin-on-Disk tests
E_s	Strain energy
E_ξ	Viscous damping energy
EDC	Energy dissipated per cycle
$EDC_{F,d}$	Energy dissipated per cycle computed in terms of force-displacement relationship
$EDC_{M,\theta}$	Energy dissipated per cycle computed in terms of moment-rotation relationship
f	Frequency
F_{act}	Average activation force developed by an EDD in its hysteresis cycles
$F_{act,1}$	Activation force of an EDD in its first hysteresis cycle
$F_{act,i}$	Activation force of an EDD in its i hysteresis cycle
$F_{act,ideal}$	Ideal activation force of an EDD

$F_{act,st}$	Average activation force developed by an EDD in its hysteresis cycles in the steady behaviour
$F_{act,x}$	BRFD longitudinal activation force (x direction)
$F_{act,y}$	BRFD transversal activation force (y direction)
F_{max}	Average maximum forces developed by an EDD in its hysteresis cycles
$F_{max,1}$	Maximum force of an EDD in its first hysteresis cycle
$F_{max,i}$	Maximum force of an EDD in its i hysteresis cycle
$F_{max,st}$	Average maximum force developed by an EDD in its hysteresis cycles in the steady behaviour
$F_{max,x}$	BRFD longitudinal maximum force (x direction)
$F_{max,y}$	BRFD transversal maximum force (y direction)
f_y	Yielding strength of steel
F_P	Bolt axial tension
F_μ	Friction force
$F_{\mu,a}$	Force needed to shear the adhered asperities
$F_{\mu,d}$	Force needed to supply the energy deformation
$F_{\mu,i}$	Total intrinsic friction force
$F_{\mu,k}$	Kinetic friction force
$F_{\mu,s}$	Static friction force
Fb	Total base shear
H	Hardness of the material
H_{IT}	Hardness in Berkovich scale
HV	Hardness in Vickers scale
I	Moment of inertia
$I_{\overline{BA}}$	Moment of inertia of BRFD's $\overline{BA}$ elements
$I_{\overline{OB}}$	Moment of inertia of BRFD's $\overline{OB}$ elements
IDR	Interstorey drift
k	Nondimensional parameter to compact BRFD's analytical formulation
k_eq	Torque coefficient
K_x	BRFD initial longitudinal stiffness in the (x direction)
K_y	BRFD initial transversal stiffness in the (y direction)
l	Distance between bolts
M_s	Sliding moment
$M_{s,i}$	Interface sliding moment
n_i	Number of friction interfaces
n_{st}	Number of hysteresis cycles to reach the steady behaviour
n_{tot}	Total number of hysteresis cycles
p	Mean contact pressure
$P_{i,j}$	Importance proportion of the standardised importance index $\tilde{r}_{i,j}$
p_m	Mean contact pressure of the pin
$p_{m,d}$	Mean contact pressure of the friction pads in the device
p_r	Mean real pressure
pv	Parameter for PoD tests setting

pv_{BRFD}	pv parameter in the BRFD
pv_{PoD}	pv parameter for the PoD test
Ra	Superficial roughness
$r_{i,j}$	Importance index of importance parameter i for the the $F_{act,x}$-K_x couple j
$\tilde{r}_{i,j}$	Standardised importance index of parameter i for the the $F_{act,x}$-K_x couple j
r_e	Equivalent radius of a circular dissipative area
R_e	Outer radius of a circular dissipative area
R_i	Inner radius of a circular dissipative area
S_i	Entropy of $P_{i,j}$
S_{tot}	Total sliding distance of pins in the Pin-on-Disk tests
S_w	Length of the wear tracks
t	Thickness
T	Torque
t_{eq}	BRFD equivalent thickness
t_{tr}	Friction interface transition time
$T_{0,X}$	Main period of a structure in the X direction
$T_{0,Y}$	Main period of a structure in the Y direction
v	Sliding velocity
v_x	Sliding velocity in the x direction
v_y	Sliding velocity in the y direction
v_t	Tangential sliding velocity
$v_{t,x}$	Tangential sliding velocity in the x direction
$v_{t,y}$	Tangential sliding velocity in the y direction
W	Nominal applied load
wr	Wear rate
wr_d	Wear rate measured on the disk
wr_p	Wear rate measured on the pin
x	x-axis in a local reference system
X	X-axis in a global reference system
y	y-axis in a local reference system
Y	Y-axis in a global reference system
z	z-axis in a local reference system
Z	Z-axis in a global reference system
α	Angle between $\overline{BA}$ and $\overline{OA}$ segments of BRFD scheme
β	Angle between $\overline{BA}$ and $\overline{OB}$ segments of BRFD scheme
γ	Angle between $\overline{OB}$ and $\overline{OA}$ segments of BRFD scheme
ΔF_{act}	Difference between $F_{act,1}$ and $F_{act,st}$
ΔF	Difference between F_{act} and F_{max}
ΔF_P	Stud bolt axial tension loss
Δg	Weight loss
ΔT	Temperature variation

ΔV	Volume loss
Δx	Displacement along the local x direction
Δy	Displacement along the local y direction
$\Delta\beta$	Variation of β angle in BRFD scheme
ε	Strain
η_j	Comprehensive index of the $F_{act,x}$-K_x couple j
θ_{max}	Maximum rotation reached in an hysteresis cycle
κ_i	Comprehensive weight of importance parameter i
λ_i	Subjective weight of importance parameter i
μ	friction coefficient
μ_a	Adhesional friction coefficient
μ_d	Plowing component of the friction coefficient
μ_{fast}	COF in correspondence of high sliding velocities
μ_i	Intrinsic friction coefficient
μ_k	Kinetic friction coefficient
μ_l	Friction coefficient associated with the overall BRFD linear behaviour
$\mu_{l,an}$	μ_l computed analytically
$\mu_{l,an,x}$	$\mu_{l,an}$ computed along the x direction
$\mu_{l,an,y}$	$\mu_{l,an}$ computed along the y direction
$\mu_{l,EDC}$	μ_l computed from the EDC
$\mu_{l,EDC,x}$	$\mu_{l,EDC}$ computed along the x direction
$\mu_{l,EDC,y}$	$\mu_{l,EDC}$ computed along the y direction
$\mu_{l,x}$	μ_l along x direction
$\mu_{l,x,fast}$	μ_{fast} associated with the overall BRFD linear behaviour computed along the x direction
$\mu_{l,x,slow}$	μ_{slow} associated with the overall BRFD linear behaviour computed along the x direction
$\mu_{l,y}$	μ_l along y direction
$\mu_{l,y,fast}$	μ_{fast} associated with the overall BRFD linear behaviour computed along the y direction
$\mu_{l,y,slow}$	μ_{slow} associated with the overall BRFD linear behaviour computed along the y direction
μ_r	Friction coefficient associated with the rotational mechanism of the friction interface of the BRFD
$\mu_{r,an}$	μ_r computed analytically
$\mu_{r,an,x}$	$\mu_{r,an}$ computed along the x direction
$\mu_{r,an,y}$	$\mu_{r,an}$ computed along the y direction
$\mu_{r,EDC}$	μ_r computed from the EDC
$\mu_{r,EDC,x}$	$\mu_{r,EDC}$ computed along the x direction
$\mu_{r,EDC,y}$	$\mu_{r,EDC}$ computed along the y direction
$\mu_{r,x}$	μ_r along the x direction
$\mu_{r,x,fast}$	μ_{fast} associated with the rotational mechanism of the friction interface of the BRFD computed along the x direction
$\mu_{r,x,slow}$	μ_{slow} associated with the rotational mechanism of the friction interface of the BRFD computed along the x direction
$\mu_{r,y}$	μ_r along the y direction

$\mu_{r,y,fast}$	μ_{fast} associated with the rotational mechanism of the friction interface of the BRFD computed along the y direction
$\mu_{r,y,slow}$	μ_{slow} associated with the rotational mechanism of the friction interface of the BRFD computed along the y direction
μ_s	Static friction coefficient
μ_{slow}	COF in correspondence of low sliding velocities
μ_{st}	COF measured in the steady-state condition
ξ_{eq}	Equivalent damping
$\xi_{eq,hyst}$	Equivalent damping coefficient
ρ	Mass density
$\rho_{C,V}$	Columns base shear utilisation factor
$\rho_{C,\theta}$	Column base rotation utilisation factor
σ_z	Distribution of pressure on a surface
τ_a	Contact average shear strength
Φ	Reinforcing steel bars diameter
ω	Rotational sliding velocity
ω_i	Objective weight of importance parameter i

1 Introduction

1.1 Motivations

Precast Reinforced Concrete (RC) structures have been widely used for industrial and commercial buildings in the most developed countries since the '60s. These structural systems consist of modular, quickly installable, mass-produced elements that cover large spans. The connection of those elements defines the global structural systems, and it is responsible for the structural response in the presence of vertical and lateral loads, (e.g. gravity or earthquakes).

During those decades of economic growth, buildings were constructed without considering seismic design criteria, resulting in designs that only accounted for gravity loads. Those buildings are characterised by poor or absent connections between structural elements and poorly detailed columns with inadequate confinement and with 90° bend hooks ties only. As a result, precast RC structures often face a significant seismic risk in earthquake-prone areas.

This issue was highlighted in the 2000 FIB report (fib, 2003), which emphasised the combined effect of high seismic vulnerability and exposure in such structures. All the collapsed structures had poor or totally lacking connections between elements and inadequate elements detailing, which led to premature structural collapse and the brittle failure of the columns. On the contrary, structures with well detailed elements and efficient joints showed optimal performances and a correct development and placement of plastic hinges. The topic of precast RC structures vulnerability is particularly sensitive in the Southern European territories (Batalha et al., 2019; Casotto et al., 2015; Sousa et al., 2021), where the late update of both the seismic regulations and the national seismic hazards maps is one of the main responsible for the high number of seismically inadequate precast RC buildings.

Precast RC structures are commonly used for industrial and commercial buildings, but they are also used for constructing schools, shopping malls, gyms and swimming pools. If an earthquake damages these buildings, it can have a major impact on the buildings themselves and the surrounding community (Brookshire et al., 1997). The 2012 Emilia Earthquake is a clear example of how a seismic event can significantly impact an area with numerous precast RC structures (Bournas et al., 2014; Demartino et al., 2018; Ercolino et al., 2016; Grimaz and Malisan, 2014). This event took place in one of the most important Italian industrial areas, and precast RC structures were the most hit structural typology. Thousands of buildings in the region were designed without seismic detailing and collapsed during the seismic event, resulting in 28 casualties, hundreds of injured and displaced people (Liberatore et al., 2013; Magliulo et al., 2014) as summarised in Figure 1.1. The 58% of the local activities were closed or relocated, affecting the regional

economy with enormous losses still visible nowadays. The computed global losses (i.e. direct and indirect losses) averaged 13 billions €. The social effects were huge: the closure of the activities led to job losses, forcing thousands of people to move and decreasing the demography of the hit area (Krausmann, 2014).

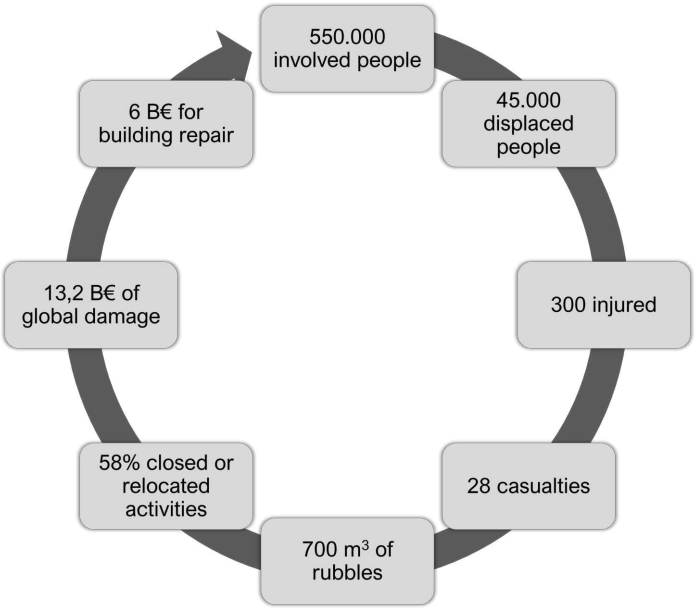

FIGURE 1.1: Emilia Earthquake economical and social impact (Region, 2024).

Besides the social and economic impact, the Emilia Earthquake also had a significant environmental impact. The demolition processes produced 700 m^3 of rubble that, together with the reconstruction processes, is responsible for an increment of CO_2 emissions (UNEP, 2022). It is clear that the seismic retrofit of precast RC structures is essential to prolong their service life and mitigate seismic losses. This is a particular sensitive topic that allow the pursuit of goals 11 (sustainable cities and communities), 12 (responsible consumption and production) and 13 (climate action) of the UN 2030 Agenda for Sustainable Development (UN, 2023). In fact, those goals are associated with the increment of resilience, which is defined as "*a process linking a set of adaptive capacities to a positive trajectory of functioning and adaptation after a disturbance*" (Norris et al., 2008). By adapting the concept of resilience to the civil field, it can be affirmed that the more resilient is a building, the quicker is the restoring process after a seismic event (Basaglia et al., 2020, 2018). According to Francis and Bekera (2014), the resilience capacity of a system is a combination of its adaptive capacities, restorative capacities and absorptive capacities. By adapting these concepts to the earthquake engineering, it can be affirmed that while adaptive and restorative capacities are ruled by external factors, absorptive capacities can be increased by improving the seismic response of a structure, i.e. avoiding structural and non-structural damage.

The most common solutions adopted to improve the seismic response of a structure involve traditional techniques and passive control techniques based on energy dissipation.

Traditional retrofitting techniques, like concrete or steel jacketing and fibre-reinforced polymer (FRP) wrapping, are usually adopted to increase the structural elements' strength, especially the columns. In addition, steel bracings are added to increase global stiffness and steel connections are placed between structural

elements to improve their connectivity (Belleri et al., 2015). Nonetheless, the adoption of traditional techniques requires the execution of additional works at the foundation level and, in case of significant seismic events, can still substantially damage the structure.

Passive control techniques primarily rely on the yielding or friction properties of metallic materials to dissipate seismic energy (Christopoulos and Filatrault, 2006). Implementing Passive Energy Dissipation Devices (PEDDs) proved to be an effective and affordable solution compared to traditional retrofitting methods, preventing damage to structural and non-structural elements. PEDDs are typically installed on the frame braces with a strong impact on the existing structural system, often requiring additional supporting elements and decreasing the usable surface area due to their dimensions (Constantinou et al., 2001; Dal Lago et al., 2021; Martínez-Rueda, 2002; Soong and Spencer, 2002). Moreover, since PEDDs usually work along a single axis, introducing additional dampers along all main directions is essential to guarantee isotropic energy dissipation. However, this is not always possible. For example, introducing devices in all directions is unfeasible for buildings with frames aligned along one principal axis and orthogonal beams not effectively connecting the main frames (e.g. precast RC buildings). This aspect highlights the need for a device that can improve the seismic performance of a precast RC structure even if the building lacks a 3D structural configuration.

Passive control techniques are known to have less environmental impact when compared to traditional techniques (Pomponi and Moncaster, 2016, 2017), especially if the adopted devices are easily restorable and can survive several shocks without damage. This is confirmed in the recent work of Cavalieri et al. (2023), where a significant reduction of CO_2 emissions is computed when retrofitting precast RC structures using innovative solutions instead of traditional ones.

1.2 Objectives and methodology

The need for structural connections improvement and minimally invasive energy dissipation devices brings to the concept of dissipative beam-to-column joints, meeting both requirements in one device. The objectives of this thesis are the conceptualization, prototyping, mechanical and numerical definition of an innovative Friction Damper (FD) installed as a beam-to-column joint in precast RC structures and able to develop bidirectional damping. The damping principle of the developed device is based on friction: FDs are usually characterised by a limited damping degradation even after performing a substantial number of hysteresis cycles. This properties is considered particularly valuable by the author. Moreover, since the energy dissipation involves a limited area of the device, the main elements of a FDs remain intact even after several seismic events. This aspect reflects the circular economy principles, which should be considered when designing new solutions (EC, 2020).

The conceptualization study assesses the feasibility and effectiveness of this innovative device and uses a Multi-Criteria Decision-Making (MCDM) approach to identify the optimal device configuration. Conceptualisation studies are often used as proof-of-concept tools when introducing innovative solutions and are usually characterised by a simplified analytical and numerical characterisation of the object of study (Zhang et al., 2021).

The device's prototyping allows the definition of the material's selection and assembling methodology. An experimental investigation is performed for the development of the novel FD by using Pin-on-Disk (PoD) tests and highlights the main tribological aspects useful for the full-scale tests. PoD tests are set to simulate the real use condition of the device in development under the action of subsequent earthquakes. Sliding surface's material and machining processes are selected taking into account the main body of the device, and the need of reducing the friction's abrasive component and the particle formation during sliding.

The mechanical study assesses the device's mechanical behaviour when subject to mono-directional and bi-directional displacements. The experimental tests are performed following EN 15129 (CEN, 2018) guidelines and investigating different frequencies and displacement amplitudes.

The numerical study allows the definition of a numerical model implementable inside FEM softwares and that reproduces the device's behaviour. The numerical model is calibrated using the results of the mechanical study and compared to the simplified analytical model.

The presented BRFD received the patent n.102020000013738/2022 of the Italian Patent and Trademark Office, Ministry of Economic Development.

1.3 Thesis outline

The present thesis is divided into 8 Chapters.

Chapter 2 focuses on the state-of-the-art review of passive control techniques. §2.1 describes the main properties of PEDDs, with a particular focus on FDs in §2.2. §2.3 focuses on dissipative connections, presenting the recent developments to retrofit precast RC structures.

Chapter 3 focuses on the conceptualization study of the novel device. §3.1 describes the device layout and its structural impact, and §3.2 discusses the analytical model to define the simplified numerical implementation of the device. §3.3 presents the properties of a precast RC structure used as a case study, and §3.4 highlights the influence of the device on the frame's structural behaviour. §3.5 carries out a sensitivity analysis and conducts an importance analysis using a MCDM approach to identify the optimal device configuration for the case study.

Chapter 4 focuses on the tribological study to define the surfaces of the friction interface of the novel device. §4.1 recalls concepts of tribology that are useful for the research and describes how an FD behaves from the tribological point of view. §4.2 shows an overview of the possible surface selection considering literature findings. §4.3 and 4.4 focus on the PoD methodology and the experimental setup. §4.5 and §4.6 show the outcomes of the tribological campaign in terms of surface characterisation and wear test results.

Chapter 5 shows the preliminary mono-directional test results and aims to assess the surfaces selected in Chapter 4. §5.1 defines the device prototyping by considering the main findings of Chapter 4. §5.2 defines the experimental setup and testing protocols, while §5.3 shows the main results.

Chapter 6 shows the bidirectional test results and aims to assess the device's bidirectional behaviour. §6.1 defines the experimental setup and testing protocols, with a particular focus on the definition of the parameters to select the better-performing configuration. §6.2 shows the main results.

Chapter 7 focuses on the definition of a numerical model that reproduces the devices's behaviour. §7.1 recalls the Opensees elements used for the numerical implementation. §7.2 defines a first simplified numerical model that reproduces the overall behaviour of the device. §7.3 defines a refined numerical model that resembles the real geometry of the BRFD and simulates the real behavior and interactions of the main elements of the BRFD. Both models are calibrated by using the experimental results of Chapter 6 and different friction models and compared to the analytical model in §7.4.

Chapter 8 reports the main remarks and findings of the thesis. This final Chapter also shows further research developments.

References

Basaglia, Alberto, Alessandra Aprile, Enrico Spacone, and Luca Pelà (2020). "Assessing community resilience, housing recovery and impact of mitigation strategies at the urban scale: a case study after the 2012 Northern Italy Earthquake". In: *Bulletin of Earthquake Engineering* 18 (13), pp. 6039–6074. DOI: 10.1007/s10518-020-00919-8.

Basaglia, Alberto, Alessandra Aprile, Enrico Spacone, and Francesco Pilla (2018). "Performance-based Seismic Risk Assessment of Urban Systems". In: *International Journal of Architectural Heritage* 12 (7-8), pp. 1131–1149. DOI: 10.1080/15583058.2018.1503371.

Batalha, Nádia, Hugo Rodrigues, and Humberto Varum (2019). "Seismic performance of RC precast industrial buildings—learning with the past earthquakes". In: *Innovative Infrastructure Solutions* 4 (1). DOI: 10.1007/s41062-018-0191-y.

Belleri, Andrea, Mauro Torquati, Paolo Riva, and Roberto Nascimbene (2015). "Vulnerability assessment and retrofit solutions of precast industrial structures". In: *Earthquakes and Structures* 8 (3), pp. 801–820. DOI: 10.12989/eas.2015.8.3.801.

Bournas, Dionysios A., Paolo Negro, and Fabio F. Taucer (2014). "Performance of industrial buildings during the Emilia earthquakes in Northern Italy and recommendations for their strengthening". In: *Bulletin of Earthquake Engineering* 12 (5). DOI: 10.1007/s10518-013-9466-z.

Brookshire, David S., Stephanie E. Chang, Hal Cochrane, Robert A. Olson, Adam Rose, and Jerry Steenson (1997). "Direct and Indirect Economic Losses from Earthquake Damage". In: *Earthquake Spectra* 13 (4), pp. 683–701. DOI: 10.1193/1.1585975.

Casotto, C., V. Silva, H. Crowley, R. Nascimbene, and R. Pinho (2015). "Seismic fragility of Italian RC precast industrial structures". In: *Engineering Structures* 94, pp. 122–136. DOI: 10.1016/j.engstruct.2015.02.034.

Cavalieri, Francesco, Davide Bellotti, Martina Caruso, and Roberto Nascimbene (2023). "Comparative evaluation of seismic performance and environmental impact of traditional and dissipation-based retrofitting solutions for precast structures". In: *Journal of Building Engineering* 79, p. 107918. DOI: 10.1016/j.jobe.2023.107918.

CEN (2018). *Anti-seismic devices (UNI EN 15129:2018)*.

Christopoulos, Constantin and Andrè Filatrault (2006). *Principles of passive supplemental damping and seismic isolation*. IUSS Press. ISBN: 978-88-7358-037-9.

Constantinou, Michael C., Panos Tsopelas, Wilhelm Hammel, and Ani N. Sigaher (2001). "Toggle-Brace-Damper Seismic Energy Dissipation Systems". In: *Journal of Structural Engineering* 127 (2). DOI: 10.1061/(ASCE)0733-9445(2001)127:2(105).

Dal Lago, Bruno, Muhammad Naveed, and Marco Lamperti Tornaghi (2021). "Tension-only ideal dissipative bracing for the seismic retrofit of precast industrial buildings". In: *Bulletin of Earthquake Engineering* 19 (11), pp. 4503–4532. DOI: 10.1007/s10518-021-01130-z.

Demartino, Cristoforo, Ivo Vanzi, Giorgio Monti, and Concetta Sulpizio (2018). "Precast industrial buildings in Southern Europe: loss of support at frictional beam-to-column connections under seismic actions". In: *Bulletin of Earthquake Engineering* 16 (1). DOI: 10.1007/s10518-017-0196-5.

EC (2020). *Circular Economy Principles for Buildings Designs*. European Commission.

Ercolino, M., G. Magliulo, and G. Manfredi (2016). "Failure of a precast RC building due to Emilia-Romagna earthquakes". In: *Engineering Structures* 118, pp. 262–273. DOI: 10.1016/j.engstruct.2016.03.054.

fib (2003). *Seismic design of precast concrete building structures: state-of-art report*. Vol. 27. International Federation for Structural Concrete (fib). ISBN: 978-2-88394-067-3.

Francis, Royce and Behailu Bekera (2014). "A metric and frameworks for resilience analysis of engineered and infrastructure systems". In: *Reliability Engineering & System Safety* 121, pp. 90–103. DOI: 10.1016/j.ress.2013.07.004.

Grimaz, S. and P. Malisan (2014). "Near field domain effects and their consideration in the international and Italian seismic codes". In: *Bollettino di Geofisica Teorica ed Applicata* 55 (4), pp. 717–738. DOI: 10.4430/bgta0130.

Krausmann, Elisabeth (2014). *STREST, report on lessons learned from recent catastrophic events*. Institute for the Protection and Security of the Citizen (Joint Research Centre). DOI: 10.2788/618.

Liberatore, Laura, Luigi Sorrentino, Domenico Liberatore, and Luis D. Decanini (2013). "Failure of industrial structures induced by the Emilia (Italy) 2012 earthquakes". In: *Engineering Failure Analysis* 34, pp. 629–647. DOI: 10.1016/j.engfailanal.2013.02.009.

Magliulo, Gennaro, Marianna Ercolino, Crescenzo Petrone, Orsola Coppola, and Gaetano Manfredi (2014). "The Emilia Earthquake: Seismic Performance of Precast Reinforced Concrete Buildings". In: *Earthquake Spectra* 30 (2), pp. 891–912. DOI: 10.1193/091012EQS285M.

Martínez-Rueda, Juan Enrique (2002). "On the Evolution of Energy Dissipation Devices for Seismic Design". In: *Earthquake Spectra* 18 (2). DOI: 10.1193/1.1494434.

Norris, Fran H., Susan P. Stevens, Betty Pfefferbaum, Karen F. Wyche, and Rose L. Pfefferbaum (2008). "Community Resilience as a Metaphor, Theory, Set of Capacities, and Strategy for Disaster Readiness". In: *American Journal of Community Psychology* 41 (1-2), pp. 127–150. DOI: 10.1007/s10464-007-9156-6.

Pomponi, Francesco and Alice Moncaster (2016). "Embodied carbon mitigation and reduction in the built environment – What does the evidence say?" In: *Journal of Environmental Management* 181, pp. 687–700. DOI: 10.1016/j.jenvman.2016.08.036.

Pomponi, Francesco and Alice Moncaster (2017). "Circular economy for the built environment: A research framework". In: *Journal of Cleaner Production* 143, pp. 710–718. DOI: 10.1016/j.jclepro.2016.12.055.

Region, Emilia-Romagna (2024). *Open Ricostruzione*. URL: https://openricostruzione.regione.emilia-romagna.it/ricostruzione-attivitaproduttive.

Soong, T.T. and B.F. Spencer (2002). "Supplemental energy dissipation: state-of-the-art and state-of-the-practice". In: *Engineering Structures* 24 (3). DOI: 10.1016/S0141-0296(01)00092-X.

Sousa, R., N. Batalha, V. Silva, and H. Rodrigues (2021). "Seismic fragility functions for Portuguese RC precast buildings". In: *Bulletin of Earthquake Engineering* 19 (15), pp. 6573–6590. DOI: 10.1007/s10518-020-01007-7.

UN (2023). *The Sustainable Development Goals Report 2023*. URL: https://sdgs.un.org/goals.

UNEP (2022). *2022 Global Status Report for Buildings and Construction: Towards a Zero-emission, Efficient and Resilient Buildings and Construction Sector*. United Nations Environment Programme.

Zhang, Yichen, Raffaele De Risi, and Nicholas Andrew Alexander (2021). "A frictional sliding on a sprung slope (FSSS) device that axiomatically confers energy dissipation with re-centring to post-tensioned (PT) frames: A conceptual study". In: *Engineering Structures* 244. DOI: 10.1016/j.engstruct.2021.112794.

2
State-of-the-art

2.1 Passive energy dissipation devices

Conventional methods for the design of seismic-resistant structures rely on the ductile behaviour of the structural elements. The inelastic response of these structural elements dissipates the seismic energy in input, leading to structural damage. Adequate seismic design requires the yielding of the structure, protecting the building from collapse under higher-intensity earthquakes. However, the experienced damage may be so critical that a structural demolition is needed. Moreover, codes require activity continuity for strategic buildings, which results in avoiding structural damage under higher-intensity earthquakes. These design criteria are so strict that their application can be unfeasible or extremely expensive when using conventional methods (Martínez-Rueda, 2002).

As a response to the conventional design approach, the scientific community started to present innovative approaches by incorporating Energy Dissipation Devices (EDDs) into structures (Soong and Spencer, 2002). These devices protect the structure from damage by absorbing the seismic input energy. The aim is to concentrate the hysteretic dissipation in specially designed and detailed regions of the structure, avoiding the inelastic behaviour of the structural elements, except perhaps under catastrophic events. While this objective can be achievable for new constructions, the inelastic behaviour of the structural elements may be unavoidable when retrofitting existing structures (Martínez-Rueda, 2002).

EDDs can be divided into three main groups (Christopoulos and Filatrault, 2006):

- *Active systems*. These systems perform real-time monitoring of the structural stresses and eventually apply a set of forces to restore the initial or ideal condition. These devices comprise a monitoring system, a control system and an actuator system. To correctly perform, active systems require constant electric power, limiting their application in the seismic field. During a seismic event, an energy shortage can arise, affecting the correct functioning of the device.
- *Semi-active systems*. These devices behave similarly to the active systems, but the electric dependency is lower, and the control system can modify the device only locally. These devices have a recent development, but their application is still limited.
- *Passive systems*. These devices activate as a function of the elements' internal stresses generated during the seismic event. This system proved to be very efficient and cheap, and for these reasons, it has been largely applied in the seismic field.

Among the mentioned systems, the Passive Energy Dissipation Devices (PEDDs) found wider diffusion and are object of continuous research. The devices are usually linked to the main structural elements and behave as semi-rigid connections with high damping properties. PEDDs are designed to deform only for severe earthquakes and before the yielding or buckling of the main structural elements occurs. Hence, the main structural elements remain undamaged, while the energy dissipation occurs by the hysteretic behaviour of the devices. PEDDs can be divided into three main groups (Christopoulos and Filatrault, 2006), as a function of the activation mechanism:

- *Displacement-Activated*. These devices dissipate energy using the relative displacements that arise between the connection points during the seismic event. Their performance is frequency-independent, and the generated forces are in-phase with the internal stresses of the structure. As a result, the maximum forces of the structure, which arise in correspondence with the pick ground acceleration (PGA), occur simultaneously with the maximum force of the device. Isolators and hysteretic dampers fall into this group.
- *Velocity-Activated*. These devices dissipate energy using the relative velocity that arises between the connection points during the seismic event. Their performance is frequency-dependent, and the generated forces are out-of-phase with the internal stresses of the structure. As a result, the maximum forces of the structure, which arise in correspondence with the pick ground acceleration (PGA), occur at a different time from the maximum force of the device. Because of this asynchronous behaviour, the design forces of the structural elements and the foundation in correspondence with the device's installation point are lower than the ones obtained using displacement-activated devices. Viscous and viscoelastic dampers fall into this group.
- *Motion-Activated*. These devices modify the frequencies of the seismic input using a secondary vibration system. An example is the Tuned-Mass Damper (TMD), which consists of a mass-hook secondary system connected and in resonance, but out-of-phase, with the main structure. As a result, the TMD absorbs the seismic input energy while the structure remains unaltered.

Among the mentioned activation mechanisms, the ones based on displacement and velocity have found large applications in the civil field. In particular, displacement-activated devices are easier to construct than the velocity-activated ones. For this reason, in the following, the focus is on the displacement-activated devices, in particular on the hysteretic devices.

2.1.1 Seismic design philosophy when using energy dissipation devices

Conventional design approaches for seismic-resistant structures are ductility-based (capacity design) and rely on the application of force reduction factors to a specific design seismic force. This simplified methodology is conceived for linear dynamic analyses and approximates the nonlinear behaviour of the structure while considering the structural energy dissipation capacity and deformation capacity (Martínez-Rueda, 2002). The capacity design approach aims to ensure that the seismic ductility demand does not exceed the ductility supply; hence, this approach expects to dissipate the seismic energy by damaging the structural elements. However, when introducing EDDs, the capacity design is inadequate because it cannot correctly represent the damping capacity of those devices.

Following the pioneering work of Housner (1956), numerous authors investigated the possibility of developing energy-based design approaches by relying on the balance between the seismic energy demand and the energy supply of the structure. Although a satisfactory design procedure has not been achieved, when studying the seismic response of a structural system, it is becoming customary to analyse the energy balance to improve the seismic design, particularly when adopting EDDs. In fact, comparing the energy balance of the structural system with and without EDDs provides a way to evaluate the systems' efficiency in terms of dissipated energy.

Source-sink analogies are particularly useful for visually understanding the energy balance principle and the dissipation mechanism of the seismic input energy. In these analogies, a sink represents the structural system, and a water flow represents the energy: when the water reaches the sink border, the structure fails. Figures 2.1(a) and 2.1(b) show the source-sink analogy for a fixed base system without (Popov et al., 1993) and with EDDs (Martínez-Rueda, 2002), respectively. The seismic input energy E_i equals the sum of strain energy E_s (elastic and displacement dependant), kinetic energy E_k (elastic and velocity dependant), viscous damping energy E_ξ (inelastic and velocity dependant) and hysteretic energy E_h (inelastic and displacement dependent). E_h is associated with the inelastic behaviour of the structure and is considered the main responsible for the energy dissipation of the seismic input energy. When considering a fixed base system with EDDs (Figure 2.1(b)), an additional hysteretic energy associated with the device E_{hd} increases the overall dissipated energy. During the design process, it is possible to minimise E_h, eventually to zero, avoiding structural damage.

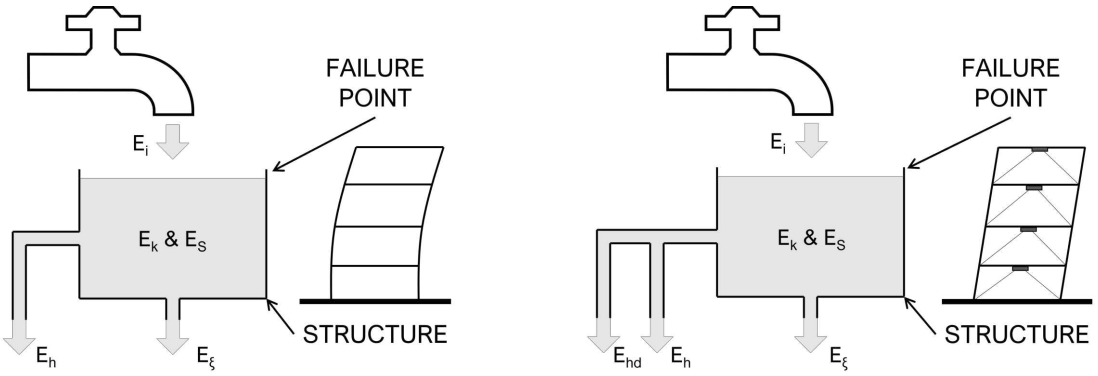

FIGURE 2.1: Source-sink analogy for seismic input energy dissipation: (a) fixed base system and (b) fixed base system with EDDs.

Starting from the '80s and '90s, the research community realised the crucial relationship between structural damage and displacements. The Direct Displacement Based Design (DDBD) was first introduced by Priestley (1993) and was subjected to extended research in Europe, New Zealand and North America during the '90s and the first half of the '00s. This design approach aimed to improve the capacity design approach, where the structural system is designed to limit a specific force demand (*Force-Based Design*). In the DDBD the structural system is designed to achieve a specific performance level, defined as an interstorey drift limit, under a specific seismic intensity level (*Displacement-Based Design*).

The DDBD simplifies the structural system into an equivalent SDOF system characterised by a secant stiffness K_e at a maximum displacement Δd and an equivalent damping coefficient ξ_{eq} representative of the

structural ductility and the eventual EDD presence. The maximum displacement Δd is a design limit and it is associated to the designed structural damage. As a result, when adopting the DDBD, the damage level is a key design element (Priestley et al., 2007).

The DDBD is a useful simplified design approach but has a few limits. The first one is associated with the definition of the equivalent SDOF system, which is accurate only for regular structures where the principal modeshapes are well representative of the overall structure. The second limit is associated with the position of the EDDs inside the structure, which the approach does not account for. As a result, the design of the required EDD is not straightforward.

It is worth noting that when the mentioned approaches were defined, the computational capacity of the computers was limited. As a result, the definition of simplified designed methods was crucial.

To improve the design of the EDDs for a specific structure when subjected to the design seismic input, during the last decade researchers adopted sensitivities analyses to identify the better-performing configuration, which can be defined as the configuration that minimises the difference between seismic input energy E_i and dissipated energy E_{hd} (Jaisee et al., 2021). The seismic input energy is strictly related to the natural period associated with the structure and the dynamic characteristics associated with the ground motion. The dissipated energy is strictly related to the mechanical properties of the EDDs, especially the activation force F_{act}. When performing a sensitivity analysis, it is possible to correlate the difference between seismic input energy and dissipated energy with the activation force of the EDD, obtaining a graph resembling Figure 2.2. The structural performance worsens for F_{act} values too small or too big, while the ideal activation force $F_{act,ideal}$ is in a central area of the graph. It has been observed that fluctuations of the ideal value of ±20% do not significantly influence the structural response, identifying the better-performing zone as the grey area of Figure 2.2.

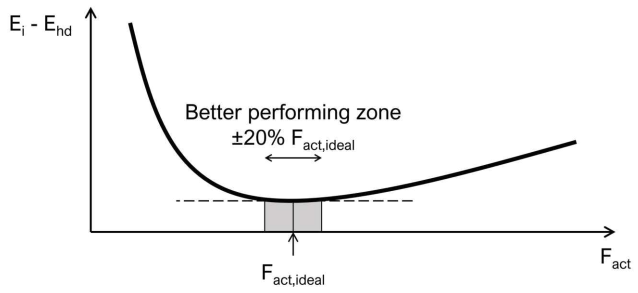

FIGURE 2.2: Identification of the better-performing EDD in a sensitivity analysis.

Sensitivity analyses were then updated into mathematical approaches based on the Genetic Algorithm (GA) (Apostolakis and Dargush, 2009; Cimellaro and Retamales, 2007) and the Multi-Criteria Decision-Making (MCDM) approach (Guo et al., 2017). Both methods vary the position and properties of the EDDs to identify better-performing configuration by considering the effects of multiple-factors, not only the minimization of the difference between seismic input energy E_i and dissipated energy E_{hd}.

GA and MCDM approaches are useful when developing new EDDs, especially to determine how the novel device interacts with a structural system. Moreover, the application of these approaches helps in the identification of simplified design methods for the proposed device. However, GA and MCDM approaches require

the performance of several nonlinear dynamic analyses, which can be computationally demanding. Hence, the adoption of these methods is usually limited to the research field.

2.1.2 Hysteretic devices and their applications

Hysteretic devices are, to date, classified as yielding and friction devices, and energy dissipation occurs thanks to the mechanical and friction properties of the devices' main elements. In general, hysteretic devices are manufactured using traditional materials and, when properly designed, require little maintenance and offer an economical and reliable solution for energy dissipation. Furthermore, experimental studies highlighted that the energy dissipation capacity of the hysteretic devices is usually unaffected by their temperature increment during the seismic response (Martínez-Rueda, 2002).

In general, hysteretic devices connect the main elements of a structure to a braced systems. However, most of these devices were first conceived as a part of base-isolation systems and only in a second moment have been integrated into a braced systems. The first developments of yielding devices started in Japan (Muto, 1969) and New Zealand (Kelly et al., 1972) between the '60s and '70s, and during the '80s and '90s pioneering solutions have been proposed by the scientific community, like the Lead Extrusion Devices (LEDs) by Robinson and Greenbank (1976), the Buckling Restrained Braces (BRBs) by Watanabe et al. (1988) and the Added Damping and Stiffness (ADAS) systems by Tsai et al. (1993). Pioneering works on friction devices started in Canada in the '80s with the work of Pall et al. (1980) and have been optimised by Grigorian et al. (1993) and revised by Aiken et al. (1992), who presented the Sumitomo Friction Device, in the United States in the '90s. Since those decades, hysteretic devices were object of continue research, developments and revision by the scientific community (Castaldo, 2014; Christopoulos and Filatrault, 2006; Soong and Dargush, 1997).

2.2 The evolution of friction dampers

During the last decades, numerous authors focused on friction dampers contributing to the evolution of this promising dissipating system. In the following, a historical overview of friction devices is presented by focusing on pioneering works and highlighting how the design of these devices evolved.

2.2.1 Devices for wall elements

The first studies on friction dampers aimed to provide additional damping to a structural system by installing devices connected to infill panels and wall elements.

Tyler (1977a) proposed a device that used PTFE sliding elements to join the infill panels with the frame members. As represented in Figure 2.3, the device consisted of layered PTFE sliding elements connected with high-strength bolts to steel plates and the infill panels. Tyler (1977b) conducted an experimental test on a prototype of the device and observed that when adopting PTFE as friction material, the obtained hysteresis cycles had a perfectly rectangular shape. The sliding forces of the joint were set to be compatible with the infill panels' load capacity. By adopting this solution, it was possible to simultaneously provide supplemental damping and consider the secondary elements in the design of the main structural system.

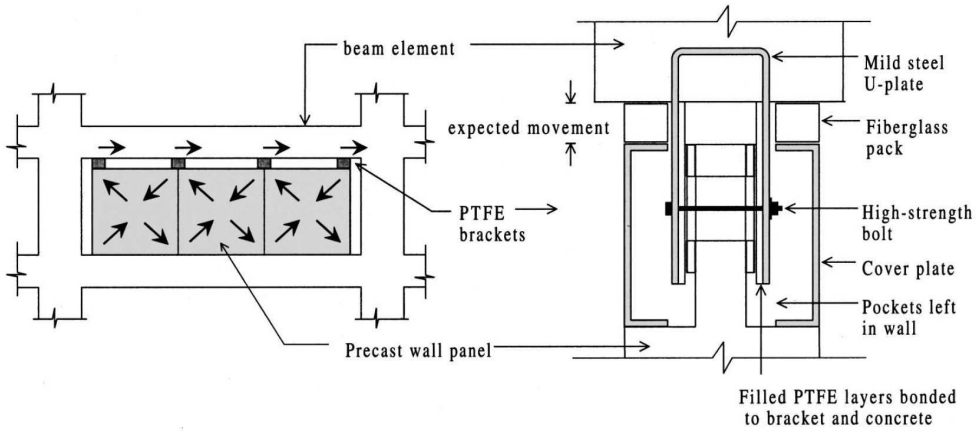

FIGURE 2.3: PTFE sliding elements (Tyler, 1977a).

Despite the promising behaviour exhibited by the proposed solution, Tyler refrained from pursuing additional studies. As a result, practical design guidelines necessary for calibrating the proposed device to ensure optimal structural performance were not presented (Martínez-Rueda, 2002).

Pall et al. (1980) adopted a similar approach by developing a friction device that joins the main structure to precast and cast-in-situ concrete walls. Figure 2.4 shows the possible applications outlined by Pall et al. (1980). The proposed device consisted of brake-lining pads inserted between sliding steel plates connected by high-strength bolts. The coefficient of friction of the brake material and the torque applied to the bolts determined the slipping force of the device. In the experimental investigations conducted by Pall and Marsh (1981), the device exhibited reliable and repeatable hysteresis cycles, with a negligible force degradation over many more cycles than the number expected by a seismic event.

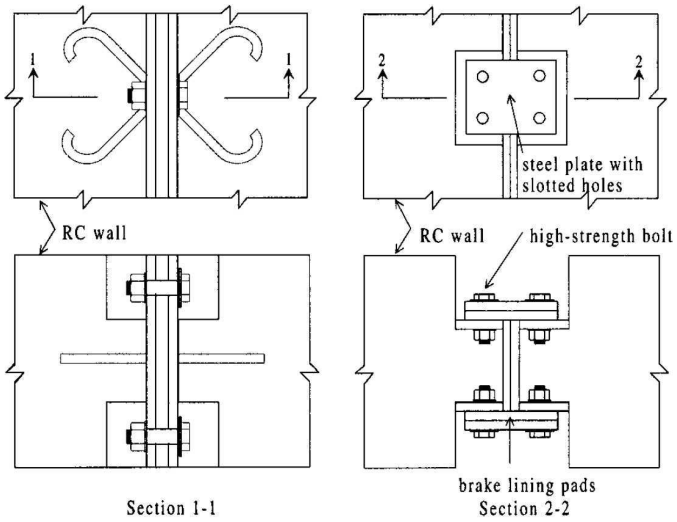

FIGURE 2.4: Friction joints for concrete walls (Pall and Marsh, 1981).

Pall and Marsh (1981) performed a series of nonlinear time history analyses on a concrete wall building of 20-storey by applying several intensity levels of the El Centro 1940 Earthquake NS component. The study revealed that the device required calibration to identify the ideal slipping force for better seismic performance of the building. More precisely, the design criteria followed was the minimization of the

stresses at the base of the walls.

The studies presented by Pall and Marsh highlighted the promising behaviour of friction dampers in controlling structural failure and increasing hysteretic damping. However, their investigation considered only a single earthquake record without evaluating how the seismic excitation influences the structural system response. Moreover, practical design guidelines necessary for calibrating the proposed device to ensure optimal structural performance were not presented (Martínez-Rueda, 2002).

2.2.2 Devices for bracing systems

Pall (1983) conducted further research on friction dampers by focusing on solutions assembled within the intersection of steel braces. Braced frames are an economical solution usually adopted in steel structures to decrease the lateral displacement caused by wind and moderate earthquakes. However, when major earthquakes occur, frame braces do not perform well: their energy dissipation capacity is limited, especially for tension-only configurations, and are subjected to buckling. As a result, the energy dissipation decreases very rapidly.

Figure 2.5 shows the bracing system suggested by Pall (1983) for tension-only and tension-compression configurations. Friction dampers are placed in each brace and are designed to slip under severe earthquakes and before the yielding of the main structural elements.

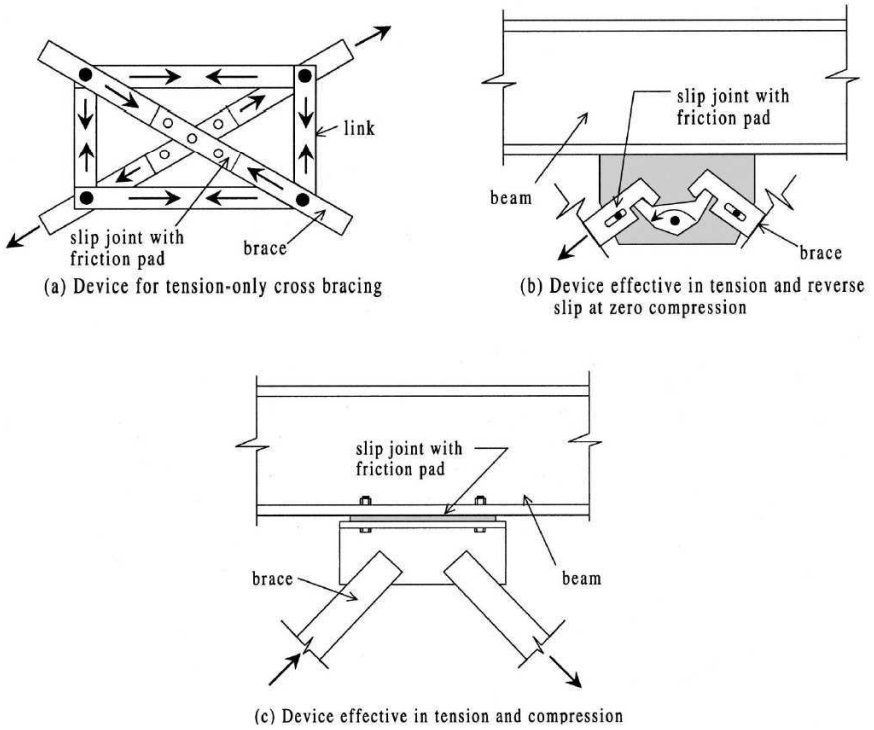

FIGURE 2.5: Friction devices for bracing systems (Pall, 1983).

Pall (1983) performed a series of nonlinear time history analyses on a 10-storey steel frame by applying several intensity levels of the El Centro 1940 Earthquake NS component. The study compared the performance of a moment-resting frame, a braced moment-resisting frame and a friction-damped moment-resting frame. While in the friction-damped configuration all the elements maintained the elastic behaviour,

yielding occurred in several elements when considering the moment-resting and braced moment-resisting configurations.

Pall's friction devices proved to be an efficient solution for energy dissipation in moment-resisting and braced moment-resisting frames. However, studies showed that the load capacity was relatively low and, in addition, the device manufacturing required precision work and specialised training for the installation, resulting in additional expenses (Jaisee et al., 2021).

To overcome these limits, FitzGerald et al. (1989) suggested the introduction of a slotted bolted connection (SBC). SBCs are bracing element connections that slide on a gusset plate connected with high-strength bolts, as visible in Figure 2.6(a). The slipping force depends on the friction coefficient of the gusset plate and the axial tension of the bolts. Experimental studies were conducted on a prototype and Belville washers (see the exploded view of Figure 2.6(b)) are used to maintain a constant bolt tension over the subsequent cycles. The results show reliable and repeatable rectangular-shaped hysteresis cycles.

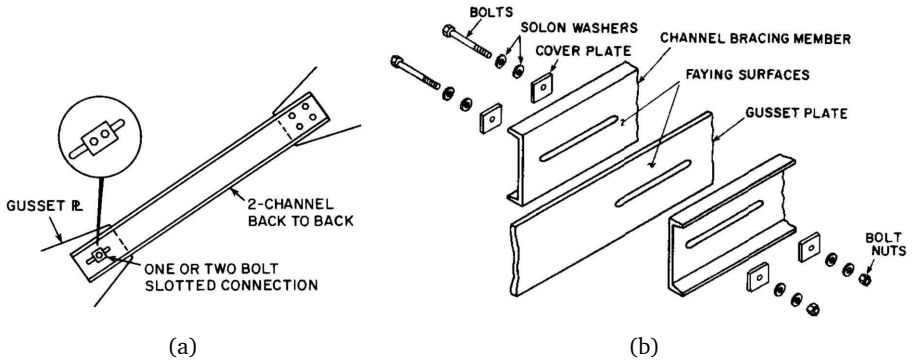

(a) (b)

FIGURE 2.6: SBC suggested by FitzGerald et al. (1989): (a) bracing connection and (b) exploded view.

The device presented by FitzGerald proved to be very efficient and the optimal structural performance was possible by varying the slipping force. Tremblay and Stiemer (1993) conducted additional research on SBCs with promising results.

Grigorian et al. (1993) conducted additional studies on SBCs by focusing on the tribological aspects involved in the sliding phenomena of the friction pads. Friction pads are the plates that dissipate energy by sliding on each other. Grigorian et al. (1993) manufactured the prototype of Figure 2.7(a) and compared the performance of a SBC for steel-steel and steel-bronze friction pad coupling. The results in terms of hysteresis cycles of Figure 2.7(b) show that steel-bronze coupling exhibited a reliable and repeatable rectangular-shaped hysteresis cycle.

Grigorian et al. (1993) also conducted nonlinear time history analyses on a simple frame by considering four earthquake records. For all the selected records, columns remained elastic, the SBC avoided bracing's yielding and buckling, and the energy dissipated averaged 85% of the seismic input energy.

Grigorian et al. (1993) developed a reliable friction device that is low-cost and simple to assemble. Moreover, the easy availability of the adopted materials made the SBC a very attractive solution that it's still adopted and object of research nowadays (Lee et al., 2016; Rodgers et al., 2017; Swain et al., 2016).

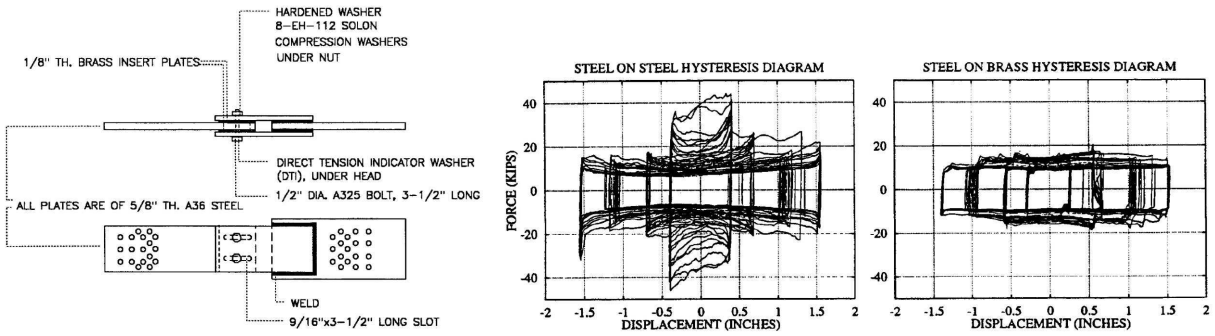

(a) (b)

FIGURE 2.7: SBC investigated by Grigorian et al. (1993): (a) test specimen and (b) recorded hysteresis cycles.

2.2.3 Rotational friction dampers

The first conceptualisation of a rotational friction devices was present in the work of Takai et al. (1988). The device was intended for base isolation and consisted of a sophisticated assembly of four friction dampers, as shown in Figure 2.8. Cone disk springs transmit the axial force of the clamping bolts to the friction surfaces and keep the pressure constant. Brake lining pads and stainless steel disks were responsible for the rotational friction.

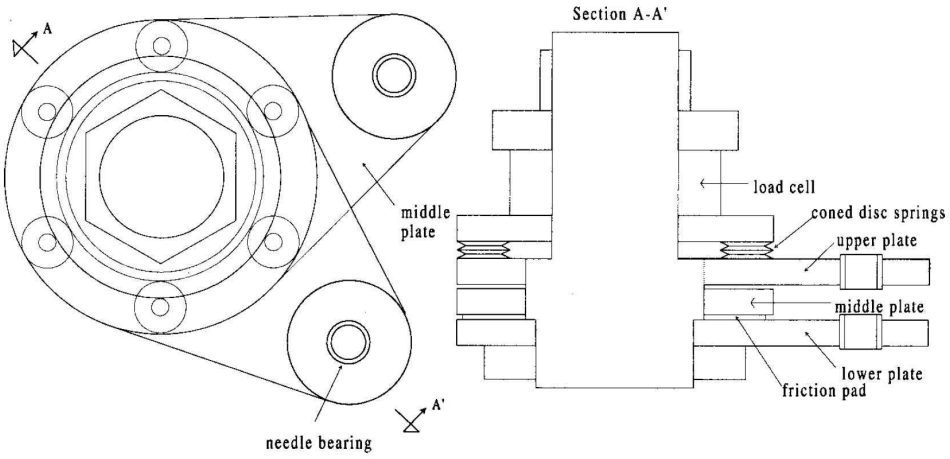

FIGURE 2.8: Friction devices for base isolation system (Takai et al., 1988).

Takai et al. (1988) conducted several analytical and dynamic studies that validated the efficiency of the proposed solution and revealed the friction force independence of the sliding velocity. Moreover, the results confirmed that simple bilinear models adequately predict the hysteretic behaviour of well-designed friction dampers (Martínez-Rueda, 2002).

Mualla and Belev (2002) conducted additional research on the rotational friction mechanism and presented the Rotational Friction Damper (RFD). The device was assembled by connecting a vertical steel plate and two horizontal steel plates with friction pads, washers and nuts, as visible in Figure 2.9(a). When the frame oscillates, the horizontal plates rotate around the vertical plates (see Figure 2.9(b)), dissipating energy and limiting the frame's lateral displacements.

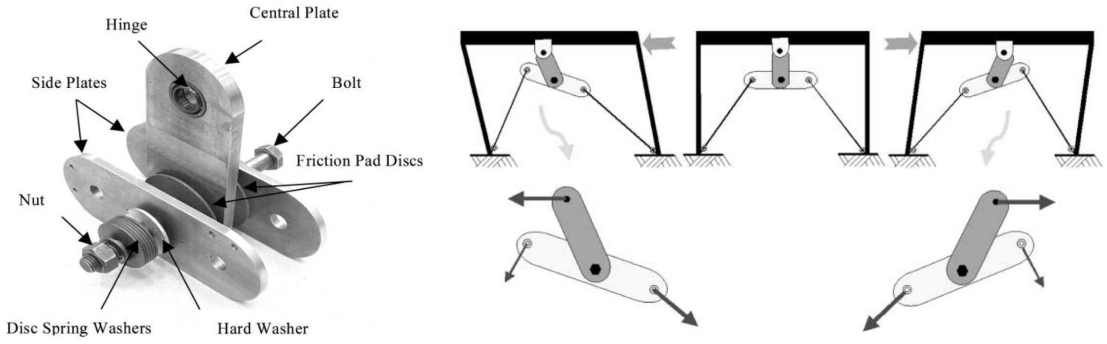

FIGURE 2.9: RFD presented by Mualla and Belev (2002): (a) device layout and (b) frame application.

Mualla and Belev (2002) conducted numerical and dynamic tests on an RFD prototype and observed that the choice of the friction pads' material highly influenced the device's performance. Moreover, the results highlighted the device was velocity-independent, but after a specific displacement range, the device was amplitude-dependent.

Additional studies were conducted on the RFD presented by Mualla and Belev (2002), performing non-linear time history analyses on several buildings. The results exhibited that the RFD was suitable for new structures and efficient in retrofitting existing buildings. Moreover, the adopted solution avoided alteration of the building layout, leaving the building's occupants undisturbed (Jaisee et al., 2021).

2.2.4 Low-invasivity concepts

From the end of the '90s, researchers observed that the seismic retrofit with conventional and innovative techniques was particularly invasive when applied to highly vulnerable buildings. In those cases, these retrofitting techniques may raise undesired effects, such as a significant amount of construction work, a large increment of building weight and base shear, alteration of building layout and severe disturbance to the building occupants. Moreover, when the base shear significantly increments, the redesign scheme also requires retrofitting of the foundation system. To overcome these problems, Martinez-Rueda suggested alternative redesign techniques based on low-invasivity concepts, incorporating friction devices using a local and global approach (Martínez-Rueda, 2002).

The local approach (Martinez-Rueda and Elnashai, 1995) was developed as an alternative to steel bracing systems without or with added damping devices. The introduction of bracing systems usually results in a significant disturbance of the occupants and a loss of space availability and functioning. The local approach consists of rotational friction dampers (Figure 2.10(a)) or yielding devices (Figure 2.10(b)) connected to the existing beam-to-columns joint, considered as the point of the expected plastic hinges formation. The calibration of the devices is obtained by assessing the moment associated with the plastic hinge formation.

Numerical and experimental tests were conducted on a prototype of the configuration in Figure 2.10(a). The selection of friction material consisted of steel and brass, as suggested by Grigorian et al. (1993), while Belleville washers were included to prevent loss of bolt clamping. The manufactured prototype performed

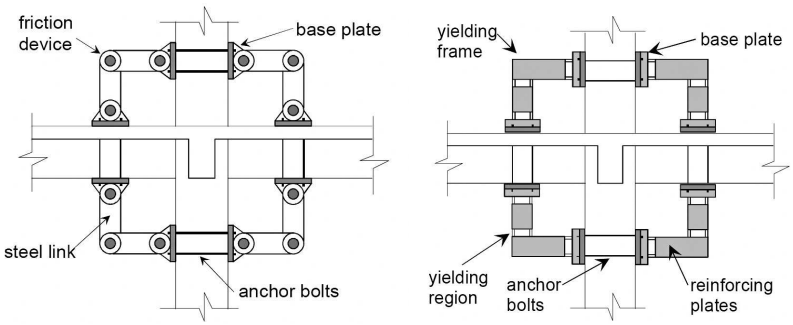

FIGURE 2.10: Low-invasivity redesign adopting the local approach (Martinez-Rueda and Elnashai, 1995): (a) friction dampers and (b) yielding devices configurations.

well and the numerical study exhibited that the adopted solution prevented the structural collapse by incrementing the shear base below 20%.

Although Martinez-Rueda's local approach was economical and valuable in theory, it sometimes required the installation of numerous devices. As a consequence of this, Martınez-Rueda (2000) introduced the global approach by redesigning the bracing systems. Two configurations were suggested: a polygonal-arch bracing and an arch bracing (Figures 2.11(a) and 2.11(b), respectively). The configurations consisted of two bracing systems that connected the frame's upper-centre point with the columns' base points and an added RFD system. The geometry adopted by the bracing systems allowed the rotational movement of the hysteretic device while avoiding loss of space availability.

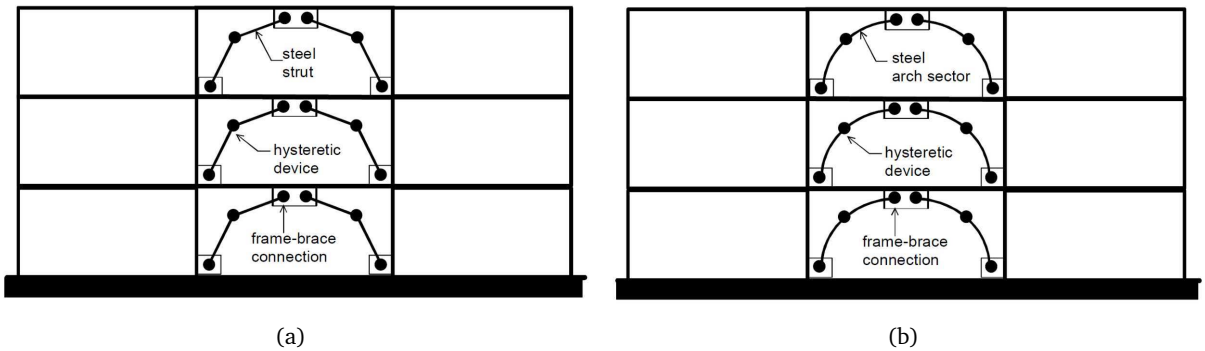

FIGURE 2.11: Low-invasivity redesign adopting the global approach (Martınez-Rueda, 2000): (a) polygonal-arch bracing and (b) arch bracing configurations.

The calibration of the RFD in the global approach required a rotational strength to guarantee a stable and elastic behaviour of the bracing elements. However, the forces developed by the RFD needed to limit the excessive later strength gain to avoid incompatibilities with existing elements' strength, foundations included.

It is worth noting that the applications of low-invasivity redesign techniques modify the flexural and shear demand in correspondence with their application points. As a result, some of the existing elements may require strengthening if needed (Martínez-Rueda, 2002). However, the suggested approach resulted in a valuable solution to limit the loss of space availability for both existing and new buildings.

2.3 Dissipative connections

The concepts of low-invasivity redesign techniques introduced in §2.2.4 focused on the impact of retrofitting works and on the loss of space availability, leading researchers to develop the so-called *dissipative connections*. These devices aimed to connect the main structural elements, especially beams and columns, and to dissipate energy during the seismic event, preventing structural damage.

Dissipative connections found large applications in steel and precast RC structures, where the connection between structural elements is crucial for the seismic performance of the building.

Steel moment-resisting frames (SMRF) were widely used as lateral-resisting systems because of their high-ductile capabilities, which allowed them to withstand large deformations without significative degradation of the structural elements. However, during the 1995 Kobe Earthquake (Japan) a significant number of SMRFs collapsed due to the brittle failure of the connections, showing the importance of fatigue failure for this structural typology.

Precast RC structures spread out for industrial and commercial buildings in industrially developed countries starting in the '60s thanks to the possibility to cover large spans with quick-installable mass-produced elements. When designed for gravity loads only, those buildings are characterised by poor or absent connections between structural elements and poorly detailed columns, resulting in a remarkable seismic risk due to the combined effect of high seismic vulnerability and exposure, as highlighted in the early 2000 state-of-the-art FIB report (fib, 2003).

In the following, an overview of the most interesting solutions is presented, focusing also on the structural typologies.

2.3.1 Steel Frames

The firsts examples of dissipative connections were studied for SMRF by incorporating post-tensioned (PT) steel bars and EDD. Christopoulos et al. (2002) suggested the introduction of PT steel bars to add re-centring capabilities to MRSFs and the use of EDDs to dissipate energy. However, Christopoulos et al. (2002) observed a loss of tension in the PT bars at the beam-to-column interface when using the yielding of dissipative elements. To overcome this problem, Kim and Christopoulos (2008) performed additional studies on this solution and suggested the adoption of FDs in the configuration of a bolted web friction device (WFD), as reported in Figure 2.12, selecting nonasbestos organic (NAO) brake lining pads and stainless steel to obtain the friction interface.

Kim and Christopoulos (2008) performed experimental and numerical studies and observed that the adopted friction interface exhibited stable hysteresis cycles without a significative strength degradation.

Tsai et al. (2008) conducted additional studies on WFD by adopting oversized circular holes instead of the more traditional slotted holes (see Figure 2.13(a)) to allow the gap opening between beams and columns (see Figure 2.13(b)). The friction device was assembled using bronze and steel as friction interface and high-strength bolts with Belleville washers to maintain a constant tension on the bolts.

Tsai et al. (2008) performed analytical and experimental studies on the proposed connection. The first one allowed the definition of the hysteresis cycle law of the BWFD, highlighting the flag-shaped loop typical of

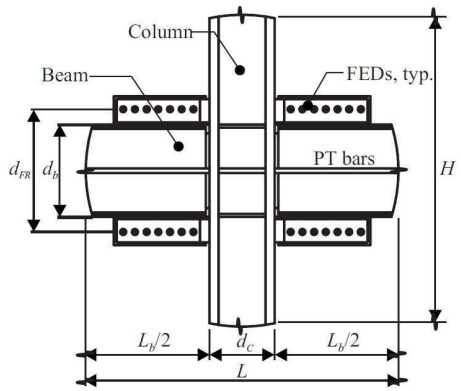

FIGURE 2.12: Self-centring friction connection presented by Kim and Christopoulos (2008).

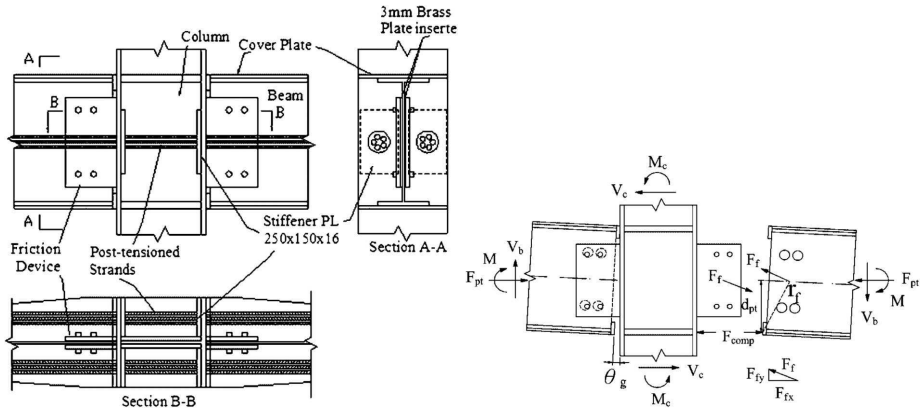

(a) (b)

FIGURE 2.13: Self-centring friction connection presented by Tsai et al. (2008): (a) installation scheme and (b) deformed configurations.

re-centring systems. The second one experimentally confirmed the re-centring behaviour of the connection and the steadiness of the system thanks to the adoption of Belleville washers. However, it was observed that excessive interstorey drifts may result in a loss of tension in PT bars, resulting in a loss of the re-centring capability of the system.

Additional studies on SMRF aimed to improve the traditional double split tee joint by adding a damping component (Latour et al., 2015). Ferrante Cavallaro et al. (2017) improved this idea by presenting the so-called FREEDAM joint in Figure 2.14. The connection consisted of a friction interface placed at the bottom flange of the beam, while high-strength bolts and Belleville washers were adopted to connect the beam and column to the friction device.

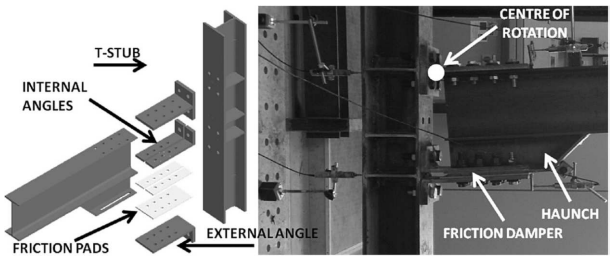

FIGURE 2.14: Configuration of the FREEDAM joint (Ferrante Cavallaro et al., 2017).

Ferrante Cavallaro et al. (2017) performed extensive experimental studies investigating several friction materials (aluminium, bronze, carbide materials) with different hardness. The results showed that coupling steel and harder materials led to a steadier hysteresis cycle and friction coefficient. Moreover, the difference between static and dynamic friction coefficients is irrelevant. Despite the promising behaviour of the solution, the study did not investigate the effects on a concrete frame and design methods were not provided.

2.3.2 Reinforced concrete frames

2.3.2.1 Translational friction based devices

Song et al. (2014) applied the self-centring approach adopted in PT steel frames to PT concrete frames by introducing the connection represented in Figure 2.15. The solution consisted of a bolted WFD with oversized circular holes, similar to the Tsai et al. (2008) configuration, and high-strength bolts with Belleville washers that connected the beam and column. Aluminium and steel constituted the friction interface. The end of the beam was cast inside a steel jacket to protect the beam and column spalling.

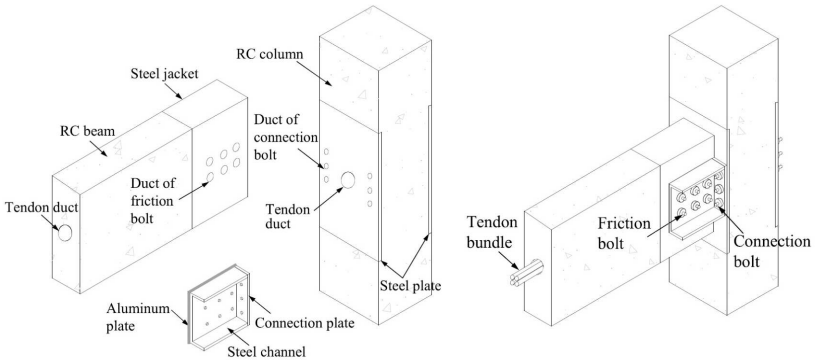

FIGURE 2.15: Connection with bolted WFD connection suggested by (Song et al., 2014).

Song et al. (2014) conducted experimental studies on the WFD and the complete connection. The WFD exhibited a steady rectangular-shaped hysteresis cycle, while the complete connection exhibited the typical flag-shaped hysteresis cycle of re-centring systems. Despite the promising behaviour of the solution, the study did not investigate the effects on a concrete frame and design methods were not provided.

During the last decade, several authors studied dissipative connections for PT concrete frames, adopting solutions similar to Song et al. (2014). Eldin et al. (2020) introduced the configuration of Figure 2.16(a), where a translational FD was connected to a PT concrete frame. The study performed an incremental dynamic analysis (IDA) on PT concrete frames with different heights, exhibiting a significant reduction of interstorey drifts and an increment of base shear.

Huang et al. (2020) presented the alternative redesign of Figure 2.16(b), using a bolted WFD with grooved surfaces and an NAO-stainless steel friction interface to connect the beam and column. Huang et al. (2020) performed analytical and numerical studies that confirmed the efficiency of the solution but highlighted a loss of tension on the PT tendons.

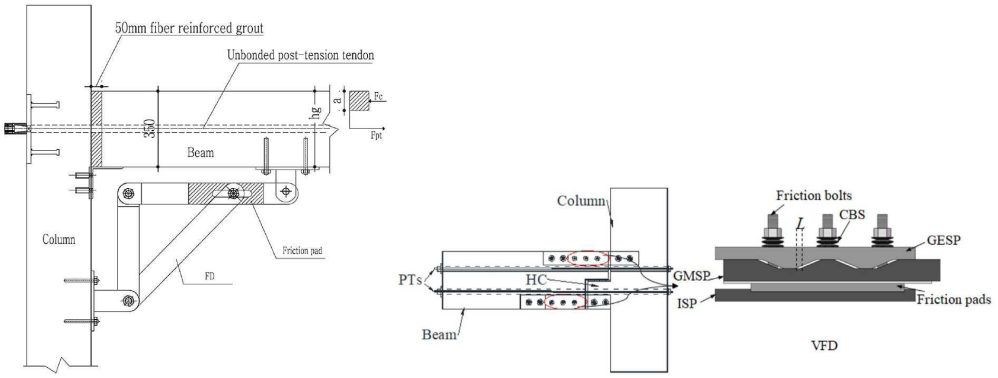

(a) (b)

FIGURE 2.16: Latest friction dissipative connections for PT concrete frame: devices suggested by (a) Eldin et al. (2020) and (b) Huang et al. (2020).

2.3.2.2 Rotational friction based devices

Starting from the middle of the '00s, several authors studied the integration of RFDs as beam-to-column connections for precast RC structures by following the low-invasivity concepts with the local approach of Martinez-Rueda and Elnashai (1995) (§2.2.4).

Morgen and Kurama (2004) presented devices for PT precast RC structures that connect beams and columns and dissipate energy when the joint rotates, as represented in Figure 2.17. The idea of the authors was to combine the re-centring capabilities of a PT frame and the energy dissipation of an RFD, obtaining a self-centring dissipating system.

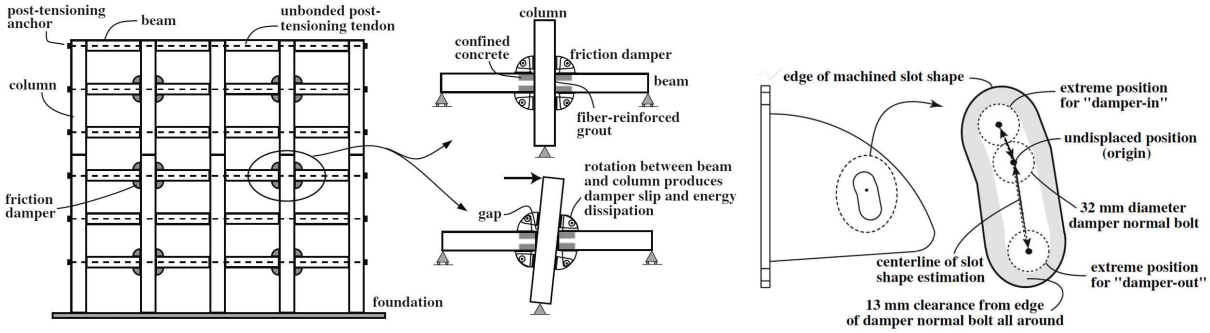

(a) (b)

FIGURE 2.17: Dissipative connections for PT precast RC structures presented by Morgen and Kurama (2009): (a) frame installation and (b) device focus.

Morgen and Kurama (2004) performed experimental studies on a beam-to-column connection without and with the device, observing that the beam and columns degraded less in the configuration with the device. The authors conducted additional studies focusing on the mechanical behaviour of the RFD alone and investigated how different friction interfaces affect the overall RFD behaviour (Morgen and Kurama, 2009). The results showed that the energy dissipation provided by the device was independent of displacement amplitude and frequency. Despite the interesting solution, the authors did not present guidelines for performance-based seismic design and for the device itself.

Valente (2013) conducted numerical research on the device presented by Morgen and Kurama (2004) by investigating the effects of such a device on existing precast RC structures in seismic regions. The author performed nonlinear time history analyses on different typologies of precast structures and conducted a sensitivity analysis to select the optimal devices' activation force. The results of the study highlighted the effectiveness of the device, which reduced the interstorey drift and the formation of the plastic hinge in correspondence with the base columns. However, the introduction of the device resulted in a moderate increment of base shear, which can lead to additional foundation work.

Colajanni et al. (2021) conducted studies on hybrid steel trussed concrete beams, usually adopted for precast RC structures, by updating the solution presented by Morgen and Kurama (2004). The dissipative connection presented by Colajanni et al. (2021) consisted of two main components (see Figure 2.18(a)): a horizontal T-stub bolted connection and a vertical RFD that allows the relative rotations of the beam. High-strength bolts connected the element of these two components, while their preload was responsible for the slipping force.

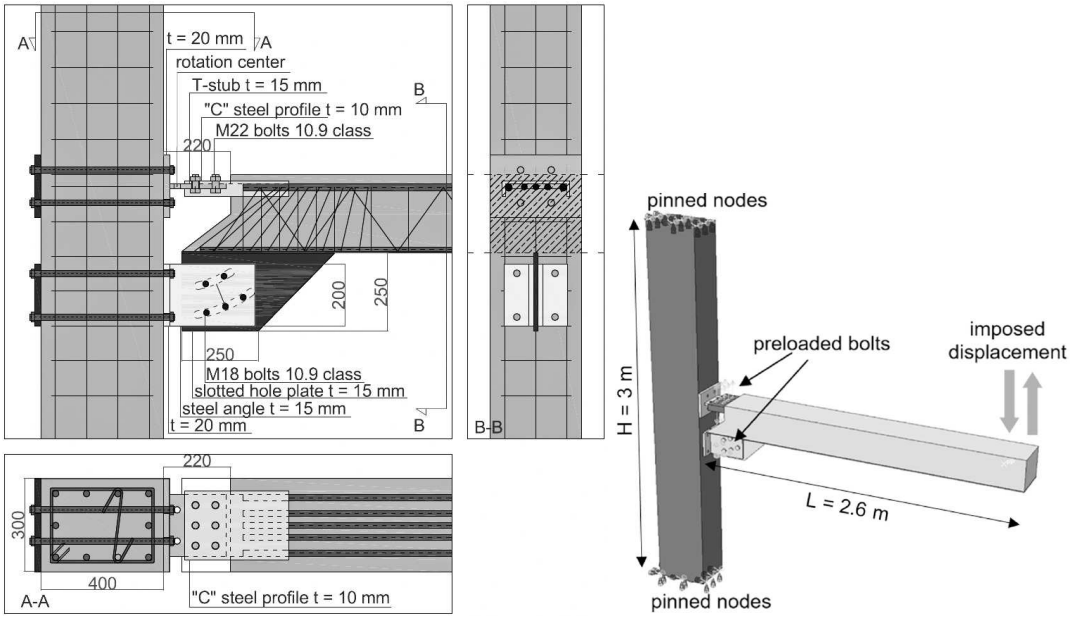

FIGURE 2.18: Dissipative connections for hybrid steel trussed concrete beams presented by Colajanni et al. (2021): (a) frame installation and (b) numerical study.

Colajanni et al. (2021) performed a numerical study to assess the feasibility of the proposed connection by imposing monotonic and cyclic displacements at the end of the beam, as reported in Figure 2.18(b). During the simulation, the elements of the connection remained elastic except for the T-stub element associated with the centre of rotation, while the beam and column remained undamaged. The study primarily aimed to determine the feasibility of the proposed solution. However, to validate the connection and investigate the solution's effectiveness during a seismic event, further research is necessary.

Martinelli and Mulas (2010) presented a dissipative connection for precast RC structures that resembled the configuration of Martinez-Rueda and Elnashai (1995). Figure 2.19 shows a detailed view of the device and how it is installed as a beam-to-column connection.

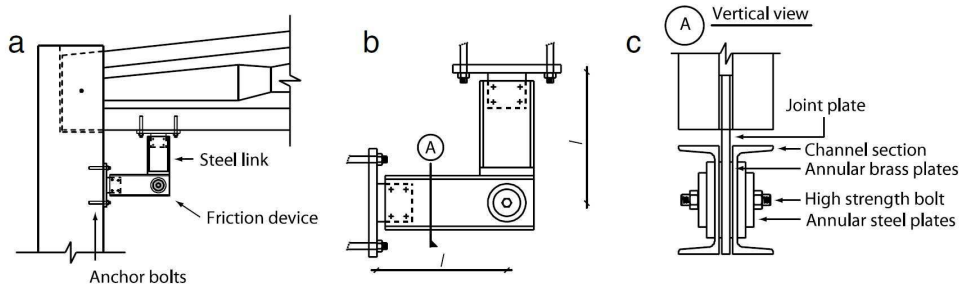

FIGURE 2.19: Dissipative connection with RFD presented by Martinelli and Mulas (2010).

Martinelli and Mulas (2010) conducted a numerical study on a precast RC structure equipped with the device, observing a significant reduction of interstorey drift and an increment of energy dissipation. However, the device produced a moderate increment of the structural stiffness, which led to an increment of the base shear. Moreover, the study was exclusively numerical, missing the experimental validation.

Belleri et al. (2017) updated the solution presented by Martinelli and Mulas (2010) by introducing a re-centring element to obtain a self-centring device, as shown in Figure 2.20(a). The RFD consisted of a brass-steel friction interface and high-strength bolts with Belleville washers, as represented in Figure 2.20(b).

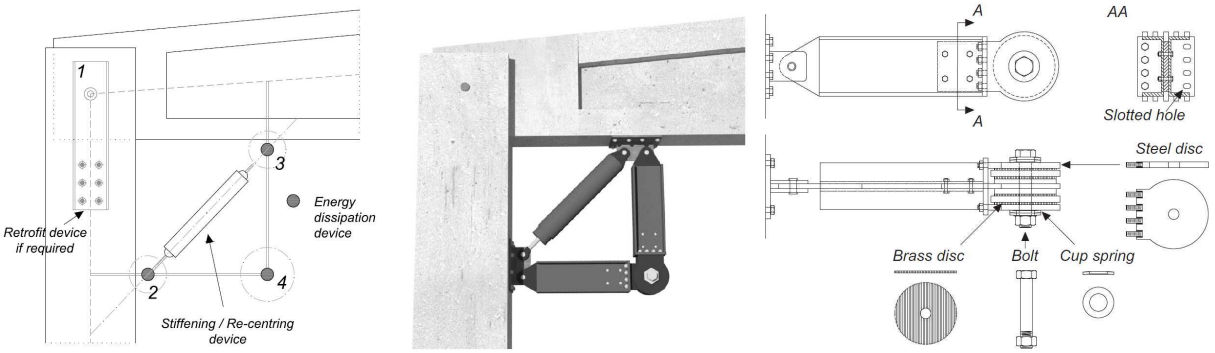

(a) (b)

FIGURE 2.20: Dissipative connections with re-centring presented by Belleri et al. (2017): (a) frame installation and (b) device detail.

Belleri et al. (2017) conducted an analytical and numerical study by applying the presented device inside a precast RC structure. The analytical study carried out formulations to associate the coefficient of friction and bolts' tension to the rotational sliding moment of the device. The numerical study exhibited an improvement of the structural performance under seismic action, with a reduction of interstorey drifts and a moderate increment of the base shear, similar to the results of Martinelli and Mulas (2010). Again, the study was exclusively numerical, missing the experimental validation and design guidelines.

Javidan and Kim (2019) used the design solution presented by Martinelli and Mulas (2010) and Belleri et al. (2017) to define a device for retrofitting RC structures with soft-first-storey. The device consisted of an RFD with high-strength bolts and a clamping force distribution plate connected to a hinged long link, as detailed in Figure 2.21(a). Since RC structures had rigid beam-to-column connections, the device was installed in a pin-jointed steel frame attached to the existing structure, as represented in Figure 2.21(b).

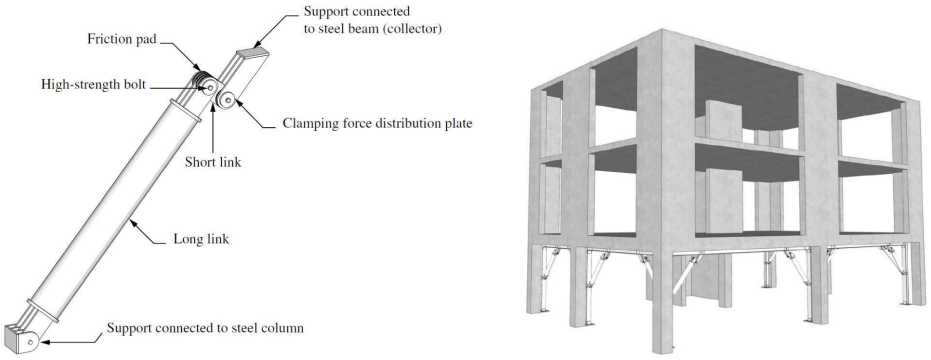

(a) (b)

FIGURE 2.21: Dissipative connections for soft-first-storey structures presented by Javidan and Kim (2019): (a) device detail and (b) frame installation.

Javidan and Kim (2019) developed an analytical formulation for the device's behaviour and conducted experimental tests to validate the solution. A numerical study was finally conducted by performing dynamic analysis on a soft-first-storey RC structure with and without the proposed solution. The results highlighted a significant reduction of interstorey drift, confirming that the application of such a solution can significantly benefit the seismic behaviour of this structural typology.

2.3.2.3 Yielding based devices

Pollini et al. (2018) suggested the use of carbon-wrapped steel tubes as an alternative solution to friction devices for retrofitting precast RC structures. The solution, which was derived from automotive engineering and crash tests, combined the yielding properties of steel tubes with the strength of carbon fibres. When subjected to axial load, the device of Figure 2.22(a) folds itself, as shown in Figure 2.22(b): the steel tube dissipates energy while the carbon fibre limits the outer movements of the steel.

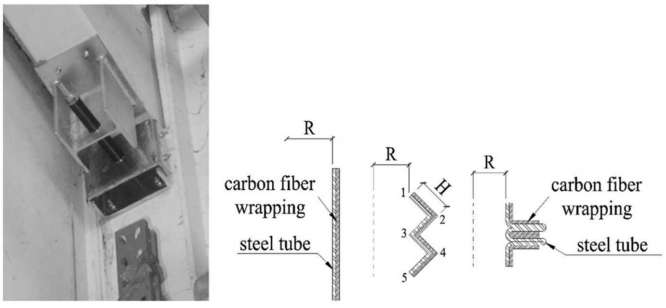

(a) (b)

FIGURE 2.22: Dissipative connections for presented by Pollini et al. (2018): (a) beam-to-column application and (b) folding mechanism.

Pollini et al. (2018) conducted experimental tests to evaluate the mechanical behaviour of the device and performed a dynamic analysis to assess the efficiency of the solution when installed in a precast RC structure. The device exhibited a good behaviour during the buckling process and good repeatability of energy dissipation performances. The numerical simulation exhibited a reduction of the shear base, but the plasticization of the device caused a gap between the beam and columns. For this reason, such devices

require a specific investigation to assess if the residual displacement affects the primary and secondary elements.

Huang et al. (2021) developed an additional example of a dissipative connection for precast RC structures that uses the yielding of steel tube elements. The novel replaceable device consisted of concrete-filled steel tubes with short lengths and web openings, as represented in Figure 2.23. By adopting concrete-filled steel tubes, the device had two advantages: the increment of steel stability during the yielding, and the confinement effect on the concrete. Thus, the concrete-filled steel tube structure acquired a high load-carrying capacity, good ductility and strong plastic deformation capacity. The web opening allowed the correct placement of the plastic hinge in the tubes. The device was conceived to be connected at the end of the beam through a bolted connection (see Figure 2.23), simplifying the replacement after the earthquake.

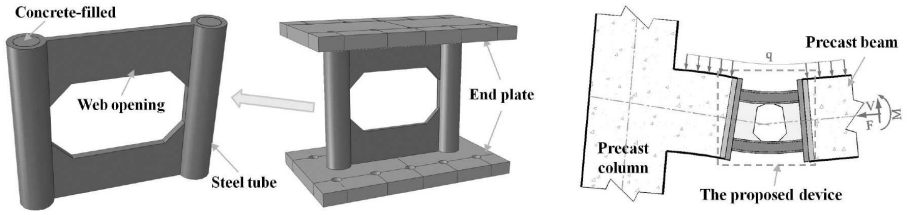

FIGURE 2.23: Replaceable dissipative connection presented by Huang et al. (2021).

The work of Huang et al. (2021) aimed to validate the feasibility of the proposed solution. The authors performed experimental tests applying cyclic loads to investigate the ultimate load-carrying capacity, hysteretic behaviour, energy dissipation and ductility level. These results were used to validate a finite element (FE) model of the device and used to execute a parametric study to investigate the influence of geometric parameters on the performance of the device. Finally, the study analysed the seismic performance of a precast concrete beam-column joint using the device and compared it with that of the monolithic joint. The results showed that the seismic performance of the precast joint significantly improved in terms of the deformation capacity, energy dissipation, and ductility. Furthermore, a significant reduction of damage in beam and column members was observed.

Bressanelli et al. (2021) investigated the behaviour of beam-to-column connection for precast RC structures that used the yielding of a crescent moon shape. Firstly, the authors performed a sensitivity numerical study to identify the device's ideal shape by focusing on the symmetry of the developed hysteresis cycles. Experimental monotonic and cyclic tests were conducted, which confirmed the numerical simulations. Figure 2.24(a) shows the final configuration, and Figure 2.24(a) shows the associated hysteresis cycles.

The work of Bressanelli et al. (2021) included a simple design methodology through nonlinear static and nonlinear time history analysis considering a portal frame of a precast RC structure. The design methodology was validated by performing a NLTHA on a single-storey precast RC structure and focusing on the in-plane and the out-of-plane frames behaviour. The results showed a significant decrement of IDR in both planes' directions, but results on the shear base variation were absent.

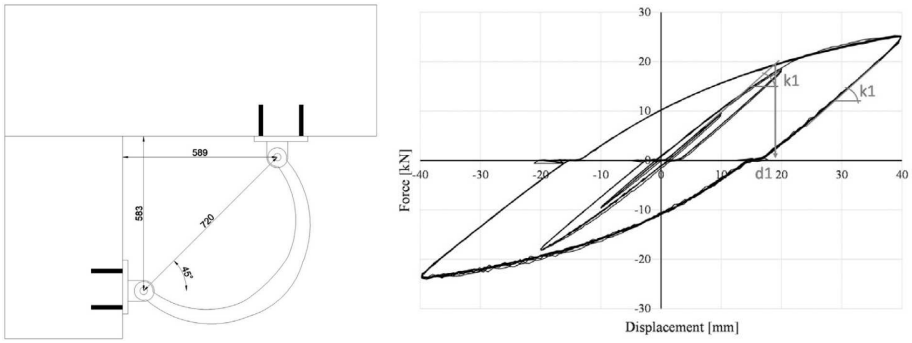

(a) (b)

FIGURE 2.24: Dissipative connections for presented by Bressanelli et al. (2021): (a) beam-to-column application and (b) developed hysteresis cycle.

2.4 Conclusive remarks

Seismic-resistant structures are traditionally designed to rely on the ductile behaviour of the structural elements. The inelastic response of these elements is responsible for dissipating the seismic energy, which leads to structural damage. To ensure adequate seismic design, the structural elements yield, protecting the building from collapse under higher-intensity earthquakes. However, the damage experienced may be so severe that structural demolition becomes necessary. Moreover, codes require the activity continuity for strategic buildings, which means avoiding structural damage under higher-intensity earthquakes. The application of these design criteria can be difficult or extremely expensive when using conventional methods (Martínez-Rueda, 2002).

As a response to the conventional design approach, the scientific community presented innovative approaches by incorporating energy dissipation devices (EDDs) into the structures (Soong and Spencer, 2002). These devices are designed to protect the structure from damage by absorbing the seismic input energy. The aim is to concentrate the hysteretic dissipation in specially designed and detailed regions of the structure, avoiding the inelastic behaviour of the structural elements.

Staring from the end of the ’90s, researchers observed that the seismic retrofit with conventional and innovative techniques was particularly invasive when applied to highly vulnerable buildings. In those cases, these retrofitting techniques raised undesired effects, such as a significant amount of construction work, a large increment of building weight and base shear, alteration of building layout and severe disturbance to the building occupants. Moreover, when the base shear significantly increments, the redesign scheme also requires retrofitting of the foundation system. To overcome these problems, Martínez-Rueda (2002) suggested alternative redesign techniques based on low-invasivity concepts by incorporating friction devices using a local and global approach.

The concepts of low-invasivity redesign techniques led researchers to develop the so-called *dissipative connections*. These devices aimed to connect the main structural elements, especially beams and columns, and to dissipate energy during the seismic event, preventing structural damage. Dissipative connections found large applications in steel and precast RC structures, where the connection between structural elements is crucial for the seismic performance of the building.

The devices presented in §2.3 proved to be very efficient in terms of energy dissipation and base shear reduction without limiting the buildings' usable surface area, which is an important aspect when the activity of the building requires open-spaces. Moreover, the easy replaceability of the devices is a useful property that must be considered when developing a friction device.

Since dampers usually work along a single axis, introducing additional devices along all main directions is essential to guarantee isotropic energy dissipation. However, this is not always possible. For example, introducing devices in all directions is unfeasible for buildings with frames aligned along one principal axis and orthogonal beams not effectively connecting the main frames (e.g. precast RC buildings). This aspect highlights the need for a device that can improve the seismic performance of a precast RC structure even if the building lacks a 3D structural configuration.

The need for a dissipative device that can improve the overall seismic performance of a precast RC structure and has a low architectonical and environmental impact led the author to develop a bidirectional damping device installed as a beam-to-column joint. This device unifies the concepts of RFDs and movable plate system, obtaining a so-called Bidirectional Rotational Friction Damper (BRFD) that produces a damping effect along two main directions (Aprile et al., 2023). Furthermore, the device's ability to dissipate energy through friction enables it to remain undamaged during multiple seismic events while maintaining its damping capacity.

The following Chapter 3 shows the conceptualization study of the 2D dissipative connection object of the present thesis.

References

Aiken, Ian D., Douglas K. Nims, and James M. Kelly (1992). "Comparative study of four passive energy dissipation systems". In: *Bulletin of the New Zealand Society for Earthquake Engineering* 25 (3), pp. 175–192. DOI: 10.5459/bnzsee.25.3.175-192.

Apostolakis, G. and G. F. Dargush (2009). "Optimal seismic design of moment-resisting steel frames with hysteretic passive devices". In: *Earthquake Engineering & Structural Dynamics*. DOI: 10.1002/eqe.944.

Aprile, Alessandra, Eleonora Grossi, and Matteo Zerbin (2023). "A Novel Friction Damper for Seismic Retrofit of Precast RC Structures with Poor Connections". In: ed. by Ilki Alper, Çavunt Derya, and Selim Çavunt Yavuz. Springer - Lecture Notes in Civil Engineering (LNCE), pp. 1384–1394. DOI: 10.1007/978-3-031-32519-9_140.

Belleri, Andrea, Alessandra Marini, Paolo Riva, and Roberto Nascimbene (2017). "Dissipating and re-centring devices for portal-frame precast structures". In: *Engineering Structures* 150. DOI: 10.1016/j.engstruct.2017.07.072.

Bressanelli, Michele Egidio, Marco Bosio, Andrea Belleri, Paolo Riva, and Piergiovanni Biagiotti (2021). "Crescent-Moon Beam-To-Column Connection for Precast Industrial Buildings". In: *Frontiers in Built Environment* 7. DOI: 10.3389/fbuil.2021.645497.

Castaldo, Paolo (2014). *Integrated Seismic Design of Structure and Control Systems*. Springer International Publishing. ISBN: 978-3-319-02614-5. DOI: 10.1007/978-3-319-02615-2.

Christopoulos, Constantin and Andrè Filatrault (2006). *Principles of passive supplemental damping and seismic isolation*. IUSS Press. ISBN: 978-88-7358-037-9.

Christopoulos, Constantin, Andre Filiatrault, Chia-Ming Uang, and Bryan Folz (2002). "Posttensioned Energy Dissipating Connections for Moment-Resisting Steel Frames". In: *Journal of Structural Engineering* 128 (9), pp. 1111–1120. DOI: 10.1061/(ASCE)0733-9445(2002)128:9(1111).

Cimellaro, Gian Paolo and Rodrigo Retamales (2007). "Optimal softening and damping design for buildings". In: *Structural Control and Health Monitoring* 14 (6). DOI: 10.1002/stc.181.

Colajanni, Piero, Lidia La Mendola, Alessia Monaco, and Salvatore Pagnotta (2021). "Design of RC joints equipped with hybrid trussed beams and friction dampers". In: *Engineering Structures* 227. DOI: 10.1016/j.engstruct.2020.111442.

Eldin, Mohamed Nour, Assefa Jonathan Dereje, and Jinkoo Kim (2020). "Seismic retrofit of RC buildings using self-centering PC frames with friction-dampers". In: *Engineering Structures* 208. DOI: 10.1016/j.engstruct.2019.109925.

Ferrante Cavallaro, G., A. Francavilla, M. Latour, V. Piluso, and G. Rizzano (2017). "Experimental behaviour of innovative thermal spray coating materials for FREEDAM joints". In: *Composites Part B: Engineering* 115. DOI: 10.1016/j.compositesb.2016.09.075.

fib (2003). *Seismic design of precast concrete building structures: state-of-art report*. Vol. 27. International Federation for Structural Concrete (fib). ISBN: 978-2-88394-067-3.

FitzGerald, T. F., Thalia Anagnos, Mary Goodson, and Theodore Zsutty (1989). "Slotted Bolted Connections in Aseismic Design for Concentrically Braced Connections". In: *Earthquake Spectra* 5 (2), pp. 383–391. DOI: 10.1193/1.1585528.

Grigorian, C. E., T. S. Yang, and E. P. Popov (1993). "Slotted Bolted Connection Energy Dissipators". In: *Earthquake Spectra* 9 (3). DOI: 10.1193/1.1585726.

Guo, Anxin, Zhenliang Liu, Suchao Li, and Hui Li (2017). "Seismic performance assessment of highway bridge networks considering post-disaster traffic demand of a transportation system in emergency conditions". In: *Structure and Infrastructure Engineering* 13 (12), pp. 1523–1537. DOI: 10.1080/15732479.2017.1299770.

Housner, George William (1956). "Limit design of structures to resist earthquakes". In: 1st World Conference on Earthquake Engineering, pp. 1–11.

Huang, Linjie, Zhen Zhou, Xiaogang Huang, and Yongwei Wang (2020). "Variable friction damped self-centering precast concrete beam–column connections with hidden corbels: Experimental investigation and theoretical analysis". In: *Engineering Structures* 206. DOI: 10.1016/j.engstruct.2019.110150.

Huang, Wei, Gaoxing Hu, Xinwei Miao, Xinyi Liu, and Haiqiao Xie (2021). "SEISMIC PERFORMANCE OF CONCRETE-FILLED STEEL TUBE DEVICES FOR PRECAST CONCRETE BEAM-COLUMN CONNECTIONS". In: *Journal of Mechanics of Materials and Structures* 16 (1), pp. 63–88. DOI: 10.2140/JOMMS.2021.16.63.

Jaisee, Sujit, Feng Yue, and Yi Hao Ooi (2021). "A state-of-the-art review on passive friction dampers and their applications". In: *Engineering Structures* 235, p. 112022. DOI: 10.1016/j.engstruct.2021.112022.

Javidan, Mohammad Mahdi and Jinkoo Kim (2019). "Seismic Retrofit of Soft-First-Story Structures Using Rotational Friction Dampers". In: *Journal of Structural Engineering* 145 (12). DOI: 10.1061/(ASCE)ST.1943-541X.0002433.

Kelly, J. M., R. I. Skinner, and A. J. Heine (1972). "Mechanisms of energy absorption in special devices for use in earthquake resistant structures". In: *Bulletin of the New Zealand Society for Earthquake Engineering* 5 (3), pp. 63–88. DOI: 10.5459/bnzsee.5.3.63-88.

Kim, Hyung-Joon and Constantin Christopoulos (2008). "Friction Damped Posttensioned Self-Centering Steel Moment-Resisting Frames". In: *Journal of Structural Engineering* 134 (11). DOI: 10.1061/(ASCE)0733-9445(2008)134:11(1768).

Latour, Massimo, Vincenzo Piluso, and Gianvittorio Rizzano (2015). "Free from damage beam-to-column joints: Testing and design of DST connections with friction pads". In: *Engineering Structures* 85. DOI: 10.1016/j.engstruct.2014.12.019.

Lee, Chang-Hwan, Jaeho Ryu, Jintak Oh, Chang-Hee Yoo, and Young K. Ju (2016). "Friction between a new low-steel composite material and milled steel for SAFE Dampers". In: *Engineering Structures* 122, pp. 279–295. DOI: 10.1016/j.engstruct.2016.04.056.

Martinelli, Paolo and Maria Gabriella Mulas (2010). "An innovative passive control technique for industrial precast frames". In: *Engineering Structures* 32 (4). DOI: 10.1016/j.engstruct.2009.12.038.

Martinez-Rueda, J.Enrique and A.S. Elnashai (1995). "A novel technique for the retrofitting of reinforced concrete structures". In: *Engineering Structures* 17 (5). DOI: 10.1016/0141-0296(95)00019-4.

Martínez-Rueda, Juan Enrique (2002). "On the Evolution of Energy Dissipation Devices for Seismic Design". In: *Earthquake Spectra* 18 (2). DOI: 10.1193/1.1494434.

Martınez-Rueda, J. E. (2000). "Incorporation of hysteretic devices on bracing systems of low invasivity: A new approach for the seismic redesign of framed structures". In: New Zealand Society for Earthquake Engineering. ISBN: 9780958215435.

Morgen, Brian G. and Yahya C. Kurama (2004). "A Friction Damper for Post-Tensioned Precast Concrete Moment Frames". In: *PCI Journal* 49 (4), pp. 112–133. DOI: 10.15554/pcij.07012004.112.133.

Morgen, Brian G. and Yahya C. Kurama (2009). "Characterization of two friction interfaces for use in seismic damper applications". In: *Materials and Structures* 42 (1). DOI: 10.1617/s11527-008-9365-y.

Mualla, Imad H. and Borislav Belev (2002). "Performance of steel frames with a new friction damper device under earthquake excitation". In: *Engineering Structures* 24 (3). DOI: 10.1016/S0141-0296(01)00102-X.

Muto, Kiyoshi (1969). “Earthquake resistant design of 36-storied Kasumigaseki building”. In: 4th World Conference on Earthquake Engineering.

Pall, Avtar S. (1983). “Friction Devices for aseismic design of buildings”. In: 4th Canadian Conference on Earthquake Engineering, pp. 475–484.

Pall, Avtar S. and Cedric Marsh (1981). “Friction-Damped Concrete Shearwalls”. In: *ACI Journal Proceedings* 78 (3). DOI: 10.14359/6916.

Pall, Avtar S., Cedric Marsh, and Paul Fazio (1980). “Friction Joints for Seismic Control of Large Panel Structures”. In: *PCI Journal* 25‘ (6), pp. 38–61. DOI: 10.15554/pcij.11011980.38.61.

Pollini, Andrea Vittorio, Nicola Buratti, and Claudio Mazzotti (2018). “Experimental and numerical behaviour of dissipative devices based on carbon-wrapped steel tubes for the retrofitting of existing precast structures”. In: *Earthquake Engineering & Structural Dynamics* 47 (5), pp. 1270–1290. DOI: 10.1002/eqe.3017.

Popov, Egor P., Tzong-Shuoh Yang, and Carl E. Grigorian (1993). “New Directions in Structural Seismic Designs”. In: *Earthquake Spectra* 9 (4), pp. 845–875. DOI: 10.1193/1.1585743.

Priestley, M. J. N., G. M. Calvi, and M. J. Kowalsky (2007). *Displacement-based seismic design of structures*. IUSS Press : Distributed by Fondazione EUCENTRE. ISBN: 978-88-6198-000-6.

Priestley, M.J.N. (1993). “Myths and Fallacies in Earthquake Engineering – Conflicts Between Design and Reality”. In: NZSEE.

Robinson, W. H. and L. R. Greenbank (1976). “An extrusion energy absorber suitable for the protection of structures during an earthquake”. In: *Earthquake Engineering & Structural Dynamics* 4 (3), pp. 251–259. DOI: 10.1002/eqe.4290040306.

Rodgers, G.W., J.G. Chase, R. Causse, J. Chanchi, and G.A. MacRae (2017). “Performance and degradation of sliding steel friction connections: Impact of velocity, corrosion coating and shim material”. In: *Engineering Structures* 141. DOI: 10.1016/j.engstruct.2017.02.070.

Song, Liang-long, Tong Guo, and Cheng Chen (2014). “Experimental and numerical study of a self-centering prestressed concrete moment resisting frame connection with bolted web friction devices”. In: *Earthquake Engineering & Structural Dynamics* 43 (4), pp. 529–545. DOI: 10.1002/eqe.2358.

Soong, T. T. and G. F. Dargush (1997). *Passive Energy Dissipation Systems in Structural Engineering*. John Wiley & Sons. ISBN: 0-471-96821-8.

Soong, T.T. and B.F. Spencer (2002). “Supplemental energy dissipation: state-of-the-art and state-of-the-practice”. In: *Engineering Structures* 24 (3). DOI: 10.1016/S0141-0296(01)00092-X.

Swain, Subhransu S., Sanjaya K. Patro, and Ravi Sinha (2016). “Numerical methodology for dynamic analysis of buildings with friction dampers”. In: *Bulletin of the New Zealand Society for Earthquake Engineering* 49 (3), pp. 245–266. DOI: 10.5459/bnzsee.49.3.245-266.

Takai, H., T. Uno, and K. Nagai (1988). “Study on the friction damper as the device of a base isolation system”. In: 9th World Conference on Earthquake Engineering, Vol. 5, pp. 803–807. ISBN: 9784895800105.

Tremblay, R. and S. F. Stiemer (1993). “Energy dissipation through friction bolted connections in concentrically braced steel frames”. In: Proceedings of Seminar on Seismic Isolation, Passive Energy Dissipation, and Active Control.

Tsai, Keh-Chyuan, Huan-Wei Chen, Ching-Ping Hong, and Yung-Feng Su (1993). “Design of Steel Triangular Plate Energy Absorbers for Seismic-Resistant Construction”. In: *Earthquake Spectra* 9 (3), pp. 505–528. DOI: 10.1193/1.1585727.

Tsai, Keh-Chyuan, Chung-Che Chou, Chi-Lon Lin, Pei-Ching Chen, and Sheng-Jhih Jhang (2008). “Seismic self-centering steel beam-to-column moment connections using bolted friction devices”. In: *Earthquake Engineering & Structural Dynamics* 37 (4), pp. 627–645. ISSN: 0098-8847.

Tyler, R. G. (1977a). “Damping in building structures by means of PTFE sliding joints”. In: *Bulletin of the New Zealand Society for Earthquake Engineering* 10 (3), pp. 139–142. DOI: 10.5459/bnzsee.10.3.139-142.

Tyler, R. G. (1977b). “Dynamic tests on PTFE sliding layers under earthquake conditions”. In: *Bulletin of the New Zealand Society for Earthquake Engineering* 10 (3), pp. 129–138. DOI: 10.5459/bnzsee.10.3.129-138.

Valente, Marco (2013). “Improving the Seismic Performance of Precast Buildings using Dissipative Devices”. In: *Procedia Engineering* 54. DOI: 10.1016/j.proeng.2013.03.073.

Watanabe, Atushi, Yasuyoshi Hitomi, Eiichiro Saeki, Akira Wada, and Morihisa Fujimoto (1988). “Properties of brace encased in buckling-restraining concrete and steel tube”. In: Ninth World Conference on Earthquake Engineering, Vol. IV.

3 Conceptualization study

The author developed a Bidirectional Rotational Friction Damper (BRFD) that can be installed as a beam-to-column joint. This device combines the concepts of RFDs and movable plate system, providing damping along two main directions. Furthermore, the BRFD can dissipate energy through friction, remaining undamaged during multiple seismic events while maintaining its damping capacity.

The present chapter shows the conceptualisation study of the BRFD to assess the feasibility and effectiveness of this innovative solution by a multi-criteria decision-making (MCDM) approach.

3.1 Device layout and its structural impact

The BRFD is obtained by assembling layered steel plates, combining RFDs and a movable plate system to achieve a bidirectional behaviour. Figure 3.1(a) shows an axonometric view of the BRFD, while Figure 3.1(b) shows an example of its installation within one of the main portal frames at a 45° inclination angle from the existing beam as a beam-to-column joint. In the following, lowercase letters indicate the local reference system of the BRFD and, in general, of an element, while uppercase letters indicate the global reference system of the structure. It is worth noting that the plane generated by the BRFD's local x- and y-axis is inclined at 45° and perpendicular to the global XZ plane. Furthermore, the connection braces are hinged to the existing beam and column to allow the rotations around the global Y axis only and the deformations along the BRFD local x axis.

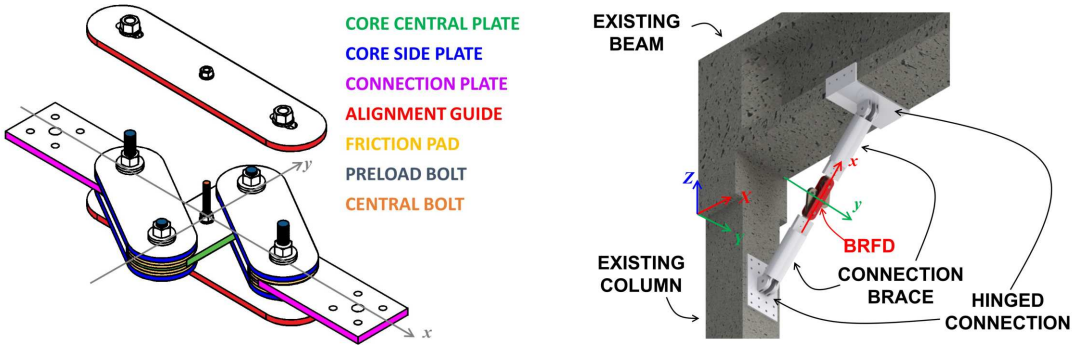

(a) (b)

FIGURE 3.1: BRFD (a) axonometric view and (b) example of installation as a beam-to-column joint.

Core plates are the primary components of BRFD and are held together with four preload stud bolts. In each core plate's ends, friction pads are interlocked and kept in contact by the pressure generated by the stud bolts; as the device activates, the core plates' ends rotate around the stud bolts, and the friction pads slide on each other, dissipating energy and obtaining the deformed shape of Figure 3.2(a). A general displacement can be decomposed into a longitudinal component Δ_x and a transversal component Δ_y. Consequently, the BRFD's activation force has two components: a longitudinal component $F_{act,x}$ (local x-direction) and a transversal component $F_{act,y}$ (local y-direction). Two alignment guides with slotted holes are placed at the top and bottom of the device to keep preload bolts aligned with the central bolt, ensuring controlled displacements.

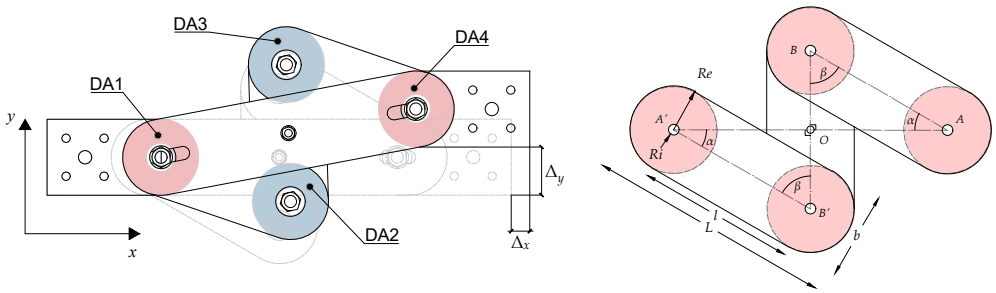

(a) (b)

FIGURE 3.2: BRFD (a) bidirectional deformation shape and (b) core with circular contact areas highlighted in red colour.

When introducing the BRFD inside a precast RC frame, the static scheme of the columns is expected to change from cantilever (Figures 3.3(a) and 3.3(c)) into double-fixed elements (Figures 3.3(b) and 3.3(d)), resulting in a structural stiffness increment in both in-plane and out-of-plane frame's directions (see Figure 3.3).

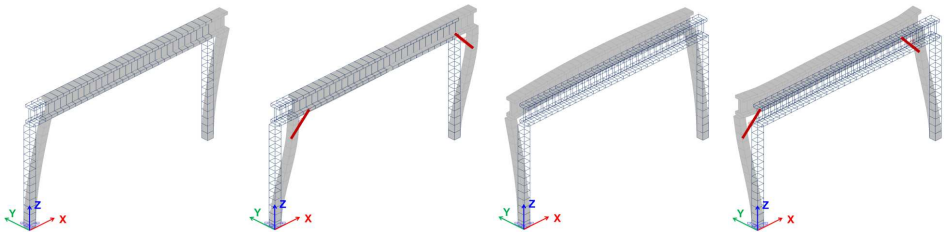

(a) (b) (c) (d)

FIGURE 3.3: Main frame deformation in X direction (a) without and (b) with BRFD, and deformation in Y direction (c) without and (d) with BRFD.

Three main conditions drive the BRFD design:

1. BRFD's steel elements shall not enter the plastic domain;
2. RC beams and columns shall not slide on each other during seismic motion; if the beam-to-column connection is poor o totally lacking (like in many pre-seismic code constructions), a post-installed mechanical fastening is required when near fault earthquakes are expected (Aprile et al., 2023);

3. RC beams and columns shear demand shall not exceed the capacity, while RC beams and columns shall not yield.

3.2 Simplified analytical model

The analytical model here implemented aims to describe the BRFD behaviour using a simplified approach. As previously mentioned, the energy dissipation results from the relative rotation of the friction surfaces around the stud bolts, which maintain them coupled with each other. Assuming the circular contact area of Figure 3.2(b), the relative motion between two surfaces begins when the interface sliding moment $M_{s,i}$ is reached:

$$M_{s,i} = \int_{\rho=R_i}^{R_e} \int_{\theta=0}^{2\pi} \rho^2 \frac{\mu F_P}{\pi(R_e^2 - R_i^2)} d\rho d\theta = \frac{2}{3}\mu F_P \frac{R_e^3 - R_i^3}{R_e^2 - R_i^2} \tag{3.1}$$

where μ is the interface friction coefficient (here assumed constant to keep the model simple), F_P is the stud bolts axial tension, R_e and R_i are outer and inner radius, respectively, and ρ and θ are the radial and angular coordinates (Belleri et al., 2017).

The BRFD motion starts when the bending moment at nodes *A*, *B*, *A'* and *B'* of Figure 3.2(b) equal the total sliding moment M_s expressed by Eq. 3.2, where $M_{s,i}$ is given by Eq. 3.1 and n_i is the number of sliding interfaces of the device's contact areas, depending on the plate's number.

$$M_s = n_i M_{s,i} \tag{3.2}$$

As a result, nodes *A*, *B*, *A'* and *B'* can be considered as rigid nodes when bending moment values are lower than M_s, and as hinged nodes for values equal to M_s.

This behaviour is statically reproduced using a rotational spring with a stiffness K_R that is highly stiff for bending moment values lower than M_s, and it is highly soft for bending moment values equal to M_s. Figure 3.4(a) shows the static scheme associated with the BRFD core obtained by introducing the rotational springs. Nodes *A*, *B*, *A'* and *B'* are hinged and connected with beams of length $l = L - b$ (see Figure 3.2(b))), which represents the stud bolt's distance. Additionally, each node is equipped with a rotational spring of stiffness K_R, which replicates the rotational friction behaviour.

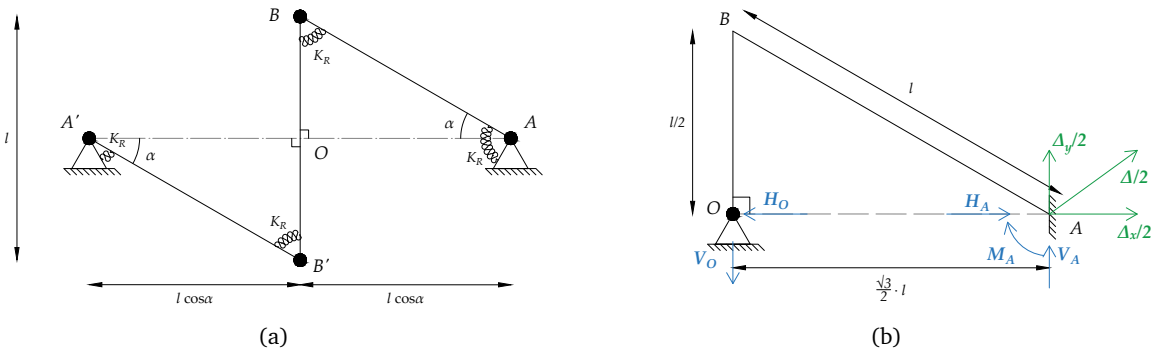

FIGURE 3.4: BRFD core simplified static scheme (a) in the *sliding* configuration with rotational springs and (b) in the *before sliding* configuration.

To compute the relationship between the sliding moment M_s and the BRFD's activation forces, the configuration *before sliding* Figure 3.4(b) is considered in the following. As previously mentioned, nodes *A*, *B*, *A'* and *B'* can be considered as rigid nodes before sliding occurs while the alignment guides maintain the central symmetry around node *O*, allowing the static scheme of Figure 3.4(a) to be transformed into the one of Figure 3.4(b), analysing only the upper half. It is worth noting that, because of the central symmetry, when analysing the half BRFD the displacements are halves with respect to the overall BRFD displacements, while the forces are equal to the overall BRFD forces.

When a generic displacement $\frac{\vec{\Delta}}{2} = \frac{\vec{\Delta_x}}{2} + \frac{\vec{\Delta_y}}{2}$ is applied to node *A* in the *before sliding* configuration of Figure 3.4(b), the reaction forces H_O, V_O, H_A, V_A and M_A are generated on nodes *O* and *A* respectively. More precisely, the reaction forces H_A, V_A and M_A coincides with the forces transferred by the BRFD into the existing structures. If $\Delta_s/2$ is the generic displacement that generates the moment M_s on nodes *A* and/or *B*, then H_A and V_A equal the longitudinal and transversal components ($F_{act,x}$ and $F_{act,y}$, respectively) of the activation force of the BRFD.

To better understand the mechanical behaviour of the BRFD, longitudinal ($\Delta_x/2$) and transversal ($\Delta_y/2$) displacements are studied separately. This allows to focus on the relationship between the sliding moment M_s and the activation forces and initial stiffness of the BRFD. In addition, to maintain the analytical model simple, only flexural deformation is considered in the analysis.

3.2.1 Longitudinal behaviour

When the BRFD is subjected to longitudinal displacements ($\Delta_x/2$), the static scheme of Figure 3.4(b) can be simplified into the one of Figure 3.5(a). *A* is a rigid node that can slide along *x*-directions, while *O* is a hinged node. When the longitudinal force F_x is applied to node *A*, the displacement $\Delta_x/2$ occurs and the reaction forces H_O, V_O, V_A and M_A are generated. It is worth noting that in the half BRFD analysed, the displacements are halves with respect to the overall BRFD displacements, while the forces are equal to the overall BRFD forces.

The static scheme of Figure 3.5(a)) is one-time hyperstatic and has been analytically resolved by applying the Principle of Virtual Works (PVW). Figures 3.5(b)), 3.5(c)) and 3.5(d)) report, respectively, the obtained diagrams of bending moment, shear and axial forces. Node *B* reaches the higher value of bending moment M_B, consequently when longitudinal displacement occurs, the BRFD activates when $M_B = M_s$. The relationship between M_s and the longitudinal activation force $F_{act,x}$ is described as follows:

$$F_{act,x} = \frac{2M_s}{l} \tag{3.3}$$

The displacement $\Delta_x/2$ is computed by applying the PVW and the initial longitudinal stiffness K_x is obtained from the ratio between F_x and Δ_x: The DD's initial longitudinal stiffness is calculated as follows:

$$K_x = \frac{F_x}{\Delta_x} = \frac{E}{l^3}\left(\frac{1}{12I_{\overline{OB}}} + \frac{1}{8I_{\overline{BA}}}\right)^{-1} \tag{3.4}$$

where $I_{\overline{OB}}$ and $I_{\overline{BA}}$ are the moments of inertia of $\overline{OB}$ and $\overline{BA}$ elements (see Figure 3.4(b)), which represent the core central and core side plates, respectively. To maintain the analytical model as general as possible,

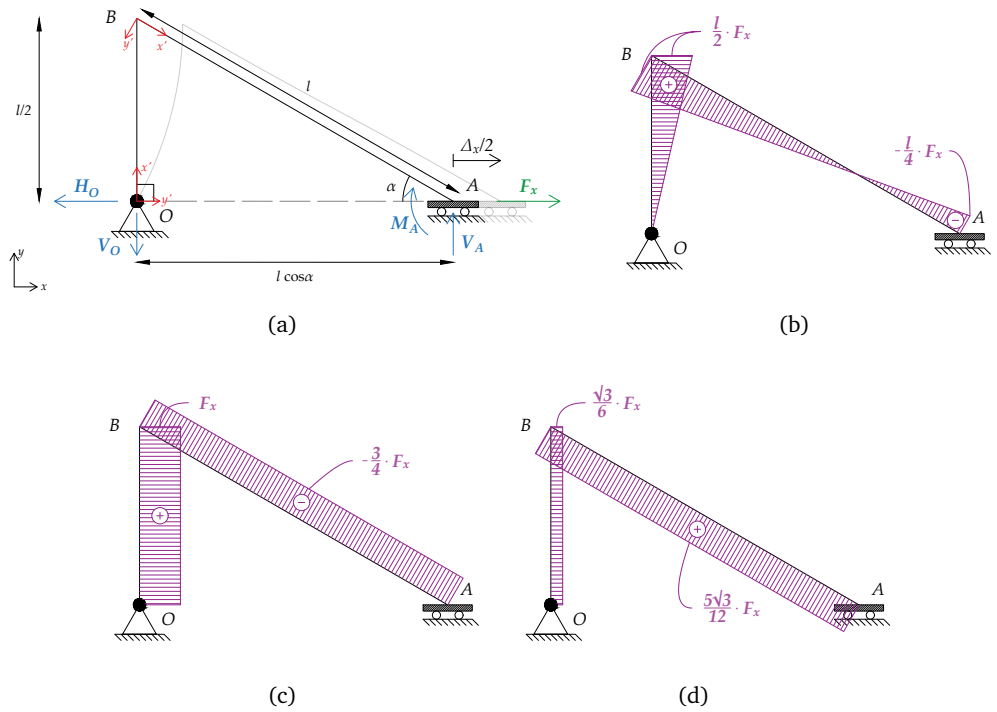

FIGURE 3.5: BRFD's longitudinal component (a) static scheme, (b) bending moment, (c) shear and (d) axial forces diagrams.

$I_{\overline{OB}}$ and $I_{\overline{BA}}$ are kept independent to each other: in the real device, core central and core side plates have a different stratification, and they can have a different geometry, which affects their inertia. However, when core central and core side plates have the same section, Eq. 3.4 can be written as follows:

$$K_x = \begin{cases} \frac{48}{7}\frac{EI}{l^3} & \text{for } n_i = 2 \quad \rightarrow I_{\overline{OB}} = I; I_{\overline{BA}} = 2I \\ 12\frac{EI}{l^3} & \text{for } n_1 = 4 \quad \rightarrow I_{\overline{OB}} = 2I; I_{\overline{BA}} = 3I \end{cases} \tag{3.5}$$

From Eq. 3.5 it can be observed that when incrementing the number of friction interfaces and, consequently, the number of core's plates, the initial stiffness K_x increments as well.

The dissertation of the analytical study of the longitudinal behaviour is visible in Appendix A (§A.1).

3.2.2 Transversal behaviour

When the BRFD is subjected to transversal displacements ($\Delta_y/2$), the static scheme of Figure 3.4(b) can be simplified into the one of Figure 3.6(a). A is a rigid node that can slide along y-directions, while O is a hinged node. When the tansversal force F_y is applied to node A, the displacement $\Delta_y/2$ occurs and the reaction forces H_O, V_O, H_A and M_A are generated. It is worth noting that in the half BRFD analysed, the registered displacements are halves with respect to the overall BRFD displacements, while the registered forces are equal to the overall BRFD forces

The static scheme of Figure 3.6(a) is one-time hyperstatic and has been analytically resolved by applying the PVW. Figures 3.6(b)), 3.6(c)) and 3.6(d)) report, respectively, the obtained diagrams of bending moment, shear and axial forces. Node A reaches the higher value of bending moment M_A, consequently when

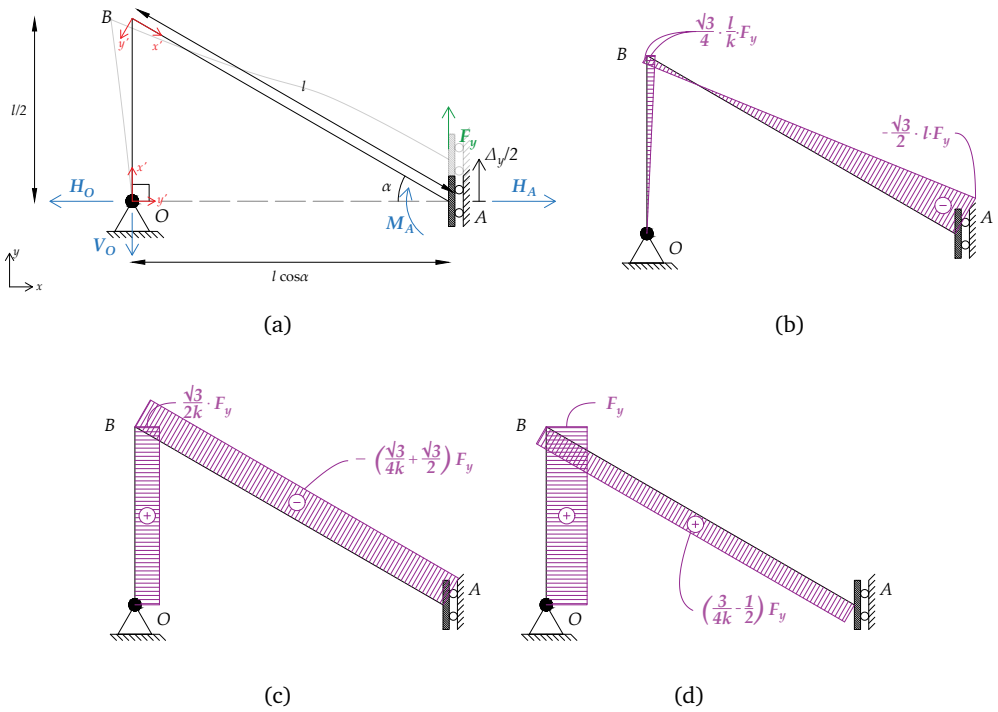

FIGURE 3.6: BRFD's transversal component (a) static scheme, (b) bending moment, (c) shear and (d) axial forces diagrams.

transversal displacement occurs, the BRFD activates when $M_A = M_s$. The relationship between M_s and the transversal activation force $F_{act,y}$ is described as follows:

$$F_{act,y} = \frac{2\sqrt{3}}{3}\frac{M_s}{l} \tag{3.6}$$

The displacement $\Delta_y/2$ is computed by applying the PVW and the initial longitudinal stiffness K_y is obtained from the ratio between F_y and Δ_y:

$$K_y = \frac{F_y}{\Delta_y} = \frac{E}{l^3}\left[\frac{1}{16k^2 I_{OB}} + \frac{2}{I_{BA}}\left(\frac{1}{4k}-\frac{1}{2}\right)^2\right]^{-1} \tag{3.7}$$

where $I_{\overline{OB}}$ and $I_{\overline{BA}}$ are the moments of inertia of $\overline{OB}$ and $\overline{BA}$ elements (see Figure 3.4(b)), which represent core central and core side plates respectively, and $k = I_{\overline{BA}}/(2I_{\overline{OB}}) + 1$ is an non-dimensional parameter introduced to compact the formulation. To maintain the analytical model as general as possible. $I_{\overline{OB}}$ and $I_{\overline{BA}}$ are kept independent to each other: in the real device, core central and core side plates have a different stratification and they can have a different geometry, which affect their inertia. However, when core central and core side plates have the same section, Eq. 3.7 can be written as follows:

$$K_y = \begin{cases} \frac{32}{5}\frac{EI}{l^3} & \text{for } n_i = 2 \quad \rightarrow I_{\overline{OB}} = I; I_{\overline{BA}} = 2I \\ \frac{21}{2}\frac{EI}{l^3} & \text{for } n_i = 4 \quad \rightarrow I_{\overline{OB}} = 2I; I_{\overline{BA}} = 3I \end{cases} \tag{3.8}$$

From Eq. 3.8 it can be observed that when incrementing the number of friction interfaces and, consequently, the number of core plates, the initial stiffness K_y increments as well.

The dissertation of the analytical study of the transversal behaviour is visible in Appendix A (§A.2).

3.2.3 Bidirectional behaviour

When the BRFD is subjected to a generic displacement $\frac{\vec{\Delta}}{2} = \pm\frac{\vec{\Delta_x}}{2} \pm \frac{\vec{\Delta_y}}{2}$, the reaction forces and the internal forces diagrams of Figure 3.4(b)) are computed by combining the solutions of §3.2.1 and §3.2.2. More precisely, Eq. 3.9 represent the reaction forces when Δ_x and Δ_y are applied with the same and opposite sign, while Eq. 3.10 represent the condition that F_x and F_y shall satisfy to reach the sliding moment M_s at nodes A and B at the same time.

$$\begin{cases} H_A = H_O = \pm F_x \pm \frac{\sqrt{3}}{2k} F_y \\ V_A = V_O = \pm \frac{\sqrt{3}}{6} F_x \pm F_y \\ M_A = \mp \frac{l}{4} F_x \mp \frac{\sqrt{3}}{2} l F_y \end{cases} \quad \text{for } \frac{\vec{\Delta}}{2} = \pm\frac{\vec{\Delta_x}}{2} \pm \frac{\vec{\Delta_y}}{2} \tag{3.9}$$

$$\begin{cases} M_B = \pm \frac{l}{2} F_x \pm \frac{\sqrt{3}}{4k} l F_y = \pm M_s \\ M_A = \mp \frac{l}{4} F_x \mp \frac{\sqrt{3}}{2} l F_y = \mp M_s \end{cases} \quad \text{for } \frac{\vec{\Delta}}{2} = \pm\frac{\vec{\Delta_x}}{2} \pm \frac{\vec{\Delta_y}}{2} \tag{3.10}$$

If F_x and F_y satisfy the condition of Eq. 3.10, the dimensionless interaction domain of Figure 3.7 is obtained. The blue dots indicate a mono-directional loading condition, the orange dots indicate a loading condition with Δ_x and Δ_y applied with the same sign, and the green dots indicate a loading condition with Δ_x and Δ_y applied with the opposite sign.

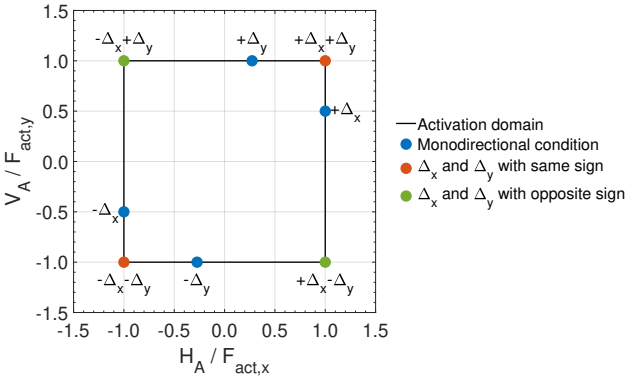

FIGURE 3.7: Longitudinal and transversal components of the BRFD's simplified analytical hysteresis cycles.

The interaction domain of Figure 3.7 is rectangular and indicates that the activation forces of the BRFD remain constant and equal to the mono-directional conditions of §3.2.1 and §3.2.2, independently from the loading direction. This behaviour permits the consideration of the longitudinal and transversal components of the BRFD as unrelated, allowing the definition of a simplified uncoupled hysteretic behaviour.

3.2.4 The simplified hysteresis cycle

One of the main hypotheses of the simplified analytical model for the BRFD is that the nodes associated with the dissipative areas can be considered as hinged nodes once the device activates (see Figure 3.2(a)). As a result, when the BRFD is subjected to the longitudinal force $F_{act,x}$, which activates the kinematic along the local x-direction, the rigid node B becomes a hinged node (see Figure 3.8(a)). Similarly, when the BRFD is subjected to the transversal force $F_{act,y}$, which activates the kinematic along the local y-direction, the rigid node A becomes a hinged node (see Figure 3.8(b)).

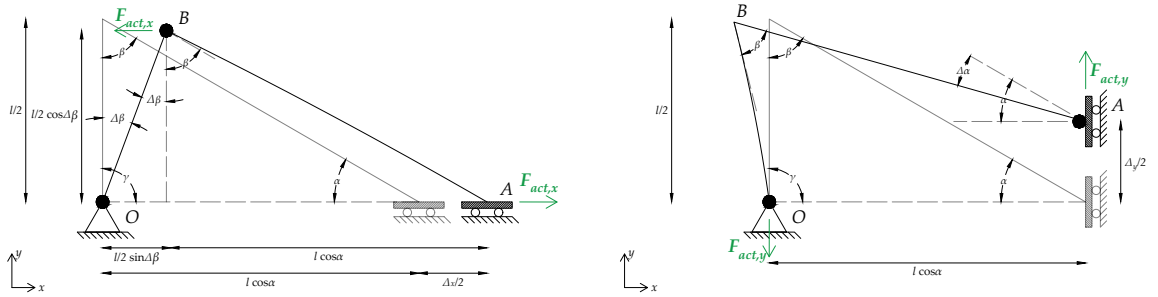

FIGURE 3.8: BRFD core simplified kinematic when (a) longitudinal and (b) transversal displacements occur.

When longitudinal displacement occurs, the bending moment around node B equals M_s and, because of the friction mechanism, it cannot increase. The relationship between M_s and the longitudinal activation force $F_{act,x}$ is described as follows:

$$F_{act,x}(\Delta\beta) = \frac{2M_s}{l\cos(\Delta\beta)} \tag{3.11}$$

where $\Delta\beta$ is the angle $\overline{OB}$ element generates with respect to its original position when moving. The distance between nodes B and O changes when the BRFD activates along the longitudinal direction, becoming $l/2\cos(\Delta\beta)$.

When transversal displacement occurs, the bending moment of node A equals M_s and, because of the friction mechanism, it cannot increase. Moreover, the relationship between M_s and the transversal activation force $F_{act,y}$ is given by Eq. 3.6, since the distance between nodes A and O keeps equal to $\sqrt{3}/2l$.

Figure 3.9 shows the shape of the two hysteresis cycles associated with BRFD's longitudinal (blue line) and transversal (red line) components (x- and y-direction, respectively). The shapes are obtained by combining the Eqs. 3.3, 3.11 and 3.4 for the longitudinal component, and Eqs. 3.6 and 3.7 for the transversal component.

The BRFD's hysteresis cycle associated with its longitudinal component exhibits a force increment when incrementing the displacement. This increment is a function of $\cos(\Delta\beta)$, but for small displacement Δx, typical of seismic devices real use condition, the increment can be assumed as linear. The BRFD's hysteresis cycle associated with its transversal component exhibits a force constancy when incrementing the displacement. It is worth noting that the two components are unrelated and independent of each other.

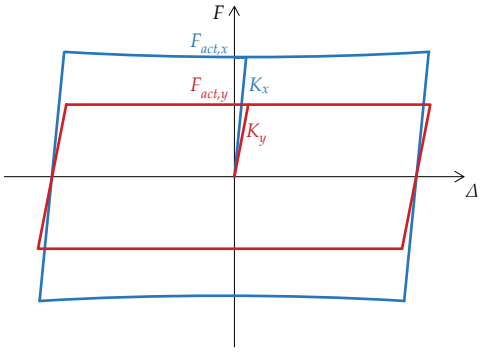

FIGURE 3.9: Longitudinal and transversal components of the BRFD's simplified analytical hysteresis cycles.

This behaviour simplifies the numerical implementation of the BRFD, as it can be defined as a link with two separated hysteresis laws, one for each component.

The presented analytical model assumes a constant friction coefficient μ, according to Coulomb's law. For instance, the shapes of Figure 3.9 can be significantly affected by the real μ behaviour during the real use conditions. This topic may be relevant and will be the focus of Chapters 5 and 6 during the execution of mechanical testing. In fact, the here presented simplified analytical model is useful to understand the BRFD's influence when implemented inside a precast RC structure, which is the main goal of the present chapter.

3.3 Case study

To evaluate the influence of the BRFD on a structure's behaviour during a seismic event, a case study is conducted on a single-story, single-bay precast reinforced concrete structure, whose geometry is represented in Figure 3.10. Main frames (shown in Figure 3.10(b)) consist of 7 m height square columns and 15 m length prestressed I-shaped beams connected by three 15 m length prestressed PI-shaped slabs. It is worth noting that the prestressed PI-shaped slabs cannot be considered a proper connection between the two parallel main frames (X direction); as a result, the case study lacks secondary frames (Y direction).

Figure 3.11 shows the reinforcement detailing of columns and beams, while the material properties were assessed by on-site sampling: the concrete has a cylindrical compressive strength of 38 MPa and a Young modulus of 33 GPa, reinforcing steel bars have a yielding stress of 544 MPa and a Young modulus of 200 GPa, prestressed steel bars have a yielding stress of 1670 MPa and a Young modulus of 200 GPa.

Given the absence of proper out-of-plane frames in the Y direction, the BRFD is only inserted inside the main frames in the X direction, as shown in Figure 3.1(b).

3.3.1 Case study numerical implementation

The case study was numerically implemented in Opensees (McKenna, 2011) using STKO (Petracca et al., 2017) as pre- and post-processor with the scheme of Figure 3.12. I-shaped beams are modelled as *elastic beams* hinged at the ends, while, to check an eventual yielding, the square columns are modelled as *fibre*

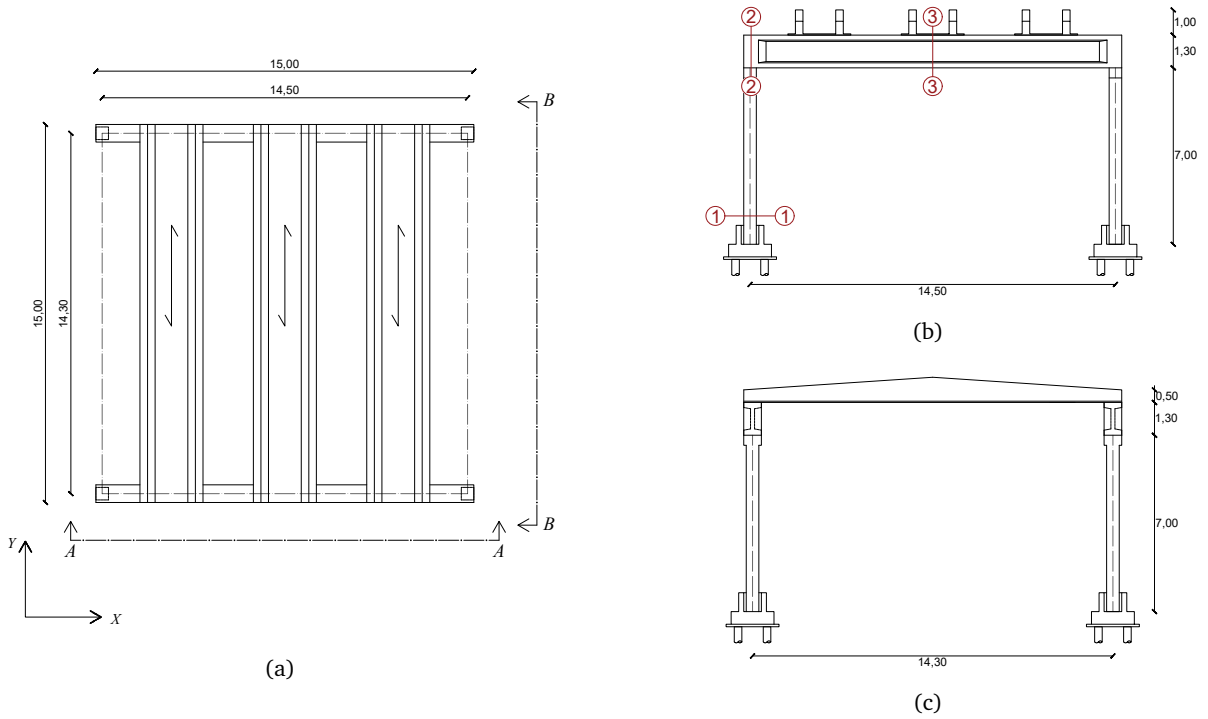

FIGURE 3.10: Precast RC structure used as a case study: a) top view, b) A-A view and c) B-B view. Dimensions in m.

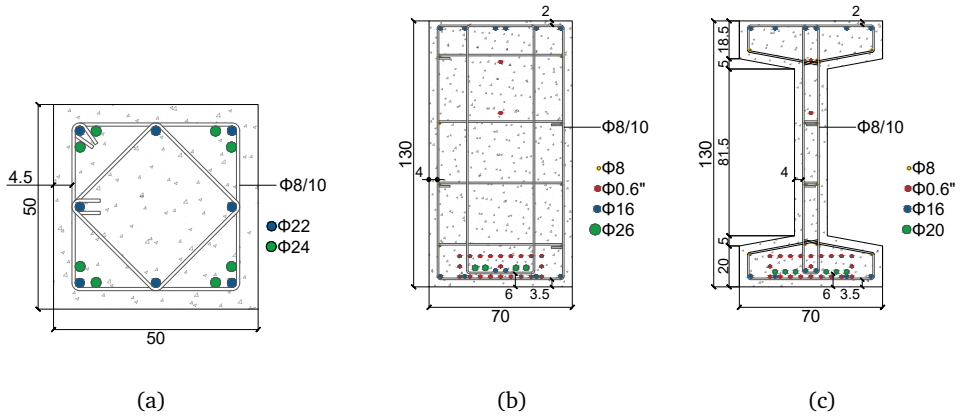

FIGURE 3.11: Elements detailing: a) column base (section 1-1), b) beam end (section 2-2) and c) beam centre (section 3-3). Dimensions in mm.

sections with a fixed base. To validate the numerical implementation of the columns, the relationship between the bending moment (M) and the curvature (χ) was analytically computed and compared with the numerical one in Fig. 3.13(a). The comparison highlights the good matching between analytical and numerical previsions, validating the adopted modelling approach. The roof is simulated with a *diaphragm constrain* type in *X-Y* plane using a control node at the centre of the roof.

The BRFDs are modelled using *ZeroLength* links with two different *Steel01* materials along their local x and y directions to describe the two components of the BRFD hysteretic laws described in §3.2.4. More precisely, the orientation of the longitudinal component (x) of the BRFD coincides with the axial direction

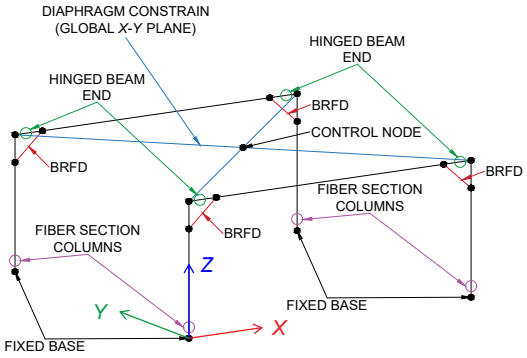

FIGURE 3.12: Numerical implementation scheme of the case study.

of the *ZeroLength* links, while the orientation of the transversal component (y) of the BRFD coincides with the global Y direction. Figs. 3.13(b) and 3.13(c) compare the analytical (A tag) and the numerical (N tag) previsions of the BRFD longitudinal and transversal components, respectively. The comparison highlights the good matching between analytical and numerical previsions in both longitudinal (x) and transversal (y) directions, validating the adopted modelling approach.

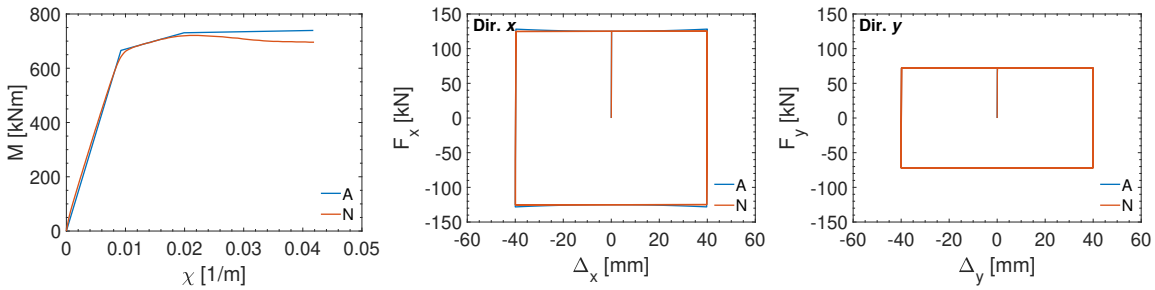

(a) (b) (c)

FIGURE 3.13: Comparison between analytical (A) and numerical (N) previsions in terms of (a) columns $M-\chi$ relationship and BRFD $F-\Delta$ relationship along its (b) longitudinal x and (c) transversal y directions.

3.4 Case study quasi-static performance

A quasi-static analysis was performed to preliminarily evaluate the influence of the BRFD when installed inside the case study. The control node located at the top of the structure (see Figure 3.12) was subjected to a sinusoidal displacement law with an amplitude of ±300 mm and a frequency of 0.05 Hz for three cycles and a time step increment of 0.001 s. The quasi-static analysis was performed in both X and Y directions.

Three different frames have been modelled: F0, which represents the case study without the BRFDs, F1, which represents the case study with the elastic properties of the BRFDs, and F2, which represents the case study with the hysteretic properties of the BRFDs. Table 3.1 describes the properties of the implemented frames in terms of linear elastic period along directions X and Y, $T_{0,X}$ and $T_{0,Y}$ respectively, and BRFD's properties in terms of activation forces along its local x- and y-direction, $F_{act,x}$ and $F_{act,y}$ respectively,

and initial stiffness along its local x- and y-direction, K_x and K_y respectively. The values of the BRFD properties reported in Table 3.1 come from the results of §3.5.3 and are here used as an example. The linear elastic periods of F0 in the X and Y directions are equal: this is caused by the frame's square plant and the symmetric detailing of the columns. It is worth noting that the presence of the BRFD decreases the elastic period of the case study by about 45% in both X and Y directions. This is because the BRFD elastic stiffness increases the rigidity of the beam-to-column node, causing the columns static scheme to change from cantilever into double-fixed elements.

TABLE 3.1: Description of the three implemented frames and BRFD's properties.

Frame	Description	$T_{0,X}$ [s]	$T_{0,Y}$ [s]	$F_{act,x}$ [kN]	$F_{act,y}$ [kN]	K_x [kN/m]	K_y [kN/m]
F0	No BRFD	0.77	0.77	-	-	-	-
F1	BRFD elastic properties	0.41	0.44	-	-	$1{\cdot}10^6$	$9{\cdot}10^5$
F2	BRFD hysteretic properties	0.41	0.44	125	72	$1{\cdot}10^6$	$9{\cdot}10^5$

Figure 3.14 shows the results of the quasi-static analysis in terms of top displacement and total base shear relationship in directions X and Y, Figures 3.14(a)) and 3.14(b) respectively. F0 exhibits a similar hysteresis cycle in the X and Y direction due to the steel yielding at the square columns footings; this similarity is due to the frame's square plant and the symmetric detailing of the columns (see Figure 3.14(a)). F1 exhibits a higher stiffness than F0, with higher forces and smaller displacement associated with the columns yielding. Furthermore, the hysteresis cycle in the X direction differs from the one in the Y direction; this difference is caused by the dissimilar changes in the frame's static scheme that the BRFDs induce in the two global directions. More precisely, the column goes from a cantilever to a fixed scheme along the X direction and from a cantilever to a semi-fixed scheme along the Y direction. In fact, the columns yield simultaneously at the base and the top sections in the X direction, while in the Y direction, the columns yield firstly at the base and then at the top section. F2 combines the behaviours of F0 and F1: F2 exhibits the same stiffness as F1 until the BRFD activates, then behaves more similarly to F0, registering a similar hysteresis cycle in the X and Y direction.

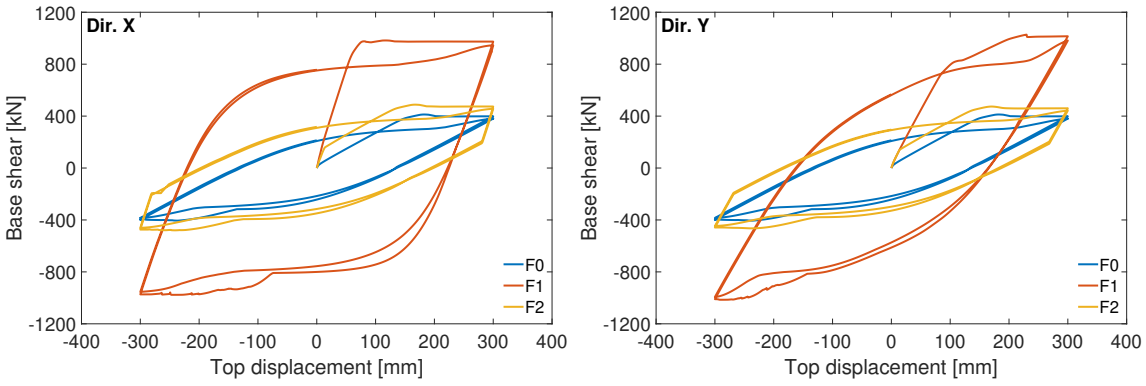

(a) (b)

FIGURE 3.14: Case study quasi-static performance using a cyclic displacement law along (a) X and (b) Y direction.

The BRFD positively influences the case study's structural behaviour, unaltering the top displacement associated with the column yielding and slightly increasing the related total base shear. Moreover, when the BRFD activates, it restores the original static scheme of the structure, allowing the columns to behave as cantilevers.

3.5 Case study dynamic performance

To investigate the benefits of the BRFD on the case study during a seismic event, Nonlinear Time History Analyses (NLTHAs) were performed on frames F0, F1 and F2 using natural ground motions. Seven pairs of ground motions were selected from the European Strong Motion database (EC, 2023); the ground motions are spectrum-compatible for a high seismic area in Italy (i.e. L'Aquila (NTC2018, 2018)) and are scaled to match the Life-Safety limit state assuming soil type B and Importance Class III according to Eurocode 8-1 (CEN, 2005). Table 3.2 summarises the properties of the selected ground motions, including the original Peak Ground Accelerations (PGA) ad Scale Factors (SF) applied in X and Y directions.

TABLE 3.2: Properties of the selected ground motions.

TH n°	**Earthquake event**	**Station ID**	**Magnitude (Richter scale)**	**EC8 soil class**	**Original PGA X [g]**	**Original PGA Y [g]**	**SF X**	**SF Y**
1	Central Italy (24/08/2016)	PZII	6.0	B	0.05	0.05	8.65	8.49
2	Central Italy (30/10/2016)	MZ24	6.6	C	0.76	1.02	0.38	0.51
3	Central Italy (26/10/2016)	NOR	5.9	B	0.21	0.12	1.82	3.24
4	Friuli 1st shock (06/05/1976)	TLM1	6.4	B	0.32	0.35	1.24	1.11
5	Emilia 2nd shock (29/05/2012)	T0819	5.5	C	0.26	0.25	1.52	1.56
6	Umbria Marche (26/09/1997)	CSA	6.0	C	0.11	0.17	3.70	2.27
7	Emilia 1st shock (20/05/2012)	MRN	6.1	C	0.26	0.26	1.49	1.48
	Average values		*6.1*		*0.28*	*0.32*	*2.68*	*2.67*

NLTHA were performed in Opensees (McKenna, 2011) using Matlab (MathWorks, 2022) as a pre-and post-processing tool. The results are assessed considering the total base shear (Fb), interstorey drift (IDR), columns' base rotation and shear utilisation factors ($\rho_{C,\theta}$ and $\rho_{C,V}$), and equivalent damping (ξ_{eq}). The columns' utilization factors are a-dimensional and are defined as follows:

$$\rho_{C,\theta} = \frac{\theta_{Ed}}{\theta_y} \tag{3.12}$$

$$\rho_{C,V} = \frac{V_{Ed}}{V_{Rd}} \tag{3.13}$$

Columns' utilisation factors are computed as a ratio between demand and capacity: values lower than 1 indicate the satisfaction of the columns' safety checks. The rotation capacity was set as the rotation associated with the base column yielding θ_y computed according to Eurocode 8-3 (CEN, 2011), while the shear capacity as the shear associated with the shear failure V_{Rd} computed according to Eurocode 8-3 (CEN, 2011). It is worth noting that when defining $\rho_{C,\theta}$, the choice to associate the capacity rotation with the yielding rotation of the column was driven by one of the main objectives of this work, which is to avoid structural damage to the building.

The equivalent damping ξ_{eq} is computed from the acceleration spectrum in ADRS (Acceleration-Displacement Response Spectrum) format (Fajfar, 1999) once the top displacement and total base shear demand are determined.

3.5.1 Sensitivity analysis

To investigate the effects of the BRFD's activation forces ($F_{act,x}$ and $F_{act,y}$) and initial stiffnesses (K_x and K_y) on the case study during a seismic event, the F2 frame was subjected to a sensitivity analysis.

The analytical model developed in Section §3.2 allows to describe $F_{act,y}$ as a function of $F_{act,x}$ and K_y as a function of K_x as follow:

$$F_{act,y} = \frac{2\sqrt{3}M_s}{3l} = \frac{\sqrt{3}}{3}F_{act,x} \tag{3.14}$$

$$K_y = \begin{cases} \frac{32}{5}\frac{EI}{l^3} \cong 0.93K_x \approx 0.9K_x & \text{for } n_i = 2 \\ \frac{21}{2}\frac{EI}{l^3} \cong 0.88K_x \approx 0.9K_x & \text{for } n_i = 4 \end{cases} \tag{3.15}$$

Eqs. 3.14 and 3.15 are obtained by merging Eqs. 3.3 with 3.6 and Eqs. 3.5 with 3.8, respectively.

When performing the sensitivity analysis, $F_{act,x}$ and K_x varied as a function of the BRFD feasibility while $F_{act,y}$ and K_y were computed according to Eqs. 3.14 and 3.15. Considering the BRFD feasibility, $F_{act,x}$ was set to range between 25 and 250 kN, while K_x between 105 and 106 kN/m. The main objective of this sensitivity analysis is to identify the $F_{act,x}$-K_x couple which better improves the case study performance under the selected seismic action.

Figure 3.15 summarises the sensitivity analysis results in terms of $\rho_{C,\theta}$, $\rho_{C,V}$, IDR and ξ_{eq} as mean values of the NLTHA with seven ground motions for each $F_{act,x}$-K_x couple. The response levels are expressed using different colours, as shown on the scaling bar of each graph. In the graphs associated with $\rho_{C,\theta}$ and $\rho_{C,V}$ (Figures 3.15(a) and 3.15(b) respectively), green shades are associated with the satisfaction of the columns' safety checks, while red shades corresponds to unsatisfactory columns' safety checks. In the graph associated with IDR (Figure 3.15(c)), the darker blue colour shades indicate lower interstorey drift values, which are usually associated with a lower damage level (Priestley et al., 2007). In the graph associated with ξ_{eq} (Figure 3.15(d)), the lighter yellow colour shades indicate higher equivalent damping values, which are associated with a better overall performance of the BRFD.

When incrementing $F_{act,x}$ values, F2 performance improves and exhibits a decrement in column base rotations and interstorey drifts: for $F_{act,x}$ values higher than 100 kN, $\rho_{C,\theta}$ are lower than 0.50, and IDR are lower than 1%. However, when incrementing $F_{act,x}$ values, F2 exhibits an increment of total base shear,

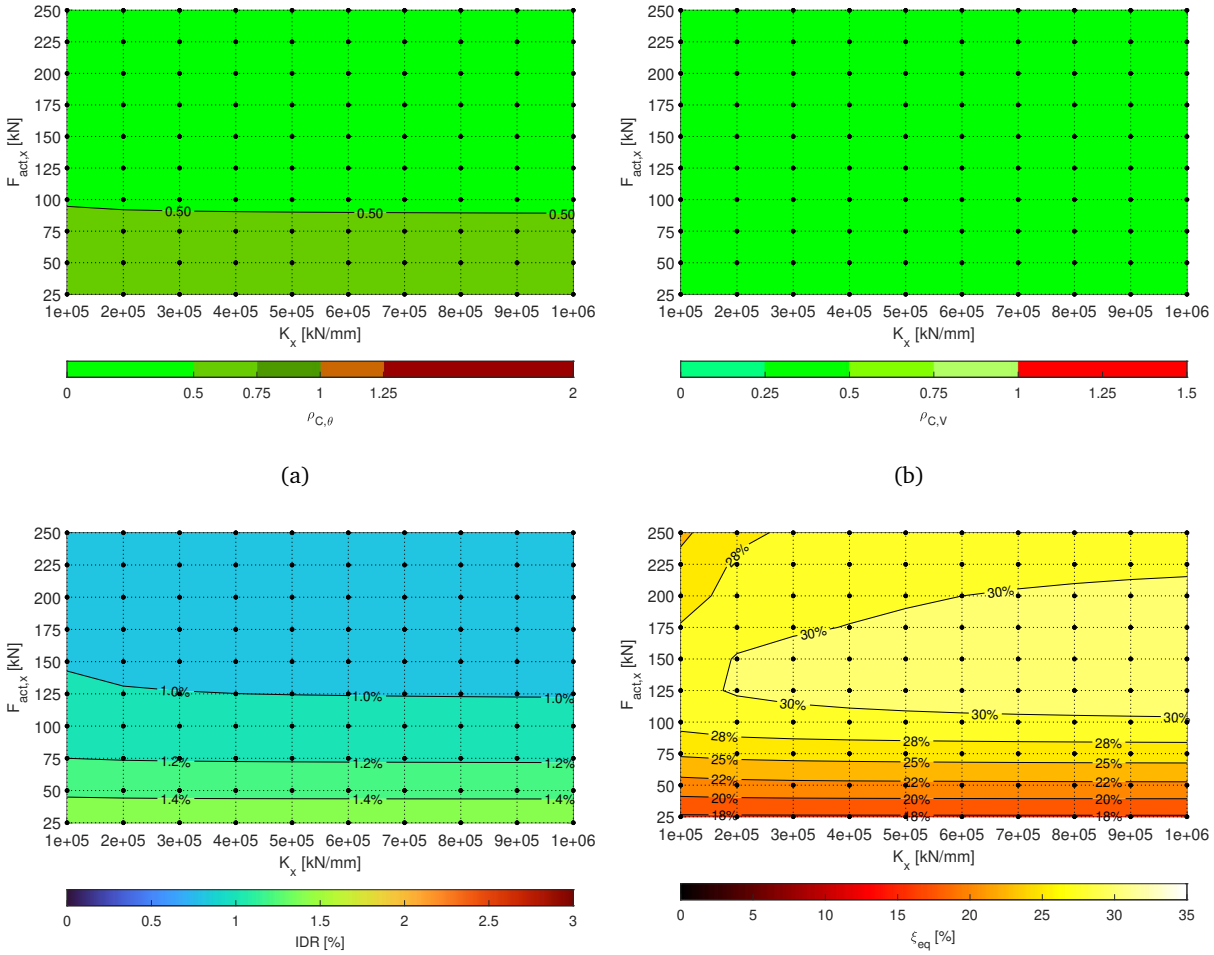

FIGURE 3.15: Sensitivity analysis results in terms of (a) column rotation and (b) shear factors, (c) interstorey drifts and (d) equivalent damping.

which may affect the columns' shear check and the equivalent damping. This behaviour is typical of additional damping systems and has been observed by several authors (Barzegar et al., 2020; Constantinou et al., 2001; Martínez-Rueda, 2002; Soong and Spencer, 2002). It is worth noting that the columns' shear failure V_{Rd} is 196 kN, which is quite a high value and leads to $\rho_{C,V}$ lower than 0.50 for all the investigated $F_{act,x}$-K_x combinations. As a result, in this case, the increment of total base shear is insignificant, but it is a critical aspect to be considered, especially when the columns' detailing is poor for the shear capacity.

When incrementing K_x, F2 performance improves (especially when associated with higher $F_{act,x}$ values) and exhibits an increment of equivalent damping: for K_x higher than $5{\cdot}10^5$ kN/m and $F_{act,x}$ values between 100 and 200 kN, ξ_{eq} is higher than 30%.

The sensitivity analysis highlights that, for a better improvement of F2 dynamic performance, $F_{act,x}$ ideal values range between 100 and 200 kN, while K_x ideal values are higher than $5{\cdot}10^5$ kN/m.

3.5.2 Importance analysis using a multi-criteria decision-making (MCDM) approach

To better identify the optimal configuration of the BRFD for the case study, an importance analysis using a multi-criteria decision-making (MCDM) approach was conducted. The adopted approach uses the entropy-right method to consider the multiple-factors effect of columns' safety checks ($\rho_{C,\theta}$ and $\rho_{C,V}$) and performance parameters (IDR and ξ_{eq}) to identify the most important $F_{act,x}$-K_x couple in terms of F2 overall performance.

The adopted MCDM approach follows the work of Guo et al. (2017). The parameters meaningful for the identification of the most the most important $F_{act,x}$-K_x couple are called importance indexes $r_{i,j}$, and in the present study are divided into two groups: the first one considers the columns' safety checks associated with rotation and shear factors ($\rho_{C,\theta}$ and $\rho_{C,V}$ respectively), the second group considers the overall F2 performance in terms of interstorey drift and equivalent damping (IDR and ξ_{eq} respectively). These parameters are firstly standardised as non-dimensional parameters, following Eqs. 3.16 and 3.17, where i is the importance index and j is the $F_{act,x}$-K_x couple. Eq. 3.16 is adopted if the value of $r_{i,j}$ increases with its importance while, on the contrary, Eq. 3.17 is adopted if the value of $r_{i,j}$ decreases with its importance. More precisely, Eq. 3.16 is adopted to standardise ξ_{eq} values and Eq. 3.17 is adopted to standardise $\rho_{C,\theta}$, $\rho_{C,V}$ and IDR values.

$$\tilde{r}_{i,j} = \frac{r_{i,j} - \min(r_{i,j})}{\max(r_{i,j}) - \min(r_{i,j})} \tag{3.16}$$

$$\tilde{r}_{i,j} = \frac{\max(r_{i,j}) - r_{i,j}}{\max(r_{i,j}) - \min(r_{i,j})} \tag{3.17}$$

The standardised importance parameters are firstly collected inside the matrix $\mathbf{r} = [\tilde{r}_{i,j}]_{m\times n}$, where m is the total number of importance indexes and n the total number of $F_{act,x}$-K_x couple, and then combined together according to the entropy-right method. The proportion of importance $P_{i,j}$ is defined as:

$$P_{i,j} = \tilde{r}_{i,j} / \sum_{j=1}^{n} \tilde{r}_{i,j} \tag{3.18}$$

The entropy of $P_{i,j}$ is computed following as:

$$S_i = -\frac{1}{\ln(n)} \sum_{j=1}^{n} P_{i,j} \ln(P_{i,j}) \tag{3.19}$$

where it is assumed that $P_{i,j}\ln(P_{i,j}) = 0$ when $P_{i,j} = 0$. In fact, indexes i with less importance have small values of entropy S_i. Each importance index is associated with a weight that comprehends an objective weight ω_i, which is defined a function of the entropy following Eq. 3.20, and a subjective expert-based weight λ_i. In this work, the selected groups are assumed to have the same importance, which results in equal λ_i values following the hierarchy scheme of Figure 3.16.

$$\omega_i = \frac{1 - S_i}{m - \sum_{i=1}^{m} S_i} \tag{3.20}$$

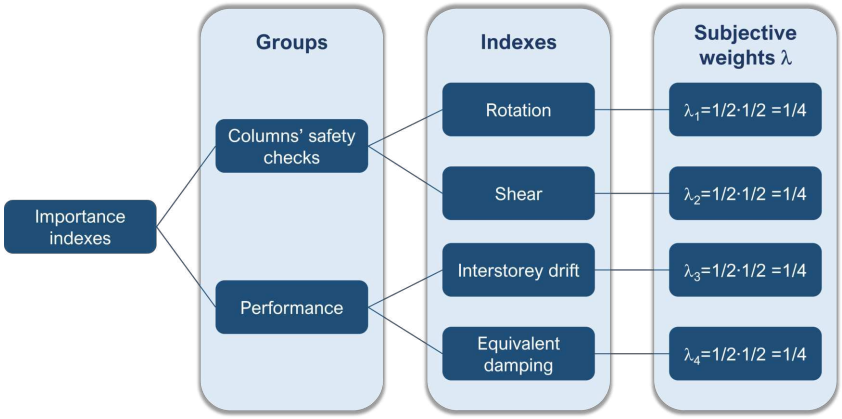

FIGURE 3.16: Subjective weights adopted in the importance analysis.

The comprehensive indexes η_j are finally obtained by combining the standardised importance indexes with the comprehensive weight κ_i (Eq. 3.21): the $F_{act,x}$-K_x couple with the highest η_j value is the most important and resembles the optimal solution.

$$\kappa_i = \frac{\lambda_i \omega_i}{m - \sum_{i=1}^{m} \lambda_i \omega_i} \tag{3.21}$$

$$\eta_j = \frac{n \sum_{j=1}^{n} \kappa_i \tilde{r}_{i,j}}{\sum_{j=1}^{n} \sum_{i=1}^{m} \kappa_i \tilde{r}_{i,j}} \tag{3.22}$$

Figure 3.17 shows the results of the importance analysis in terms of performance level from *"Really good"* (white colours) to *"Really bad"* (red colours) with an additional area associated with *"BRFD unfeasible"* (black region). This additional area is obtained considering BRFDs with maximum length of 90 cm with μ equal to 0.45, according to authors findings (Grossi et al., 2023a,b), and the $F_{act,x}$ values that are effectively obtainable from the geometry associated with each K_x. In fact, lower values of K_x are associated with smaller BRFD's plate width and a smaller range of available studs' diameters and applicable torque. As a result, higher values of $F_{act,x}$ are not reachable for the lower K_x values.

F2 exhibits the best performance when $F_{act,x}$ ranges between 100 and 150 kN and K_x is higher than $6{\cdot}10^5$ kN/m (see the white area of Figure 3.17), confirming the remarks concerning the sensitivity analysis of §3.5.1. More precisely, the MCDM approach suggests a solution with $F_{act,x}$ equals to 125 kN and K_x equals to 10^6 kN/m as the most important, i.e., the optimal BRFD configuration.

The optimal BRFD configuration identified using the MCMD approach represents the case study when located in the site selected at the beginning of §3.5. A change in the structure or the site location can affect the obtained results and the optimal BRFD configuration.

3.5.3 Dynamic performance without and with BRFD

To investigate the benefits of the BRFD on the dynamic response of the case study during a seismic event, NLTHA were performed on frames F0, F1 and F2 using natural ground motions. F1 and F2 frames were

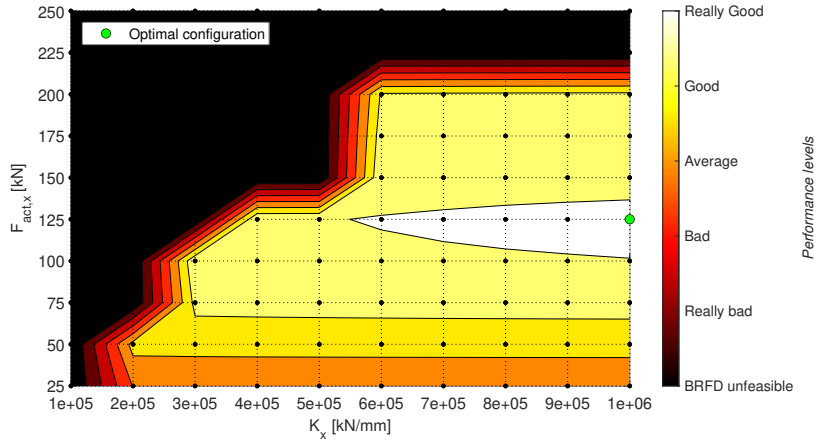

FIGURE 3.17: Performance level map considering only the feasible BRFD configurations.

modelled, implementing the characteristics of Table 3.1, using the BRFD optimal configuration properties.

Figure 3.18 compares the dynamic performance of F0, F1 and F2 in terms of Fb, IDR, $\rho_{C,\theta}$ and $\rho_{C,V}$ as mean values of the NLTHA with seven ground motions. Given the frame's square plant and the symmetric detailing of the columns, the response of F0 and F2 in the X direction resembles the one in the Y direction; on the contrary, the response of F1 in the X direction differs from the one in the Y direction, confirming what already highlighted in §3.4.

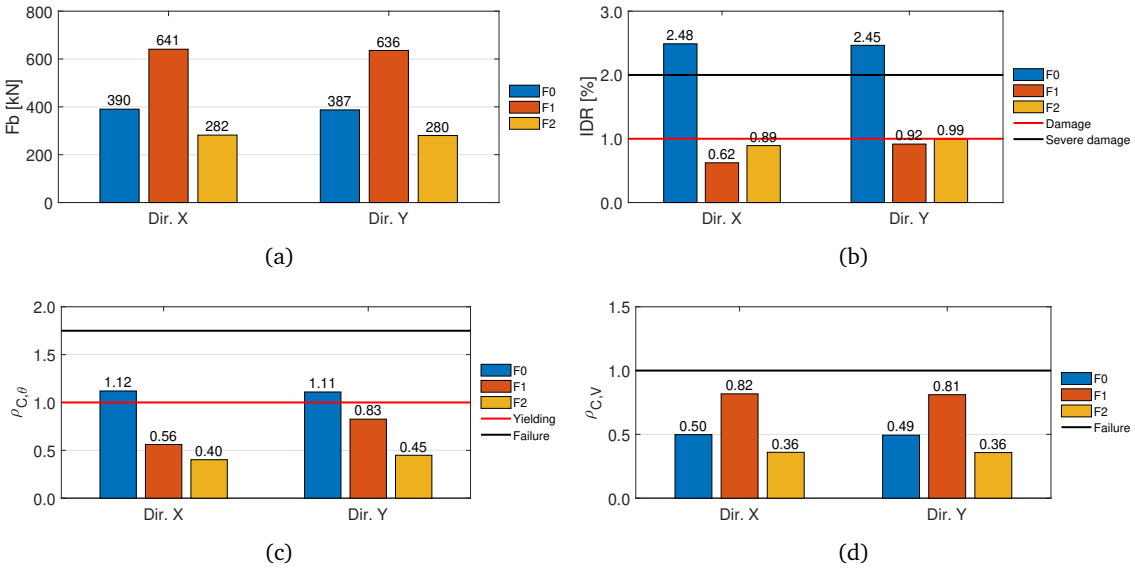

FIGURE 3.18: F0, F1 and F2 dynamic performance: (a) total base shear, (b) interstorey drift, (c) column rotation and (d) shear factors.

F0 results indicate that while the shear checks are perfectly satisfied with $\rho_{C,V}$ values lower than 0.5 (see Figure 3.18(d)), the damage registered by the columns is quite significant. In fact, $\rho_{C,\theta}$ values are higher than 1 (see the red line of Figure 3.18(c)), and IDR values are higher than 2%, usually associated with high damage of structural and non-structural elements (Priestley et al., 2007) (see the black line of Figure 3.18(b)).

F1 results indicate an overall performance improvement, with $\rho_{C,\theta}$ and $\rho_{C,V}$ values lower than 1, and IDR values lower than 1%. However, Fb values exhibit an average increment of 64% with respect to F0. While in this case study, the structural response is not affected by this increment, limiting the total base shear increment is a good practice, especially for structures with poor shear detailing. Despite the total base increment, F1 avoids panels and structural damage (red and black lines of Figure 3.18(b)).

F2 exhibits the best overall performance improvement, with $\rho_{C,\theta}$ and $\rho_{C,V}$ values lower than 1, and IDR values lower than 1%. Moreover, Fb values exhibit an average decrement of 28% with respect to F0. It can be confirmed that F2 results in a particularly effective solution that combines the satisfaction of the columns' safety checks and an average 62% decrement of IDR without a significant alteration of the existing structural system, avoiding structural and non-structural damage (red and black lines of 3.18(b)).

3.6 Conclusive remarks

The present chapter shows the conceptualisation study of an innovative seismic protection device called Bidirectional Rotational Friction Damper (BRFD) for precast RC structures with poor connections. The BRFD behaves as a beam-to-column joint and damper at once; the device unifies the concepts of Rotational Friction Dampers and movable plate system, producing a damping effect along two main directions. Furthermore, the device's ability to dissipate energy through friction enables it to remain undamaged during multiple seismic events while maintaining its damping capacity.

The BRFD behaviour is described as a combination of two components, a longitudinal (local x direction) and a transversal (local y direction) one, identifying an activation force ($F_{act,x}$ and $F_{act,y}$) and an initial stiffness (K_x and K_y) for each one.

To evaluate the influence of the BRFD on a structure's behaviour during a seismic event, a case study is conducted on a single-story, single-bay precast RC structure that lacks secondary frames, allowing the implementation of BRFD inside the main frames only. Quasi-static and nonlinear time history analyses were performed on the case study, identifying three different frames: F0, which represents the case study without BRFDs, F1, which represents the case study with the elastic properties of the BRFD, and F2, which represents the case study with the hysteretic properties of the BRFD.

To identify the optimal configuration of the BRFD for the case study, a sensitivity analysis was carried out on F2, performing an importance analysis using a multi-criteria decision-making (MCDM) approach.

The main findings are summarised in the following:

- The simplified analytical model indicates that the two behaviours in the two directions are unrelated and independent. Moreover, the hysteresis cycles can be described using a bilinear hysteretic law. This behaviour simplifies the numerical implementation of the BRFD, as it can be defined as a link with two separated hysteresis laws, one for each component.
- The quasi-static analysis shows that the BRFDs application positively influence the case study's structural behaviour, unaltering the top displacement associated with the column yielding and slightly increasing the related total base shear. Moreover, when the BRFDs activate, the original static scheme of the structure is restored, allowing the columns to behave as cantilevers.

- The sensitivity analysis performed on F2 highlights that the dynamic performance better improves when the activation force ranges between 100 and 200 kN for $F_{act,x}$ and between 58 and 115 kN for $F_{act,y}$, and when the initial stiffness is higher than $5{\cdot}10^5$ kN/m for K_x and higher than $4{\cdot}10^5$ kN/m for K_y.
- The importance analysis performed using the MCDM approach suggests that the optimal BRFD configuration is obtained when $F_{act,x} = 125$ kN, $F_{act,y} = 72$ kN, $K_x = 10^6$ kN/m and $K_y = 9{\cdot}10^5$ kN/m.
- The introduction of the BRFD positively benefits the case study's dynamic performance, significantly reducing interstorey drift (62%) and a reduction of total base shear (28%) without altering the existing structural scheme, avoiding structural and non-structural damage.

Obviously, the dynamic results of the present Chapter are representative of the case study when located in the site selected at the beginning of §3.5. Since the obtained results are dependent on both the structural layout and location site hazard, the MCMD approach can be proposed as an effective design tool for the BRFD sizing.

As a summary, the conceptualisation analysis performed on BRFD highlights that such a system can effectively improve a precast RC structure's behaviour during seismic events. However, further research is needed to fully develop the potential of the device. More precisely, the following Chapters are focused on the prototyping of the BRFD, on the execution of mechanical tests on a real-scale prototype, and on the development of a numerical model which includes a friction law that considers the influence of sliding velocity, pressure and temperature.

References

Aprile, Alessandra, Eleonora Grossi, and Matteo Zerbin (2023). "A Novel Friction Damper for Seismic Retrofit of Precast RC Structures with Poor Connections". In: ed. by Ilki Alper, Çavunt Derya, and Selim Çavunt Yavuz. Springer - Lecture Notes in Civil Engineering (LNCE), pp. 1384–1394. DOI: 10.1007/978-3-031-32519-9_140.

Barzegar, Vahid, Simon Laflamme, Austin Downey, Meng Li, and Chao Hu (2020). "Numerical evaluation of a novel passive variable friction damper for vibration mitigation". In: *Engineering Structures* 220. DOI: 10.1016/j.engstruct.2020.110920.

Belleri, Andrea, Alessandra Marini, Paolo Riva, and Roberto Nascimbene (2017). "Dissipating and re-centring devices for portal-frame precast structures". In: *Engineering Structures* 150. DOI: 10.1016/j.engstruct.2017.07.072.

CEN (2005). *Eurocode 8: Design of Structures for Earthquake Resistance. Part 1: General rules, seismic actions and rules for buildings (UNI EN 1998-1)*.

CEN (2011). *Eurocode 8: Design of Structures for Earthquake Resistance. Part 3: Assessment and retrofitting of buildings (UNI EN 1998-3)*.

Constantinou, Michael C., Panos Tsopelas, Wilhelm Hammel, and Ani N. Sigaher (2001). "Toggle-Brace-Damper Seismic Energy Dissipation Systems". In: *Journal of Structural Engineering* 127 (2). DOI: 10.1061/(ASCE)0733-9445(2001)127:2(105).

EC (2023). *European Strong-Motion Database*. URL: http://www.isesd.hi.is/.

Fajfar, Peter (1999). "Capacity spectrum method based on inelastic demand spectra". In: *Earthquake Engineering & Structural Dynamics* 28 (9), pp. 979–993. ISSN: 0098-8847.

Grossi, Eleonora, Alessandra Aprile, and Matteo Zerbin (2023a). "Tribological investigation on metal mating surfaces to explore real use conditions of a novel friction damper for seismic applications". In: *Engineering Structures* 278, p. 115473. ISSN: 01410296. DOI: 10.1016/j.engstruct.2022.115473.

Grossi, Eleonora, Enrico Baroni, Alessandra Aprile, Annalisa Fortini, Matteo Zerbin, and Mattia Merlin (2023b). "Tribological Behavior of Structural Steel with Different Surface Finishing and Treatments for a Novel Seismic Damper". In: *Coatings* 13 (1), p. 135. DOI: 10.3390/coatings13010135.

Guo, Anxin, Zhenliang Liu, Suchao Li, and Hui Li (2017). "Seismic performance assessment of highway bridge networks considering post-disaster traffic demand of a transportation system in emergency conditions". In: *Structure and Infrastructure Engineering* 13 (12), pp. 1523–1537. DOI: 10.1080/15732479.2017.1299770.

Martínez-Rueda, Juan Enrique (2002). "On the Evolution of Energy Dissipation Devices for Seismic Design". In: *Earthquake Spectra* 18 (2). DOI: 10.1193/1.1494434.

MathWorks (2022). *MATLAB*.

McKenna, Frank (2011). "OpenSees: A Framework for Earthquake Engineering Simulation". In: *Computing in Science & Engineering* 13 (4), pp. 58–66. DOI: 10.1109/MCSE.2011.66.

NTC2018 (2018). *Decreto ministeriale del 17 Gennaio 2018, Aggiornamento delle «Norme tecniche per le costruzioni»*.

Petracca, Massimo, Francesca Candeloro, and Guido Camata (2017). *STKO user manual*. ASDEA Software Technology.

Priestley, M. J. N., G. M. Calvi, and M. J. Kowalsky (2007). *Displacement-based seismic design of structures*. IUSS Press : Distributed by Fondazione EUCENTRE. ISBN: 978-88-6198-000-6.

Soong, T.T. and B.F. Spencer (2002). "Supplemental energy dissipation: state-of-the-art and state-of-the-practice". In: *Engineering Structures* 24 (3). DOI: 10.1016/S0141-0296(01)00092-X.

4
Tribological investigation

This Chapter shows the tribological investigation performed for the development of the BRFD using Pin-on-Disk (PoD) tests and highlights the main tribological aspects useful for the full-scale tests. The BRFD can be identified as a tribological system thanks to the presence of two contact surfaces (two friction pads in contact) under a constant nominal load (the bolt torque). As a result, a tribological experimental investigation is an indisputably useful tool in the developing of the BRFD or any new FD.

4.1 Concepts of tribology

In order to fully understand the tribological behaviour of a friction device, concepts of tribology must necessarily be involved. Tribology is defined as "*the science and technology of interacting surfaces in relative motion*" (Bhushan, 2013). Tribology analyzes interface's behaviour such as friction, wear and lubrication, which are strictly related to the surface material, the surface shape of mating materials and the operating environment.

For technological applications, the texture of the mating surfaces is crucial in the analysis of their interaction. Roughness (R_a) is one of the most important parameters used to define the surface texture and indicates the variation in the height of the surface asperities to a reference plane, as schematize in Figure 4.1. It can be measured either in a single line or along a set of parallel lines creating a surface map.

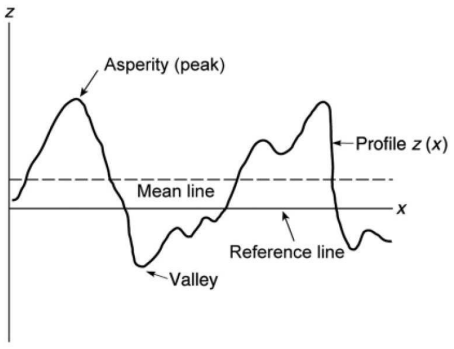

FIGURE 4.1: Schematic of a surface profile for roughness measure (Bhushan, 2013).

Friction is defined as "*the resistance to motion during sliding or rolling, that is experienced when one solid body moves tangentially over another with which it is in contact*" (Bhushan, 2013) and has been clearly stated that friction is not a material property but the response of a system. Friction can occur in dry or lubricated

condition, depending on the presence of lubricant layers inside the friction interface. Due to the typical condition of seismic friction dampers, this tribological study will be focused on dry conditions.

The friction force is the resistive tangential force that act in the opposite direction of the motion and it is defined as static friction force ($F_{\mu,s}$) if it is required to initiate the motion with μ_s its associated friction coefficient, or as kinetic friction force ($F_{\mu,k}$) if it is required to maintain the motion with μ_k its associated friction coefficient. As highlighted in Figure 4.2, the static friction force is usually higher or equal to the kinetic friction force.

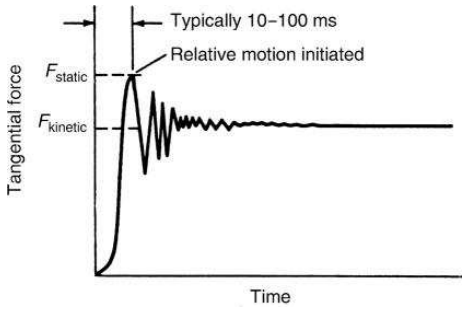

FIGURE 4.2: Tangential friction force as function of time (Bhushan, 2013).

Sliding friction obeys to two following classic rules:

1. The friction force F_μ is directly proportional to the nominal load W, as for equation 4.1,

$$F_\mu = \mu W \tag{4.1}$$

   where μ is the friction coefficient.

2. The friction force is independent of the apparent area of contact between the contacting bodies.

To these rules, a third one is usually added and states that the kinetic friction force is independent to the sliding velocity, once the motion is started. However, this rule, is not true and it may have a relevant influence, depending on the coupling properties. For this reason, The influence of the sliding velocity must be investigated during the development of a friction device to ensure its correct and constant performance.

Widely accepted sliding friction theories are the ones proposed from the works of Bodwen and Tabor starting from 40's (Bowden et al., 1943; Bowden and Tabor, 1942). Two solid metals in contact by a nominal force, as for Figure 4.3, develop a high pressure at the individual asperities contact causing their local welding, which are consequentially sheared due to the sliding motion of the surfaces. It has been later argued that asperities do not have necessarily to weld, but their adhesion is sufficient to consider the friction mechanism. Adhesion is defined as "*the bonding across interface asperities so that a finite normal force (adhesive force) is required to separate the solids bodies*" (Bhushan, 2013).

In order to maintain the sliding motion, in addition to the frictional force to overcome adhesion, an amount of energy is required for micro-scale deformations. These deformations are mostly grooving or plowing of the surfaces due to the hardness of asperities or particles trapped between the two surfaces. Under the assumption of minimal interaction between adhesion and deformation, the total intrinsic frictional force

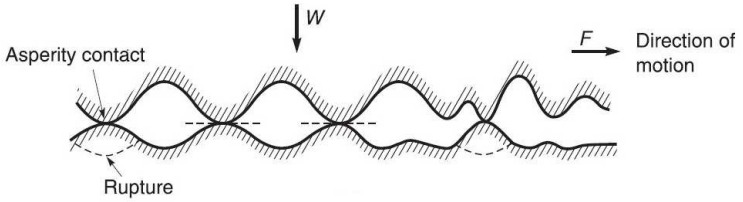

FIGURE 4.3: Schematic of two rough surfaces in sliding contact (Bhushan, 2013).

($F_{\mu,i}$) equals the force needed to shear the adhered asperities ($F_{\mu,a}$) and the force needed to supply the energy deformation ($F_{\mu,d}$), as for equation 4.2 or equation 4.3 in term of friction coefficients.

$$F_{\mu,i} = F_{\mu,a} + F_{\mu,d} \tag{4.2}$$

$$\mu_i = \mu_a + \mu_d \tag{4.3}$$

For a dry contact, the classical theory of adhesion defines the adhesive friction part $F_{\mu,a}$ as:

$$F_{\mu,a} = A_r \tau_a \tag{4.4}$$

where A_r is the real contact area and τ_a the contact average shear strength. The adhesional friction coefficient μ_a can be written as

$$\mu_a = \frac{A_r \tau_a}{W} \tag{4.5}$$

$$= \frac{\tau_a}{p_r} \tag{4.6}$$

where p_r is the mean real pressure.

The adhesion strength is function of the mechanical properties and the physical-chemical interactions of the contacting surfaces. These contacts can be either elastic or plastic, depending on the surfaces roughness and the mechanical properties of the surfaces. For plastic contacts, typical of metallic interfaces, the adhesional friction coefficient can be defined as

$$\mu_a = \frac{\tau_a}{H} \tag{4.7}$$

where H is the hardness of the softer of the contacting materials. It is to underline that, differently to elastic contacts, μ_a is independent of the surface roughness.

Before the sliding begin, the plowing component μ_d largely controls the static friction. However, the magnitude of the plowing contribution depends on:

- surface roughness;
- relative hardness;
- size, shape and hardness of wear debris.

When one of the sliding surfaces is harder than the other one, the asperities of the harder surface plows into the softer one, producing wear grooves once the shear strength is exceeded. Moreover, also wear particles trapped inside the friction interface can plow the softer surface.

In metal pairs the deformation component is generally dominant compered to the adhesion one. It can be reduced by reducing surface roughness, by selecting materials of almost equal hardness and by removing wear and contaminant particles from the interface. However, the dominant mechanism of energy dissipation in metals pairs is the plastic deformation, aiming that this component is crucial when developing a seismic device.

Strictly related to adhesion and plowing friction components is the wear, defined as the "*damage or removal of material from one or both of two contacting surfaces in relative motion*" (Bhushan, 2013). Usually, wear occurs trough the interaction of the surfaces's asperities. During the relative motion, material of the contacting surfaces is usually displaced altering the properties of the solid body near the interface. Subsequently, the material is removed from one of the two surfaces and transferred to the mating one or may be loose as wear particle. In the first case there is no net volume or mass loss despite one of the surfaces is worn.

Wear arises from mechanical and chemical means and is generally incremented by the heat developed from frictional sliding. Among the several distinct wear phenomena, which have in common the solid material removal, adhesive and abrasive wear can be considered as the most relevant during seismic friction dampers activities. Adhesive wear occurs when two solid surfaces in sliding contact shear the adhered asperities, resulting in a continues detachment and attachment of asperities fragment from one surface to the other one. As the sliding continues, these fragments can be loose as wear particles. Abrasive wear occurs when the asperities of a hard surface or hard particles slide on a softer surface, damaging the interface by plastic deformation. Metallic surfaces in relative sliding motion usually register plastic grooves.

4.1.1 Relevant friction sliding mechanisms

Two contacting surfaces subjected to sliding friction are able to show different mechanism depending on surface roughness, hardness and physical-chemical properties. The following cited friction mechanisms are considered by the author as the most relevant for the optimal development of the tribological interface of a seismic damping device and must be considered in the selection of mating surfaces.

4.1.1.1 Resting time dependence of the static friction coefficient

The static friction coefficient is very sensible to the resting time (such as dwell time, time of sticking or duration of contact) and is able to increase or decrease. When two contacting solids are subjected to rest time, the adhesional effects increase and, consequentially, the static friction coefficient increases as well; this is the typical behaviour of dry contacts. Clean contact are also subjects to static friction growth while, on the opposite, if the interface is contaminated by low shear-strength species, the static friction coefficient decrease.

4.1.1.2 Stick-Slip mechanism

The stick-slip phenomenon is a typical sliding behaviour that occurs when the sliding velocity does not remain constant as function of distance and time, producing an oscillatory form. Figure 4.4 represent the typical stick-slip behaviour in a friction force graph. During the stick phase, the friction force increase reaching the $F_{\mu,s}$ value and the slip phase occurs at the interface. The friction force decrease rapidly reaching the $F_{\mu,k}$ value and a steady sliding phase occurs.

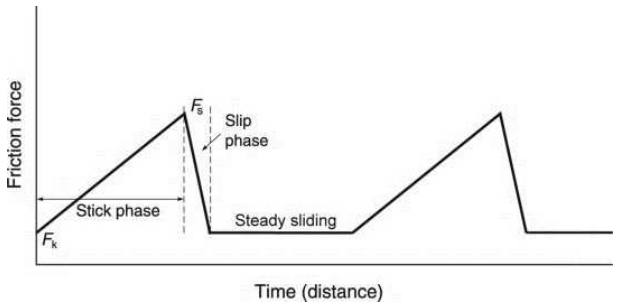

FIGURE 4.4: Stick-slip behaviour in friction force graph as function of time/distance (Bhushan, 2013).

The stick-slip process arises when the static friction coefficient is remarkably greater than the kinetic friction coefficient and, also, when the kinetic friction coefficient vary with the velocity. This effect can be reduced selecting a tribological pair with similar values of μ_s and μ_k.

4.1.1.3 Interface useful lifetime

During the sliding process, changes can occur in the condition of the interface which can affect friction and wear properties. As pictured in Figure 4.5, after the initial "run-in" period the friction coefficient generally stabilized but, after a certain period of time, reaches a transition period that increase it leading to a second steady sliding plateau.

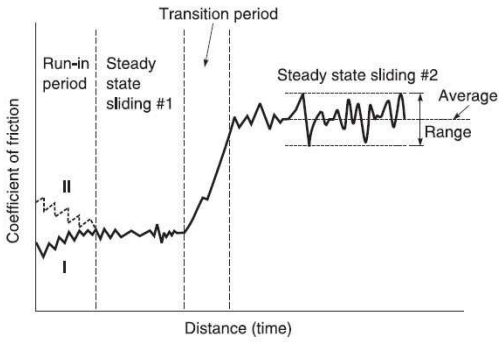

FIGURE 4.5: General behaviour of friction coefficient as function of time (Bhushan, 2013).

This process can continue reaching more than two plateaus, but the difference between two steady-states COF values is function of the mechanical properties of the friction interface and can be determined only experimentally. For engineering applications, the first steady state period is usually considered crucial and it defines the useful interface life.

4.1.2 Tribological behaviour of friction devices

The tribological system of a seismic friction device usually includes two metallic plates with a bolt that keeps them coupled by its tension force, which consequentially acts as normal load W. The developed frictional interface is a metallic one and the deformation component is expected to be dominant.

The bolt tension arise the adhesive component of friction involving interfaces asperities, as showed in Figure 4.6(a). It has been observed by Grigorian et al. (1993) that, as the sliding begin, the adhered asperities are continually sheared and exchanged between the two surfaces in contact, as showed in Figure 4.6(b). The arised adhesive wear particles lead to outward displacement of the plates in the axial bolt direction. These displacements result in an increment of bolt tension and, consequentially, in the normal force between the sliding plates. As previously defined, the friction force is directly proportional to W, aiming that the increment of W is reflected into the increment of the registered tangential friction force.

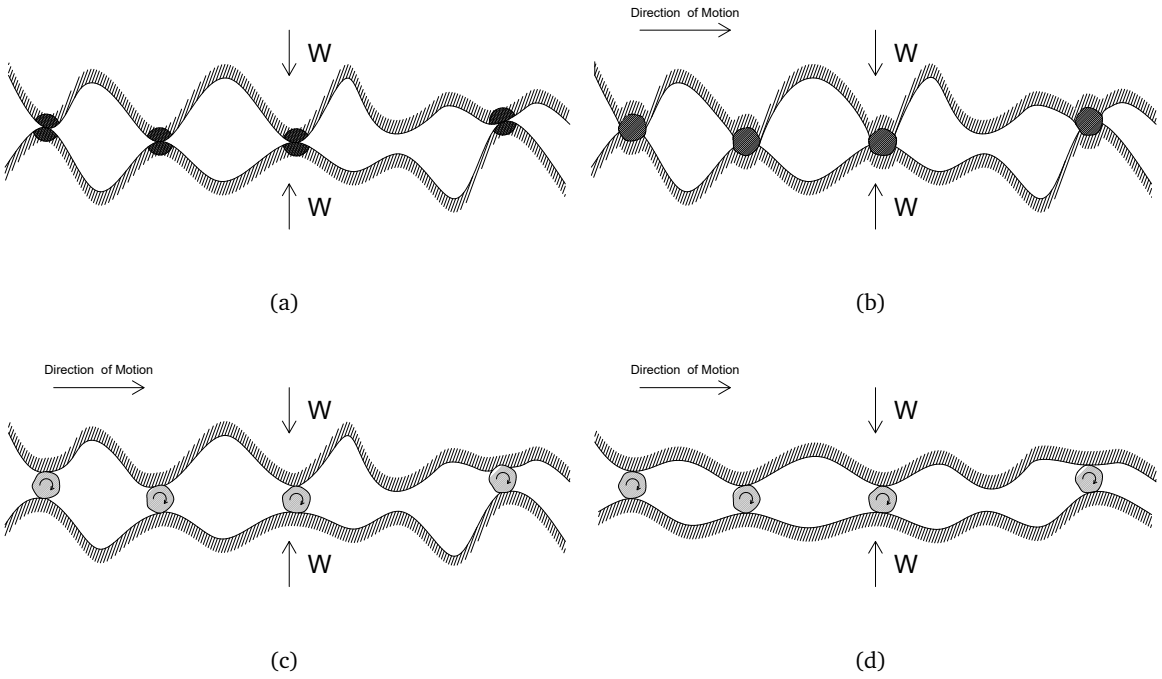

FIGURE 4.6: Evolution of friction interface during sliding. The adhesive component (a) involves the asperities and adhesive wear particles (b) start to be exchanged between the two surfaces. As the sliding continues, adhesive particles start to act as abrasive wear particles (c) leading to an increase of wear grooves (d).

As the sliding continues, a quote of these particle act as abrasive particles as showed in Figure 4.6(c), leading to abrasive wear, while the rest are reabsorbed by the surfaces or fall out from the connection. The abrasive wear presence is confirmed from the grooves on one or both steel plates, leading to the configuration pictured in Figure 4.6(d), depending on the relative hardness. The eventual particles reabsorption and fall out results in the reduction of normal force and, consequentially, the tangential slip force decreases. Consequently, friction's adhesive and deformation components both play a significant role in the overall FD's behaviour.

4.2 On the selection of the mating surfaces

During the development of a new FD, the selection of mating surfaces sets a crucial point, and a full comprehension of the involved tribological aspects is needed to design a device that can perform a wide and stable hysteresis cycle. FDs usually include metallic plates coupled with several preloaded bolts. In this study, the mating surfaces are chosen among common metals suitable for structural purposes.

A first main aspect to consider during the selection of mating surfaces, which is connected to the friction's adhesive component, is the difference between μ_s and μ_k friction coefficients that must be kept as smaller as possible. FDs are subjected to oscillatory displacements and during the motion reverse, due to the subsequent decrement and increment of sliding velocity, if μ_s is remarkably greater than μ_k the stick-slip process arises leading to an unstable hysteresis cycle (Bhushan, 2013). This behaviour is typical of unmachined steel-steel couplings (Latour et al., 2014). In addition, roughness plays a significant role in interface frictional behaviour, particularly on the static friction coefficient, which increase as roughness increments (Bhushan, 2013). Some researchers have investigated the influence of different machining (Ivkovic et al., 2000) and cutting (Funke and Schubert, 2016) processes, observing an increment in static friction associated to milling processing. Further research has been conducted on ground (Liang et al., 2018) surfaces, showing that lower values of initial roughness reached higher and more stable values of static and kinetic friction coefficient and smaller transition times (Bhushan, 2013).

A second main aspect to consider is the selection of mating surfaces that show a μ_k as constant as possible during the sliding motion. This steadiness can be obtained acting on the friction's deformation component, by reducing the wear's abrasive component or particles formation during the sliding motion (Bhushan, 2013).

The combination of different material surfaces, with a remarkable different hardness, such as steel-brass and steel-bronze couplings, leads to a decrement of the abrasive component. Brass and bronze have a lower hardness than steel and they have been traditionally used as pads against steel to realize frictional coupling in FDs since the '80s (Pall, 1983). Brass and bronze pads lead to the formation of abrasive grooves mostly on their side, so that a device can be fully restored by a simple replacement of these pads. Steel-brass couplings have shown lower wear rate (Grigorian et al., 1993) and a more stable hysteresis cycle (Latour et al., 2014) than the simple steel-steel couplings; however, a decrement in sliding friction force has also been registered (Rodgers et al., 2017). Steel-bronze couplings have shown a constant and predictable hysteresis cycle; however, unneglectable stick-slip effect and a decrement in sliding friction force have also been registered (Morgen and Kurama, 2009).

The coupling of different steel surfaces with remarkably different hardness, such as mild steel and hard steel or tempered steel, also leads to a decrement of the abrasive component. Investigations on the influence of steel hardness have shown the development of stable hysteresis cycles with low wear rate, even after some repetitions, simulating subsequent earthquakes (Chanchi Golondrino et al., 2020). It has also been emphasized that hard steel and tempered steel, coupled with mild steel, are able to perform more stable hysteresis cycles than brass (Khoo et al., 2012; Zimbru et al., 2018). Recent investigations on the useful wear life of tempered steel against mild steel and brass, have highlighted that the second pair reaches higher distance life (Bhushan, 2013) and lower coefficient of friction decrement (Fereidouni et al., 2020).

An alternative approach for the reduction of wear rate is the adoption of organic material pads coupling with steel in the friction interface, as developed by automotive braking technology. Studies focused on new low-composite materials (Lee et al., 2016) and non-asbestos organic materials (Huang et al., 2020; Huang et al., 2018; Kim and Christopoulos, 2008) have proved the development of predictable, repeatable, and stable hysteresis cycles. However, organic material pads are not allowed for structural use in civil constructions applications, as outlined by EN 15129 (CEN, 2018).

The reduction of wear particles formation is strictly related to the reduction of wear rate and can be reached with superficial treatments like coatings and shot peening. Coatings must be carefully selected, taking in account of the properties that coatings give to the substrate of the surfaces. If the selected coating is susceptible to abrasion, the formed wear particles can increase the wear effect or act as lubricant (Rodgers et al., 2017). Moreover, it must be considered that if the device acts in dry conditions, the selected coating must perform well in this configuration. Phosphate-based coatings, for example, are not suitable to dry conditions, leading to an unstable friction coefficient and wear rate (Saffarzade et al., 2020). On the contrary, aluminium-based and nickel-based coatings have registered an interesting behaviour leading to friction devices with stable hysteresis cycles (Ferrante Cavallaro et al., 2017; Latour et al., 2014; Latour et al., 2015; Manojkumar et al., 2014; Zimbru et al., 2018).

Shot peening is characterized by a difficult theoretical analysis due to its stochastic nature and the considerable number of variables that control its efficiency (Das et al., 2020; Vaxevanidis et al., 2006), leading to a wide selection of shots (balls' size, shape, and material), targets (material and prestress conditions) and flows (velocity or air-blast pressure, angle of impingement and standoff distance). Surfaces subjected to shot peening have registered an increment of superficial hardness and a decrement of wear rate in sliding conditions, leading to a more stable frictional behaviour even in dry conditions (Mitrovic et al., 2014). Further investigations have aimed to improve the tribological properties of stainless steel (Gopi et al., 2020) and screw underhead of bolted joints (Croccolo et al., 2020).

The tribological behaviour of friction interfaces is strictly related to mean contact pressure, sliding velocity and dry or lubricated conditions (Bhushan, 2013); for this reason, a tribological experimental investigation is an indisputably useful tool in the developing of any new FD. Friction interfaces are usually investigated trough PoD tests, recognized as economic and efficient, particularly for the study of brake systems (Sinha et al., 2020).

4.3 Pin-on-Disk test methodology

PoD tests, which are commonly used during tribological investigation, consist of a fixed pin subjected to a uniform vertical load, sliding on a rotating disk. Pins can be nonrotating balls, flat-ended or hemispherical-ended cylinders (Bhushan, 2013). Previous studies have observed that PoD tests are an economical and efficient method to investigate brake behaviour (Sinha et al., 2020), but they must be set to reproduce the real use condition. It has been reported that a good approximation of the real use condition is achievable making use of the parameter pv, where p is the mean contact pressure and v the sliding velocity (Verma et al., 2015). To derive accurate results, pv values reached during the PoD tests must be similar to the ones expected for the braking system during the real use. Taking advantage of the strong mechanical

analogy existing between braking systems and FDs, in this study the PoD test methodology for interfaces characterization of the novel FD has been based on testing protocols addressed for braking systems.

An example of possible inaccuracy has been observed during the preliminary tests of this tribological campaign, in which PoD tests have been set only according to the device's expected mean contact pressure ($p_{m,BRFD}$). During these preliminary tests, PoD set-up has included a single disk (8 mm thick and 165 mm diameter) and two cylindrical pins (P1 and P2, 3 mm and 6 mm diameter respectively) made of steel S355JR ($f_y = 355$ MPa), and two different normal loads (L1 and L2, 100 N and 50 N respectively). These tests consisted of 300 s oscillatory sliding at 1 Hz frequency on an average 80 mm circular arc track.

Figures 4.7(a) and 4.7(b) show the profilometry of disk's wear grooves for P1 and P2 subjected to L1, respectively, at the end of the test. P1's shape is conical and highlights the higher values of contact pressure and the sharp shape-effect due to its small diameter. P2's shape is trapezoidal and highlights the lower values of contact pressure and the smoother shape-effect due to its bigger diameter. It is clearly visible that P2-L1 wear grooves resemble better the flat wear grooves expected for the real-scale FD in development.

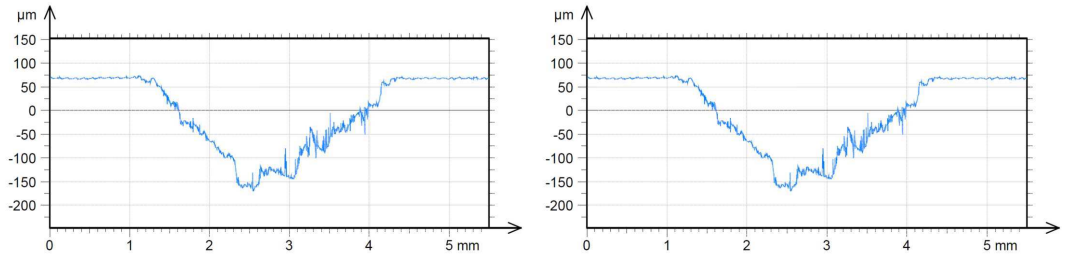

(a) (b)

FIGURE 4.7: Wear grooves' 2D profilometry of (a) P1 and (b) P2 subjected to L1.

The different groove shapes registered are related to the Hertz's contact pressure distribution between the cylindrical pins and the disk. For a cylindrical indenter on a flat surface, under the hypothesis of rigid bodies, the distribution of pressure σ_z can be expressed as follows (Fischer-Cripps, 2007):

$$\sigma_z = -\frac{1}{2} p_m \left(1 - \frac{r^2}{R^2}\right)^{-1/2} \quad 0 \leq r \leq R \tag{4.8}$$

where p_m is the mean contact pressure, R the pin's radius and r the radial coordinate that ranges between 0 and R.

Figure 4.8 shows the comparison of theoretical pressure distributions developed by P1 and P2 when both subjected to L1 and L2 as function of the unidimensional coordinate r/R. As can be observed in Figure 4.8, σ_z reaches minimum values at the center of the pins $(r/R = 0)$, with $\sigma_{z,min} = -1/2 p_m$, while it approaches theoretically infinity at the edges of the pin $(r/R = 1)$. P1-L1 registers the higher σ_z values and the higher difference between $\sigma_{z,min} = \sigma_z\,(r/R = 0)$ and $\sigma_{z,max} = \sigma_z\,(r/R = 0.99)$, while P2-L2, on the opposite, registers the lower σ_z values and an almost flat distribution of pressure.

Table 4.1 lists pins' mean contact pressure p_m, the ratio between pins' mean contact pressure and the device's expected mean contact pressure $p_m/p_{m,d}$, $\sigma_{z,min}$ and $\sigma_{z,max}$ values, the difference between $\sigma_{z,min}$ and $\sigma_{z,max}$, the ratio $\sigma_{z,max}/f_y$ and the ratio between PoD and expected device pv parameter, pv_{PoD}/pv_{BRFD}. While P1-L1 better approaches the device's expected mean contact condition, with $p_m/p_{m,BRFD} = 0.82$,

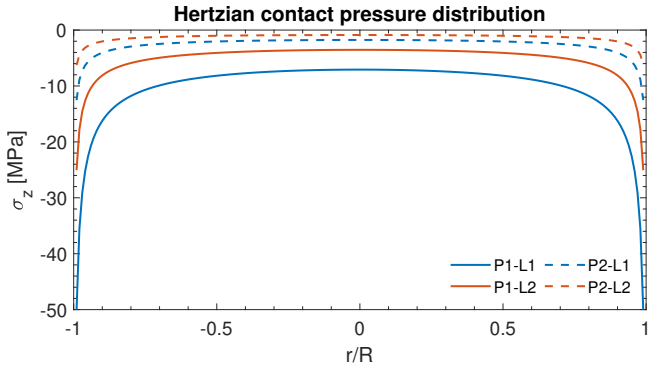

FIGURE 4.8: Comparison of Hertz's contact pressure distribution between pin and disk for preliminary tests.

the real pin's contact pressure distribution is extremely high, even for the lower load combination P1-L2. Moreover, P1 registers the higher values of $\sigma_{z,max}/f_y$, which ranges between 0.141 and 0.071, and the higher values of pv_{PoD}/pv_{BRFD}, which ranges between 10.15 and 5.07. Consequently, P1 is more prone to wedging grooves, highlighting the inappropriate PoD setting, especially for P1-L1. Differently, P2 registers an overall better contact pressure distribution, with lower $\sigma_{z,min}$ and $\sigma_{z,max}$ values and differences when subjected to both L1 and L2. P2 registers the lower values of $\sigma_{z,max}/f_y$, which ranges between 0.035 and 0.017, and the lower values of pv_{PoD}/pv_{BRFD}, which ranges between 2.54 and 1.27. Consequently, P2 is less prone to wedging grooves highlighting a more appropriate PoD setting, especially for P2-L2.

TABLE 4.1: PoD preliminary tests Hertz's pressure comparison.

	p_m [MPa]	$p_m/p_{m,d}$	$\sigma_{z,min}$ [MPa]	$\sigma_{z,max}$ [MPa]	$\sigma_{z,max}$-$\sigma_{z,min}$ [MPa]	$\sigma_{z,max}/f_y$	pv_{PoD}/pv_{BRFD}
P1-L1	14.15	0.82	7.07	50.14	43.07	0.141	10.15
P1-L2	7.07	0.41	3.54	25.07	21.53	0.071	5.07
P2-L1	3.54	0.21	1.77	12.54	10.77	0.035	2.54
P2-L2	1.77	0.10	0.88	6.27	5.38	0.017	1.27

As a summary, the PoD preliminary tests have highlighted that assuming $p_m/p_{m,BRFD}$ ratio close to unit leads to an inaccurate representation of the contact behaviour, with high values of Hertzian contact pressure σ_z and hight differences between $\sigma_{z,min}$ and $\sigma_{z,max}$. On the contrary, assuming pv_{PoD}/pv_{BRFD} ratio close to unit leads to a better representation of the contact behaviour, with low values of Hertzian contact pressure σ_z and low differences between $\sigma_{z,min}$ and $\sigma_{z,max}$. This second approach allows to select both the pin diameter and the applied load representing the FD's real use conditions.

Further studies about brake friction behaviour have shown the importance of developing a conformal contact between two sliding surfaces before the actual tests (Federici et al., 2019, 2018, 2017). During the wear process, the presence of wear debris forms friction layers, which are responsible for the transmission of the friction force between two mating surfaces. More precisely, wear debris tend to accumulate in the proximity of the surfaces forming a primary and a secondary plateau. The primary plateau consists of hard particles and fibers protruding from the brake pad surfaces, while the secondary plateau consists of piled up wear debris compacted against the primary plateau. The more compacted the secondary plateau is, the

more stable and smooth the Coefficient of Friction (COF) is (Federici et al., 2018). As a result, a running-in stage before the actual test allows a better development and establishment of COF behaviour.

4.4 Experimental campaign

The tribological investigation has been performed at the Metallurgy Laboratory of the University of Ferrara, Italy. The PoD testing equipment is composed by a 6 mm diameter cylindrical flat-ended pin that slides on a 160 mm diameter rotating disk, schematically represented in Figure 4.9 with highlighted in red the adopted pin's tracks.

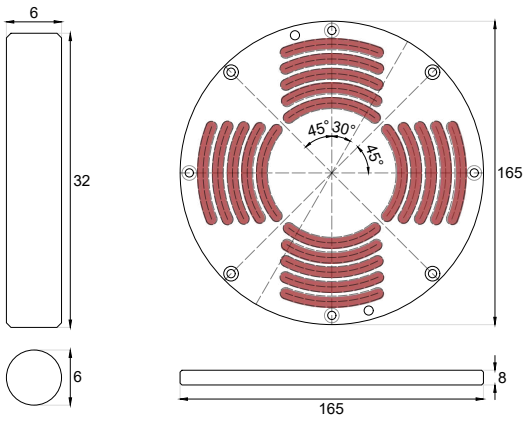

FIGURE 4.9: Comparison of Hertz's contact pressure distribution between pin and disk for preliminary tests.

The objective of this tribological investigation is the selection of mating surfaces with a balanced compromise between friction coefficient steadiness as function of time/displacements and process costs, including both production costs and running-in phase execution costs required before the FD's installation. Since the main body of the developed FD is made of steel S355JR (CEN, 2015), the testing mate surfaces have been selected based on the lower ware rate exhibited when coupled with this material, such as: steel S355JR itself (CEN, 2015), bronze CuSn12 (Copper et al., 2017), brass OT58 (Copper et al., 2017), shot peened steel S355JR (CEN, 2015), nickel base coating and zinc base coating. Contextually, the requirement of a low-cost process has led to the selection of machine processes traditionally used in surfaces machining, such as turning and milling, considering different roughness values. Table 4.2 and Table 4.3 list the information of considered materials and machine processes, with respective tags that will be used in the following. Figure 4.10 shows the main disks and pins used during the executed tribological investigation.

TABLE 4.2: Materials information.

Material	Material Code	Specimen Tag
Steel	S355JR	ST
Bronze	CuSn12	BZ
Brass	OT58	BS

TABLE 4.3: Machining process information.

Machining process and additional treatment	Nominal roughness *Ra* [μm]	Specimen Tag
Turning	0.8	T0.8
Turning	1.6	T1.6
Turning	3.2	T3.2
Turning	6.3	T6.3
Milling	0.8	M0.8
Milling	1.6	M1.6
Milling	3.2	M3.2
Milling	6.3	M6.3
Shot peening	1.0	SP1
Shot Peening	2.0	SP2
Nickel base coating	-	NI
Zinc base coating	-	ZN

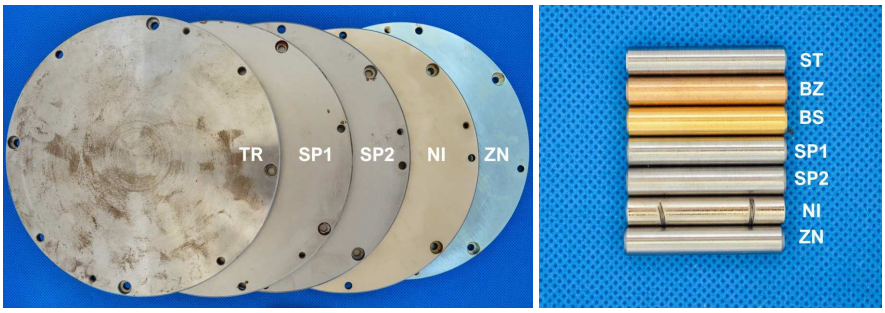

(a) (b)

FIGURE 4.10: Main (a) disks and (b) pins used for the tribological investigation.

The characterization of the reference material and the additional treatments was performed on a cross-section of the disks to determine the initial roughness and the treatment thickness. A Talysurf CCI-Lite non-contact 3D profilometer (Taylor Hobson, Leicester, UK) was used to evaluate the average roughness of each specimen over three different measurements. In accordance with the literature (Liang et al., 2018; Vaxevanidis et al., 2006), the samples' surface roughness was evaluated by calculating *Ra* parameter following the UNI EN ISO 25178-2:2022 standard (CEN, 2022), while evaluation length and cut-off following the UNI EN ISO 21920-3:2021 (ISO, 2021). *Ra* is defined as the mean difference in height from the mean height on the considered profile. An optical microscope Leica dMi8 A (Leica Microsystem, Wetzlar, Germany) with acquisition software LAS v4.13 was used to measure and evaluate the average thickness of each treatment over ten different measurements.

Hardness measurements were carried out by instrumented nanoindentation, using different indenters according to literature (Sriraman et al., 2016; Wu et al., 2007). An AntonPaar NHT2 nanoindenter (An-ton Paar GmbH, Graz, Austria) with a Berkovich penetrator was used to determine ZN and NI hardness, with a preset load of 20 mN with a 2 mN/s loading rate, a 5 s holding time and a final 2 mN/s de-loading rate

step. Five indentions were made in each test for statistical analysis and consistency inspection. The hardness and the reduced elastic modulus were calculated by fitting the load–displacement (P–h) curve using the Oliver–Pharr method. A Fischerscope HM2000 (Helmut-Fischer GmbH, Sindelfingen, Germany) with a Vickers indenter was used to determine the hardness along the cross-section of the shot peened samples SP1 and SP2. A 20 mN load was applied with a 2 mN/s loading rate, maintained for a 5 s holding time and a final 2 mN/s de-loading rate step. To evaluate the hardness as a function of the depth along the cross-section an indentation profile with 30 µm steps was carried out. The hardness was calculated from three measurements in each position. To compare the hardness values, the resultant Berkovich's hardness values (H_{IT}) were converted to Vickers scale (HV) according to UNI EN ISO 14577-1:2015 (ISO, 2015).

Wear tests were performed to evaluate COF over time and the wear rate of disks and pins for each selected coupling. A TR20-LE (Ducom Instruments, Bengaluru, India) tribometer (see Figure 4.11(a)) set on pin-on-disk reciprocating configuration and software WinDucom were used to monitor the COF values over time. Tests were performed under dry conditions and at room temperature, in accordance with the ASTM G99-17 standard. During the tests, pins were subjected to a 50 N vertical load while disks were rotating at 1 Hz and 2 Hz oscillatory frequencies. The setting was calibrated to reproduce the actual condition of the BRFD and assuming for the disk rotation frequencies typical of the structural system in which a FD is usually installed. In the real use conditions, the typical values of the pv parameter for the device (pv_{BRFD}) under development ranges between 0.10 and 0.20. Setting circular arc pin track with an average of 54 mm arc length and considering oscillatory frequencies of 1 Hz and 2 Hz, the associated maximum linear speed equals 0.111 m/s and 0.222 m/s, respectively. Applying a vertical 50 N load, the pv parameter for the PoD test (pv_{PoD}) reaches values similar to the pv_{BRFD} ones, registering a pv_{PoD}/pv_{BRFD} ratio close to the unit.

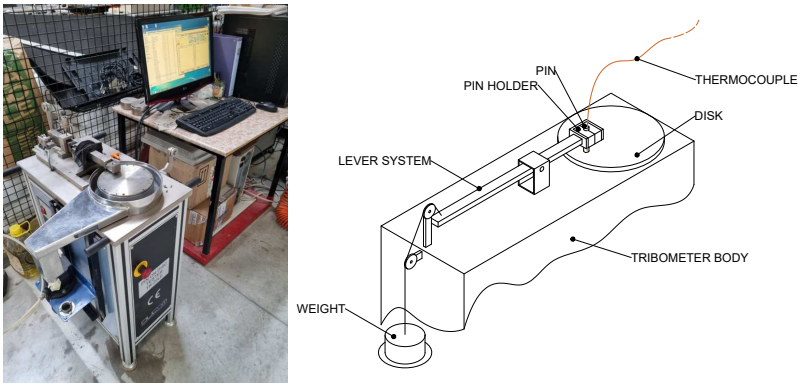

(a) (b)

FIGURE 4.11: Tribometer equipment (a) and PoD tests set-up schematics (b).

During the wear tests, COF was continuously measured by the tribometer, equipped with a load cell to measure the frictional force, an encoder to control the rotational speed, and a linear variable differential transformer (LVDT) to assess the system's wear. A K-thermocouple connected to a TC-08 thermocouple data logger (Pico Technology, St Neots, United Kingdom) was placed in the proximity of the frictional interface to measure the pin's interface temperature, assessing the eventual influence of temperature on COF behaviour, according to the set-up schematic of Figure 4.11(b). After each test, the pins were ultrasonically cleaned in acetone bath to remove the remnant wear debris.

A Kern ABT 100-5NM (Kern, Balingen, Germany) analytical balance with an accuracy resolution of 0.01 mg was used to measure the pins' weight loss and evaluate the pins' wear rate, wr_p. Pins were weighted before and after the PoD tests, and the average weight loss was evaluated over three different tests. More precisely, wr_p evaluation (expressed in mm^3/Nm) has been carried out using equation 4.9, where Δg (expressed in g) is the pin's mass loss, ρ is the pin's mass density (expressed in g/mm^3), S_{tot} is the total sliding distance (expressed in m) and W is the pin's applied load (expressed in N):

$$WR_p = \frac{\Delta g}{\rho S_{tot} W} \tag{4.9}$$

A Talysurf CCI-Lite non-contact 3D profilometer (Taylor-Hobson, Leicester, UK) was used to analyse disks' wear track and evaluate disks' wear rate, wr_d. More precisely, wr_d evaluation (expressed in mm^3/Nm) has been carried out using the equation 4.10, where ΔV (expressed in mm^3) is the disk's volume loss, A_w (expressed in mm^2) is the wear track's area, S_w (expressed in mm) is the wear track's length, S_{tot} is the total sliding distance (expressed in m) and W is the pin's applied load (expressed in N).

$$WR_d = \frac{\Delta V}{S_{tot} W} = \frac{A_w S_w}{S_{tot} W} \tag{4.10}$$

The wear testing procedure has been set by taking into account the typical break-in curve shape of treated surfaces of Figure 4.12. Blau (2005) reported that, commonly, treated surfaces are characterized by two steady-state stages with associated transition times (t_{tr}), defined as the time needed to reach a steady-state stage, and the mean steady-state COF values (μ_{st}) registered during the steady-state stage. The first steady-state stage is originated from the treated surface (a harder layer, a coating layer or trapped coating wear debris) and coincides with the surface treatment useful life (Fereidouni et al., 2020), lasting until the treated layer is completely removed. The surface treatment useful life ends as the friction coefficient unstably increases after the steady-state stage. Once the substrate is exposed to wear, the second steady-state stage is reached and lasts until the end of the test.

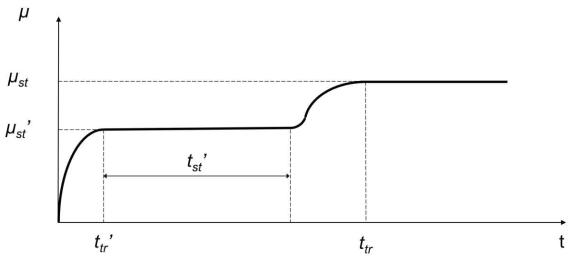

FIGURE 4.12: Curve shape of the most common break-in of treated surfaces.

To evaluate the consistency of μ, the mean steady-state μ_{st} value is associated with a coefficient of variation cv_μ defined as the ratio between the mean standard deviation and mean μ_{st} value in the steady-state stage.

The wear tests have been divided into four different parts, called Part 1, Part 2, Part 3 and Part 4. Part 1, which consisted of a total 80 tests, focused on the effects of roughness on COF behaviour, considering grooves geometry realized by turning and milling the steel disks surfaces (tags that start with T and M respectively). Steel S355JR (CEN, 2015) was assumed as reference material, and roughness values between

$Ra = 0.8$ μm and $Ra = 6.3$ μm were realized according to the typical values obtainable by the chosen surfaces machining process. Part 1 allowed the selection of the disks' machining process to use as reference for the following tests. Part 2, which consisted of a total 20 tests, focused on the effects of different metals (bronze and brass, BZ and BS tags respectively), coupled to steel, on COF behaviour. Part 3, which consisted of a total 40 tests, focused on the effects of additional steel treatments, coupled to steel, on COF behaviour. Shoot peened surfaces have been machined to reach two different values of roughness, more precisely Ra =1.0 μm (SP1) and Ra =2.0 μm (SP2). The final Part 4, which consisted of a total 30 tests, focused on the effects, of pin's different metals, coupled with disk's different treatments, on COF behaviour. The considered treatments were selected among the ones that registered the best performance during Parts 2 and 3. This last part aimed to identify the final friction mating surfaces for the FD in development.

For each tribological coupling an initial long test (LT) of 900 s duration has been performed, to observe the overall COF behaviour, and evaluate an adequate running-in time to develop a well compacted secondary plateau. Subsequently, four interrupted tests (IT) have been performed: each of them has a running-in stage of 300 s duration and five steady stages of 30 s, 60 s, 90 s and 120 s duration respectively. The repetition of steady stages was aimed to simulate subsequent earthquakes, including their typical durations, and to detect eventual COF degradation. Table 4.4 summarizes the tests procedure as well as the total sliding distance.

TABLE 4.4: Tribological test procedure summary.

Test tag	Frequency [Hz]	Total sliding time [s]	Total sliding distance [m]	Running-in stage time [s]	Running-in stage distance [m]	Steady stage time [s]	Steady stage distance [m]
LT	1	900	97.20	-	-	-	-
	2	900	194.40	-	-	-	-
IT30	1	450	48.60	300	32.40	30	3.24
	2	450	97.20	300	64.80	30	6.48
IT60	1	600	64.80	300	32.40	60	6.48
	2	600	129.60	300	64.80	60	12.96
IT90	1	750	81.00	300	32.40	90	9.72
	2	750	162.00	300	64.80	90	19.44
IT120	1	900	97.20	300	32.40	120	12.96
	2	900	194.40	300	64.80	120	25.92

4.5 Characterization of the surfaces

4.5.1 Roughness evaluation

Figures 4.13, 4.14 and 4.15 show the tridimensional topography of the investigated disks reconstructed according to §4.4 and used to evaluate their initial roughness *Ra*, listed in Table 4.5. Turned disks show a segmented texture (see Figure 4.13)), with picks that increase with the nominal roughness and *Ra* values that range from 0.77 (T0.8) to 6.93 μm (T6.3), which are close to the nominal roughness. Milled disks show a scratchy texture (see Figure 4.14)), with picks that increase with the nominal roughness and *Ra* values that range from 0.58 (M0.8) to 9.07 μm (M6.3), which slightly differ from the nominal roughness. NI, SP1 and SP2 conditions show a non-periodical texture (see Figure 4.15)), with *Ra* values that ranges

between 0.97 and 2.20 µm. ZN condition (see Figure 4.15(d))) shows a topography comparable with T0.8, with an average *Ra* value of 0.53 µm. NI, SP1 and SP2 exhibit the highest deviation from T0.8 topography, with a significant change in both texture morphology and roughness. On the contrary, ZN exhibits only a decrement compared to the T0.8 initial roughness.

TABLE 4.5: Roughness values *Ra* of the disks and thickness values *t* of the galvanizing treatments.

Condition	***Ra* [µm]**	***t* [µm]**
T0.8	0.77 ± 0.01	-
T1.6	2.06 ± 0.01	-
T3.2	3.83 ± 0.02	-
T6.3	6.93 ± 0.02	-
M0.8	0.58 ± 0.02	-
M1.6	1.81 ± 0.05	-
M3.2	6.00 ± 0.52	-
M6.3	9.06 ± 0.04	-
P1	0.97 ± 0.03	-
P2	1.77 ± 0.12	-
NI	2.20 ± 0.10	9.1 ± 0.9
ZN	0.52 ± 0.07	Max: 8.2 ± 0.9 Min: 4.8 ± 1.3

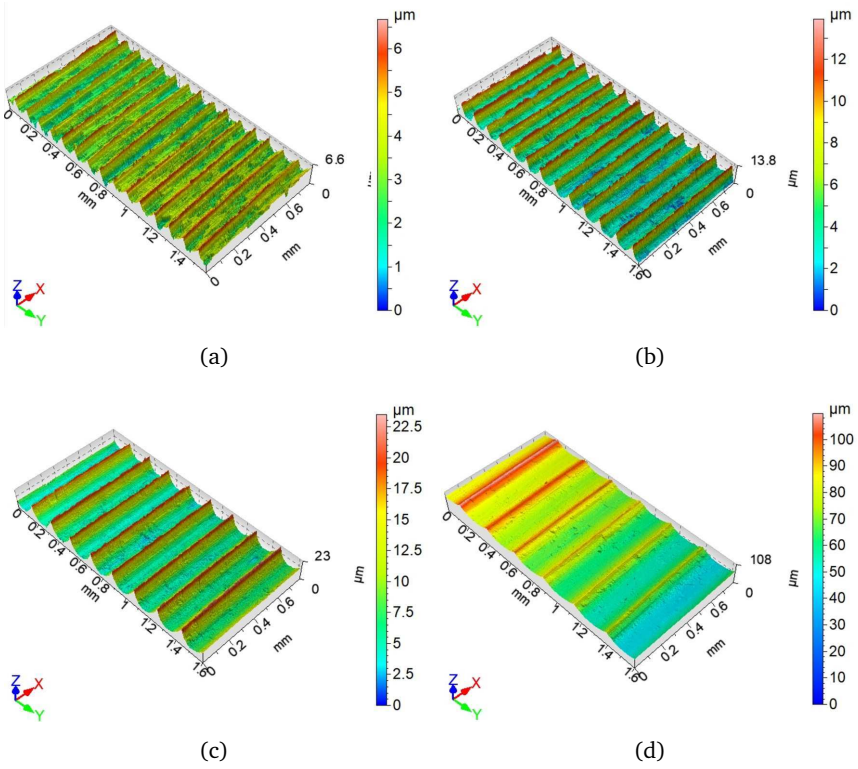

FIGURE 4.13: Tridimensional topography reconstruction of the investigated turned disks: a) T0.8, b) T1.6, c) T3.2 and d) T6.3.

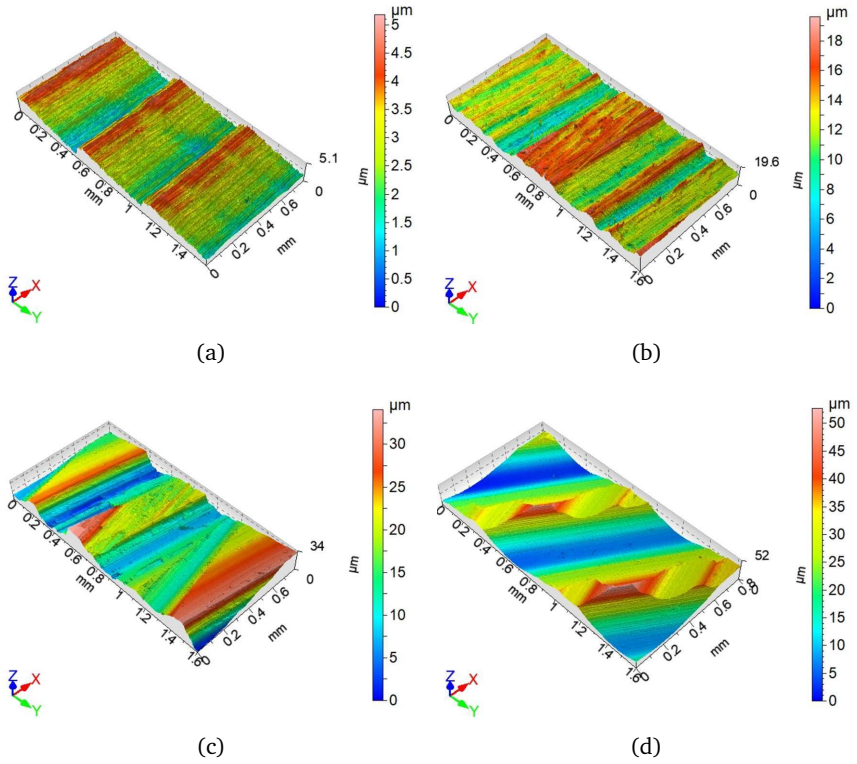

FIGURE 4.14: Tridimensional topography reconstruction of the investigated milled disks: a) M0.8, b) M1.6, c) M3.2 and d) M6.3.

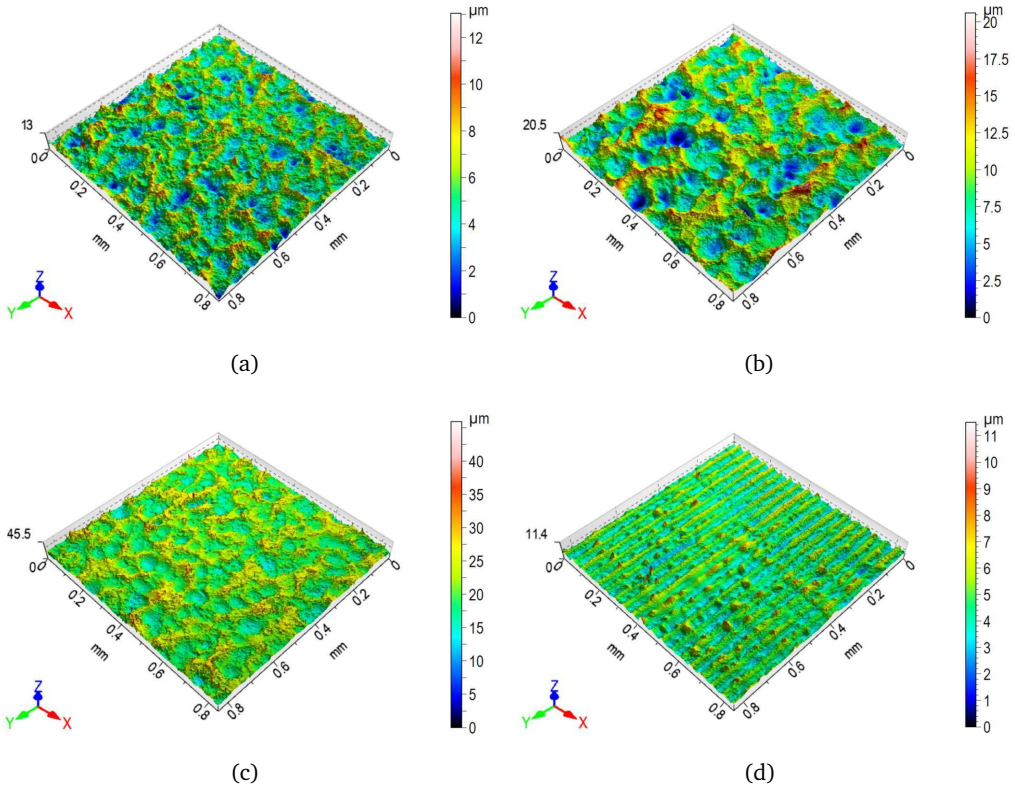

FIGURE 4.15: Tridimensional topography reconstruction of the investigated treated disks: a) SP1, b) SP2, c) NI and d) ZN.

Figures 4.16(a) and 4.16(b) show the optical micrographs of the cross-sections for NI and ZN disks, respectively, obtained according to §4.4 and used to evaluate the thickness of the coatings t, listed in Table 4.5. Despite the irregular superficial texture, NI displays an almost constant thickness that is 9.1 µm on average. On the contrary, the thickness of ZN varies with values ranging between 4.8 and 8.2 µm in correspondence to the valleys and picks, respectively, resulting from the turning. This is responsible for the lower roughness of ZN specimen compared to the reference T0.8, as previously described during the tridimensional topography analysis.

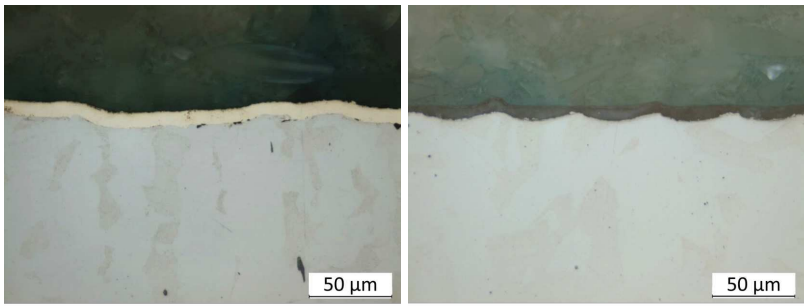

(a) (b)

FIGURE 4.16: Optical micrographs for thickness measurements of a) NI and b) ZN conditions.

4.5.2 Hardness evaluation

Figure 4.17 shows the Vickers hardness values through the cross-section of SP1 and SP2 disks, over three different replicas. As the impact of the shots with the specimen's surface causes plastic deformation, the hardness reaches its largest values in the sub-superficial zone of the sample and gradually reduces with depth (Trung et al., 2016). SP2 showed a sub-superficial hardness (452 ± 31 HV) higher than SP1 (320 ± 17 HV), but in both cases that increment faded between 75 and 100 µm of depth. It is worth noting that, a large variation of the results is shown; however, this variation is compatible with the ones registered by Trung et al. (2016). The presence of the different microstructural constituent along the cross-section is easily detectable when a 20 mN load is used, resulting in a higher variation of the regis-tered data.

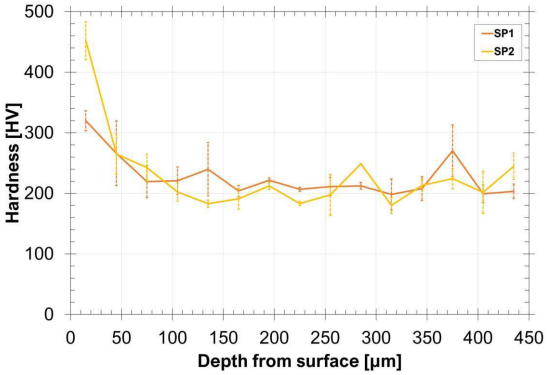

FIGURE 4.17: Cross-section hardness variation as a function of depth of SP1 and SP2 conditions.

Vickers hardness values for each considered treated surface are listed in Table 4.6. Ac-cording to UNI ISO 14577-1 (ISO, 2015), H_{IT} values for NI and ZN were converted in HV to allow the comparison between the

sub-superficial properties of all the surfaces. Based on the experimental data, NI showed the highest hardness and, on the contrary, ZN the lowest one confirming literature data (Sriraman et al., 2016; Sriraman et al., 2012; Wu et al., 2007).

TABLE 4.6: Values of sub-superficial Vickers hardness of the studied surfaces [HV].

Disk	T&M	SP1	SP2	NI	ZN
Hardness [HV]	228 ± 45	452 ± 31	320 ± 17	607 ± 59	60 ± 8

4.6 Wear tests results

4.6.1 Wear tests part 1 results: effects of different surface textures

Part 1 considers the friction coupling of turned and milled steel disks (tags that start with T and M respectively) with different roughness, tagged in Table 4.3, with ST pins.

4.6.1.1 Long tests results

Part 1 LT tests were performed to evaluate an adequate running-in period for the following IT tests. Figures 4.18(a) and 4.18(b) show the average evolution of μ for the tests performed at 1 Hz and 2 Hz. All the investigated couplings register an overall similar behaviour, reaching only one steady-state stage at both sliding frequencies, with μ_{st} values around 0.66 both at 1 Hz and 2 Hz. This behavior is typical of steel-steel couplings in dry sliding conditions, as reported by Blau (2005).

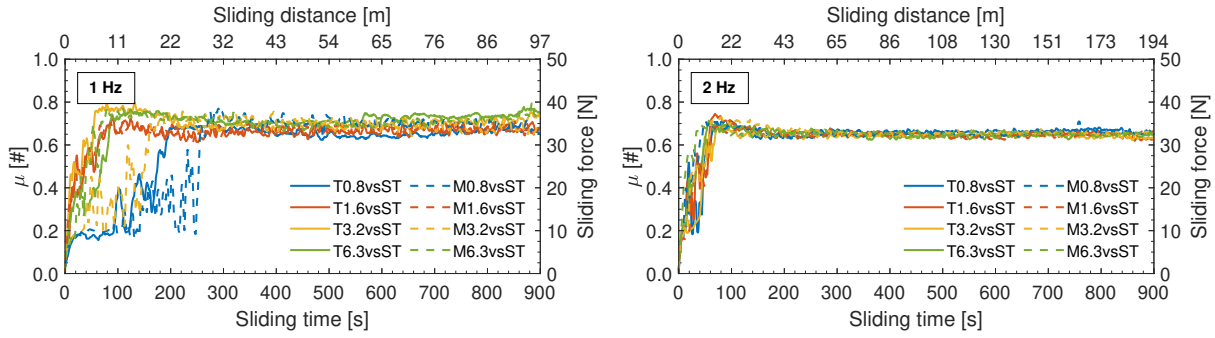

(a) (b)

FIGURE 4.18: Part 1 LT results as function of sliding time, distance and sliding frequency: COF and sliding forces at (a) 1 Hz and (b) 2 Hz.

Concerning the transition time, the t_{tr} values are higher than 100 s at 1 Hz tests and lower than 100 s at 2 Hz tests. It is worth noting that t_{tr} decreases when incrementing the superficial roughness, with T0.8 and M0.8 registering the longer t_{tr} values. This is particularly visible during the tests performed at 1 Hz sliding frequency, while during the tests performed at 2 Hz sliding frequency the influence of the superficial roughness is irrelevant.

Considering the results of Part 1 LT, and to ensure the achievement of the COF's steady stages, Part 1 IT-RI tests duration is set at 300 s, as reported in Table 4.4.

4.6.1.2 Interrupted tests results

Figures 4.19(a) and Figure 4.19(b) show the mean COF behaviour, at 1 and 2 Hz respectively, during the IT running-in stages for each machine process and roughness. All the investigated couplings register an overall similar behaviour: a transition time t_{tr} higher than 100 s at 1 Hz tests and lower of 100 s at 2 Hz tests; a steady-state COF μ_{st} of about 0.70 and 0.65 at 1 and 2 Hz, respectively. More precisely, μ_{st} values slightly decrease with an increment of the sliding velocity. Figures 4.19(c) and Figure 4.19(d) show the mean cumulative dissipated energy E_{PoD} during the sliding, at 1 and 2 Hz respectively, of the IT running-in stages for each machine process and roughness. All the investigated couplings register an overall similar behaviour: after reaching the steady-state stage E_{PoD} increases more rapidly reaching about 0.95 kJ and 1.99 kJ at 1 and 2 Hz, respectively.

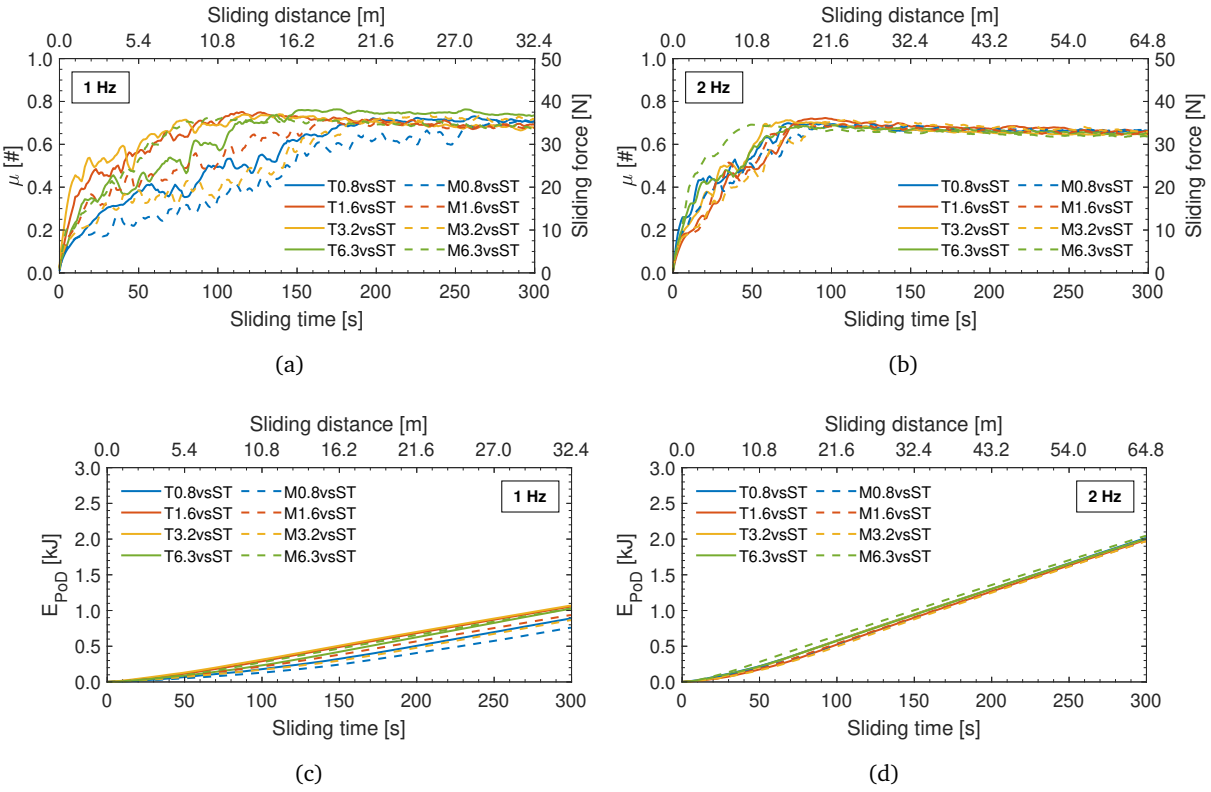

FIGURE 4.19: Part 1 RI results as function of sliding time, distance and sliding frequency: COF and sliding forces at (a) 1 Hz and (b) 2 Hz and cumulated dissipated energy at (c) 1 Hz and (d) 2 Hz.

It can be observed that all the investigated couplings produce similar μ_{st} and E_{PoD} values at the end of the running-in stages, consequently, it is derived that machine process and roughness only influence t_{tr}. This influence is clearly visible in tests performed at 1 Hz sliding frequency (Figure 4.19(a)), where t_{tr} decreases with the increment of roughness, and milled surfaces register higher t_{tr} values than the corresponding turned surfaces, except for T6.3vsST and M6.3vsST, which have a reversed behaviour. Similar results are registered at 2 Hz sliding frequency (Figure 4.19(b)); however, due to the sliding velocity increment, the t_{tr} variability with machine process and roughness is not as evident as in 1 Hz tests.

Figures 4.20 and 4.21 show the mean COF behaviour, at 1 and 2 Hz respectively, during the IT steady

stages for each machine process and roughness. All the investigated couplings register an overall similar behaviour: COF mean values range between 0.71 and 0.67 respectively at 1 and 2 Hz, and reach the steady-state values in less than 10 s. Again, μ_{st} values slightly decrease with an increment of the sliding velocity, as previously remarked during running-in stages.

It is to underline that all the investigated surfaces reach similar μ_{st} values during the IT tests, both at 1 and 2 Hz, consequently machine process and roughness do not significantly influence the steady stages.

One of the main results of Part 1 is the importance of performing the running-in stages to obtain an almost constant COF behaviour in a t_{tr} as short as possible. This has been previously reported also in the work of Federici et al. (2019, 2018, 2017) and it is clearly visible in Figure 4.22, which show in double axis graphs the mean μ_{st} (blue colour) and t_{tr} (orange colour) values as function of disks roughness during the running-in and steady stages at 1 Hz (filled dots) and 2 Hz (empty dots) sliding frequencies.

During running-in stages, both turned and milled disks', respectively reported in Figures 4.22(a) and 4.22(c), register μ_{st} mean values that range between 0.69 and 0.75 at 1 Hz sliding frequency, and between 0.66 and 0.68 at 2 Hz sliding frequency, while t_{tr} mean values range between 69 and 270 s at 1 Hz sliding frequency, and between 36 and 85 s at 2 Hz sliding frequency. Disks' roughness affects only t_{tr}, decreasing with increasing roughness, while μ_{st} is almost constant over the considered roughness range. The COF's coefficient of variation, cv_{μ}, registers meaningful values ranging between 10 and 25% at 1 Hz sliding frequency, and between 5 and 11% at 2 Hz sliding frequency, as highlighted by the coloured areas of Figure 4.22. Similarly, t_{tr}'s coefficient of variation, cv_t, registers values ranging between 15 and 66% at 1 Hz sliding frequency, and between 16 and 36% at 2 Hz sliding frequency, as highlighted by the coloured areas of Figure 4.22. Disks' roughness affects both cv_{μ} and cv_t, but produces a higher impact on cv_t.

During steady stages, both turned and milled disks', respectively reported in Figures 4.22(b) and 4.22(d), register a μ_{st} mean values that range between 0.66 and 0.73 at 1 Hz sliding frequency, and between 0.62 and 0.66 at 2 Hz sliding frequency, while t_{tr} mean values range between 6 and 13 s at both 1 and 2 Hz sliding frequencies. Disks' roughness does not affect both μ_{st} and t_{tr}, which remained almost constant. cv_{μ} registers negligible values ranging between 3 and 6% at 1 Hz sliding frequency, and between 2 and 4% at 2 Hz sliding frequency, as highlighted by the coloured areas of Figure 4.22. Similarly, cv_t registers values ranging between 5 and 12% at 1 Hz sliding frequency, and between 4 and 15% at 2 Hz sliding frequency, as highlighted by the coloured areas of Figure 4.22. Disks' roughness does not affect both cv_{μ} and cv_t , which remain almost constant.

Tables 4.7 and 4.8 complete the general overview of Part 1 experimental results conducted at 1 Hz and 2 Hz sliding frequency, respectively. Tables 4.7 and 4.8 collect values of mean steady-state friction coefficient μ_{st} with its coefficient of variation cv_{μ}, transition time t_{tr} with its coefficient of variation cv_t, pins' wear rate wr_p with its coefficient of variation $cv_{wr,p}$, disks' wear rate wr_d with its coefficient of variation $cv_{wr,d}$ and finally the cumulated dissipated energy E_{PoD} during the sliding for each performed test and investigated coupling.

Concerning the pin and disk wear rates, the following values are reported at 1 and 2 Hz sliding frequency, respectively: wr_p ranges between 5.42E-03 and 8.02E-03 mm^3/Nm, and between 4.52E-03 and 6.45E-03 mm^3/Nm; $cv_{wr,p}$ ranges between 5 and 21%, and between 6 and 20%. WR_d ranges between 5.94E-03

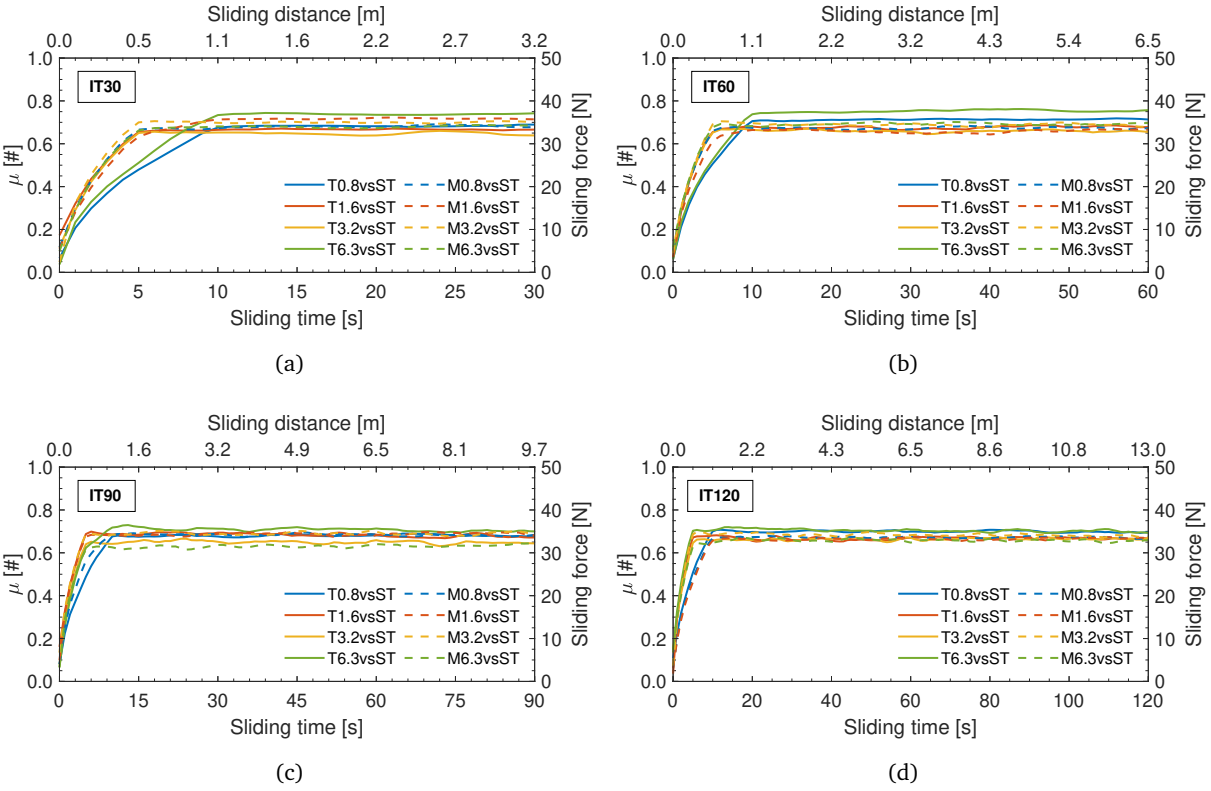

FIGURE 4.20: Part 1 IT results as function of sliding time and distance at 1 Hz sliding frequency: (a) 30 s, (b) 60 s, (c) 90 s and (d) 120 s sliding time.

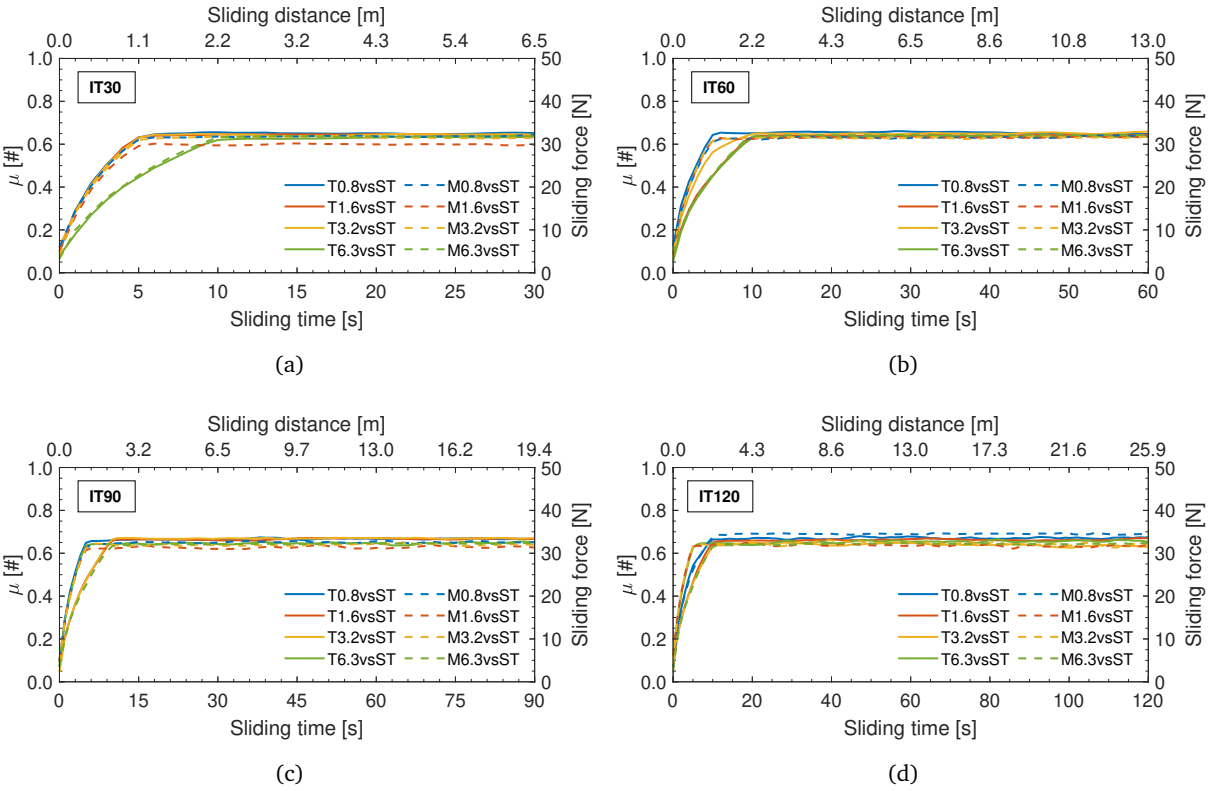

FIGURE 4.21: Part 1 IT results as function of sliding time and distance at 2 Hz sliding frequency: (a) 30 s, (b) 60 s, (c) 90 s and (d) 120 s sliding time.

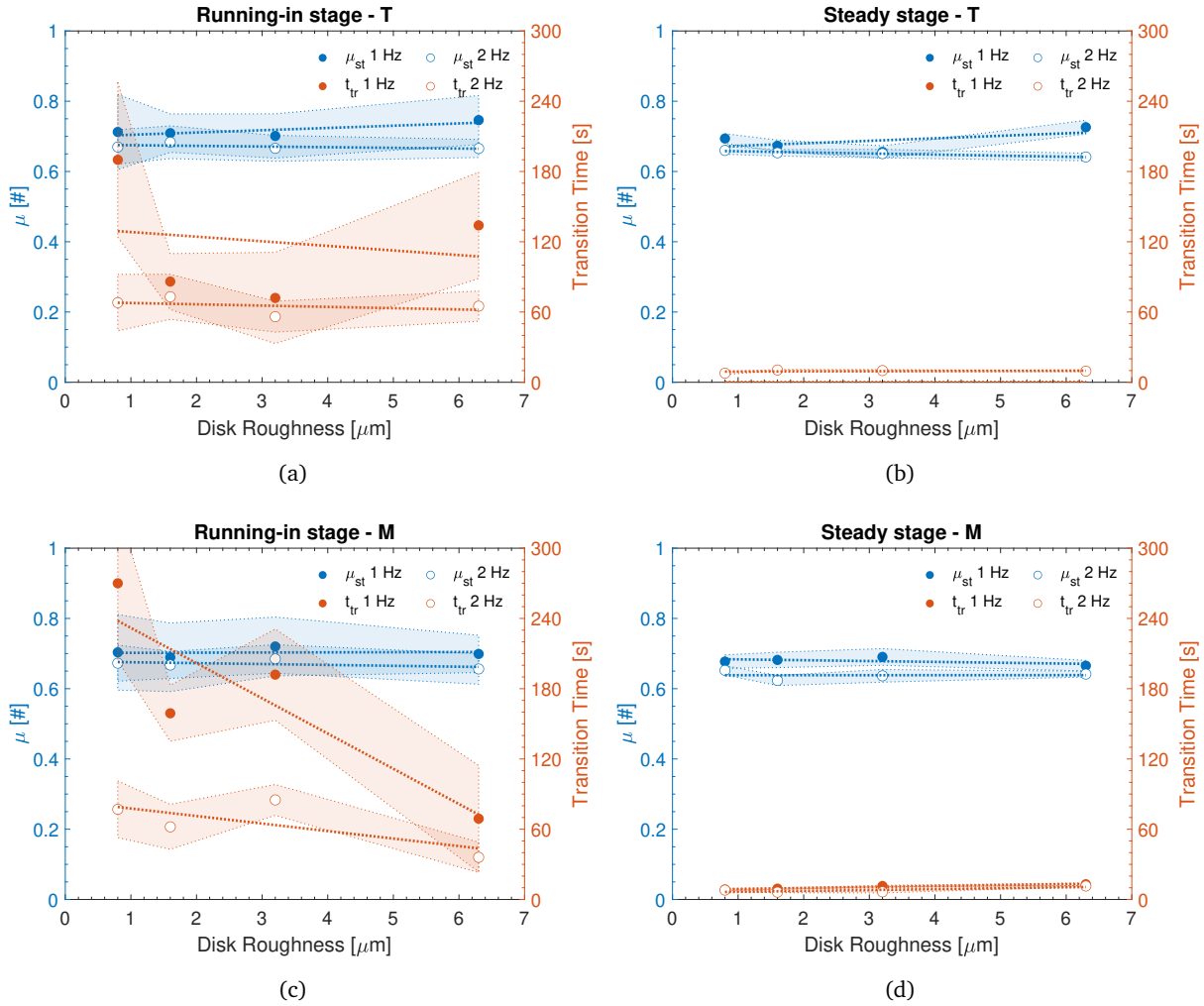

FIGURE 4.22: Part 1 mean COF and transition time values as function of disks roughness during running-in stages for (a) turned and (c) milled disks and during steady stages for (b) turned and (d) milled disks.

and 1.01E-02 mm^3/Nm, and between 4.61E-03 and 6.56E-03 mm^3/Nm; $cv_{wr,d}$ ranges between 1 and 5% and between 1 and 4%. Disks' roughness and machine processes do not affect significantly wr_p, while, on the contrary, moderately affect wr_d. Generally, disks with lower values of Ra register lower wr_d as well as lower $cv_{wr,d}$.

Concerning the cumulated dissipated energy, the investigated coupling registered similar values. During running-in stages, E_{PoD} ranges around 0.95 kJ and 1.99 kJ at 1 Hz and 2 Hz respectively, E_{PoD} increases linearly with the sliding time, ranging between 0.10 kJ and 0.43 kJ at 1 Hz, and between 0.19 kJ and 0.83 kJ at 2 Hz. Disks' roughness and machine processes do not affect significantly E_{PoD}, which is kept almost constant with the tests' duration and approximately double from 1 Hz to 2 Hz.

Disks wear grooves are not significantly affected by roughness and machine processes. Figure 4.23 shows the wear grooves made by ST pins on turned (a-d) milled (e-h) disks. It can be observed that wear grooves are very similar to each other, and both pins and disks register weight losses. Figure 4.24 shows the obtained grooves through a profilometer scanned view, proving that abrasive wear has occurred. It is clearly visible

TABLE 4.7: Part 1 tests mean results at 1 Hz.

		T0.8vsST	**T1.6vsST**	**T3.2vsST**	**T6.3vsST**	**M0.8vsST**	**M1.6vsST**	**M3.2vsST**	**M6.3vsST**
Running-in stage	μ_{st}	0.71	0.71	0.70	0.75	0.70	0.69	0.72	0.70
	cv_{μ}	25%	10%	11%	14%	25%	20%	19%	11%
	t_{tr} [s]	190	86	72	134	270	159	192	69
	cv_t	35%	28%	54%	34%	24%	15%	20%	66%
Steady stage	μ_{st}	0.69	0.67	0.66	0.73	0.68	0.68	0.69	0.67
	cv_{μ}	3%	3%	4%	5%	4%	4%	6%	3%
	t_{tr} [s]	11	9	6	10	9	9	12	13
	cv_t	8%	7%	10%	12%	11%	6%	5%	9%
Wear	wr_p [mm^3/Nm]	6.26E-03	6.96E-03	6.77E-03	8.02E-03	5.42E-03	7.35E-03	6.33E-03	6.68E-03
	$cv_{wr,p}$	5%	20%	20%	15%	14%	21%	8%	17%
	wr_d [mm^3/Nm]	6.14E-03	8.25E-03	8.66E-03	9.77E-03	5.94E-03	6.71E-03	6.76E-03	1.01E-02
	$cv_{wr,d}$	2%	2%	1%	2%	3%	4%	5%	2%
E_{PoD} [kJ]	IT-RI	0.89	1.05	1.07	1.02	0.76	0.94	0.86	1.03
	IT30	0.10	0.10	0.10	0.11	0.10	0.11	0.11	0.10
	IT60	0.22	0.21	0.21	0.23	0.21	0.21	0.22	0.22
	IT90	0.32	0.33	0.31	0.34	0.32	0.33	0.33	0.30
	IT120	0.44	0.43	0.42	0.45	0.42	0.42	0.44	0.42

TABLE 4.8: Part 1 tests mean results at 2 Hz.

		T0.8vsST	**T1.6vsST**	**T3.2vsST**	**T6.3vsST**	**M0.8vsST**	**M1.6vsST**	**M3.2vsST**	**M6.3vsST**
Running-in stage	μ_{st}	0.67	0.68	0.67	0.67	0.67	0.67	0.68	0.66
	cv_{μ}	11%	10%	8%	5%	10%	8%	9%	9%
	t_{tr} [s]	68	73	56	65	77	62	85	36
	cv_t	36%	26%	24%	20%	31%	31%	16%	36%
Steady stage	μ_{st}	0.66	0.65	0.65	0.64	0.65	0.62	0.64	0.64
	cv_{μ}	3%	2%	3%	3%	3%	3%	4%	3%
	t_{tr} [s]	8	11	10	10	8	6	7	12
	cv_t	15%	4%	9%	4%	14%	7%	14%	3%
Wear	wr_p [mm^3/Nm]	5.25E-03	6.45E-03	6.22E-03	4.52E-03	5.25E-03	5.48E-03	5.94E-03	5.51E-03
	$cv_{wr,p}$	7%	13%	17%	8%	6%	9%	14%	20%
	wr_d [mm^3/Nm]	5.89E-03	4.61E-03	4.84E-03	6.56E-03	4.84E-03	5.64E-03	4.11E-03	6.63E-03
	$cv_{wr,d}$	1%	1%	2%	2%	4%	4%	1%	1%
E_{PoD} [kJ]	IT-RI	2.01	1.98	2.00	2.00	1.97	1.97	1.97	2.04
	IT30	0.20	0.20	0.20	0.18	0.19	0.18	0.19	0.18
	IT60	0.41	0.39	0.40	0.39	0.40	0.40	0.40	0.39
	IT90	0.63	0.62	0.63	0.62	0.62	0.60	0.61	0.60
	IT120	0.85	0.83	0.81	0.83	0.87	0.81	0.82	0.81

that the surface's original pattern is completely removed, while the wear debris plastically deformed the surface exhibiting pin's sliding direction.

Disks with lower roughness registered lower values of COF and wear rate variation's coefficients, reaching a more stable overall behaviour, especially T0.8vsST coupling. For this reason, turning machine process with $Ra = 0.8\mu$m (T0.8) has been selected as disk's machining reference for the following Part 2 and 3.

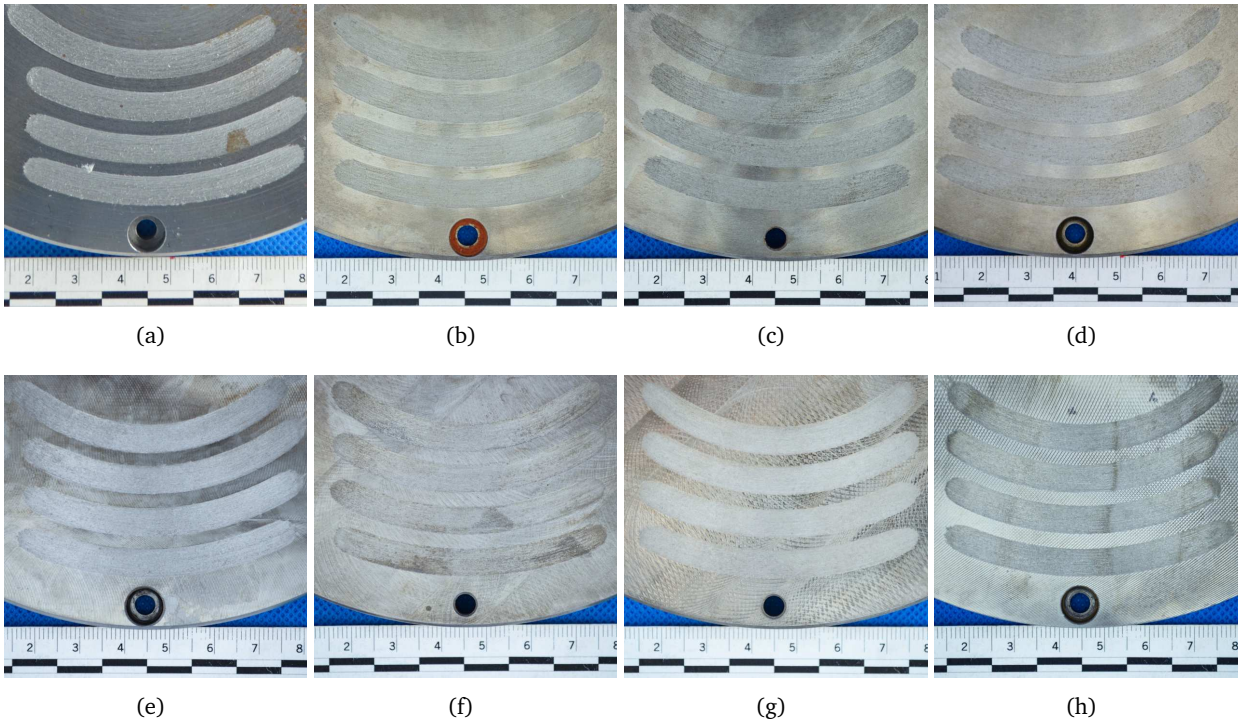

(a) (b) (c) (d)

(e) (f) (g) (h)

FIGURE 4.23: Part 1 wear grooves on (a) T0.8vsST, (b) T1.6vsST, (c) T3.2vsST, (d) T6.3vsST, (e) M0.8vsST, (f) M1.6vsST, (g) M3.2vsST and (h) M6.3vsST surfaces.

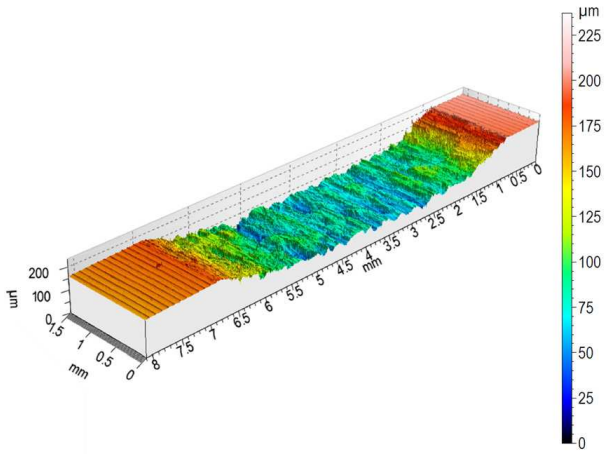

FIGURE 4.24: Part 1 wear grooves of T0.8vsST scanned using the profilometer.

4.6.2 Wear tests part 2 results: effects of different materials

Part 2 considers the friction coupling of steel with different metals: more precisely, steel disk T0.8 is coupled with ST, BZ and BS pins.

4.6.2.1 Long tests results

Part 2 LT tests were performed to evaluate an adequate running-in period for the following IT tests. Figures 4.25(a) and 4.25(b) show the average evolution of μ for the tests performed at 1 Hz and 2 Hz for each coupling, where T0.8vsST coupling is used as reference. The COF of the conditions T0.8vsBZ and T0.8vsBS

significantly decreases in respect to the reference condition T0.8vsST, averaging 0.35 and 0.25 for T0.8vsBZ and T0.8vsBS respectively.

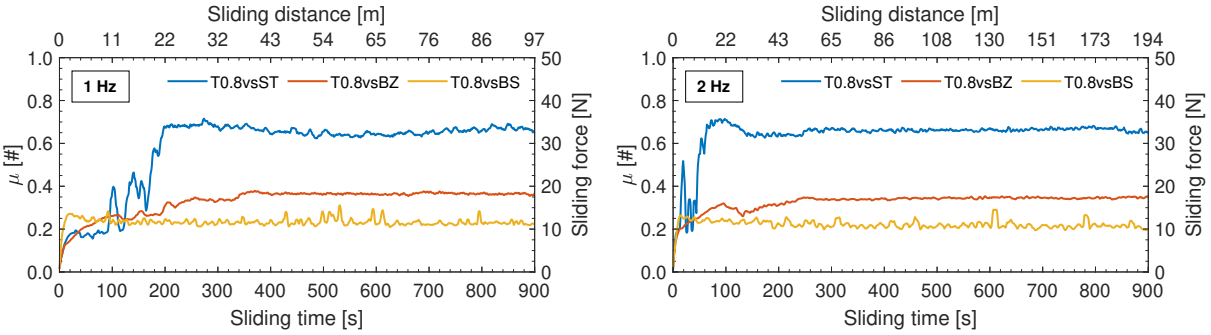

(a) (b)

FIGURE 4.25: Part 2 LT results as function of sliding time, distance and sliding frequency: COF and sliding forces at (a) 1 Hz and (b) 2 Hz.

Concerning the transition time, the t_{tr} values of the conditions T0.8vsBZ and T0.8vsBS significantly decreases in respect to the reference condition T0.8vsST, ranging around 20 s both at 1 and 2 Hz sliding frequencies. This behaviour indicates that bronze and brass particles adhere almost immediately to the disk, ensuring a steadier behaviour than the one exhibited by T0.8vsST.

Considering the results of Part 2 LT, and to ensure the achievement of the COF's steady stages, Part 2 IT-RI tests duration is set at 300 s, as reported in Table 4.4.

4.6.2.2 Interrupted tests results

Figures 4.26(a) and 4.26(b) show the mean COF behaviour, at 1 and 2 Hz respectively, during the running-in stages for each coupling, where T0.8vsST coupling is used as reference. μ_{st} value decreased from 0.71 (ST) to 0.36 (BZ) and 0.25 (BS) at 1 Hz sliding frequency, and from 0.67 (ST) to 0.35 (BZ) and 0.24 (BS) at 2 Hz sliding frequency. In addition, cv_{μ} registers a decrement from 15% to 6% at 1 Hz sliding frequency, and from 7% to 6% at 2 Hz sliding frequency. T0.8vsST's COF value increases slowly, with t_{tr} of about 200 s and 70 s at 1 and 2 Hz sliding frequency, respectively, while both T0.8vsBZ and T0.8vsBS COF increase more rapidly, with t_{tr} of about 10 s at both frequencies, reaching values very close to μ_{st} almost instantly. In addition, T0.8vsST exhibits the higher variations, in terms of both cv_{μ} and cv_{t}, as highlighted by the coloured areas of Figure 4.26. Figures 4.26(c) and 4.26(d) show the mean cumulative dissipated energy E_{PoD} during the sliding, at 1 and 2 Hz respectively, of the running-in stages for each investigated coupling, where T0.8vsST coupling is used as reference. All the investigated couplings register an overall similar behaviour: after reaching the steady-state stage E_{PoD} increases more rapidly. However, while T0.8vsST reaches about 0.89 kJ and 2.01 kJ at 1 and 2 Hz respectively, T0.8vsBZ and T0.8vsBS are almost halved.

Figures 4.27 and 4.28 show the mean COF behaviour, at 1 and 2 Hz respectively, during the IT steady stages for each coupling, where T0.8vsST coupling is used as reference. All the investigated couplings register an overall similar behaviour, reaching the steady-state values in less than 10 s and registering a value variation almost irrelevant, as highlighted by the coloured areas. μ_{st} values are similar to the ones obtained in the

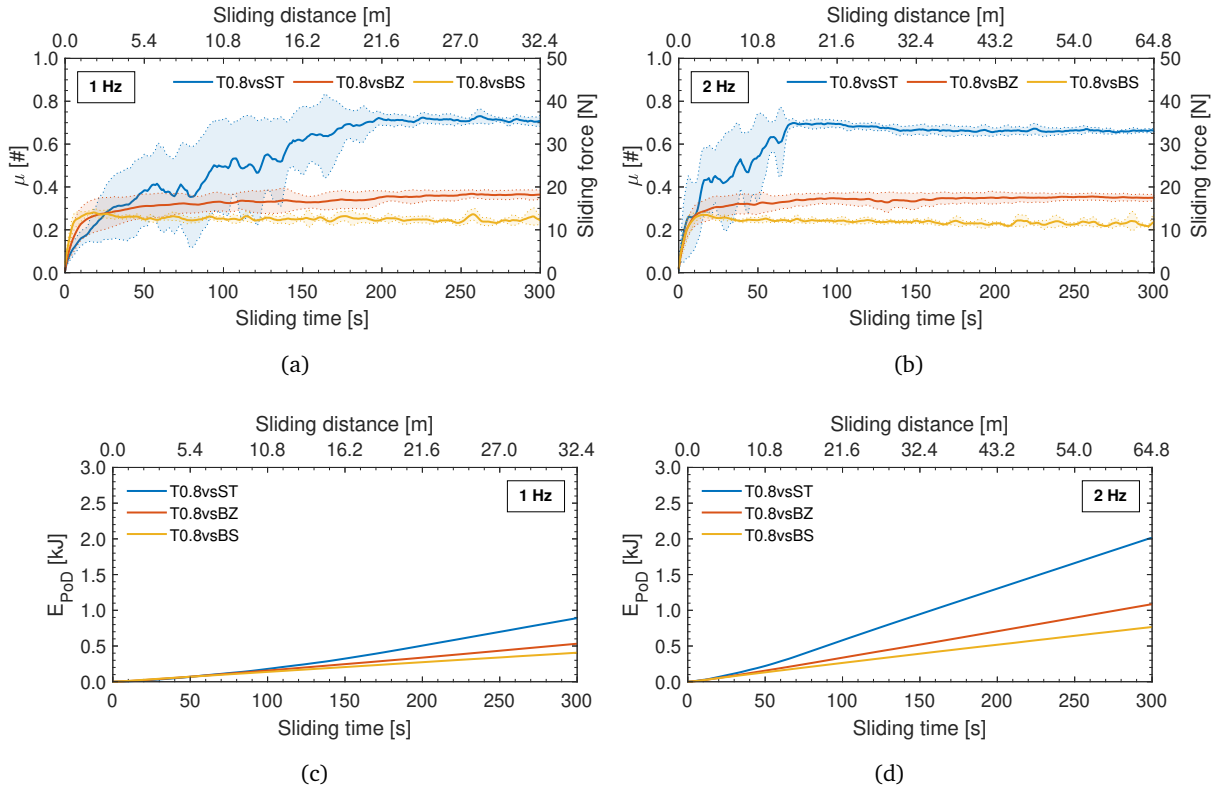

FIGURE 4.26: Part 2 RI results as function of sliding time, distance and sliding frequency: COF and sliding forces at (a) 1 Hz and (b) 2 Hz and cumulated dissipated energy at (c) 1 Hz and (d) 2 Hz.

running-in stage after reaching the steady stage and average 0.69 (ST), 0.36 (BZ) and 0.24 (BS) at 1 Hz sliding frequency, and 0.66 (ST), 0.36 (BZ) and 0.26 (BS) at 2 Hz sliding frequency.

Table 4.9 lists the numerical main results of Part 2 test in terms of mean steady-state friction coefficient μ_{st}, transition time t_{tr}, pins' wear rate wr_p and disks' wear rate wr_d together with the relative coefficient of variation and the cumulated dissipated energy E_{PoD} for each performed test and investigated coupling.

During the running-in stage, T0.8vsBS registers the overall most steady COF's behaviour, with the lowest values of cv_μ, that ranges around 6%, and cv_t, that ranges between 23% and 30%, both at 1 and 2 Hz sliding frequencies respectively. On the contrary, T0.8vsST registers the overall less steady COF's behaviour, with the highest values of cv_μ, that ranges between 15% and 7%, and CV_t, that ranges between 35% and 36%, both at 1 and 2 Hz sliding frequencies respectively.

During the steady stage, T0.8vsBZ registers the overall most steady COF's behaviour, with the lowest values of cv_μ, that ranges between 2% and 1%, and cv_t, that ranges between 10% and 6%, both at 1 and 2 Hz sliding frequencies respectively. On the contrary, T0.8vsBS registers the overall less steady COF's behaviour, with the highest values of cv_μ, that ranges around 7%, and cv_t, that ranges between 10% and 12%, both at 1 and 2 Hz sliding frequencies respectively.

Concerning the pin wear rate, T0.8vsBS registers the lowest values of wr_p, ranging between 5.40E-04 and 4.91E-04 mm^3/Nm, with a $cv_{wr,p}$ that ranges between 3% and 5%, both at 1 and 2 Hz sliding frequencies respectively. Differently, T0.8vsST registers the highest values of wr_p, ranging between 6.26E-03 and

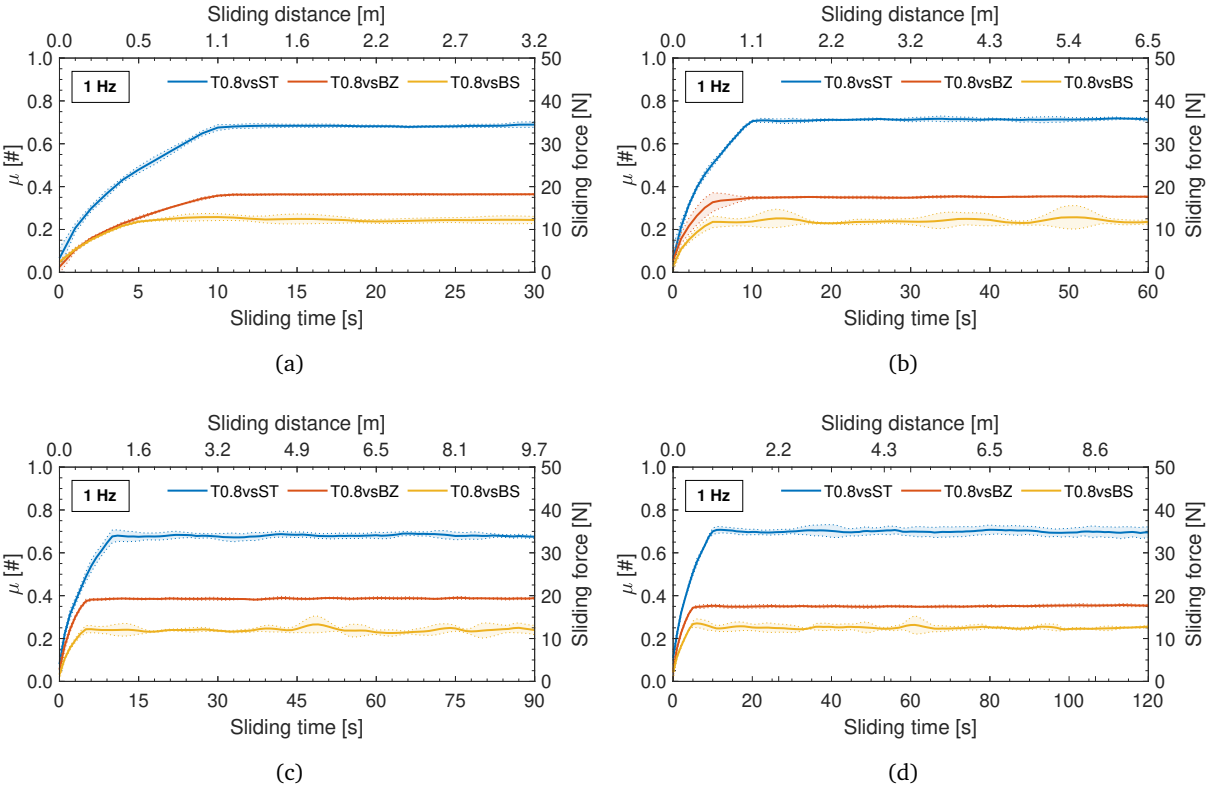

FIGURE 4.27: Part 2 IT results as function of sliding time and distance at 1 Hz sliding frequency: (a) 30 s, (b) 60 s, (c) 90 s and (d) 120 s sliding time.

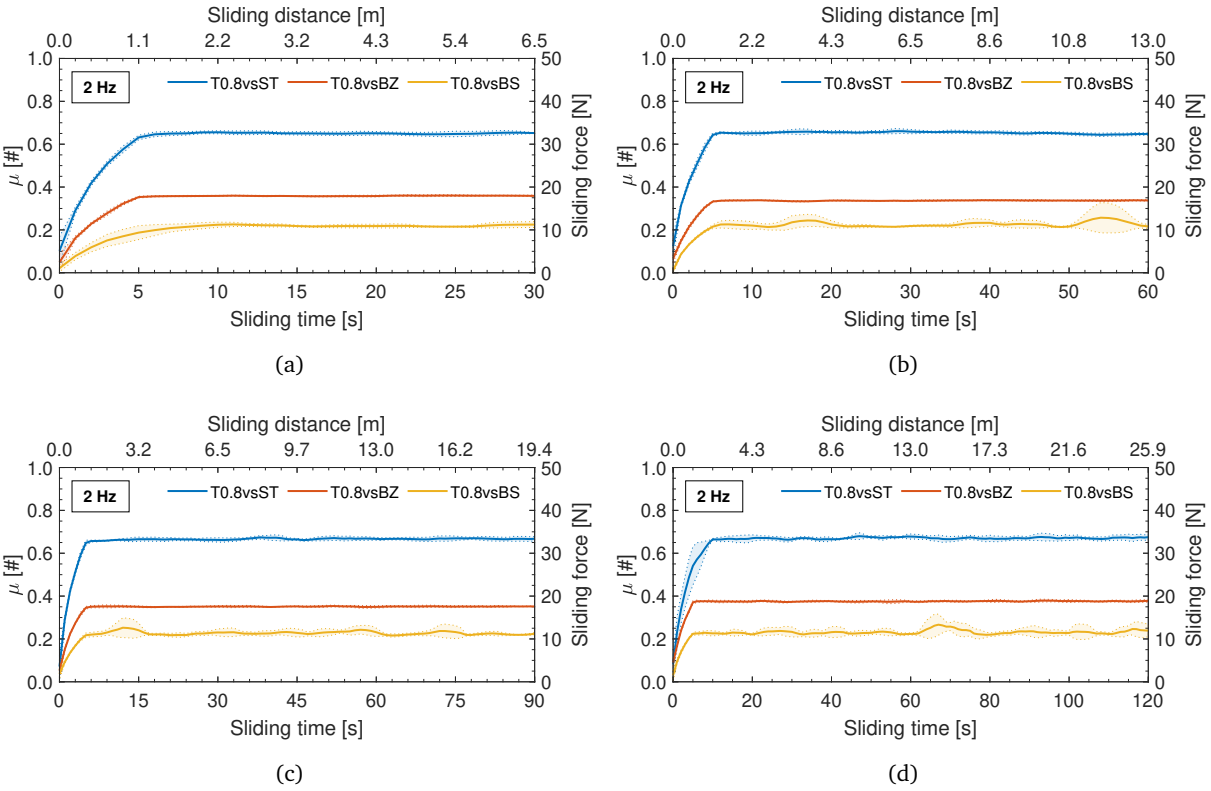

FIGURE 4.28: Part 2 IT results as function of sliding time and distance at 2 Hz sliding frequency: (a) 30 s, (b) 60 s, (c) 90 s and (d) 120 s sliding time.

TABLE 4.9: Part 2 tests mean results at 1 and 2 Hz.

		$f = 1$ Hz			$f = 2$ Hz		
		T0.8vsST	**T0.8vsBZ**	**T0.8vsBS**	**T0.8vsST**	**T0.8vsBZ**	**T0.8vsBS**
Running-in stage	μ_{st}	0.71	0.36	0.25	0.67	0.35	0.24
	cv_{μ}	25%	14%	7%	11%	9%	6%
	t_{tr} [s]	190	227	7	68	84	9
	cv_t	35%	30%	23%	36%	29%	30%
Steady stage	μ_{st}	0.69	0.36	0.24	0.66	0.36	0.23
	cv_{μ}	3%	3%	7%	3%	2%	8%
	t_{tr} [s]	11	9	7.25	7.75	6	12.25
	cv_t	8%	10%	10%	15%	6%	12%
Wear	wr_p [mm^3/Nm]	6.26E-03	1.69E-03	5.40E-04	5.25E-03	2.03E-03	4.91E-04
	$cv_{wr,p}$	5%	12%	3%	7%	11%	5%
	wr_d [mm^3/Nm]	6.14E-03	0.00	0.00	5.89E-03	0.00	0.00
	$cv_{wr,d}$	2%	0.00	0.00	1%	0.00	0.00
E_{PoD} [kJ]	IT-RI	0.89	0.53	0.41	2.01	1.08	0.76
	IT30	0.10	0.05	0.04	0.20	0.11	0.07
	IT60	0.22	0.11	0.08	0.41	0.21	0.14
	IT90	0.32	0.18	0.11	0.63	0.33	0.22
	IT120	0.44	0.22	0.16	0.85	0.48	0.30

5.25E-03 mm^3/Nm, with a $cv_{wr,p}$ that ranges between 5% and 7%, both at 1 and 2 Hz sliding frequencies respectively. Concerning the disk wear rate, T0.8vsBZ and T0.8vsBS register an absence of volume loss and no wr_d and $cv_{wr,d}$ values are detected. Differently, T0.8vsST registers values of wr_d, ranging between 6.14E-03 and 5.89E-03 mm^3/Nm, with a $cv_{wr,d}$ that ranges between 2% and 1%, both at 1 and 2 Hz sliding frequencies respectively.

Concerning the cumulated dissipated energy E_{PoD}, T0.8vsST registers the overall highest values, ranging from 0.10 kJ, during IT30 at 1 Hz test, to 2.01 kJ during IT-RI at 2 Hz test. Differently, T0.8vsBZ and T0.8vsBS register values that are almost halved the reference T0.8vsST ones, with T0.8vsBS registering the overall lowest values ranging from 0.04 kJ, during IT30 at 1 Hz test, to 0.76 kJ during IT-RI at 2 Hz test.

T0.8 disk wear grooves result significantly affected by the coupling type. Figure 4.29 shows the wear grooves made by (a) ST, (b) BZ and (c) BS pins on T0.8 disk. While in the coupling T0.8vsST both pin and disk register weight loss, in the couplings T0.8vsBZ and T0.8vsBS only the pins register weight loss. More precisely, BZ pins have chemically reacted with the disk leaving some clearer spots (see Figure 4.29(b)), while BS pins have left some wear particles inside the asperities of the disk (see Figure 4.29(c)).

4.6.3 Wear tests part 3 results: effects of different surface finishing

Part 3 considers the friction coupling of steel with steel itself when subjected to additional treatment: more precisely, SP1, SP2, NI and ZN disks are coupled to ST pins.

4.6.3.1 Long tests results

Part 3 LT tests were performed to evaluate an adequate running-in period for the following IT tests. Figures 4.30(a) and 4.30(b) show the average evolution of μ for the tests performed at 1 Hz and 2 Hz for each

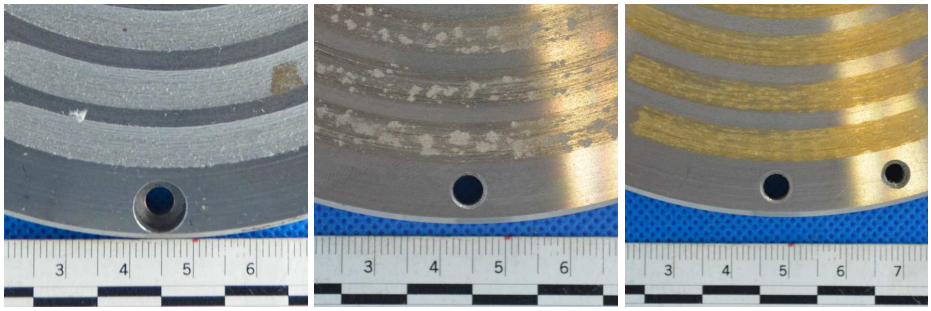

(a) (b) (c)

FIGURE 4.29: Part 2 wear grooves on (a) T0.8vsST, (b) T0.8vsBZ and (c) T0.8vsBS surfaces.

selected coupling.

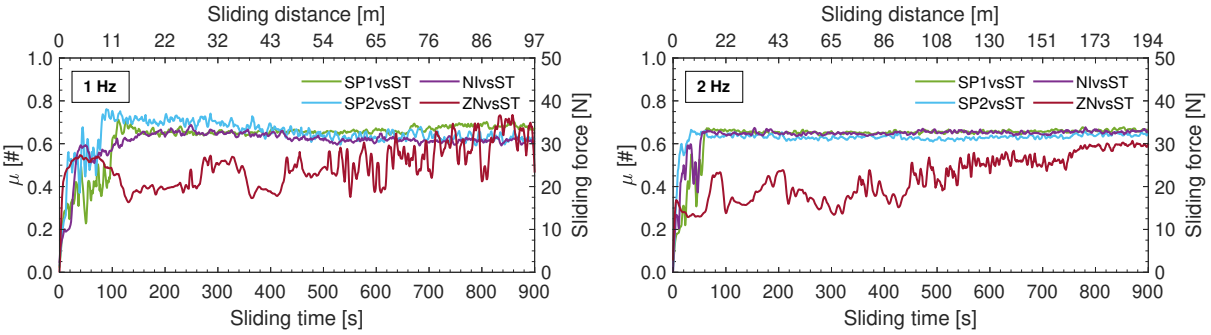

(a) (b)

FIGURE 4.30: Part 3 LT results as function of sliding time, distance and sliding frequency: COF and sliding forces at (a) 1 Hz and (b) 2 Hz.

SP1vsST, SP2vsST and NIvsST couplings display similar overall behavior, registering two similar steady-state stages. The firsts steady-state last around 63 s and 23 s at 1 Hz and 2 Hz, respectively, with μ_{st}′ values around 0.49 both at 1 Hz and 2 Hz. The second steady-state registers μ_{st} values around 0.65 both at 1 Hz and 2 Hz. The presence of the treatment's surfaces produces a higher COF variation during the sliding, with a consequent less stable response, while, after the treatment's surfaces removal, SP1vsST, SP2vsST and NIvsST couplings behave more steadily and similarly to the T0.8vsST coupling visible in 4.25. Moreover, during the first steady-state stage, SP2vsST coupling exhibits a higher COF values than SP1vsST coupling, as well as with lower transition times. This different behavior during the first steady-state stage is caused by SP2 higher superficial hardness in respect to SP1 (see Figure 4.15), as already registered by several studies on shot peening (Khun et al., 2016; Trung et al., 2016). After the harder cross-section portion removal, during the second steady-state stage, SP1 and SP2 behaves more similarly.

ZNvsST coupling reaches one steady-state stage at 1 Hz and two steady-state stages at 2 Hz. The firsts steady-state, reached at both sliding frequencies, last around 615 s and 510 s at 1 Hz and 2 Hz respectively, with μ_{st}′ values around 0.45 and 0.37 at 1 Hz and 2 Hz respectively. The second steady-state, reached only at 2 Hz, registers μ_{st} values around 0.59. The presence of the zinc wear particles trapped between the disk and the pins produces a higher COF variation during the sliding, with a consequent less stable response. After the removal of both surface treatments, ZNvsST behaves more steadily than NIvsST and similarly to

the T0.8vsST coupling visible in 4.25. It is worth noting that ZNvsST registers the longer first steady-state stage above all investigated conditions, indicating that zinc wear particles remain trapped between the disk and the pins longer with respect to the other treatments.

Considering the results of Part 3 LT tests and to ensure the achievement of the COF's steady stages, Part 3 IT-RI tests duration was set at 300 s, as reported in Table 4.4. It is worth to note that the transition time of ZNvsST is much longer than 300 s, consequently during the Part 3 IT-RI tests, ZNvsST evaluation is focused on the stability of its first steady-stage state, in which the effects of the treatment are more significant.

4.6.3.2 Interrupted tests results

Figures 4.31(a) and 4.31(b) show the mean COF behaviour, at 1 and 2 Hz respectively, during the running-in stage for each investigated coupling. SP1vsST, SP2vsST and NIvsST interfaces register an overall similar behaviour. A first steady-state stage takes place, lasting between 40 and 130 s with μ_{st} values range between 0.45 and 0.55, which is caused by the disks' additional treatments. A second steady-state stage follows, whose μ_{st} values range between 0.64 and 0.68, similarly to the reference T0.8vsST coupling. This behaviour is more evident at 1 Hz sliding frequency, while at 2 Hz sliding frequency, due to the sliding velocity increment, COF reaches straight the second steady-state. As a result, COF's behaviour of SP1vsST, SP2vsST and NIvsST couplings is affected by the additional treatment mainly during the first running-in stage. On the contrary, COF's behaviour of ZNvsST coupling is significantly affected by the additional treatment during the whole running-in stage, with μ_{st} average values between 0.41 and 0.38, at 1 and 2 Hz sliding frequencies respectively. Figures 4.31(c) and 4.31(d) show the mean cumulative dissipated energy E_{PoD} during the sliding, at 1 and 2 Hz respectively, of the running-in stages for each investigated coupling. SP1vsST, SP2vsST and NIvsST interfaces register an overall similar behaviour: after reaching the steady-state stage E increases more rapidly reaching about 0.96 kJ and 1.96 kJ at 1 and 2 Hz, respectively. Differently, ZNvsST reaches about 0.66 kJ and 1.22 kJ at 1 and 2 Hz respectively.

Figures 4.32 and 4.33 show the mean COF behaviour, at 1 and 2 Hz respectively, during the IT steady stages for each coupling. All the investigated couplings reach the steady-state values in less than 10 s, but while SP1vsST, SP2vsST and NIvsST register a value variation almost irrelevant, ZNvsST exhibits a significant COF variation, as highlighted by the coloured areas. This behaviour confirms the findings of the previous LT tests. μ_{st} values are similar to the ones obtained in the running-in stage after reaching the steady stage and average 0.67 (SP1), 0.66 (SP2), 0.64 (NI) and 0.41 (ZN) at 1 Hz sliding frequency, and 0.66 (SP1), 0.66 (SP2), 0.65 (NI) and 0.52 (ZN) at 2 Hz sliding frequency. It is worth noting that the average μ_{st} value of ZNvsST at 2 Hz exhibits a moderate increment in respect to the one obtained in the IT-RI test, especially during IT90 and I120 tests (see Figures 4.33(c) and 4.33(d)). This difference indicates that at the end of the longer tests ZNvsST reach the second steady-state stage and the complete removal of the zinc coating.

Table 4.10 lists the numerical main results of Part 3 test in terms of mean steady-state friction coefficient μ_{st}, transition time t_{tr}, pins' wear rate wr_p and disks' wear rate wr_d together with the relative coefficient of variation and the cumulated dissipated energy E_{PoD} for each performed test and investigated coupling.

During running-in stage, NIvsST registers the overall most steady COF's behaviour, with the lowest values of cv_μ, that ranges between 4% and 5%, and cv_t, that ranges between 4% and 25%, both at 1 and 2 Hz sliding frequencies respectively. On the contrary, ZNvsST registers the overall less steady COF's behaviour,

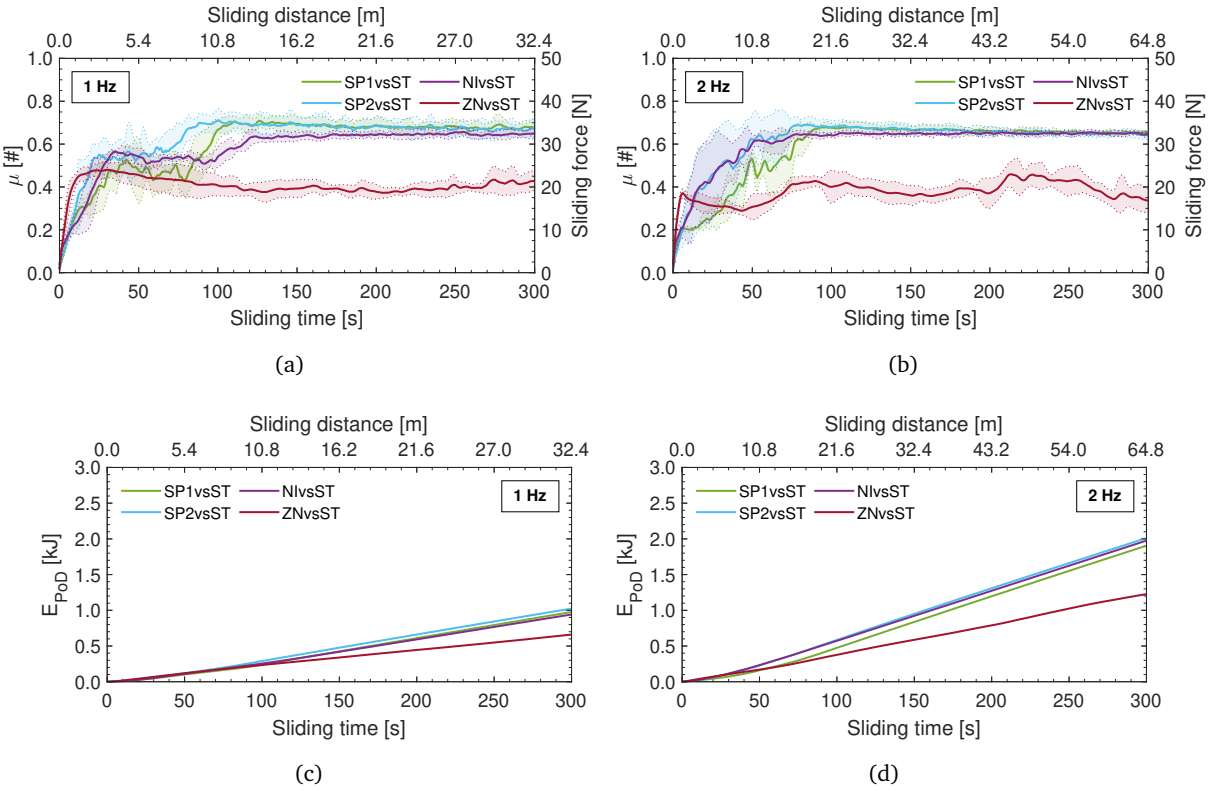

FIGURE 4.31: Part 3 RI results as function of sliding time, distance and sliding frequency: COF and sliding forces at (a) 1 Hz and (b) 2 Hz and cumulated dissipated energy at (c) 1 Hz and (d) 2 Hz.

with the highest values of cv_μ, that ranges between 10% and 12%, and cv_t, that ranges between 20% and 49%, both at 1 and 2 Hz sliding frequencies respectively.

Similarly, during steady-state stage, NIvsST registers the overall most steady COF's behaviour, with the lowest values of cv_μ, that ranges between 2% and 1%, and cv_t, that ranges around 5%, both at 1 and 2 Hz sliding frequencies respectively. On the contrary, ZNvsST registers the overall less steady COF's behaviour, with the highest values of cv_μ, that ranges between 10% and 16%, and CV_t, that ranges between 83% and 32%, both at 1 and 2 Hz sliding frequencies respectively.

Concerning the pin wear rate, ZNvsST registers the lowest values of wr_p, ranging between 5.34E-04 and 8.29E-04 mm^3/Nm, with a $cv_{wr,p}$ that ranges between 39% and 76%, both at 1 and 2 Hz sliding frequencies respectively. Differently, NIvsST registers the highest values of wr_p, ranging between 3.68E-03 and 5.19E-03 mm^3/Nm, with a $cv_{wr,p}$ that ranges between 9% and 14%, both at 1 and 2 Hz sliding frequencies respectively. Concerning the disk wear rate, ZNvsST registers the lowest values of wr_d, ranging between 1.44E-03 and 8.95E-04 mm^3/Nm, with a $cv_{wr,d}$ that ranges between 3% and 8%, both at 1 and 2 Hz sliding frequencies respectively. Differently, NIvsST registers the highest values of wr_d, ranging between 3.27E-03 and 2.80E-03 mm^3/Nm, with a $cv_{wr,d}$ that ranges between 5% and 4%, both at 1 and 2 Hz sliding frequencies respectively.

Concerning the cumulated dissipated energy E_{PoD}, SP2vsST registers the overall highest values, ranging from 0.10 kJ, during IT30 at 1 Hz test, to 2.00 kJ during IT-RI at 2 Hz test. Differently, ZNvsST registers

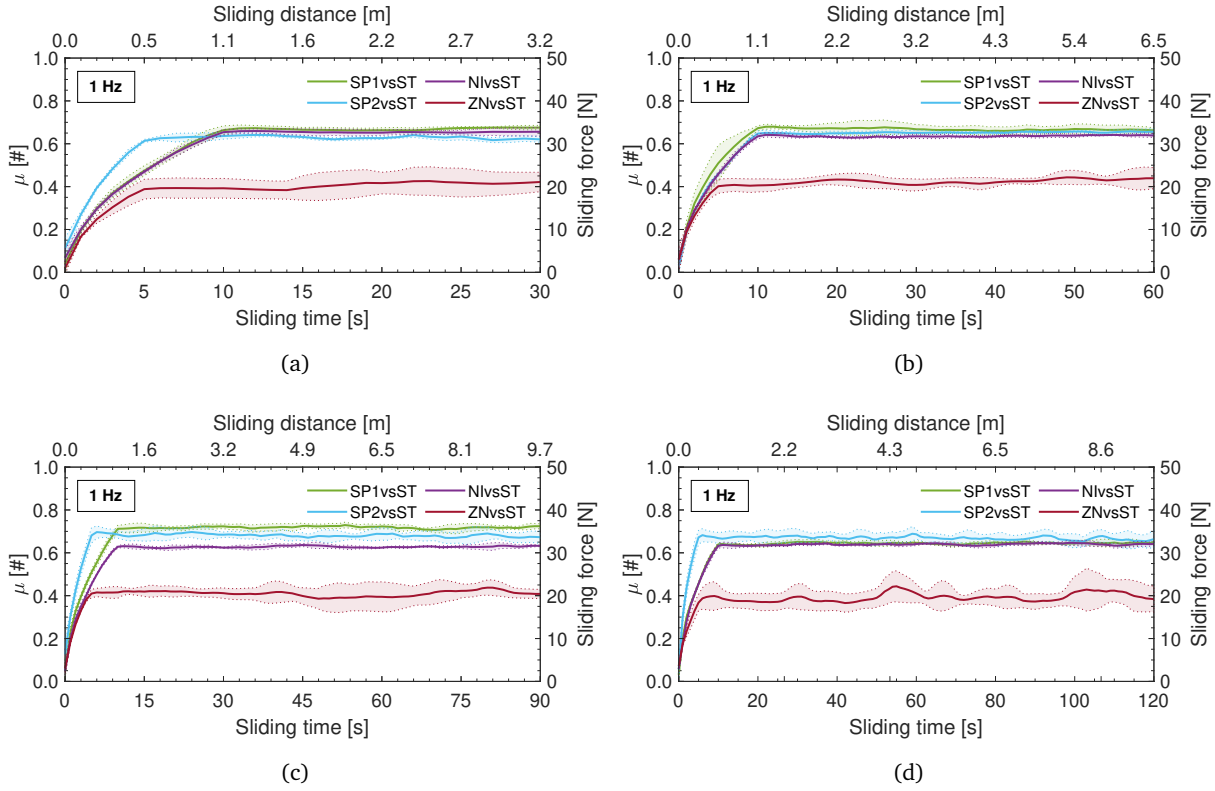

FIGURE 4.32: Part 3 IT results as function of sliding time and distance at 1 Hz sliding frequency: (a) 30 s, (b) 60 s, (c) 90 s and (d) 120 s sliding time.

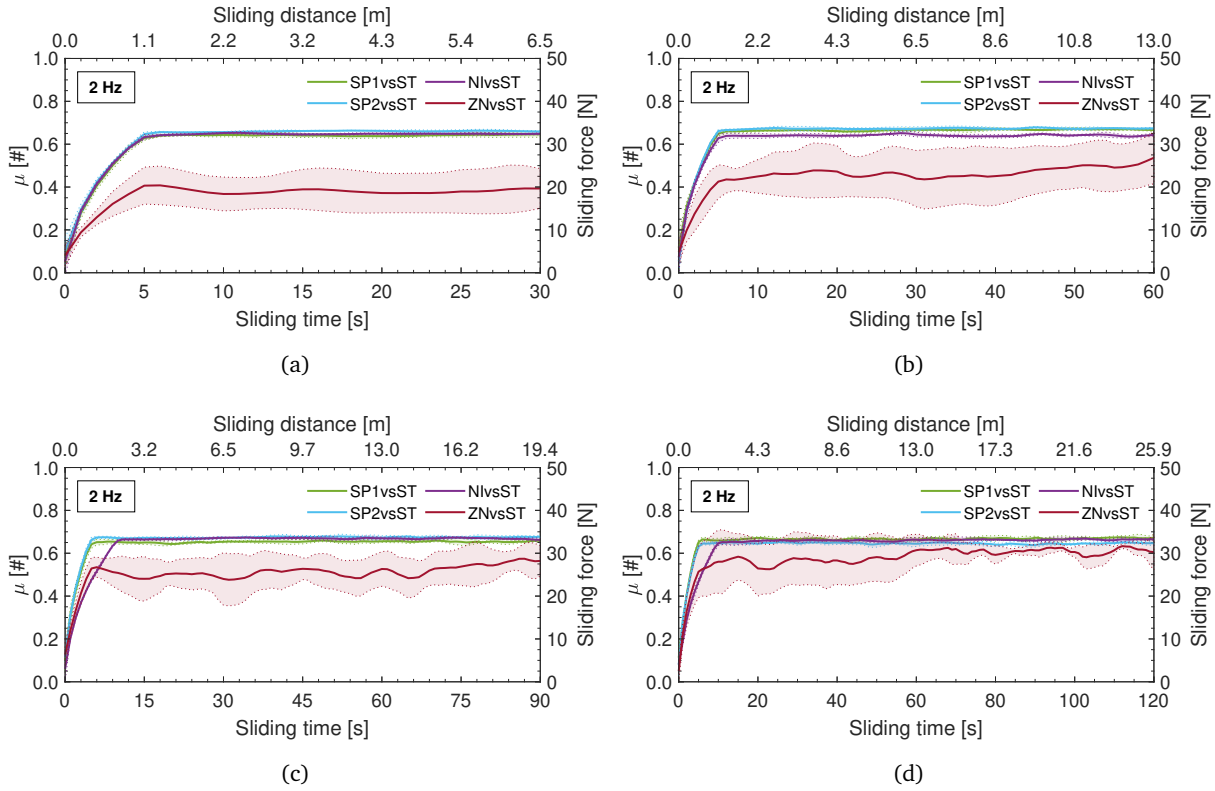

FIGURE 4.33: Part 3 IT results as function of sliding time and distance at 2 Hz sliding frequency: (a) 30 s, (b) 60 s, (c) 90 s and (d) 120 s sliding time.

TABLE 4.10: Part 2 tests mean results at 1 and 2 Hz.

		$f = 1$ Hz				$f = 2$ Hz			
		SP1vsST	**SP2vsST**	**NIvsST**	**ZNvsST**	**SP1vsST**	**SP2vsST**	**NIvsST**	**ZNvsST**
Running-in stage	μ_{st}	0.68	0.68	0.64	0.41	0.66	0.66	0.65	0.38
	cv_μ	10%	9%	6%	11%	7%	10%	7%	12%
	t_{tr} [s]	101	82	139	11	86	54	75	11
	cv_t	9%	10%	4%	20%	15%	49%	25%	49%
Steady stage	μ_{st}	0.67	0.66	0.64	0.41	0.66	0.66	0.65	0.52
	cv_μ	4%	4%	3%	12%	2%	2%	3%	20%
	t_{tr} [s]	11	7.25	11	13.25	7	6.5	9.25	53
	cv_t	10%	13%	5%	83%	7%	8%	5%	32%
Wear	wr_p [mm^3/Nm]	3.19E-03	2.94E-03	3.68E-03	5.34E-05	4.22E-03	3.84E-03	5.19E-03	8.29E-04
	$cv_{wr,p}$	6%	12%	9%	39%	13%	8%	14%	76%
	wr_d [mm^3/Nm]	3.79E-03	3.56E-03	3.27E-03	1.44E-03	1.94E-03	1.72E-03	2.80E-03	8.95E-04
	$cv_{wr,d}$	2%	4%	5%	3%	20%	3%	4%	8%
E_{PoD} [kJ]	IT-RI	0.97	1.02	0.94	0.66	1.90	2.00	1.97	1.22
	IT30	0.10	0.10	0.09	0.06	0.20	0.20	0.20	0.12
	IT60	0.21	0.20	0.19	0.13	0.42	0.42	0.40	0.29
	IT90	0.34	0.33	0.29	0.20	0.62	0.64	0.63	0.49
	IT120	0.41	0.43	0.40	0.25	0.85	0.83	0.83	0.75

the overall lowest values, ranging from 0.06 kJ, during IT30 at 1 Hz test, to 1.22 kJ during IT-RI at 2 Hz test.

Disks wear grooves are not significantly affected by additional treatments. Figure 4.34 shows the wear grooves made by ST pins on treated steel disks. It can be observed that wear grooves are very similar to each other, and both pins and disks register weight losses.

(a) (b) (c) (d)

FIGURE 4.34: Part 3 wear grooves of ST pin on (a) SP1, (b) SP2, (c) NI and (d) ZN disks.

4.6.4 Wear tests part 4 results: comparison

Among the different friction surfaces considered in Parts 2 and 3 (§4.6.2 and §4.6.3), T0.8 steel, Nickel coated steel and bronze surfaces have been selected for further investigation. Based on previous results, their coupling represents a good choice in term of balance between μ_{st}, t_{tr}, wr, respective cv values, and expected costs. For this reason, Part 4 considers the coupling between NI disks and ST, NI and BZ pins. This last part aims to select the best suitable couplings for the damping device in development.

4.6.4.1 Long tests results

Part 4 LT tests were performed to evaluate an adequate running-in period for the following IT tests. Figures 4.35(a) and 4.35(b) show the average evolution of μ for the tests performed at 1 Hz and 2 Hz for each selected coupling, where NIvsST coupling is used as reference.

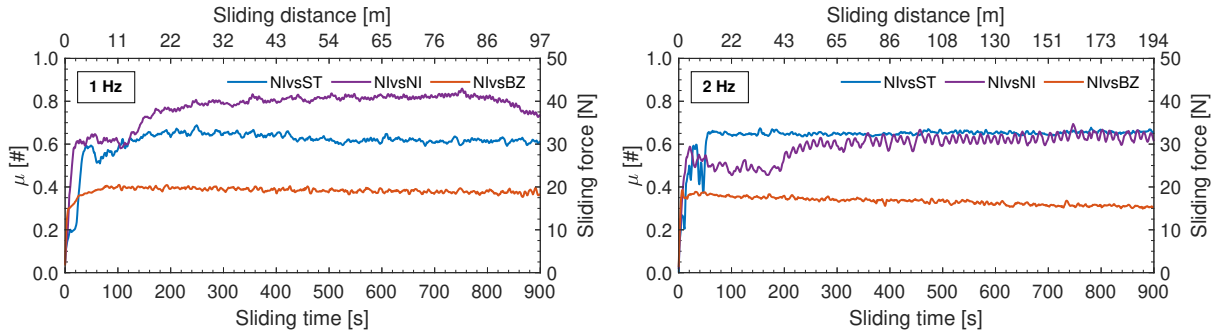

(a) (b)

FIGURE 4.35: Part 4 LT results as function of sliding time, distance and sliding frequency: COF and sliding forces at (a) 1 Hz and (b) 2 Hz.

NIvsNI exhibits a first steady-stage lasting around 150 s and with $\mu_{st}\prime$ values ranging between 0.50 and 0.60 at both 1Hz and 2 Hz sliding frequencies. After reaching the second steady-stage, NIvsNI behaves more similarly to NIvsST, but with a higher variation of COF values.

NIvsBZ reaches the steady-stage in less than 100 s at 1 Hz sliding and in around 20 s at 2 Hz sliding, with μ_{st} values averaging 0.40 at both 1Hz and 2 Hz sliding frequencies. Bronze particles adheres almost immediately to the disk, ensuring a steadier behaviour than the one exhibited by NIvsST.

Considering the results of Part 4 LT, and to ensure the achievement of the COF's steady stages, Part 4 IT-RI tests duration is set at 300 s, as reported in Table 4.4.

4.6.4.2 Interrupted tests results

Figures 4.36(a) and 4.36(b) show the mean COF behaviour, at 1 and 2 Hz respectively, during the running-in stage for each coupling, where NIvsST coupling is used as reference. NIvsNI transition stage increases rapidly reaching values close the μ_{st} one almost instantly, which ranges between 0.72 and 0.52 for 1 and 2 Hz sliding frequencies respectively, without registering two steady-state stages as NIvsST do. However, NIvsNI exhibits a higher variation respect to NIvsST, as highlighted by the coloured area of Figure 16. Similarly, NIvsBZ transition stage increases rapidly reaching values close the μ_{st} one almost instantly, which ranges between 0.40 and 0.37 for 1 and 2 Hz sliding frequencies respectively, without registering two steady-state stages as NIvsST do. In addition, NIvsBZ exhibits a lower variation respect to NIvsST, as highlighted by the coloured area of Figure 4.36. Figures 4.36(c) and 4.36(d) show the mean cumulative dissipated energy E_{PoD} during the sliding, at 1 and 2 Hz respectively, of the running-in stages for each coupling, where NIvsST coupling is used as reference. All the investigated interfaces register an overall similar behaviour: after reaching the steady-state stage E_{PoD} increases more rapidly. NIvsST and NIvsNI reach similar values, ranging around 0.99 kJ and 1.81 kJ at 1 and 2 Hz respectively. Differently, NivsBZ reaches about 0.65 kJ and 1.18 kJ at 1 and 2 Hz respectively.

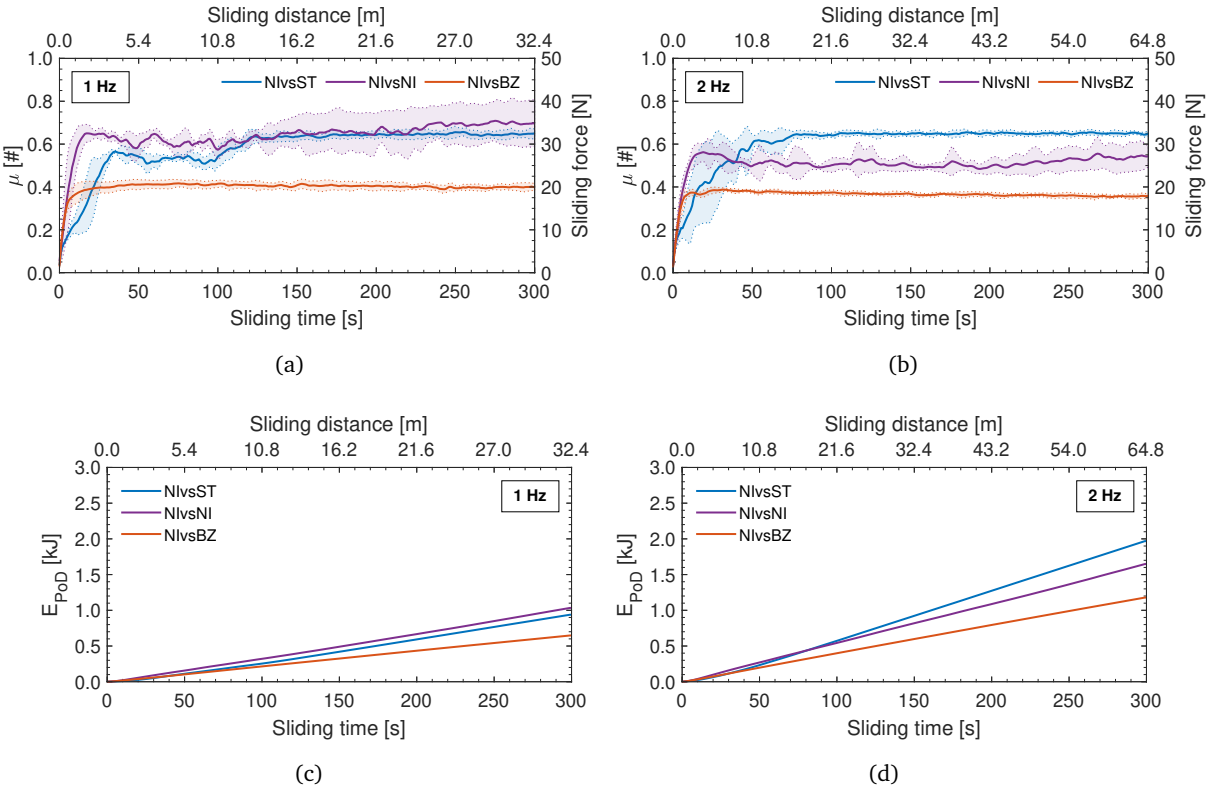

FIGURE 4.36: Part 4 RI results as function of sliding time, distance and sliding frequency: COF and sliding forces at (a) 1 Hz and (b) 2 Hz and cumulated dissipated energy at (c) 1 Hz and (d) 2 Hz.

Figures 4.37 and 4.38 show the mean COF behaviour, at 1 and 2 Hz respectively, during the IT steady stages for each coupling. All the investigated couplings reach the steady-state values in less than 10 s, but while NIvsST and NIvsBZ register a value variation almost irrelevant, NIvsNI exhibits an evident COF variation, as highlighted by the coloured areas. This behaviour confirms the findings of the previous IT-RI tests. μ_{st} values are similar to the ones obtained in the running-in stage after reaching the steady stage and average 0.64 (ST), 0.69 (NI) and 0.39 (BZ) at 1 Hz sliding frequency, and 0.65 (ST), 0.59 (NI) and 0.35 (BZ) at 2 Hz sliding frequency. It is worth noting that the average μ_{st} value of NIvsNI exhibits a moderate variation during the different tests, with CV_{μ} values averaging 7%. This variation indicates that wear particles of the nickel coating continuously affect the stability of the COF of the friction interface.

Table 4.11 lists the numerical main results of Part 3 test in terms of mean steady-state friction coefficient μ_{st}, transition time t_{tr}, pins' wear rate wr_p and disks' wear rate wr_d together with the relative coefficient of variation and the cumulated dissipated energy E_{PoD} for each performed test and investigated coupling.

During running-in stage, NIvsBZ registers the overall most steady COF's behaviour, with the lowest values of cv_{μ}, that ranges between 4% and 5%, and cv_t, that ranges between 28% and 23%, both at 1 and 2 Hz sliding frequencies respectively. On the contrary, NIvsNI registers the overall less steady COF's behaviour, with the highest values of cv_{μ}, that ranges between 10% and 9%, and cv_t, that ranges between 44% and 32%, both at 1 and 2 Hz sliding frequencies respectively.

During steady-state stage, NIvsBZ registers the overall most steady COF's behaviour, with the lowest values

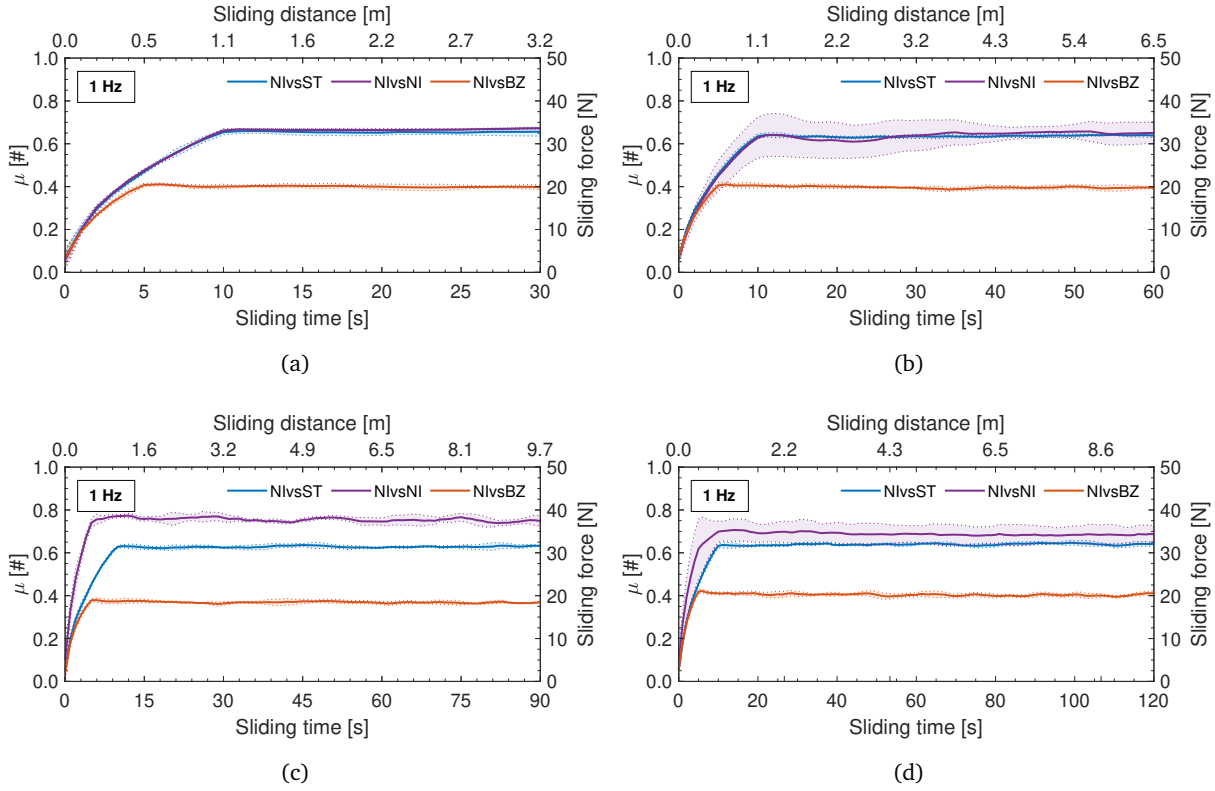

FIGURE 4.37: Part 4 IT results as function of sliding time and distance at 1 Hz sliding frequency: (a) 30 s, (b) 60 s, (c) 90 s and (d) 120 s sliding time.

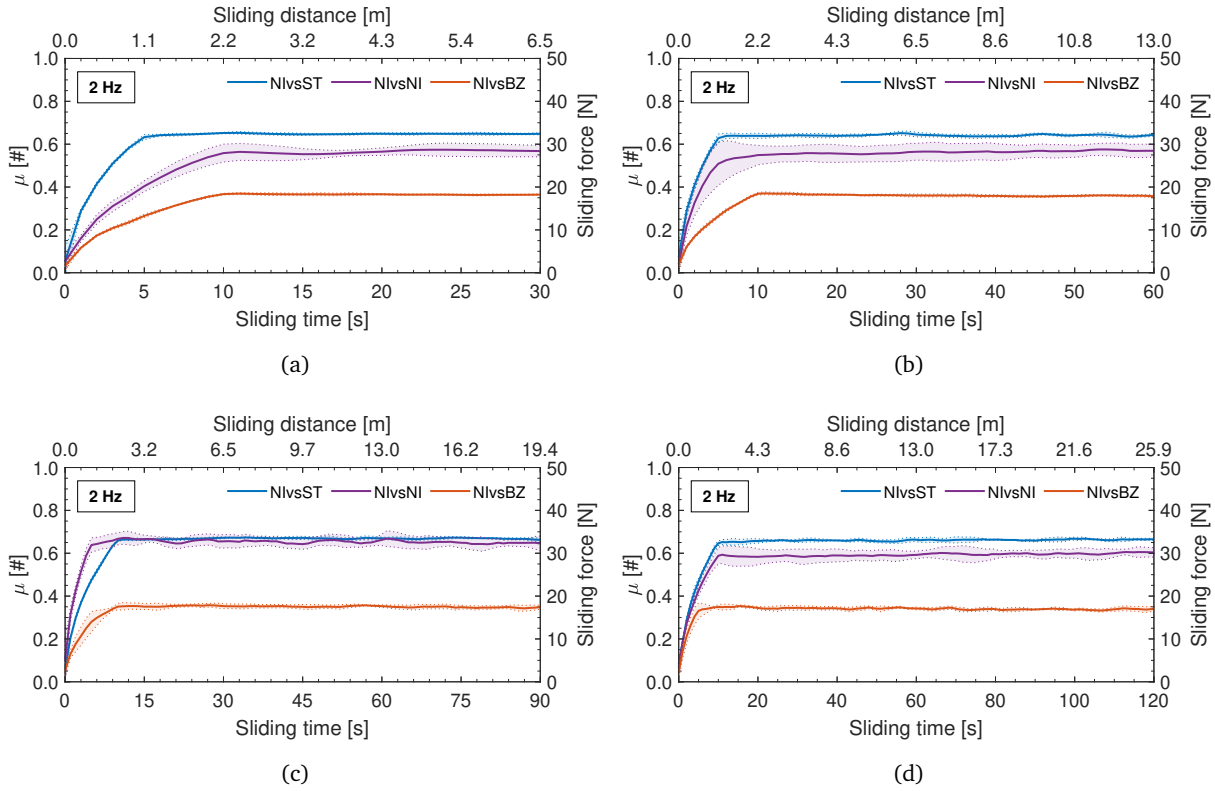

FIGURE 4.38: Part 4 IT results as function of sliding time and distance at 2 Hz sliding frequency: (a) 30 s, (b) 60 s, (c) 90 s and (d) 120 s sliding time.

TABLE 4.11: Part 4 tests mean results at 1 and 2 Hz.

		f = 1 Hz			*f = 2 Hz*		
		NIvsST	**NIvsNI**	**NIvsBZ**	**NIvsST**	**NIvsNI**	**NIvsBZ**
Running-in stage	μ_{st}	0.64	0.70	0.40	0.65	0.52	0.37
	cv_{μ}	6%	12%	5%	7%	9%	3%
	t_{tr} [s]	139	233	21	75	14	8
	cv_t	4%	44%	28%	25%	32%	23%
Steady stage	μ_{st}	0.64	0.69	0.39	0.65	0.59	0.35
	cv_{μ}	3%	6%	3%	3%	7%	4%
	t_{tr} [s]	11	9.75	9.25	9.25	11.5	9.75
	cv_t	5%	42%	4%	5%	23%	10%
Wear	wr_p [mm^3/Nm]	3.68E-03	2.82E-03	1.51E-03	5.19E-03	1.39E-03	1.41E-03
	$cv_{wr,p}$	9%	38%	10%	14%	26%	11%
	wr_d [mm^3/Nm]	3.27E-03	4.53E-03	0.00	2.80E-03	1.82E-03	0.00
	$cv_{wr,d}$	5%	4%	0.00	4%	9%	0.00
E_{PoD} [kJ]	IT-RI	0.94	1.03	0.65	1.97	1.65	1.18
	IT30	0.09	0.10	0.06	0.20	0.16	0.11
	IT60	0.19	0.20	0.13	0.40	0.35	0.22
	IT90	0.29	0.36	0.18	0.63	0.62	0.33
	IT120	0.40	0.44	0.26	0.83	0.75	0.44

of cv_{μ}, that ranges around 2%, and cv_t, that ranges between 4% and 10%, both at 1 and 2 Hz sliding frequencies respectively. On the contrary, NIvsNI registers the overall less steady COF's behaviour, with the highest values of cv_{μ}, that ranges around 5%, and cv_t, that ranges between 42% and 23%, both at 1 and 2 Hz sliding frequencies respectively.

Concerning the pin wear rate, NIvsBZ registers the lowest values of wr_p, ranging between 1.51E-03 and 1.41E-03 mm^3/Nm, with a $cv_{wr,p}$ that ranges between 10% and 11%, both at 1 and 2 Hz sliding frequencies respectively. Differently, NIvsST registers the highest values of wr_p, ranging between 3.68E-03 and 5.19E-03 mm^3/Nm, with a $cv_{wr,p}$ that ranges between 9% and 14%, both at 1 and 2 Hz sliding frequencies respectively. Concerning the disk wear rate, NIvsBZ registers an absence of volume loss and no wr_d and $cv_{wr,d}$ values are detected. Differently, NIvsNI registers the highest values of wr_d, ranging between 4.53E-03 and 1.82E-03 mm^3/Nm, with a $cv_{wr,d}$ that ranges between 4% and 9%, both at 1 and 2 Hz sliding frequencies respectively.

Concerning the cumulated dissipated energy E_{PoD}, NIvsST registers the overall highest values, ranging from 0.09 kJ, during IT30 at 1 Hz test, to 1.97 kJ during IT-RI at 2 Hz test. Differently, NIvsBZ registers the overall lowest values, ranging from 0.06 kJ, during IT30 at 1 Hz test, to 1.18 kJ during IT-RI at 2 Hz test.

Pins and disks' nickel treatment do not significantly affect disks' wear grooves, while, on the contrary, bronze significantly affects disk's wear grooves. Figure 4.39 shows the wear grooves made by (a) ST, (b) NI and (c) BZ pins on NI disk and, while in the coupling NIvsST and NIvsNI both pin and disk register weight loss, in the coupling NIvsBZ only the pins register weight loss. More precisely, BZ pins have left a slight amount of wear particles inside the asperities of the disk (see Figure 4.39(c)).

(a) (b) (c)

FIGURE 4.39: Part 4 wear grooves of NI disk with (a) ST, (b) NI and (c) BZ pins.

4.7 Conclusive remarks

The presented PoD experimental campaign has been divided in four different parts, called Part 1, Part 2, Part 3 and Part 4. Part 1 focused on the effects, on COF behaviour, of roughness and grooves geometry obtained by milling and turning S355JR steel disks surfaces. Part 1 was used to select the turning machine process with roughness $Ra = 0.8$ μm as reference for the following phases. Part 2 focused on the effects, on COF behaviour, of the coupling between the S355JR machined steel with different metals by considering bronze and brass. Part 3 focused on the effects, on COF behaviour, of the coupling between S355JR steel and S355JR steel subjected to additional treatments by considering shoot peening, nickel base and zinc base coatings. The final Part 4 focused on the effects, on COF behaviour, of the coupling between different metals with the treated steel that better performed during Parts 2 and 3.

The main findings are summarised in the following:

- The investigated couplings of Part 1 showed an overall similar behaviour. Transition times registered a significant decrement of both mean values and variation's coefficients with the increment of disks' roughness and sliding frequency. Preliminary running-in stages have proved to be very efficient to sensibly reduce transition times necessary to guarantee a steady coefficient of friction. Disks' roughness and machine processes did not significantly affect COF and pins' wear rate mean values, as well as disks' wear grooves. Test results also showed that both sides of steel-steel couplings are subjected to abrasion, whatever the machine process is used.
- The investigated couplings of Part 2 highlighted the benefits of the interaction between steel and softer metals' surfaces. More precisely, COF steadiness registered a significant increment, especially during the steady stage of T0.8vsBZ coupling. Moreover, pin's wear rates registered a significant decrement, especially for T0.8vsBS coupling. Consequently, when steel is coupled to a softer metal, only the last one is subjected to abrasion.
- The investigated couplings of Part 3 highlighted the benefits of additional steel treatments. More precisely, COF steadiness registered a significant increment already during running-in stages, especially during the steady stage of NIvsST coupling, and pin's wear rates registered a significant decrement, especially for ZNvsST coupling. However, disks' additional treatments did not affect wear grooves

formation. Consequently, when steel is coupled to treated steel, both materials are subjected to abrasion.

- The investigated couplings of Part 4 highlighted the benefits of additional steel treatments and their interaction with a softer material. More precisely, COF steadiness registered a significant increment already during running-in stages, but especially during the steady stage of NIvsBZ coupling. Moreover, pin's wear rate registered a significant decrement, especially for NIvsBZ coupling, and NI disk was not affected by wear grooves. Consequently, when steel with nickel-based coating is coupled to a softer metal, only the last one is subjected to abrasion.

As a summary, the PoD experimental campaign performed for the selection of the friction couplings of the FD in development, proved to be very efficient and permitted a better comprehension of the tribological aspects involved in the FD's mechanical behaviour. The adopted testing set-up, based on pv parameter analogy, has revealed to be proper to represent the real-use conditions of the investigated friction couplings.

A first relevant remark is related to running-in stages, which allows the development of a conformal contact between the two sliding surfaces and significantly improves COF's steadiness. An additional relevant remark is related to the advantages of the interaction between steel and softer metals, especially the interaction between nickel-treated steel and bronze, which registered the overall better COF behaviour without significant surfaces damage.

The following Chapter will be focused on the cyclic mechanical tests performed on a real scale BRFD equipped with the more promising couplings and taking account of the execution of proper running-in stages.

References

Bhushan, Bharat (2013). *Introduction to tribology*. Second edition. John Wiley & Sons Inc., p. 711. ISBN: 978-1-119-94453-9.

Blau, Peter J. (2005). "On the nature of running-in". In: *Tribology International* 38 (11-12), pp. 1007–1012. DOI: 10.1016/j.triboint.2005.07.020.

Bowden, F. P., A. J. W. Moore, and D. Tabor (1943). "The Ploughing and Adhesion of Sliding Metals". In: *Journal of Applied Physics* 14 (2). DOI: 10.1063/1.1714954.

Bowden, F. P. and D. Tabor (1942). "Mechanism of Metallic Friction". In: *Nature* 150 (3798). DOI: 10.1038/150197a0.

CEN (2015). *Hot rolled products of structural steels - Part 1: General technical delivery conditions (UNI EN 10025-1:2005)*.

CEN (2018). *Anti-seismic devices (UNI EN 15129:2018)*.

CEN (2022). *Geometrical product specifications (GPS) - Surface texture: Areal - Part 2: Terms, definitions and surface texture parameters (EN ISO 25178-2:2021)*.

Chanchi Golondrino, Jose Christian, Gregory Anthony MacRae, James Geoffrey Chase, Geoffrey William Rodgers, and George Charles Clifton (2020). "Seismic behaviour of symmetric friction connections for steel buildings". In: *Engineering Structures* 224. DOI: 10.1016/j.engstruct.2020.111200.

Copper, copper alloys Ingots, and castings (2017). *Copper and copper alloys - Ingots and castings (EN 1982:2017)*.

Croccolo, Dario, Massimiliano De Agostinis, Stefano Fini, Giorgio Olmi, Luca Paiardini, and Francesco Robusto (2020). "Tribological Properties of Connecting Rod High Strength Screws Improved by Surface Peening Treatments". In: *Metals* 10 (3). DOI: 10.3390/met10030344.

Das, Turan, Azmi Erdogan, Bilal Kursuncu, Erfan Maleki, and Okan Unal (2020). "Effect of severe vibratory peening on microstructural and tribological properties of hot rolled AISI 1020 mild steel". In: *Surface and Coatings Technology* 403. DOI: 10.1016/j.surfcoat.2020.126383.

Federici, Matteo, Mattia Alemani, Cinzia Menapace, Stefano Gialanella, Guido Perricone, and Giovanni Straffelini (2019). "A critical comparison of dynamometer data with pin-on-disc data for the same two friction material pairs – A case study". In: *Wear* 424-425, pp. 40–47. DOI: 10.1016/j.wear.2019.02.009.

Federici, Matteo, Stefano Gialanella, Mara Leonardi, Guido Perricone, and Giovanni Straffelini (2018). "A preliminary investigation on the use of the pin-on-disc test to simulate off-brake friction and wear characteristics of friction materials". In: *Wear* 410-411, pp. 202–209. DOI: 10.1016/j.wear.2018.07.011.

Federici, Matteo, Giovanni Straffelini, and Stefano Gialanella (2017). "Pin-on-Disc Testing of Low-Metallic Friction Material Sliding Against HVOF Coated Cast Iron: Modelling of the Contact Temperature Evolution". In: *Tribology Letters* 65 (4), p. 121. DOI: 10.1007/s11249-017-0904-y.

Fereidouni, Hossein, Saleh Akbarzadeh, and M. M. Khonsari (2020). "The Relation Between Subsurface Stresses and Useful Wear Life in Sliding Contacts". In: *Tribology Letters* 68 (1). DOI: 10.1007/s11249-019-1246-8.

Ferrante Cavallaro, G., A. Francavilla, M. Latour, V. Piluso, and G. Rizzano (2017). "Experimental behaviour of innovative thermal spray coating materials for FREEDAM joints". In: *Composites Part B: Engineering* 115. DOI: 10.1016/j.compositesb.2016.09.075.

Fischer-Cripps, Anthony C. (2007). *Introduction to Contact Mechanics*. Springer US. ISBN: 978-0-387-68187-0. DOI: 10.1007/978-0-387-68188-7.

Funke, R. and A. Schubert (2016). "Increase of the Coefficient of Static Friction Using Turn-milling with an Inclined Milling Spindle". In: *Procedia CIRP* 45. DOI: 10.1016/j.procir.2016.02.120.

Gopi, R., I. Saravanan, A. Devaraju, and Ganesh babu loganathan (2020). "Investigation of shot peening process on stainless steel and its effects for tribological applications". In: *Materials Today: Proceedings* 22. DOI: 10.1016/j.matpr.2019.08.215.

Grigorian, C. E., T. S. Yang, and E. P. Popov (1993). "Slotted Bolted Connection Energy Dissipators". In: *Earthquake Spectra* 9 (3). DOI: 10.1193/1.1585726.

Huang, Linjie, Zhen Zhou, Xiaogang Huang, and Yongwei Wang (2020). "Variable friction damped self-centering precast concrete beam–column connections with hidden corbels: Experimental investigation and theoretical analysis". In: *Engineering Structures* 206. DOI: 10.1016/j.engstruct.2019.110150.

Huang, Xiaogang, Zhen Zhou, Qin Xie, Congming Guo, and Canjun Li (2018). "Seismic Analysis of Friction-Damped Self-Centering Coupled-Beams for Moment-Resisting-Frames without Floor Elongation". In: *Journal of Earthquake and Tsunami* 12 (05). DOI: 10.1142/S1793431118500124.

ISO (2015). *Metallic materials - Instrumented indentation test for hardness and materials parameters - Part 1: Test method (UNI EN ISO 14577-1)*.

ISO (2021). *Geometrical product specifications (GPS) - Surface texture: Profile - Part 3: Specification operators (UNI EN ISO 21920-3:2021)*.

Ivkovic, Branko, Miroslav Djurdjanovic, and Dusan Stamenkovic (2000). "The Influence of the Contact Surface Roughness on the Static Friction Coefficient". In: *Tribology in industry* 22 (3&4), pp. 41–44.

Khoo, Hsen-Han, Charles Clifton, John Butterworth, Gregory MacRae, and George Ferguson (2012). "Influence of steel shim hardness on the Sliding Hinge Joint performance". In: *Journal of Constructional Steel Research* 72. DOI: 10.1016/j.jcsr.2011.11.009.

Khun, N. W., P. Q. Trung, and D. L. Butler (2016). "Mechanical and Tribological Properties of Shot-Peened SAE 1070 Steel". In: *Tribology Transactions* 59 (5), pp. 932–943. DOI: 10.1080/10402004.2015.1121313.

Kim, Hyung-Joon and Constantin Christopoulos (2008). "Friction Damped Posttensioned Self-Centering Steel Moment-Resisting Frames". In: *Journal of Structural Engineering* 134 (11). DOI: 10.1061/(ASCE)0733-9445(2008)134:11(1768).

Latour, M., V. Piluso, and G. Rizzano (2014). "Experimental analysis on friction materials for supplemental damping devices". In: *Construction and Building Materials* 65. DOI: 10.1016/j.conbuildmat.2014.04.092.

Latour, Massimo, Vincenzo Piluso, and Gianvittorio Rizzano (2015). "Free from damage beam-to-column joints: Testing and design of DST connections with friction pads". In: *Engineering Structures* 85. DOI: 10.1016/j.engstruct.2014.12.019.

Lee, Chang-Hwan, Jaeho Ryu, Jintak Oh, Chang-Hee Yoo, and Young K. Ju (2016). "Friction between a new low-steel composite material and milled steel for SAFE Dampers". In: *Engineering Structures* 122, pp. 279–295. DOI: 10.1016/j.engstruct.2016.04.056.

Liang, Guoxing, Siegfried Schmauder, Ming Lyu, Yanling Schneider, Cheng Zhang, and Yang Han (2018). "An Investigation of the Influence of Initial Roughness on the Friction and Wear Behavior of Ground Surfaces". In: *Materials* 11 (2). DOI: 10.3390/ma11020237.

Manojkumar, P.A., A.S. Gandhi, M. Kamaraj, and A.K. Tyagi (2014). “Sliding wear behaviour of alumina coatings prepared from mechanically milled powders”. In: *Wear* 313 (1-2). DOI: 10.1016/j.wear.2014.02.008.

Mitrovic, Slobodan, Dragan Adamovic, Fatima Zivic, Dragan Dzunic, and Marko Pantic (2014). “Friction and wear behavior of shot peened surfaces of 36CrNiMo4 and 36NiCrMo16 alloyed steels under dry and lubricated contact conditions”. In: *Applied Surface Science* 290. DOI: 10.1016/j.apsusc.2013.11.050.

Morgen, Brian G. and Yahya C. Kurama (2009). “Characterization of two friction interfaces for use in seismic damper applications”. In: *Materials and Structures* 42 (1). DOI: 10.1617/s11527-008-9365-y.

Pall, Avtar S. (1983). “Friction Devices for aseismic design of buildings”. In: 4th Canadian Conference on Earthquake Engineering, pp. 475–484.

Rodgers, G.W., J.G. Chase, R. Causse, J. Chanchi, and G.A. MacRae (2017). “Performance and degradation of sliding steel friction connections: Impact of velocity, corrosion coating and shim material”. In: *Engineering Structures* 141. DOI: 10.1016/j.engstruct.2017.02.070.

Saffarzade, Peyman, Ahmad Ali Amadeh, and Navid Agahi (2020). “Study of tribological and friction behavior of magnesium phosphate coating and comparison with traditional zinc phosphate coating under dry and lubricated conditions”. In: *Tribology International* 144. DOI: 10.1016/j.triboint.2019.106122.

Sinha, Ankur, Gloria Ischia, Cinzia Menapace, and Stefano Gialanella (2020). “Experimental Characterization Protocols for Wear Products from Disc Brake Materials”. In: *Atmosphere* 11 (10), p. 1102. DOI: 10.3390/atmos11101102.

Sriraman, K. R., P. Manimunda, R. R. Chromik, and S. Yue (2016). “Effect of crystallographic orientation on the tribological behavior of electrodeposited Zn coatings”. In: *RSC Advances* 6 (21), pp. 17360–17372. DOI: 10.1039/C5RA15490A.

Sriraman, K.R., H.W. Strauss, S. Brahimi, R.R. Chromik, J.A. Szpunar, J.H. Osborne, and S. Yue (Dec. 2012). “Tribological behavior of electrodeposited Zn, Zn–Ni, Cd and Cd–Ti coatings on low carbon steel substrates”. In: *Tribology International* 56, pp. 107–120. DOI: 10.1016/j.triboint.2012.06.008.

Trung, Pham Quang, Nay Win Khun, and David Lee Butler (Oct. 2016). “Effects of shot peening pressure, media type and double shot peening on the microstructure, mechanical and tribological properties of low-alloy steel”. In: *Surface Topography: Metrology and Properties* 4 (4). DOI: 10.1088/2051-672X/4/4/045001.

Vaxevanidis, N. M., D. E. Manolakos, A. Koutsomichalis, G. Petropoulos, A. Panagotas, I. Sideris, A. Mourlas, and S. S. Antoniou (Sept. 2006). “THE EFFECT OF SHOT PEENING ON SURFACE INTEGRITY AND TRIBOLOGICAL BEHAVIOUR OF TOOL STEELS”. In.

Verma, Piyush Chandra, Luca Menapace, Andrea Bonfanti, Rodica Ciudin, Stefano Gialanella, and Giovanni Straffelini (Jan. 2015). “Braking pad-disc system: Wear mechanisms and formation of wear fragments”. In: *Wear* 322-323, pp. 251–258. DOI: 10.1016/j.wear.2014.11.019.

Wu, Bin, Bin shi Xu, Bin Zhang, and Shi yun Dong (2007). “The effects of parameters on the mechanical properties of Ni-based coatings prepared by automatic brush plating technology”. In: *Surface and Coatings Technology* 201 (12), pp. 5758–5765. DOI: 10.1016/j.surfcoat.2006.10.013.

Zimbru, Mariana, Mario D’Aniello, Attilio De Martino, Massimo Latour, Gianvittorio Rizzano, and Vincenzo Piluso (2018). “Investigation on Friction Features of Dissipative Lap Shear Connections by Means of Experimental and Numerical Tests”. In: *The Open Construction and Building Technology Journal* 12 (1). DOI: 10.2174/1874836801812010154.

5
Preliminary mechanical tests

5.1 BRFD prototyping

The BRFD prototype in here investigated has been designed with activation forces of 10-20 kN and maximum displacements of 40 mm. These properties are representative of real-case applications, as suggested by the optimisation analysis carried out on a real case study of a precast RC structure retrofitting (D'Agostini, 2023; De Serra, 2023).

The selection of the friction interfaces to develop a reliable and steady friction coefficient μ followed the findings of the tribological investigation of Chapter 4 and the findings of Grossi et al. (2023a,b). Among the investigated surfaces, the better-performing couplings were nickelled steel vs. nickelled steel (NN) and nickelled steel vs. bronze (NB). These two configurations have been selected to manufacture the BRFD prototype and have been investigated to assess the influence of bolt axial preload and sliding velocity on the BRFD overall behaviour. The details of the design process are visible in Appendix B.

Figure 5.1 shows the drawings of the elements for the BRFD prototype assembled for the mechanical tests.

5.2 Experimental setup and testing protocol

The mechanical tests have been performed at the Structural Integrity Laboratory (Engineering Department, University of Ferrara, Italy) using an MTS servo-hydraulic testing machine with a maximum load capacity of 250 kN testing machine and control system as shown in Figure 5.2(a). The experimental layout of the BRFD prototype (see Figure 5.3(a)) slightly differs from the layout of Figure 3.1(a). Two additional steel guides (the experimental setup guides of Figure 5.3(a)) with slotted holes have been added to exclude rotations at the ends of the connection plates and, at the same time, to ensure a hinged connection to the actuator (see Figure 5.3(a)). In fact, the experimental setup guides exclude bending moment at the device ends, for the safety of the testing machine, by using the bolts couples within the slotted holes (see Figure 5.3(a)). To reduce possible friction between stud bolts and the slotted holes of the additional guide, lubricated bushes were introduced for each bolt. To assess the experimental setup, some cycles were performed on the prototype without preload of the stud bolts to measure the influence the additional guides on the recorded forces. The obtained forces resulted lower than 5% of the forces recorded on the prototype with preload of the stud bolts. At the early stage of the mechanical testing, the behaviour of the BRFD has been investigated only in the longitudinal direction, despite the bidirectional potential, focusing on the behaviour of the selected friction interfaces.

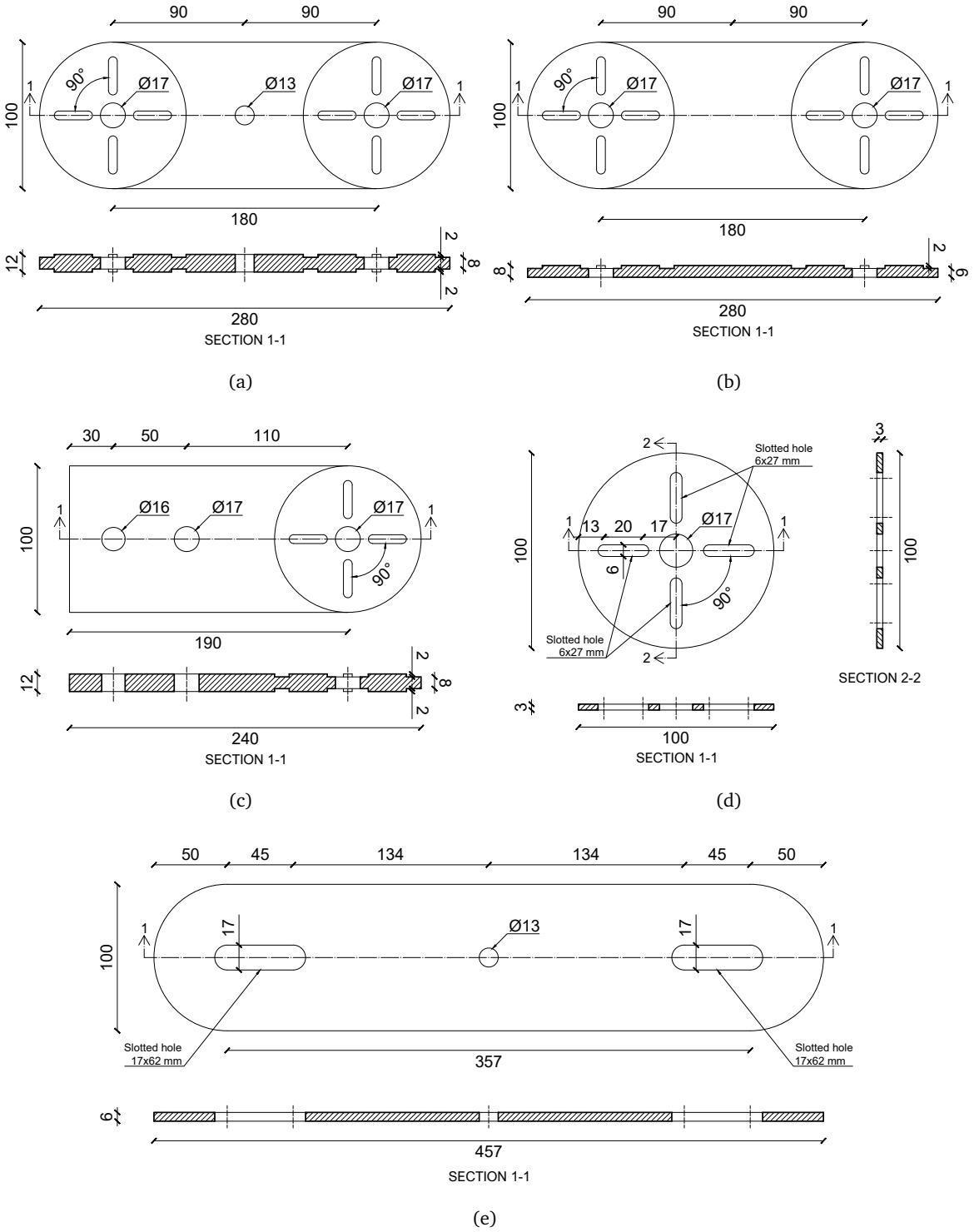

FIGURE 5.1: BRFD elements drawings: a) core central plate, b) core side plate, c) connection plate, d) friction pad and e) alignment guide. Dimensions in mm.

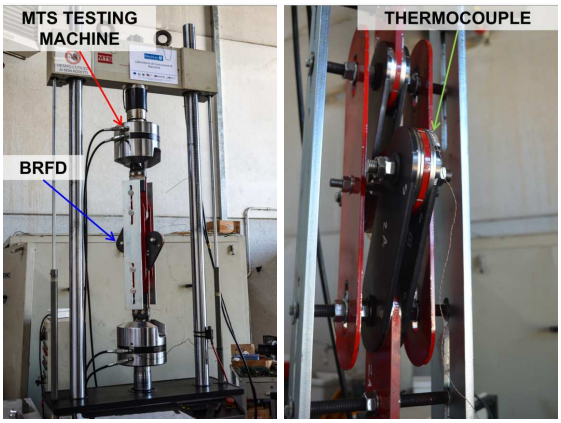

(a) (b)

FIGURE 5.2: Preliminary mechanical tests experimental setup a) general overview and b) detail of thermocouples connection.

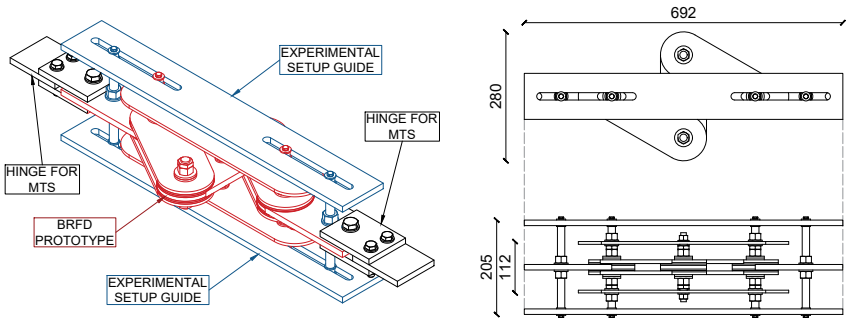

(a) (b)

FIGURE 5.3: BRFD prototype drawings: a) axonometric view with details and b) top and side view. Dimensions in mm.

The prototype has been manufactured using S355JR structural steel (CEN, 2015b), using four M16 class 8.8 (CEN, 2015a) preload stud bolts and one M12 class 8.8 (CEN, 2015a) central stud bolts. Two additional M16 class 8.8 (CEN, 2015a) stud bolts have been added to the prototype to connect the two additional steel guides. As showed in Figure 5.3(b), the overall dimension of the prototype is 70x30x20 cm^3. Nuts have been closed using a FERVI 0803/S210 manual torque wrench (FERVI SpA, Modena, Italy) to ensure the application of constant tension to the stud bolts. The torque method was adopted as it is suggested in the literature to be the most accurate among all the standardised methods (Ferrante Cavallaro et al., 2018).

During the test execution, forces and displacements of the device have been recorded by means of the MTS internal measurement system. The prototype was equipped with several sensors to detect the temperature increment in correspondence with the dissipating areas. K-thermocouples connected to a TC-08 thermocouple data logger (Pico Technology, St Neots, United Kingdom) were placed close to the BRFD's friction interface to measure the temperature increment in the proximity of the working area, assessing the amount and the effects of the temperature increment on the BRFD behaviour (see Figure 5.2(b) for the detailed view).

The testing protocols were defined according to EN15129 (CEN, 2018a), which prescribes, for friction damper devices, quasi-static incremental displacements performing at least five cycles at 25%, five cycles at 50% and ten cycles at 100% of the device maximum allowable displacement. However, several studies (among the others see the works of Chanchi Golondrino et al. (2020), Latour et al. (2014), and Morgen and Kurama (2009)) show how the performance of friction devices can be significantly influenced by the sliding velocity and the variation of bolt axial load. In addition, the tribological investigation previously performed for the BRFD development highlighted how the overall μ steadiness increases significantly after performing running-in stages (Grossi et al., 2023a,b).

Three different frequencies have been considered in defining the testing protocols: 0.05 Hz has been selected to perform the quasi-static tests while 0.50 and 1.00 Hz have been selected to perform the dynamic tests (F1, F2 and F3 tags respectively). Concerning the torque of the stud bolts, three different levels have been considered: 40, 60 and 100 Nm (T1, T2 and T3 tags respectively), which corresponds to 20%, 30% and 50% of the maximum M16 (CEN, 2015a) allowable torque. Concerning the displacement amplitudes, a maximum allowable displacement of ± 40 mm has been used to define the testing protocols. However, due to the testing equipment capacity limitation, the maximum displacement had to be decreased when incrementing the frequency, consequently, three different target displacements have been considered: ± 40, ± 20 and ± 10 mm (A1, A2 and A3 tags at frequencies F1, F2 and F3 respectively).

The testing procedure has been divided into three different steps. The first one is the running-in (RI) tests (see Table 5.1), which are performed to properly develop a conformal contact between the surfaces of friction interface. The second one is the Group 1 (G1) tests (see Table 5.2), which are performed with fixed frequency and incrementing displacement amplitude, resembling the EN15129 (CEN, 2018a) requested procedure. The final one is the Group 2 (G2) tests (see Table 5.3), which are performed with fixed displacement amplitude and incrementing frequency, focusing on the sliding velocity influence.

TABLE 5.1: Running-in test procedure.

Test group code	Fixed frequency	Fixed amplitude	Torque	Total duration
RI	0.50 Hz	± 20 mm	40 Nm	300 s

TABLE 5.2: Group 1 test procedure.

Test group code	Fixed frequency	Increment sequence	Torque level	Total duration
G1-F1	0.05 Hz	± 10 mm (25% A1) - 180 s ± 20 mm (50% A2) - 180 s ± 40 mm (100% A3) - 180 s	40 Nm 60 Nm 100 Nm	540 s
G1-F2	0.50 Hz	± 10 mm (25% A1) - 60 s ± 20 mm (50% A2) - 60 s ± 40 mm (100% A3) - 60 s	40 Nm 60 Nm 100 Nm	180 s
G1-F3	1.00 Hz	± 10 mm (25% A1) - 60 s ± 20 mm (50% A2) - 60 s ± 40 mm (100% A3) - 60 s	40 Nm 60 Nm 100 Nm	180 s

All the tests have been performed for both NN and NB configurations. RI tests considered only T1 torque, G1 tests considered T1, T2 and T3 torque, and G2 tests considered only T3 torque. All the tests have been

TABLE 5.3: Group 2 test procedure.

Test group code	Fixed amplitude	Increment sequence	Torque level	Total duration
G2	± 10 mm	0.05 Hz - 120 s 0.10 Hz - 60 s 0.15 Hz - 60 s 0.20 Hz - 30 s 0.25 Hz - 30 s 0.50 Hz - 30 s 0.75 Hz - 30 s 1.00 Hz - 30 s	100 Nm	390 s

conducted at room temperature, waiting for specimens to cool off if the increment of temperature at the end of a previous test exceeded 10% of the room temperature.

5.3 Results and discussions

The experimental results of RI, G1 and G2 tests are here presented using Matlab as post-processing software (MathWorks, 2022).

The BRFD is a device based on friction, consequently during the RI tests the recorded hysteresis cycle registers the evolution of the Figure 5.4 scheme: when the BRFD is subjected to n-cycles between $\pm d_{max}$, the hysteresis area increments until the development of a conformal contact between the sliding surfaces, reaching a stable behaviour. More precisely, when the surfaces of a friction interface start sliding, wear debris starts to accumulate forming a layer. The more compact this layer is, the more stable and smooth the coefficient of friction is (Grossi et al., 2023a).

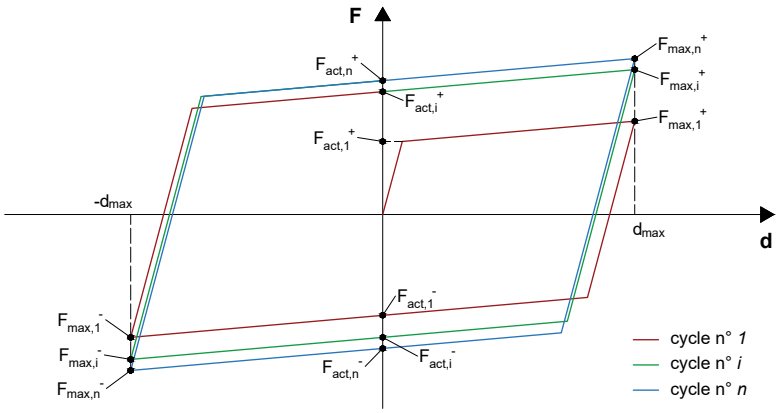

FIGURE 5.4: Hysteresis cycle evolution scheme.

The first cycle is defined by the forces ${F_{act,1}}^{+}$, the positive force developed at the first sliding, ${F_{act,1}}^{-}$, the negative force developed at zero-displacement, ${F_{max,1}}^{+}$, the force developed at the displacement $+d_{max}$, and ${F_{max,1}}^{-}$, the force developed at the displacement $-d_{max}$. Starting from the second cycle, each i-cycle's loop is defined by the forces ${F_{act,i}}^{+}$, the positive force developed at zero-displacement, ${F_{act,i}}^{-}$, the negative force developed at zero-displacement), ${F_{max,i}}^{+}$, the force developed at the displacement $+d_{max}$, and ${F_{max,i}}^{+}$, the force developed at the displacement $-d_{max}$.

To define the shape of the hysteresis cycle after the development of the friction interface coupling (i.e. when it reaches a steady behaviour), it is important to identify the transition time t_{tr}, defined as the time needed to reach a steady behaviour. For each i-cycle ($i = 1, ..., n_{tot}$) a mean activation force $F_{act,i}$ and a mean maximum force $F_{max,i}$ are calculated respectively as the average value between positive and negative forces developed at zero-displacement, and the average value between the force developed at the displacement $\pm d_{max}$ (see Eq. 5.1).

$$F_{act,i} = \frac{\left|{F_{act,i}}^{+}\right| + \left|{F_{act,i}}^{-}\right|}{2}; \qquad F_{max,i} = \frac{\left|{F_{max,i}}^{+}\right| + \left|{F_{max,i}}^{-}\right|}{2}; \qquad i = 1, ..., n_{tot} \tag{5.1}$$

Subsequently, it is evaluated the percentage difference between $F_{act,i}$ and $F_{act,i-1}$, and between $F_{max,i}$ and $F_{max,i-1}$, as for Eq. 5.2. The number of cycles n_{st} needed to reach a steady behaviour is evaluated as the bigger between the number of cycles needed to reach $dF_{act,i} < 5\%$ and the number of cycles needed to reach $dF_{max,i} < 5\%$.

$$dF_{act,i} = \left|\frac{F_{act,i} - F_{act,i-1}}{F_{act,i}}\right|; \qquad dF_{max,i} = \left|\frac{F_{max,i} - F_{max,i-1}}{F_{max,i}}\right|; \qquad i = 2, ..., n_{tot} \tag{5.2}$$

RI tests are performed with a fixed frequency f, consequently the transition time t_{tr} is defined as the ratio between n_{st} and f (see Eq. 5.3). The mean activation force $F_{act,st}$ and maximum force $F_{max,st}$ for the steady hysteresis cycles are evaluated as the average value of all $F_{act,i}$ and $F_{max,i}$ for i varying between n_{st} and the total number of cycles n_{tot} (see Eq. 5.4).

$$t_{tr} = \frac{1}{f} n_{st} \tag{5.3}$$

$$F_{act,st} = \frac{\sum_{i=n_{st}}^{n_{tot}} F_{act,i}}{n_{tot} - n_{st} + 1}; \qquad F_{max,st} = \frac{\sum_{i=n_{st}}^{n_{tot}} F_{max,i}}{n_{tot} - n_{st} + 1} \tag{5.4}$$

During G1 and G2 tests, the steady behaviour is considered reached, consequently, the mean values $F_{act,st}$ and $F_{max,st}$ are directly evaluated as the average value of all $F_{act,i}$ and $F_{max,i}$ for i varying between 1 and the total number of cycles n_{tot}.

5.3.1 Running-in (RI) test results

Figures 5.5(a) and 5.5(b) show RI test results, for NN and NB configuration respectively, in terms of hysteresis cycles as a force-displacement relationship. The difference between NN and NB hysteresis cycles is highly remarkable, both in terms of overall shape and values. NN has an initial rectangular-shaped hysteresis cycle with $F_{act,1}$ value of 2.99 kN. Once the conformal contact between the sliding surfaces is properly developed, NN exhibits a rectangular-shaped hysteresis cycle with an evident hardening effect due to the stick-slip mechanism, with $F_{act,st}$ value of 7.66 kN. NB has an initial rectangular-shaped hysteresis cycle with a slight hardening effect due to the stick-slip mechanism and $F_{act,1}$ value of 2.06 kN. Once the conformal contact between the sliding surfaces is properly developed, NB maintains the rectangular-shaped hysteresis cycle with $F_{act,st}$ value of 3.03 kN.

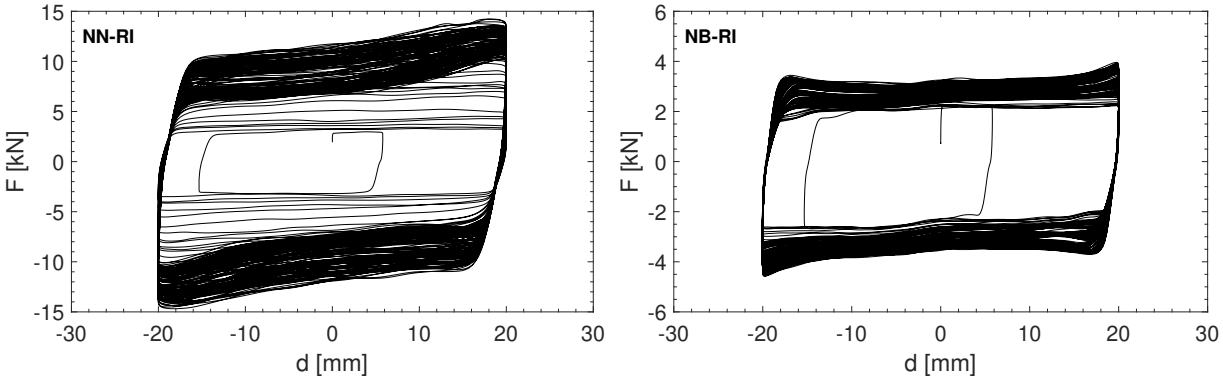

(a) (b)

FIGURE 5.5: RI tests hysteresis cycles of a) NN and b) NB configurations.

Figures 5.6(a) and 5.6(b) show RI test results, for NN and NB configuration respectively, in terms of force-time relationship. The orange dashed line highlights the trend of $F_{act,i}$ values, and the blue dashed line highlights the $F_{act,st}$ values. The difference between NN and NB both in terms of overall shape and values is here confirmed. NN force increases rapidly from around 3 kN to 11 kN then decreases slowly and stabilises around 8 kN, registering a transition time t_{tr} of 230 s (n_{st} equal 115). NB force increases slowly from around 2 kN and stabilises around 3 kN, registering a t_{tr} value of 198 s (n_{st} equal 99).

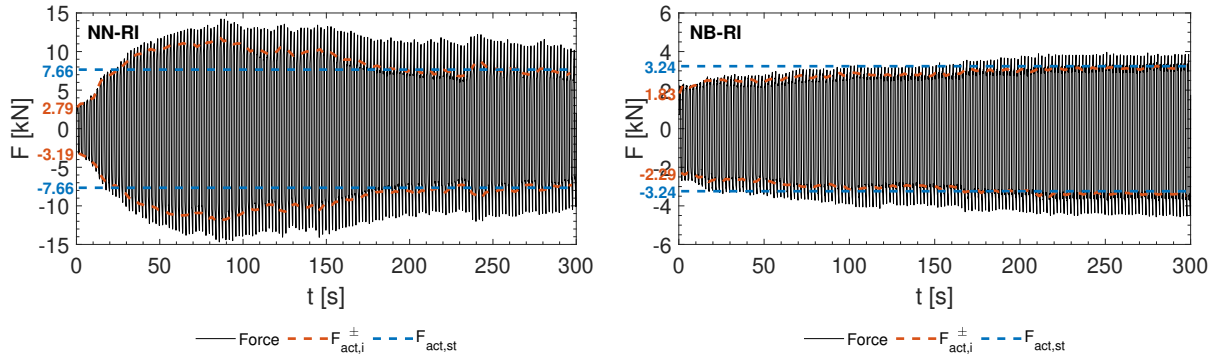

(a) (b)

FIGURE 5.6: RI tests recorded forces for a) NN and b) NB configurations.

Table 5.4 lists the main results of RI tests in terms of initial activation force $F_{act,1}$, steady activation force $F_{act,st}$, percentage increment between initial and steady activation force ΔF_{act}, coefficient of variation of the overall recorded forces cv_{Fact} and the steady behaviour $cv_{Fact,st}$, transition time t_{tr}, steadiness cycle number n_{st} and temperature increment ΔT over the initial room temperature. NN configuration exhibits a higher activation force increment (156%), a higher overall coefficient of variation (20%), a higher steady coefficient of variation (6%), a higher transition time (230 s) and a higher temperature increment (32.8°C). On the contrary, NB configuration exhibits a lower force increment (47%), a lower overall coefficient of variation (9%), a lower steady coefficient of variation (2%), a lower transition time (130 s) and a lower temperature increment (10.7°C). As a result, at the end of RI tests, both NN and NB configurations develop a conformal contact between the sliding surfaces reaching a steady behaviour; however, NB reached it

more quickly and efficiently than NN.

TABLE 5.4: RI test main results.

Configuration	$F_{act,1}$ [kN]	$F_{act,st}$ [kN]	ΔF_{act} [%]	cv_{Fact} [%]	$cv_{Fact,st}$ [%]	t_{tr} [s]	n_{st}	ΔT [°C]
NN	2.99	7.66	156	20	6	230	115	32.8
NB	2.06	3.03	47	9	2	198	99	10.7

It is worth noting that the difference between NN and NB configurations is mainly caused by the different friction interfaces adopted, confirming the findings of the tribological investigations (Grossi et al., 2023a,b). During the running-in stages, nickelled steel vs. nickelled steel coupling (NN) registered higher μ values than nickelled steel vs. bronze coupling (NB), confirming the higher force values and transition time registered by NN than the NB configuration.

5.3.2 Group 1 (G1) test results

Figures 5.7 and 5.8 show G1 test results, for NN and NB configuration respectively, in terms of hysteresis cycles as a force-displacement relationship for F1, F2 and F3 sliding frequencies.

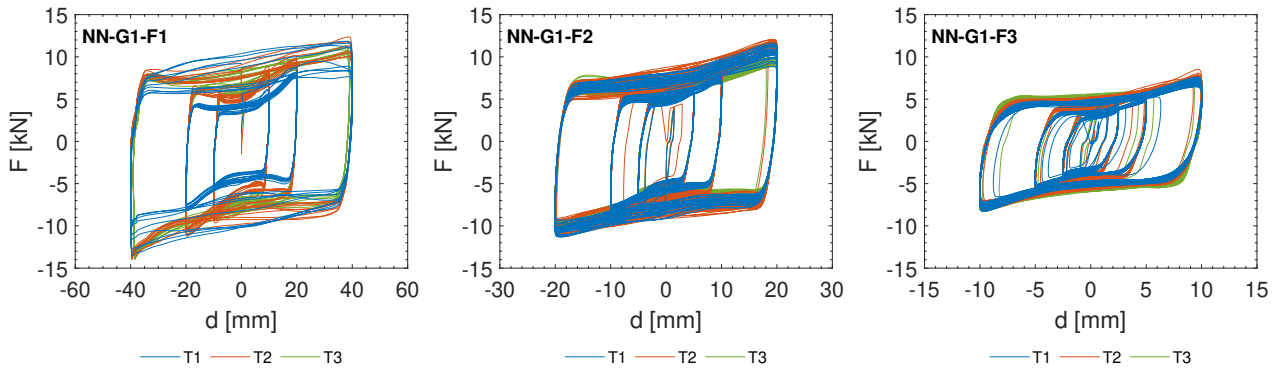

FIGURE 5.7: G1 tests hysteresis cycles for NN configuration at a) 0.05 Hz, b) 0.50 Hz and c) 1.00 Hz oscillation frequencies.

NN configuration exhibits a rectangular-shaped hysteresis cycle with an evident hardening effect due to the stick-slip mechanism also after the RI tests, resulting in higher force values when reaching higher displacement amplitude. NN configuration exhibits higher values during the tests performed with lower sliding frequencies, with an average force decrement of 55% from F1 to F3. Concerning the effects of the different torque levels, the NN configuration registers higher sliding force values during the tests performed with higher torque values, with an average sliding force increment of 22% from T1 to T3. However, it is worth noting that this difference decreases as the sliding frequency increases.

NB configuration exhibits a rectangular-shaped hysteresis cycle with a slight hardening effect due to the stick-slip mechanism also after the RI tests, resulting in almost equal force values when reaching higher displacement amplitude. NB configuration exhibits slightly higher values during the tests performed with higher sliding frequencies, with an average force increment of 4% from F1 to F3. Concerning the effects

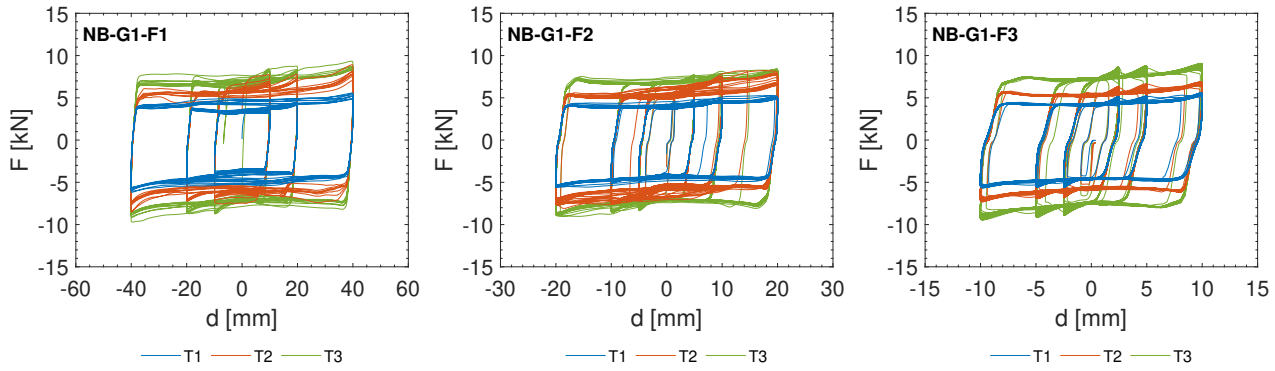

(a) (b) (c)

FIGURE 5.8: G1 tests hysteresis cycles for NB configuration at a) 0.05 Hz, b) 0.50 Hz and c) 1.00 Hz oscillation frequencies.

of the torque increment, NB configuration exhibits higher values during the tests performed with higher torque values, with an average force increment of 73% from T1 to T3. In addition, it is worth noting that this difference is not significantly influenced by the sliding frequency increments.

Tables 5.5 and 5.6 list the main results of G1 tests, for NN and NB configuration respectively, in terms of steady activation force $F_{act,st}$, maximum force $F_{max,st}$, percentage difference ΔF between $F_{act,st}$ and $F_{max,st}$, coefficient of variation of the overall recorded forces cv_F and temperature increment ΔT. During the tests, NN registers $F_{act,st}$ values ranging between 3.49 and 6.87 kN, with an overall mean value of 5.35 kN, and $F_{max,st}$ values ranging between 5.59 and 10.57 kN, with an overall mean value of 7.91 kN. The difference between $F_{max,st}$ and $F_{act,st}$ values ranges between 1.66 and 4.26 kN, with an overall mean value of 2.55 kN which corresponds to an average increment of 22% from $F_{act,st}$ to $F_{max,st}$. NB registers $F_{act,st}$ values ranging between 3.72 and 6.78 kN, with an overall mean value of 5.26 kN, and $F_{max,st}$ values ranging between 4.46 and 8.81 kN, with an overall mean value of 8.81 kN. The difference between $F_{max,st}$ and $F_{act,st}$ values ranges between 0.73 and 2.36 kN, with an overall mean value of 1.49 kN which corresponds to an average increment of 22% from $F_{act,st}$ to $F_{max,st}$.

TABLE 5.5: G1 test main results for NN configuration.

Test Tag	Torque [Nm]	$F_{act,st}$ [kN]	$F_{max,st}$ [kN]	ΔF [%]	cv_F [%]	ΔT [°C]
NN-G1-F1	40 (T1)	5.17	8.44	39	13	2.3
	60 (T2)	6.31	10.57	40	9	1.3
	100 (T3)	6.87	9.91	31	5	3.5
NN-G1-F2	40 (T1)	5.66	7.86	28	8	2.4
	60 (T2)	6.07	8.46	28	13	2.7
	100 (T3)	6.25	7.91	21	5	1.4
NN-G1-F3	40 (T1)	3.49	5.59	38	11	1.0
	60 (T2)	4.08	6.42	37	7	1.7
	100 (T3)	4.28	5.99	29	7	1.3

Both configurations exhibit a significant improvement in terms of activation force steadiness after the RI, registering cv_F values that average 9% and 4% for NN and NB respectively. Furthermore, it is worth noting that both configurations exhibit lower cv_F values when T3 is applied, registering cv_F values that average

TABLE 5.6: G1 test main results for NB configuration.

Test Tag	Torque [Nm]	$F_{act,st}$ [kN]	$F_{max,st}$ [kN]	ΔF [%]	cv_F [%]	ΔT [°C]
NB-G1-F1	40 (T1)	3.72	4.46	16	4	0.9
	60 (T2)	5.66	7.06	20	5	0.9
	100 (T3)	6.72	8.29	19	3	1.1
NB-G1-F2	40 (T1)	3.88	4.99	22	3	1.5
	60 (T2)	5.17	6.98	26	3	1.4
	100 (T3)	6.78	8.16	17	1	2.3
NB-G1-F3	40 (T1)	3.96	5.34	26	6	1.2
	60 (T2)	5.02	6.64	24	5	1.6
	100 (T3)	6.45	8.81	27	5	2.3

6% and 3% for NN and NB respectively. Concerning the temperature increment, both configurations do not reach more than a 10% increment of room temperature, registering ΔT values lower than 4°C for NN and NB respectively. Consequently, given the typical seismic event duration of 60 to 120 seconds, it is expected that the temperature increment does not influence the overall BRFD behaviour during the real use condition.

G1 tests emphasize the differences between NN and NB configuration and confirm the outcomes of the tribological campaign of Chapter 4. During the steady-state stages, nickelled steel vs. nickelled steel coupling (NN) registered higher μ and coefficient of variation values than nickelled steel vs. bronze coupling (NB). As a result, it is expected to find higher force values and coefficient of variation for NN than the NB configuration. However, it is worth noting that when the torque increments, the NN configuration reaches force values similar to the NB configuration, resulting in a higher influence on torque variation than the NB configuration.

These results can be explained by the different behaviour of the friction interface associated with NN and NB and by the actual stud bolt tension reached after the application of the controlled torque. In fact, the friction between washers and plates can affect the tension transmission, leading to lower bolts' axial forces: further investigation should consider the evaluation of the actual bolt tension to determine a proper correlation between μ and the effective axial forces of bolts.

5.3.3 Group 2 (G2) test results

Figures 5.9(a) and 5.9(a) show G2 tests (applied torque T3 and A3 fixed oscillations) results, for NN and NB configuration respectively, in terms of hysteresis cycles as force-displacement relationship, while Tab. 7 lists the registered $F_{act,st}$ and $F_{max,st}$ values as a function of the sliding frequency and their percentage difference ΔF. In both figures, the plot colours are used to highlight the increment in sliding frequency.

NN configuration exhibits a rectangular-shaped hysteresis cycle with an evident hardening effect due to the stick-slip mechanism, resulting in higher force values when reaching higher displacement amplitude, and confirming the overall behaviour registered during RI and G1 tests. During the tests, NN registers $F_{act,st}$ values averaging 5.56 kN with a coefficient of variation of 14%. Concerning the effects of the frequency increment, NN configuration registers $F_{act,st}$ higher values during the tests performed with higher sliding frequencies, with an average increment of 24% from 0.05 to 1.00 Hz.

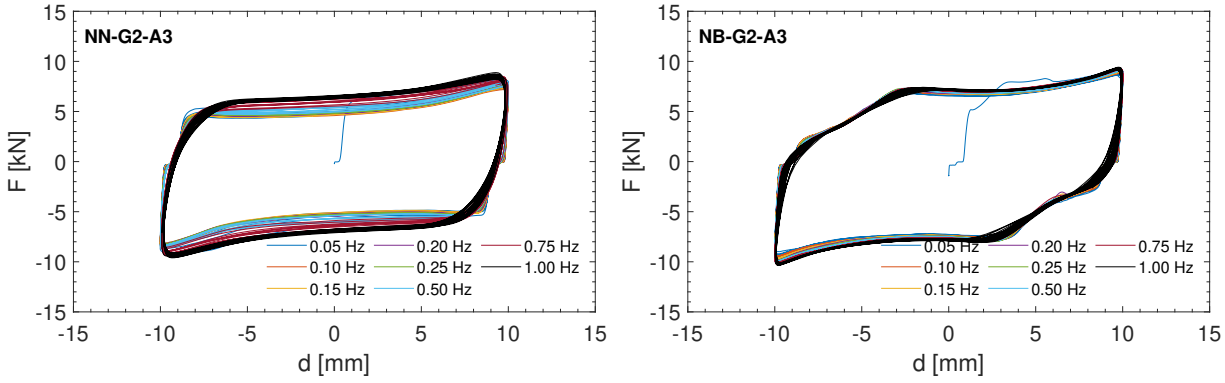

(a) (b)

FIGURE 5.9: G2 tests hysteresis cycles of a) NN and b) NB configurations.

TABLE 5.7: G1 test main results for NB configuration.

f [Hz]	NN			NB		
	$F_{act,st}$ [kN]	$F_{max,st}$ [kN]	ΔF [%]	$F_{act,st}$ [kN]	$F_{max,st}$ [kN]	ΔF [%]
0.05	5.28	8.93	41	6.93	9.37	26
0.10	4.83	8.36	42	6.93	9.57	28
0.15	4.97	8.49	41	6.99	9.82	29
0.20	5.04	8.42	40	6.98	9.95	30
0.25	5.40	8.34	35	7.59	9.98	24
0.50	5.62	8.68	35	7.49	10.05	25
0.75	6.41	9.36	31	7.42	10.26	28
1.00	6.97	9.55	27	7.57	10.33	27

NB configuration exhibits a rectangular-shaped hysteresis cycle with an evident hardening effect due to the stick-slip mechanism and a pinching effect when reversing the motion, resulting in higher force values when reaching higher displacement amplitude, differently from the overall behaviour registered during RI and G1 tests. This difference is caused by some damage experienced by the prototype stud bolts connected to the experimental setup guide at the end of the experimental campaign due to the high number of performed tests. In any case, a higher steel quality for stud bolts is suggested for further investigations.

During the tests, NB registers $F_{act,st}$ values averaging 7.24 kN with a coefficient of variation of 4%. Concerning the effects of the frequency increment, NB configuration registers slightly higher values during the tests performed with higher sliding frequencies, with an average increment of 8% from 0.05 to 1.00 Hz.

Figures 5.10(a) and 5.10(a) show G2 test results, for NN and NB configuration respectively, in terms of hysteresis cycles as a force-velocity relationship. Both configurations register an increment of the overall force values when incrementing the sliding frequency; however, it is worth noting that forces decrease when the sliding velocity increases. This behaviour, which is more evident for NN configuration, confirms the difference between $F_{act,st}$ and $F_{max,st}$ values registered during G1 tests, and it is usually associated with the stick-slip behaviour.

The hysteresis cycles in terms of force-velocity of Figure 5.10 are used to define a force-velocity relationship (*F-v fit* lines) that will be used to define the constitutive law of friction as a function of velocity in future research. More precisely, *F-v fit* lines have been determined as the mean of values $F_{act,st}$ and $F_{max,st}$ for each

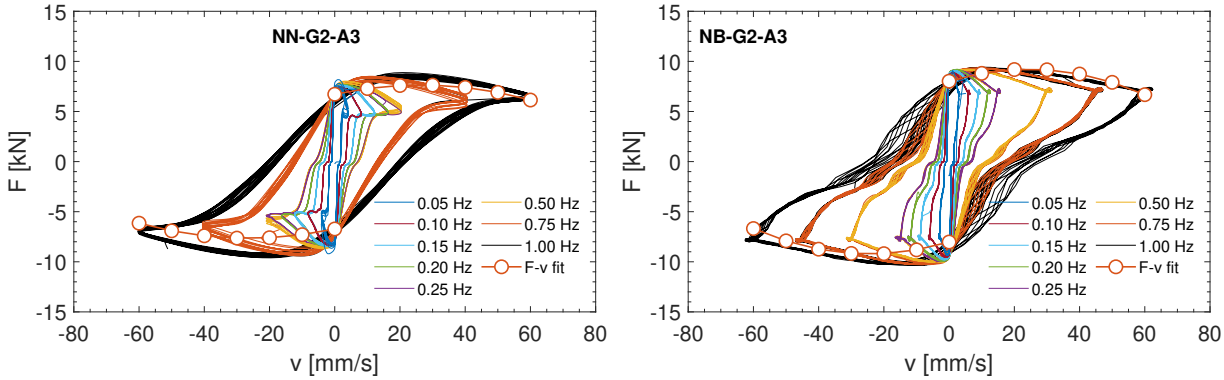

(a) (b)

FIGURE 5.10: G2 tests velocity hysteresis cycles of a) NN and b) NB configurations.

frequency value. Both NN and NB configurations show an increment of force values between 10 and 30 mm/s with a difference between minimum and maximum values that averages 20% and 28% respectively.

It is worth noting that during G2 tests NB configuration registered slightly higher values of forces than the NN configuration, contrasting the tribological campaign findings of Chapter 2. In fact, NN registered lower forces despite being associated with a higher friction coefficient μ than the NB configuration. However, this behaviour can be explained considering that G2 tests have been performed using T3 torque, and during G1-T3 tests the registered $F_{act,st}$ and $F_{max,st}$ values of NB configuration are slightly higher than NN configuration. Again, this behaviour highlights the importance of evaluating the actual stud bolt tension, regardless of the application of a controlled torque, which can be affected by friction among the washers and the plates.

5.3.4 Stud bolts preload measurement investigation

The results of the experimental campaign presented above highlight the importance of the actual stud bolts' tension evaluation. To achieve that, a measurement investigation has been conducted by applying to each stud bolt four strain gauges with a resistance of 120 Ω in a full bridge configuration as shown in the specimen of Figure 5.11.

FIGURE 5.11: Stud bolt with strain gauges installed.

The measurement system of the stud bolt tension has been calibrated applying several torque values to a stud bolt connecting two steel plates and registering the corresponding preload F_P developed by the bolts. The calibration has been performed using a FERVI 0803/S210 manual torque wrench, five different torque steps from 50 to 150 Nm and applying two different torque increment methodologies. In the first one, the increment of torque was applied without unloading the connection at each new step, while in the second

one, the increment of torque was applied by unloading the connection at each step. Figure 5.12 shows the calibration results in terms of torque and bolts preload relationship. When the torque increment is applied without unloading the connection at each new step, the recorded F_P values roughly follow the expected linear increment and the torque coefficient (CEN, 2018b) k_{eq} averages 0.32 with a coefficient of variation equal to 17%. On the contrary, when the torque increment is applied unloading the connection at each new step, the recorded F_P values better follow the expected linear increment and the torque coefficient (CEN, 2018b) k_{eq} averages 0.20 with a coefficient of variation equal to 6%. In addition, much higher F_P values are obtained by unloading the connection before the torque increment application.

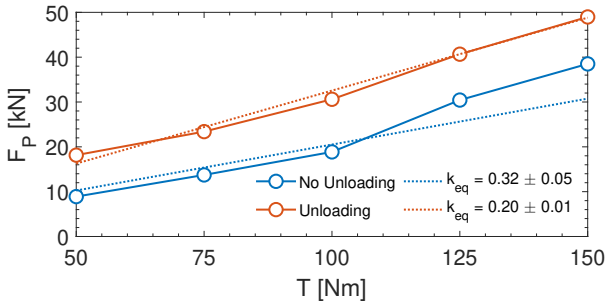

FIGURE 5.12: Strain gauges calibration results.

The results of the calibration suggest that to develop a more predictable bolt tension during the tests, the application of the torque increment should be executed by unloading the bolted connection at each increment step.

Additional G1 tests have been performed at the frequency of 0.05 Hz, torque 100 Nm and using the instrumented stud bolts. The results are reported in Figure 5.13 in terms of recorded hysteresis cycles and developed bolts preload F_P for both NN and NB configurations.

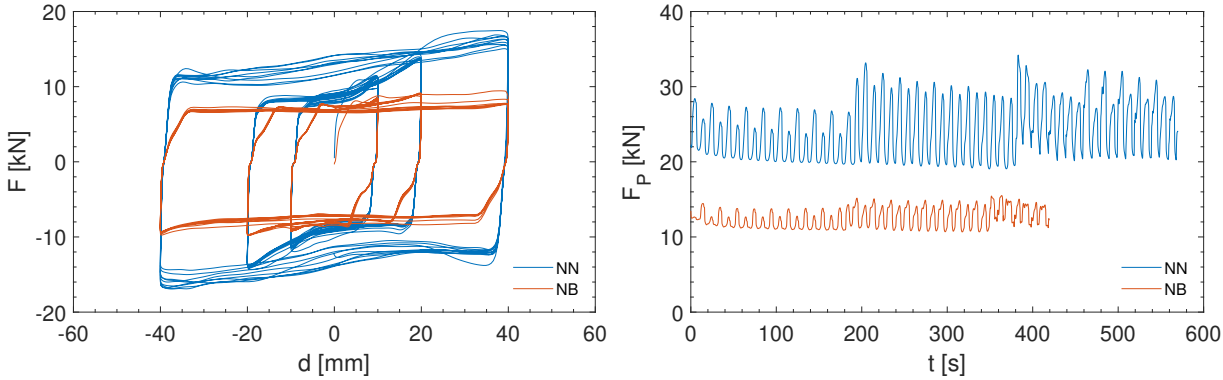

(a) (b)

FIGURE 5.13: Additional test results with instrumented stud bolts in terms of a) hysteresis cycles and b) bolts load of NN and NB configurations.

The recorded hysteresis cycles of Figure 5.13(a) have a similar shape to the ones previously recorded; however, while NB configuration reaches force values similar to the previous ones, NN configuration registers force values higher than the previous ones. This difference can be explained by the F_P values developed by NN during this test, which average 24.18 kN, and almost doubles the F_P values developed by NB configuration, which averages 12.53 kN. Considering the recorded sliding forces and bolts' preload forces, the

friction coefficients associated with NN and NB configuration are estimated to equal 0.63 and 0.52 respectively. These results do not significantly differ from the findings of the previous tribological campaign of Chapter 4.

The adopted torque technique did not produce the same F_P values in the investigated configurations, and this difference can be responsible for the peculiar results of the experimental campaign. In addition to that, it is worth noting that during the tests F_P values (see Figure 5.13(b)) are not constant, but they oscillate following the oscillations of the imposed displacements. Unfortunately, after 420 seconds of NB configuration testing, the strain gauges of the bolts broke because the sliding motion of the plates around the stud bolts cut the strain gauge wires. This measurement system was revealed to be not reliable enough and a better solution has to be sought for future tests.

5.4 Conclusive remarks

The present Chapter shows the results of the preliminary tests performed on the prototype of a novel friction damper with two different mating interfaces (NN and NB configurations). The main findings in terms of transition time, hysteresis cycle steadiness and effects of torque and sliding frequency increment are listed below:

- NN registers higher t_{tr} and cv_F values than NB configuration, both highlighting the necessity of a proper running-in stage (RI) to develop a steadier hysteresis cycle during the real use conditions.
- Both NN and NB configurations registered lower cv_F values after RI tests, especially when subjected to higher stud bolts' torque values, highlighting the improvement in terms of steadiness of hysteresis cycles after the RI.
- NN registered similar force values with the increment of stud bolts' torque value and lower force values with the increment of the sliding frequency, showing a coefficient of friction highly influenced by both bolts preload and sliding velocity. On the contrary, NB registered higher force values with the increment of the stud bolts torque value and similar force values with the increment of the sliding frequency, showing a coefficient of friction modestly influenced by both bolts preload and sliding velocity.
- The measurement investigation of the bolt tension highlighted the need for a proper torquing technique to develop a reliable stud bolt preload and the need for additional sensors, preferably embedded into the stud bolt, to measure and control the actual bolt preload.

The results of the preliminary tests allow the assessment of the selected NN and NB configurations in terms of stable and reliable hysteresis cycles for the BRFD in development, which is the main goal of this research program. Additionally, the experimental findings allow the development of preliminary numerical constitutive models to define the overall behaviour of the proposed device. Since NN and NB configurations have shown different tribological behaviours, different constitutive models will be implemented for a sound numerical calibration and prevision tool development of both cases.

The performed tests have successfully highlighted a very promising behaviour of the BRFD thanks to both good damping capacity and reliability of the hysteresis cycles, especially for the NB configuration, in here

considered the most interesting. In fact, despite the development of lower friction coefficient values than NN, the steadiness of the hysteresis cycles is considered by the authors more reliable and then preferable.

The following Chapter focuses on the investigation of BRFD bidirectional behaviour, performing additional experimental tests considering both displacement components. Moreover, several sensors are installed to detect the real stud bolts' axial tension and assess the effective influence of the bolts' preload.

References

CEN (2015a). *High-strength structural bolting assemblies for preloading - Part 1: General requirements (UNI EN 14399-1:2015)*. Norma per classe e diametro bulloni.

CEN (2015b). *Hot rolled products of structural steels - Part 1: General technical delivery conditions (UNI EN 10025-1:2005)*.

CEN (2018a). *Anti-seismic devices (UNI EN 15129:2018)*.

CEN (2018b). *Execution of steel structures and aluminium structures - Part 2: Technical requirements for steel structures (UNI EN 1090-2:2018)*.

Chanchi Golondrino, Jose Christian, Gregory Anthony MacRae, James Geoffrey Chase, Geoffrey William Rodgers, and George Charles Clifton (2020). "Seismic behaviour of symmetric friction connections for steel buildings". In: *Engineering Structures* 224. DOI: 10.1016/j.engstruct.2020.111200.

D'Agostini, Sara (2023). "Adeguamento sismico di uno stabilimento produttivo prefabbricato in c.a. mediante dissipatori innovativi DoubleDamp: zona cantina". University of Ferrara.

De Serra, Alessandra (2023). "Adeguamento sismico di uno stabilimento produttivo prefabbricato in c.a. mediante dissipatori innovativi DoubleDamp: zona produzione". University of Ferrara.

Ferrante Cavallaro, Giovanni, Massimo Latour, Antonella Bianca Francavilla, Vincenzo Piluso, and Gianvittorio Rizzano (2018). "Standardised friction damper bolt assemblies time-related relaxation and installed tension variability". In: *Journal of Constructional Steel Research* 141, pp. 145–155. DOI: 10.1016/j.jcsr.2017.10.029.

Grossi, Eleonora, Alessandra Aprile, and Matteo Zerbin (2023a). "Tribological investigation on metal mating surfaces to explore real use conditions of a novel friction damper for seismic applications". In: *Engineering Structures* 278, p. 115473. ISSN: 01410296. DOI: 10.1016/j.engstruct.2022.115473.

Grossi, Eleonora, Enrico Baroni, Alessandra Aprile, Annalisa Fortini, Matteo Zerbin, and Mattia Merlin (2023b). "Tribological Behavior of Structural Steel with Different Surface Finishing and Treatments for a Novel Seismic Damper". In: *Coatings* 13 (1), p. 135. DOI: 10.3390/coatings13010135.

Latour, M., V. Piluso, and G. Rizzano (2014). "Experimental analysis on friction materials for supplemental damping devices". In: *Construction and Building Materials* 65. DOI: 10.1016/j.conbuildmat.2014.04.092.

MathWorks (2022). *MATLAB*.

Morgen, Brian G. and Yahya C. Kurama (2009). "Characterization of two friction interfaces for use in seismic damper applications". In: *Materials and Structures* 42 (1). DOI: 10.1617/s11527-008-9365-y.

6
Bidirectional mechanical tests

6.1 Experimental setup and testing protocol

The mechanical tests were conducted at the Heavy & Light Structure Laboratory at the University of Bristol (UK). Figure 6.1(a) shows the experimental setup and the primary sensors. Two Instron servo-hydraulic testing machines with 25 kN load capacity were tuned to activate the two displacement components of the BRFD. To measure the preloading axial force, the M16 stud bolts were instrumented by installing BTMC bolt strain gauges (Tokyo Measuring Instruments Laboratory Co., Ltd., Tokyo, Japan) in a 2 mm diameter hole drilled in the centre of the threaded rebars using the gun-drilling technology (Figure 6.1(b)). Two horizontal LVDTs with a maximum displacement of 100 mm were placed near the BRFD-actuators connection element to double-check the displacements imposed by the actuators. To check the vertical displacement of the device during the tests, two vertical LVDTs with a maximum displacement of 10 mm were placed under the BRFD prototype. To investigate the effects of the temperature increment on the BRFD behaviour, type-K thermocouples were placed close to the friction interface of the prototype. The tested BRFD prototype coincides with the one described in §5.1.

Before performing the tests, the instrumented stud bolts were calibrated using an Instron Machine with a maximum load of 250 kN (Figure 6.1(c)). Specifically, each stud bolt was subjected to linear quasi-static tension to correlate the microstrain measured with the strain gauges with the axial force recorded by an extensometer connected to the testing machine. This procedure was needed to double-check the torque the manual torque wrench imposed.

G1 and G2 tests have been performed separately in longitudinal (x) and transversal (y) directions. Two different toque levels have been applied, 50 Nm (T1) and 75 Nm (T2), which correspond to an axial tension of 20 kN and 35 kN respectively.

Given the peculiar behaviour of the presented BRFD, the testing methodology was defined by combining the EN 15129 guidelines (CEN, 2018a) for friction dampers with the ones for friction isolators and the findings of the previous Chapter 5 and the ones of the works of Furinghetti et al. (2019) and Pavese et al. (2018) concerning the bidirectional characterisation of friction-based isolators. Three test groups have been defined: Group 1 (G1) tests aimed at assessing the BRFD behaviour in a monodirectional real-use condition; Group 2 (G2) tests aimed at determining the relationship between the coefficient of friction and the velocity to calibrate a numerical model; a final Group 3 (G3) aimed at assessing the BRFD behaviour in a bidirectional real-use condition. More precisely, G1 tests have been performed using a sinusoidal displacement law incrementing the displacement amplitude every ten cycles (±10, ±20, ±40 mm) and

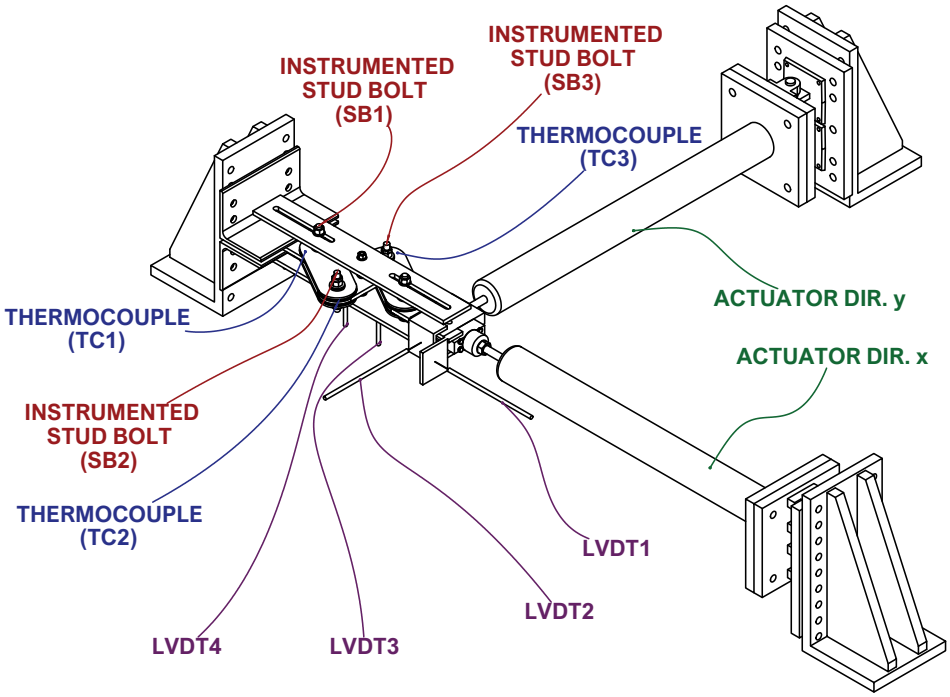

(a)

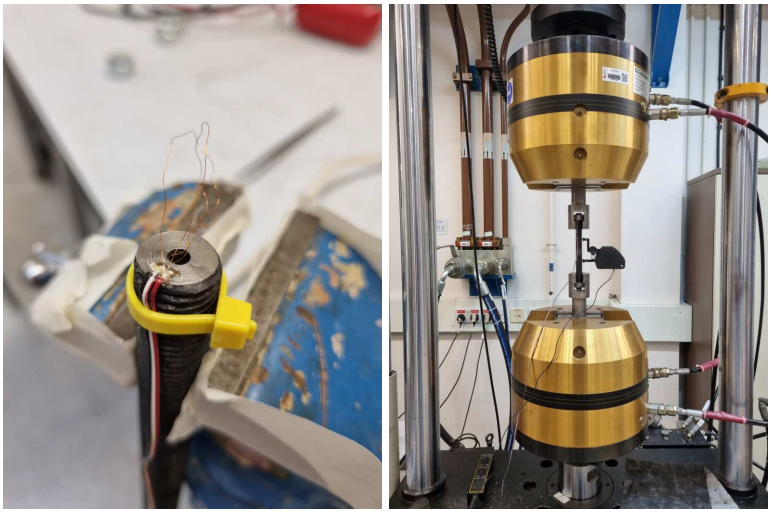

(b) (c)

FIGURE 6.1: Experimental setup a) scheme and adopted sensors, b) detail and c) calibration of the instrumented stud bolt.

investigating four different frequencies (0.05 Hz, 0.50 Hz, 1.00 Hz and 2.00 Hz, respectively tagged as F1, F2, F3 and F4). G2 tests have been performed using a triangular displacement law with fixed ±20 mm displacement amplitude and incrementing the frequency every five cycles from 0.05 Hz to 2.00 Hz in six steps. For G3 tests two 2D waveforms were selected for the mechanical testing: (i) a cloverleaf and (ii) a spiral orbit, shown in Figures 6.2(a) and 6.2(c), respectively. To assess BRFD sensitivity to amplitude and frequency, the 2D waveforms were applied with crescent amplitude (from ±10 to ±40 mm)

and with four different frequencies. Given the different analytical formulations of the waveforms, the adopted frequencies were selected to reproduce similar values of sliding velocities. Figures 6.2(b) and 6.2(d) show an example of the adopted waveforms for the cloverleaf and spiral orbit, respectively.

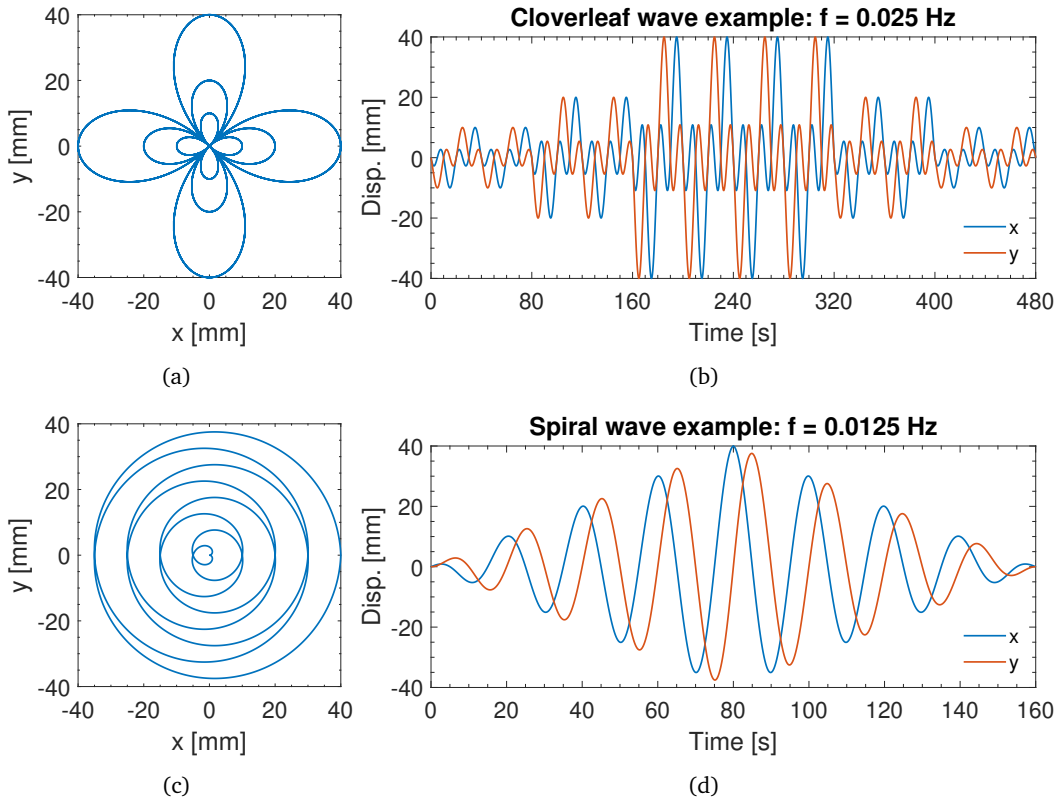

FIGURE 6.2: Adopted bidirectional curvilinear orbits: cloverleaf (a) orbit and (b) waveform, and spiral (c) orbit and (d) 2D waveform.

To increase the steadiness of the overall BRFD behaviour, a 300 s running-in (RI) has been performed in both longitudinal and transversal directions before the actual tests and using a sinusoidal displacement law at a frequency of 0.50 Hz and fixed ±20 mm displacement amplitude. Table 6.1 lists the information on the testing protocols adopted for the whole experimental campaign.

One of the main goals of the present work is the assessment of the influence of different friction pad configurations and different bolt torque levels on the overall behaviour of the BRFD. Consequently, two different configurations were tested as in the previous Chapter 5: (i) NN, i.e. nickelled steel vs nickelled steel friction pads, and (ii) NB, i.e. nickelled steel vs bronze (CuSn1249) friction pads. Both configurations were tested according to protocols of Tab. 1 with 50 Nm torque (T1). Subsequently, the NB configuration was also tested with a 75 Nm torque (T2), as it was identified as the most stable and worthy of further investigation.

Because of some experimental setup limits, the component in the y direction of the BRFD was partially activated. The deformed shape of Figure 3.2(a) is obtainable by fixing both ends of the device, but the experimental setup required hinged connections to the actuators for the safety of the equipment. Consequently, the end of the BRFD associated with the DA1 of Figure 3.2(a) was fixed, while the one associated with the DA4 of Figure 3.2(a) was hinged with two spherical hinges connected to the two actuators. This

TABLE 6.1: Test protocols of the bidirectional mechanical tests.

Test Group Code	Frequency	Amplitude	Max velocity	Total duration	Signal waveform
RI	0.50 Hz	± 20 mm	40 mm/s	300 s	Sinusoidal
G1-F1	0.05 Hz (F1)	± 10 mm - 200 s ± 20 mm - 200 s ± 40 mm - 200 s	2 mm/s 4 mm/s 8 mm/s	600 s	Sinusoidal
G1-F2	0.50 Hz (F2)	± 10 mm - 20 s ± 20 mm - 20 s ± 40 mm - 20 s	20 mm/s 40 mm/s 80 mm/s	60 s	Sinusoidal
G1-F3	1.00 Hz (F3)	± 10 mm - 10 s ± 20 mm - 10 s ± 40 mm - 10 s	40 mm/s 80 mm/s 160 mm/s	30 s	Sinusoidal
G1-F4	2.00 Hz (F4)	± 10 mm - 5 s ± 20 mm - 5 s ± 40 mm - 5 s	80 mm/s 160 mm/s 320 mm/s	15 s	Sinusoidal
G2	0.05 Hz - 100 s 0.10 Hz - 50 s 0.25 Hz - 20 s 0.50 Hz - 10 s 0.75 Hz - 6.67 s 1.00 Hz - 5 s 1.50 Hz - 3.33 s 2.00 Hz - 2.50 s	± 20 mm	4 mm/s 8 mm/s 20 mm/s 40 mm/s 60 mm/s 80 mm/s 120 mm/s 160 mm/s	200 s	Triangular
G3-F1c	0.025 Hz (F1c)	± 40 mm	11 mm/s	480 s	Cloverleaf
G3-F2c	0.25 Hz (F2c)	± 40 mm	110 mm/s	48 s	Cloverleaf
G3-F3c	0.50 Hz (F3c)	± 40 mm	221 mm/s	24 s	Cloverleaf
G3-F4c	1.00 Hz (F4c)	± 40 mm	441 mm/s	12 s	Cloverleaf
G3-F1s	0.0125 Hz (F1s)	± 40 mm	12 mm/s	160 s	Spiral
G3-F2s	0.125 Hz (F2s)	± 40 mm	118 mm/s	16 s	Spiral
G3-F3s	0.25 Hz (F3s)	± 40 mm	236 mm/s	8 s	Spiral
G3-F4s	0.50 Hz (F4s)	± 40 mm	472 mm/s	4 s	Spiral

resulted in a slight change of the static scheme associated with the component in the y direction of the BRFD presented in §3.2.2, which prevented the activation of the DA4. For this reason, only the stud bolts of DA1, DA2 and DA3 were instrumented and labelled as, respectively, SB1, SB2 and SB3, with SB1 longer than SB2 and SB3. As such, results must be read considering a transversal activation of about 50% of the maximum possible.

6.1.1 Parameters for the selection of the better-performing configuration

The better-performing configuration among NN and NB was chosen considering the shape, steadiness, and repeatability of the hysteresis cycles. To evaluate these characteristics, the following entities were computed: activation and maximum forces, F_{act} and F_{max} respectively, equivalent damping coefficient $\xi_{eq,hyst}$, stud bolts axial load loss ΔF_P, and dynamic friction coefficient μ.

The activation force F_{act} was defined as the average force at zero displacement, while the maximum force F_{max} was defined as the average force at maximum displacement (see Figure 6.3). The difference between

F_{max} and F_{act} is associated with the possible hardening effect due to the stick-slip mechanism: the more significant this difference, the more emphasised the stick-slip mechanism.

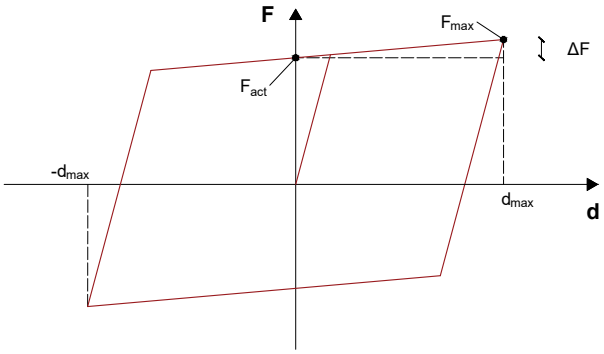

FIGURE 6.3: Computational scheme of F_{max} and F_{act}.

The equivalent damping coefficient $\xi_{eq,hyst}$ was computed using the Jacobsen (1965) formulation:

$$\xi_{eq,hyst} = \frac{EDC}{2\pi d_{max} F_{max}} \tag{6.1}$$

with *EDC* representing the energy dissipated per cycle and d_{max} the reached maximum displacement.

The stud bolts axial load loss ΔF_P was computed as the difference between the stud bolt axial tension at the end and the beginning of each test.

The evaluation of the dynamic friction coefficient μ in a friction device is extremely important for its experimental qualification and numerical implementation. In this work, μ has been computed using two different approaches: the first one uses analytical relationships, and the second one uses the dissipated energy per cycle (*EDC*), according to the standards EN 15129 (CEN, 2018a). These two approaches are then compared to assess the analytic model developed in §3.2. Furthermore, since the BRFD is a rotational friction damper, the evaluation of the friction coefficient can be computed referring to the rotational mechanism of the friction interface and the overall BRFD behaviour.

Under the hypothesis of uniform contact, the total sliding moment M_s can be written by combining Eqs. 3.1 and 3.2 as follows:

$$M_s = M_{s,i} n_i = n_i \int_{\rho=R_i}^{R_e} \int_{\theta=0}^{2\pi} \rho^2 \frac{\mu_r F_P}{\pi \left({R_e}^2 - {R_i}^2\right)} d\rho\, d\theta = n_i \mu_r F_P \frac{2}{3} \frac{{R_e}^3 - {R_i}^3}{{R_e}^2 - {R_i}^2} = n_i \mu_r F_P r_{eq} \tag{6.2}$$

where, $M_{s,i}$ is the sliding moment of a single friction interface, n_i is the number of friction interface in each dissipative area, μ_r is the friction coefficient of the friction interface associated with the rotational mechanism, F_P is the stud bolt axial load, R_e and R_i are the outer and inner dissipative area radius, while ρ and θ are radial and angular coordinates respectively. The geometrical ratio between R_e and R_i is simplified using the equivalent radius r_{eq}.

For the BRFD configuration in the experimental setup, the activation forces in x and y directions, $F_{act,x}$ and $F_{act,y}$ respectively, are computed as:

$$F_{act,x} = \frac{2M_s}{l_1}; \qquad F_{act,y} = \frac{M_s}{\sqrt{3}l_1 + l_2} \tag{6.3}$$

where l_1 represents the distance between the stud bolts, and l_2 is an additional distance to take into consideration the connection point of the transversal actuator (see Figure 6.4).

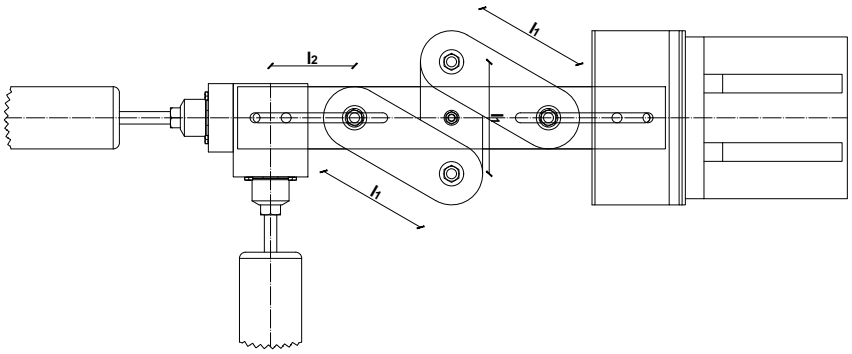

FIGURE 6.4: BRFD bolts distance scheme inside the experimental setup.

The values of $\mu_{r,an}$ are computed by joining the Eqs. 6.2 and 6.3:

$$\mu_{r,an,x} = \frac{M_s}{n_i F_P r_{eq}} = \frac{F_{act,x} l_1}{2n_i F_P r_{eq}}; \qquad \mu_{r,an,y} = \frac{M_s}{n_i F_P r_{eq}} = \frac{F_{act,y}\left(\sqrt{3}l_1 + l_2\right)}{n_i F_P r_{eq}} \tag{6.4}$$

The overall behaviour of the BRFD is simplified as a flat slider that resemble a friction isolation system with one friction interface and subjected to a vertical load F_P; Eq. 6.3 can be rewritten as follows:

$$F_{act,x} = \mu_{l,an,x} F_P; \qquad F_{act,y} = \mu_{l,an,y} F_P \tag{6.5}$$

where $\mu_{l,an,x}$ and $\mu_{l,an,y}$ are the friction coefficients associated with the overall BRFD linear behaviour along, respectively, the longitudinal (x) and transversal (y) directions. The values of $\mu_{l,an}$ are computed by joining Eqs. 6.2, 6.3 and 6.5 and are describable as a function of $\mu_{r,an}$:

$$\mu_{l,an,x} = \frac{2n_i \mu_{r,an,x} r_{eq}}{l_1}; \qquad \mu_{l,an,y} = \frac{n_i \mu_{r,an,y} r_{eq}}{\sqrt{3}l_1 + l_2} \tag{6.6}$$

The formulation of EN 15129 (CEN, 2018a), which refers to friction isolation systems, has been successfully adopted in several investigations (Furinghetti et al., 2019; Pavese et al., 2018) to estimate the friction coefficient of the system by computing the energy dissipated in terms of force-displacement hysteresis cycles $EDC_{F,d}$. Adapting this formulation to the BRFD linear overall behaviour, the linear friction coefficient is computed using Eq. 6.7.

$$\mu_{l,EDC} = \frac{EDC_{F,d}}{4d_{max} F_P} \tag{6.7}$$

The same approach is adopted to compute the friction coefficient associated with the rotational mechanism of the friction interface by evaluating the energy dissipated in terms of moment-rotation hysteresis cycles $EDC_{M,\theta}$:

$$\mu_{r,EDC} = \frac{EDC_{M,\theta}}{4\theta_{max} n_i F_P r_{eq}} \tag{6.8}$$

where θ_{max} is the maximum rotation reached during the hysteresis cycle.

It is worth noting that because of the nature of the BRFD, the evaluation of the rotational coefficient of friction μ_r in longitudinal and transversal directions is expected to show similar values between the two directions. In fact, μ_r is strictly associated with the friction interface properties of the device, which is the same in both directions. On the contrary, the evaluation of the linear coefficient of friction μ_l in longitudinal and transversal directions is expected to show different values between the two directions. In fact, μ_l is strictly associated with the overall BRFD behaviour, which differs for longitudinal and transversal directions.

6.2 Results and discussions

The experimental results of the calibration of the instrumented stud bolts, RI, G1, G2 and G3 tests are here presented using Matlab as post-processing software (MathWorks, 2022). The computational approach adopted to identify the transition time t_{tr} during the RI tests coincides with the one adopted in §5.3. More precisely, for the RI tests activation and maximum forces are computed as mean of all the performed cycles (F_{act} and F_{max}, respectively) and as a mean of the steady behaviour after the transition time ($F_{act,st}$ and $F_{max,st}$, respectively). This difference is to highlight the importance of running-in stages in stabilise the behaviour of a friction interface in a FD. For the following G1, G2 and G3 tests, activation and maximum forces are only computed as mean of all the performed cycles (F_{act} and F_{max}, respectively) because the steady behaviour is considered reached at the first cycle.

6.2.1 Calibration of the instrumented stud bolts

Figure 6.5(a) shows the relationship between the axial force F_P measured by the testing machine and the strain ε measured by the strain gauges as the mean of three repetitions. The three instrumented stud bolts show a similar behaviour, with a F_P/ε ratio that averages 29.72 kN. Consequently, independently of the length of the stud bolt, SB1, SB2 and SB3 are expected to register similar tension values in the dissipative areas.

Figures 6.5(b) and 6.5(c) show the relationship between F_P and torque T for the instrumented stud bolts when installed within the BRFD in NN and NB configuration, respectively. The results are reported as the mean of three different measures while estimating a k-factor (k_{eq}) (CEN, 2018b) by considering the tensile stress area of the stud bolts. In NN configuration (Figure 6.5(b)), SB1 registers the smaller k_{eq} value of 0.17, while SB2 and SB3 behave similarly registering a k_{eq} value of 0.20. In NB configuration (Figure 6.5(c)), SB1 and SB2 behave similarly registering a k_{eq} value of 0.14, while SB3 behaves similarly registering the higher k_{eq} value of 0.20. Variations of k_{eq} are related to the friction between washers and plates and in this study they were controlled with a manual application of a proper lubricant layer.

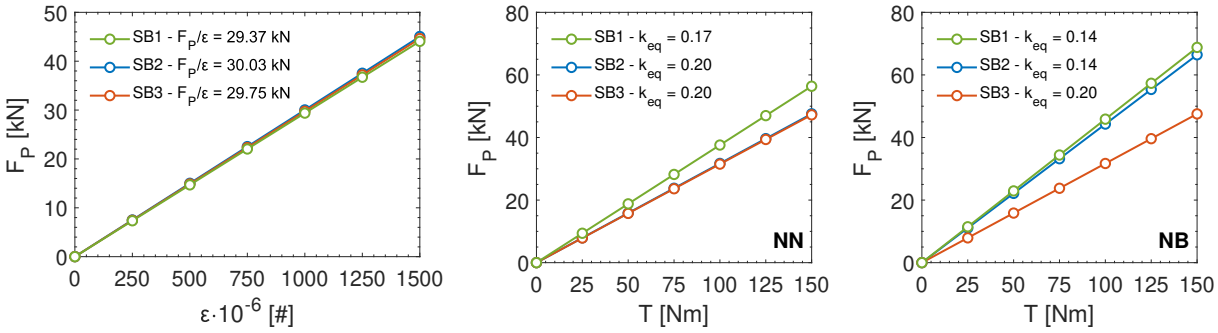

(a) (b) (c)

FIGURE 6.5: Relationship between stud bolt axial load and a) strain and torque for b) NN and c) NB configuration.

More generally, k_{eq} values decrease from NN to NB configuration, so that the stud bolt pre-stress of NB configuration is higher than NN configuration for a given torque value. This can be caused by the different materials chosen for the pads in the investigated configurations. While in the NN configuration, the friction interface is obtained by coupling two steel pads, the friction interface of the NB configuration is obtained by coupling a steel pad and a bronze pad. Since bronze is sensibly softer than steel, the adhesion between the coupling surfaces of the NB configuration reveals to be more efficient than the NN configuration.

6.2.2 Running-in (RI) test results

RI tests aim to develop a conformal contact between the sliding surfaces of the BRFD, reaching a stable behaviour. The findings of this section are useful to highlight the improvement of the BRFD in terms of steadiness after the execution of a running-in.

Figures 6.6(a) and 6.6(b) show RI test results, for NN and NB configuration respectively, in terms of hysteresis cycles as a force-displacement relationship. The difference between NN and NB hysteresis cycles is highly remarkable, both in terms of overall shape and values. NN has an initial rectangular-shaped hysteresis cycle with $F_{act,1}$ value of 6.93 kN in the x direction test and of 1.30 kN in the y direction test. Once the conformal contact between the sliding surfaces is properly developed, NN exhibits a rectangular-shaped hysteresis cycle with an evident hardening effect due to the stick-slip mechanism, with $F_{act,st}$ value of 7.15 kN in the x direction test and of 1.81 kN in the y direction test. NB has an initial rectangular-shaped hysteresis cycle with a slight hardening effect due to the stick-slip mechanism and $F_{act,1}$ value of 4.50 kN in the x direction test and of 0.63 kN in the y direction test. Once the conformal contact between the sliding surfaces is properly developed, NB maintains the rectangular-shaped hysteresis cycle with $F_{act,st}$ value of 2.10 kN in the x direction test and of 0.58 kN in the y direction test.

Figure 6.8 shows RI test results, for NN and NB configuration, in terms of force-time relationship. The orange line highlights the trend of $F_{act,i}$ values, and the green line highlights the trend of $F_{max,i}$ values. The difference between NN and NB both in terms of overall shape and values is here confirmed. During RI test in x direction, NN force first decreases rapidly from around 8 kN to 6 kN then increases slowly and stabilises around 8 kN, registering a transition time t_{tr} of 120 s (n_{st} equal 240), as represented in Figure 6.7(a). Similarly, during RI test in y direction, NN force increases rapidly from around 1 kN to 2 kN and

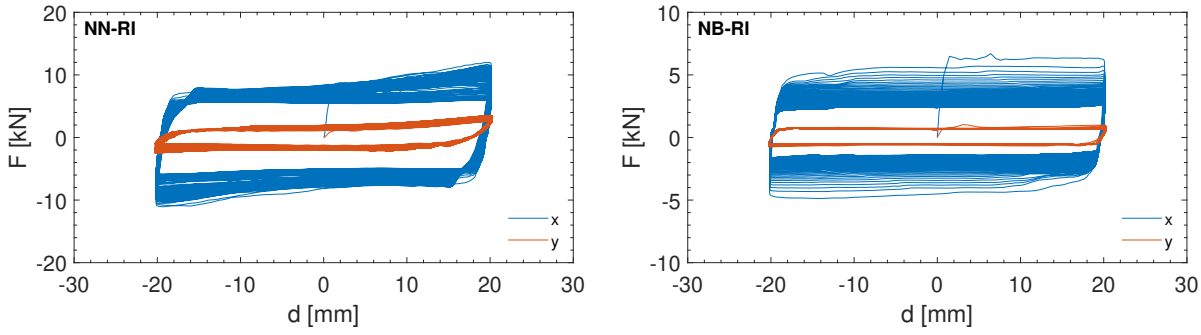

(a) (b)

FIGURE 6.6: RI tests hysteresis cycles in x and y directions of a) NN and b) NB configurations.

stabilises around 2 kN, registering a transition time t_{tr} of 26 s (n_{st} equal 52), as represented in Figure 6.7(b). During RI test in x direction, NB force decreases rapidly from around 6 kN to 2 kN and stabilises around 2 kN, registering a transition time t_{tr} of 72 s (n_{st} equal 144), as represented in Figure 6.7(c). On the contrary, during RI test in y direction, NB force increases rapidly to around 0.60 kN and quickly stabilises around 0.60 kN, registering a transition time t_{tr} of 14 s (n_{st} equal 28), as represented in Figure 6.7(d).

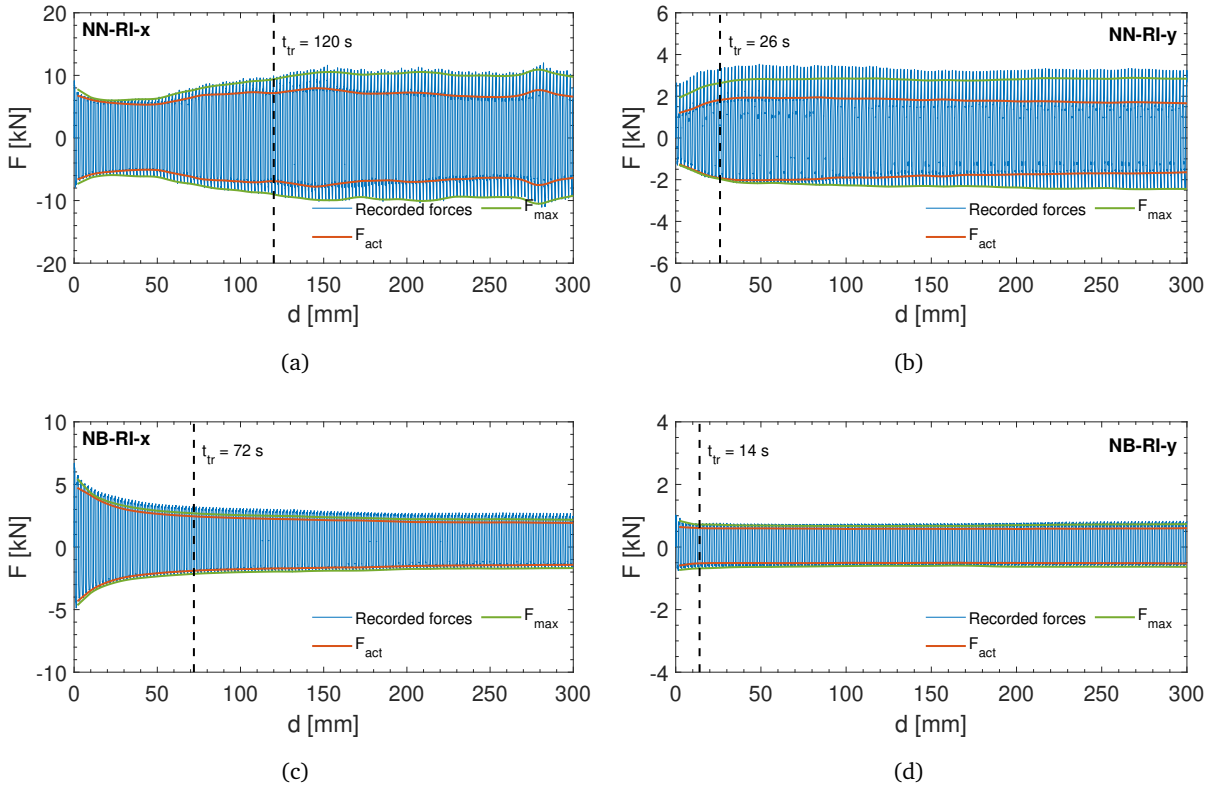

(a) (b)

(c) (d)

FIGURE 6.7: RI recorded forces of NN configuration for a) x and b) y direction tests and of NB configuration for c) x and d) y direction tests.

Table 6.2 lists the main results in terms of activation and maximum forces considering the first cycle ($F_{act,1}$ and $F_{max,1}$, respectively), the mean of the steady behaviour with its standard deviation ($F_{act,st}$ and $F_{max,st}$,

respectively), the mean of the total test duration with its standard deviation (F_{act} and F_{max}, respectively), and in terms of transition time t_{tr} with the corresponding number cycle t_{st}. As observed in the results of the preliminary mechanical tests of Chapter 5, the execution of the running-in significantly increment the steadiness of the hysteresis cycles, especially for the NB configuration. More precisely, NN coefficient of variations decreases from around 10% to the 6% in the x direction and from around 7% to 5% in the y direction. Similarly, NB coefficient of variations decreases from around 24% to the 7% in the x direction and from around 2% to 1% in the y direction.

TABLE 6.2: RI test activation and maximum forces.

Configuration	Test tag	$F_{act,1}$ [kN]	$F_{act,st}$ [kN]	F_{act} [kN]	$F_{max,1}$ [kN]	$F_{max,st}$ [kN]	F_{max} [kN]	t_{tr} [s]	n_{st}
NN	RI-x	6.93	7.15 ± 0.44	6.81 ± 0.71	8.51	10.22 ± 0.35	9.10 ± 1.60	120	240
	RI-y	1.30	1.81 ± 0.09	1.79 ± 0.13	1.97	2.82 ± 0.05	2.78 ± 0.16	26	52
NB	RI-x	4.50	2.10 ± 0.15	2.34 ± 0.56	5.79	2.34 ± 0.15	2.59 ± 0.58	72	144
	RI-y	0.63	0.59 ± 0.01	0.59 ± 0.01	0.89	0.69 ± 0.02	0.70 ± 0.03	10	20

Figure 6.8 shows RI test results, for NN and NB configuration, in terms of stud bolts axial tensions-displacement relationship, while Table 6.3 lists the main information in terms of average stud bolts axial tensions F_P, its coefficient of variation cv_{F_P} and stud bolts axial load loss ΔF_P for all the instrumented stud bolts. SB2 and SB3 register F_P values averaging 22 kN for the NN configuration and 20 kN for the NB configuration, while SB1 registers F_P values averaging 24 kN for the NN configuration and 26 kN for the NB configuration. It is worth to note that both configurations exhibits higher F_P values in correspondence of the working area are DA1 (associated with SB1); this difference may be caused by the small torque applied on the nuts of the alignment guide. Both configurations exhibits a moderate variation of the stud bolts axial tensions during the RI tests; however the in the NN configuration (see Figures 6.8(a) and 6.8(b)) this variation is more evident than in the NB configuration (see Figures 6.8(c) and 6.8(d)). Moreover, SB2 and SB3 exhibit a higher axial tension variation during the tests performed in the x direction than during the ones performed in the y direction. On the contrary, SB1 exhibits a higher axial tension variation during the tests performed in the y direction than during the ones performed in the x direction. This difference is caused by the different dissipative areas activated during the BRFD motion (see Figure 3.2(a)); during the tests performed in the x direction the working areas are DA2 and DA3 (associated with SB2 and SB3 respectively), while during the tests performed in the y direction the working area are DA1 (associated with SB1).

TABLE 6.3: RI test stud bolts axial tension and axial tension loss.

Configuration	Test tag	SB2&SB3			SB1		
		F_P [kN]	cv_{Fp}	Δ_{Fp}	F_P [kN]	cv_{Fp}	Δ_{Fp}
NN	RI-x	22.59	6.7%	14.9%	23.61	2.3%	5.9%
	RI-y	20.56	1.3%	3.5%	24.43	3.8%	8.7%
NB	RI-x	19.78	2.1%	4.9%	26.97	0.5%	1.7%
	RI-y	20.59	0.5%	1.1%	25.77	0.6%	2.2%

Concerning the coefficient of variation, SB2 and SB3 exhibit cv_{F_P} values averaging 4% and 1% for the NN and NB configurations respectively, while SB1 exhibit cv_{F_P} values averaging 3% and 1% for the NN

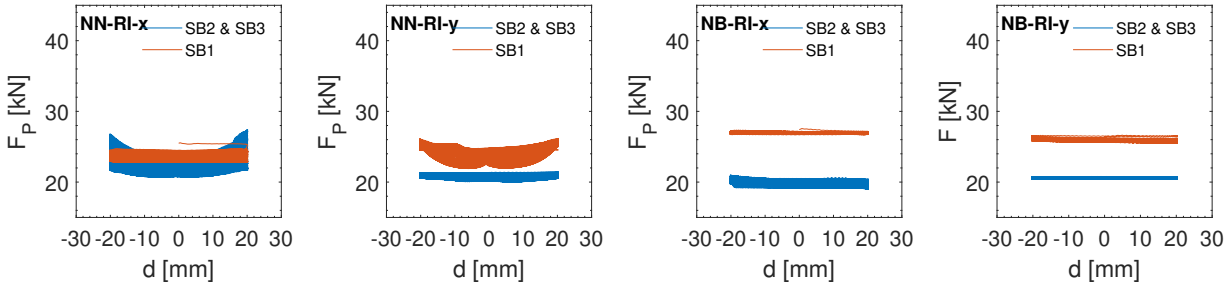

(a) (b) (c) (d)

FIGURE 6.8: RI recorded stud bolts axial tensions of NN configuration for a) x and b) y direction tests and of NB configuration for c) x and d) y direction tests.

and NB configurations respectively. Concerning the stud bolts axial load loss, SB2 and SB3 exhibit ΔF_P values averaging 9% and 3% for the NN and NB configurations respectively, while SB1 exhibit ΔF_P values averaging 7% and 2% for the NN and NB configurations respectively.

Table 6.4 lists the results of RI tests in terms of the temperature increment ΔT recorded in the dissipative areas DA1, DA2 and DA3 (see Figure 3.2(a)). As above observed for the stud bolts axial tension variation, DA2 and DA3 exhibit a higher ΔT increment during the tests performed in the x direction than during the ones performed in the y direction. On the contrary, DA1 exhibits a higher ΔT increment during the tests performed in the y direction than during the ones performed in the x direction. More precisely, DA2 and DA3 during the tests in the x directions exhibit ΔT values averaging 23.3°C and 4.1°C for the NN and NB configurations respectively, while during the tests in the y directions exhibit ΔT values averaging 1.1°C and 0.5°C for the NN and NB configurations respectively. On the contrary, DA1 during the tests in the x directions exhibits ΔT values averaging 2.2°C and 0.9°C for the NN and NB configurations respectively, while during the tests in the y directions exhibits ΔT values averaging 8.4°C and 4.7°C for the NN and NB. configurations respectively.

TABLE 6.4: RI test temperature variation.

Configuration	Test direction	$\Delta T_{DA2\&DA3}$ [°C]	ΔT_{DA1}[°C]
NN	x	23.3	2.2
	y	1.1	8.4
NB	x	4.1	0.9
	y	0.5	4.7

During the RI tests, the NB configuration exhibits a better-performing behaviour than the NN configuration, with overall steadier hysteresis cycles, lower influence of stud bolts axial tension loss and variation, and temperature increment.

6.2.3 Group 1 (G1) test results

G1 tests aim at assessing the BRFD behaviour in a real-use condition when subjected to monodirectional displacements. The findings of this section are useful to describe separately the two components (longitudinal x-direction and transversal y-direction) of the device.

6.2.3.1 T1 test results

Hysteresis cycles. Figures 6.9 and 6.10 show G1 test results, for NN and NB configuration respectively, in terms of hysteresis cycles as a force-displacement relationship for F1, F2, F3 and F4 sliding frequencies. NN and NB exhibits a similar steady overall behaviour after the RI tests, with NN registering higher force values, as expected by the higher COF values associated to the NN configuration in respect to the NB configuration.

NN configuration exhibits hysteresis cycle in the x direction (blue lines) with a mainly rectangular shape and an evident hardening effect caused by a stick-slip mechanism in correspondence with the reverse motion point, especially for more significant displacements. The hysteresis cycle shapes in the y direction (orange lines) exhibits a similar behaviour, but with a stick-slip mechanism slightly more evident.

NB configuration exhibits hysteresis cycle in the x direction (blue lines) with a mainly rectangular shape and with a slight hardening effect caused by a stick-slip mechanism in correspondence with the reverse motion point, especially for more significant displacements. The hysteresis cycle shapes in the y direction (orange lines) exhibits a similar behaviour, but with a stick-slip mechanism slightly more evident.

The fact that the hysteresis cycle for NN and NB configurations does not differ with signal frequency is a promising behaviour because it ensures that the device's behaviour during an earthquake remains consistent, regardless of the ground motion frequency content. Moreover, the similar behaviour exhibited for both NN and NB in the x and y directions highlights the stability of the BRFD. Finally, it is worth noting that the recorded hysteresis cycles of NB configuration exhibit a more rectangular and steadier shape, usually associated with a more effective damping capability, despite the lower values of recorded forces.

Activation and maximum forces. The activation forces F_{act} and the maximum forces F_{max} are computed according to §6.1.1; Table 6.5 lists the average values with the standard deviation for NN and NB configuration for the x and y directions. For NN, F_{act} values average 10.38 kN in the x direction and 1.89 kN in the y direction, while F_{max} values average 13.25 kN in the x direction and 2.76 kN in the y direction. For NB, F_{act} values average 3.52 kN in the x direction and 0.62 kN in the y direction, while F_{max} values average 3.83 kN in the x direction and 1.02 kN in the y direction.

TABLE 6.5: G1-T1 test activation and maximum forces.

Configuration	Test tag	$F_{act,st,x}$ [kN]	$F_{act,st,y}$ [kN]	$F_{max,st,x}$ [kN]	$F_{max,st,y}$ [kN]
NN	G1-T1-F1	10.00 ± 1.11	1.52 ± 0.32	11.69 ± 1.52	2.36 ± 0.85
	G1-T1-F2	12.09 ± 0.50	1.85 ± 0.32	14.78 ± 1.49	2.67 ± 1.02
	G1-T1-F3	10.15 ± 1.43	1.90 ± 0.36	13.39 ± 2.09	2.88 ± 1.07
	G1-T1-F4	9.29 ± 1.10	2.30 ± 0.54	13.15 ± 1.76	3.12 ± 0.93
NB	G1-T1-F1	5.18 ± 0.55	0.63 ± 0.03	5.08 ± 0.33	1.05 ± 0.45
	G1-T1-F2	3.22 ± 0.16	0.55 ± 0.03	3.68 ± 0.16	0.94 ± 0.42
	G1-T1-F3	2.65 ± 0.08	0.57 ± 0.04	3.11 ± 0.12	0.99 ± 0.31
	G1-T1-F4	3.04 ± 0.14	0.72 ± 0.06	3.43 ± 0.26	1.11 ± 0.3

Both configurations exhibit differences between x and y directions, with a percentage difference that averages 82% for both NN and NB configurations. This difference is higher (almost twice as large as expected) than the ideal 42% predicted by the analytical model presented in §3.2, and it is caused by the experimental

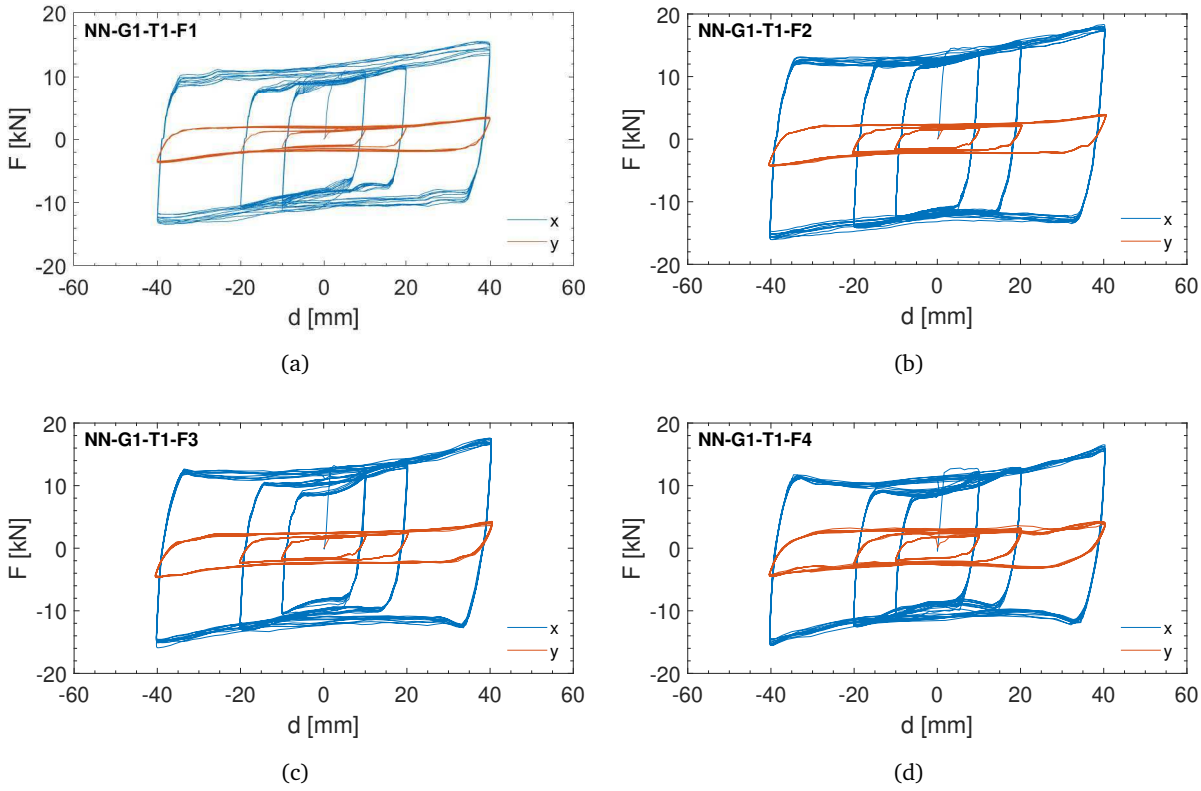

FIGURE 6.9: NN-T1-G1 test hysteresis cycles in x and y directions: a) F1, b) F2, c) F3 and d) F4 test protocols.

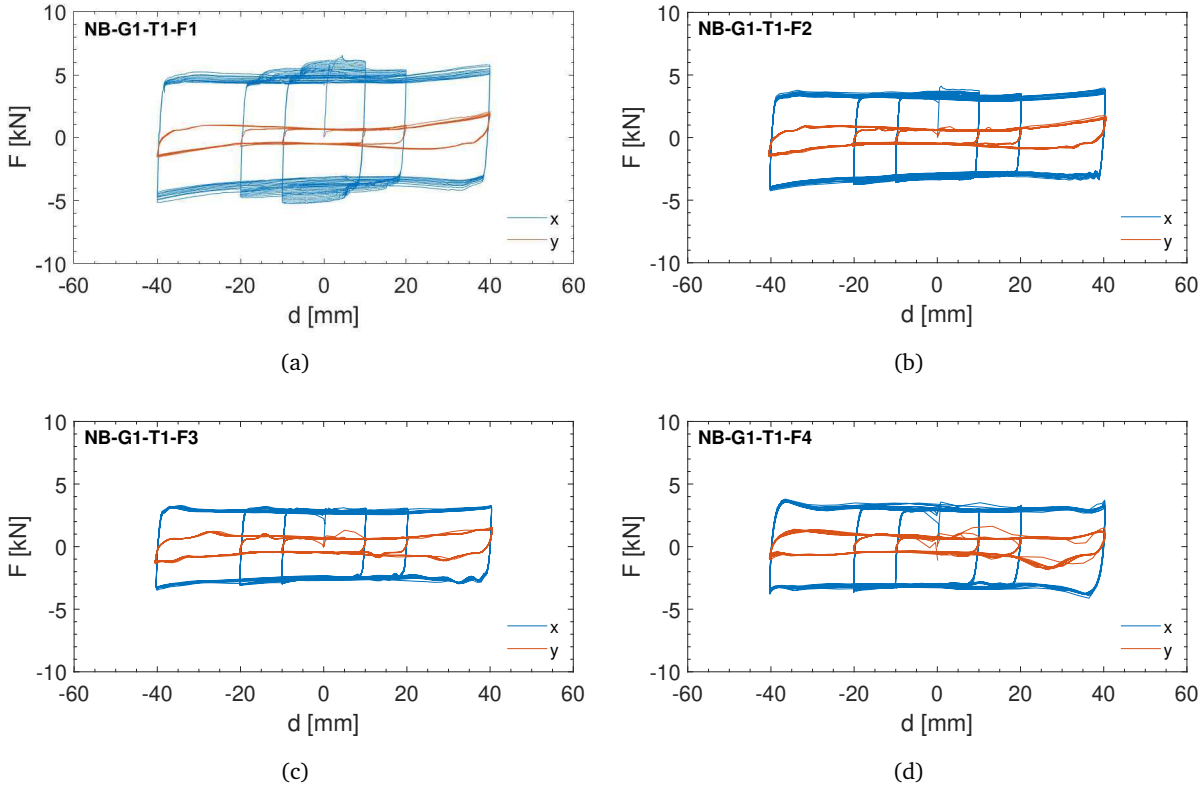

FIGURE 6.10: NB-T1-G1 test hysteresis cycles in x and y directions: a) F1, b) F2, c) F3 and d) F4 test protocols.

setup configuration, which limits the transversal component activation, and the non-ideal behaviour of the friction interface, which usually differs from the theoretical one. However, the NB configuration exhibits steadier values, with a coefficient of variation of F_{act} that averages 14% against the 20% of NN, confirming what was observed from the hysteresis cycles.

Figure 6.11 shows the percentage difference between F_{act} and F_{max} (ΔF) for NN and NB configuration in both x and y directions (Figures 6.11(a) and 6.11(b), respectively). Both configurations exhibit smaller ΔF values in the in the x direction thanks to a more rectangular loop shape of the recorded hysteresis cycles, with ΔFF values averaging 28% and 9% for NN and NB respectively. On the contrary, the slightly more evident stick-slip mechanism in the y direction is responsible for the greater ΔF values, averaging 46% and 66% for NN and NB respectively. When considering the difference between F_{act} and F_{max}, the NB configuration exhibits similar overall behaviour than the NN one, as they are associated with similar overall ΔF values (both 37%).

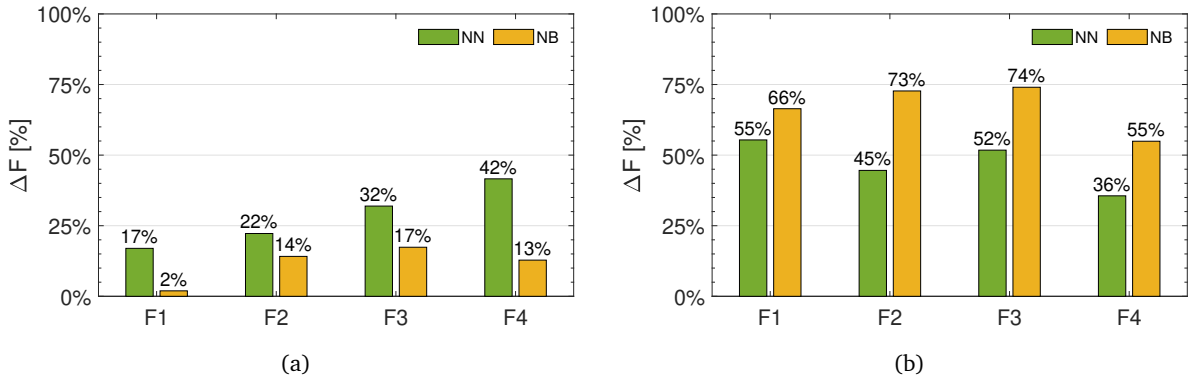

FIGURE 6.11: Difference between F_{max} and F_{act} values of G1-T1 tests in a) x and b) y directions.

Equivalent damping coefficient. The equivalent damping coefficient $\xi_{eq,hyst}$ is computed according to §6.1.1, and reported in Figure 6.12 in terms of average values with the standard deviation bar for NN and NB configuration in the x and y directions (Figures 6.12(a) and 6.12(b), respectively). Both configurations exhibited greater $\xi_{eq,hyst}$ values in the x direction, as a result of a hysteresis cycle with a more evident rectangular and wider loop shape, with $\xi_{eq,hyst}$ values averaging 47% and 55% for NN and NB respectively. On the contrary, the slightly more evident stick-slip mechanism in the y direction is responsible for the smaller $\xi_{eq,hyst}$ values, which average 42% for both NN and NB respectively.

Despite the slight different damping capacities between x and y directions, the NB configuration exhibits overall higher $\xi_{eq,hyst}$ values. Again, this similarity can be justified by the more rectangular hysteresis cycles recorded for the NB configuration, especially in the transversal direction. In fact, the more rectangular the hysteresis cycle shape is, the higher the $\xi_{eq,hyst}$ value.

Stud bolts axial load. The stud bolts axial load F_P is computed by using the relationship of §6.2.1, while the stud bolts axial load loss ΔF_P by using the relationship of §6.1.1. Table 6.6 lists the average values of F_P and ΔF_P with the coefficient of variation cv_{F_P} of SB1, SB2 and SB3 for NN and NB configuration in both x and y directions. Similarly to the previous RI tests, SB2 and SB3 exhibit a higher axial tension

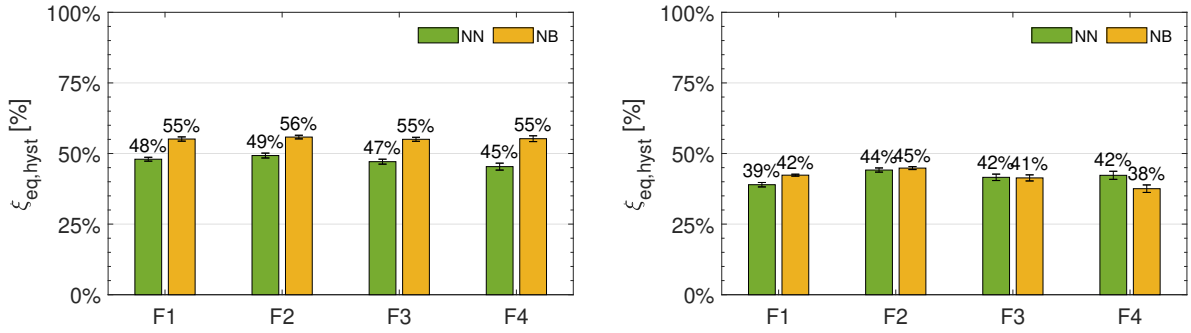

FIGURE 6.12: Equivalent damping values $\xi_{eq,hyst}$ of G1-T1 tests in a) x and b) y directions.

variation during the tests performed in the x direction than during the ones performed in the y direction. On the contrary, SB1 exhibits a higher axial tension variation during the tests performed in the y direction than during the ones performed in the x direction. This difference is caused by the different dissipative areas activated during the BRFD motion (see Figure 3.2(a)); during the tests performed in the x direction the working areas are DA2 and DA3 (associated with SB2 and SB3 respectively), while during the tests performed in the y direction the working area are DA1 (associated with SB1).

TABLE 6.6: G1-T1 test stud bolts axial tension and axial tension loss.

Configuration	Test tag	Direction	SB2&SB3			SB1		
			F_P [kN]	cv_{Fp}	Δ_{Fp}	F_P [kN]	cv_{Fp}	Δ_{Fp}
NN	G1-T1-F1	x	20.23	1.17%	1.88%	22.68	0.45%	1.28%
		y	23.70	3.62%	-3.41%	22.01	1.38%	4.52%
	G1-T1-F2	x	22.38	1.00%	-1.87%	22.75	0.33%	0.56%
		y	20.60	0.47%	1.10%	21.99	0.92%	-0.70%
	G1-T1-F3	x	23.61	1.64%	1.19%	22.02	0.17%	-0.29%
		y	19.48	2.47%	7.91%	22.41	0.73%	0.69%
	G1-T1-F4	x	24.98	1.48%	2.28%	21.87	0.11%	0.27%
		y	17.07	4.85%	16.15%	20.42	0.78%	-1.53%
NB	G1-T1-F1	x	19.59	0.14%	-0.42%	25.93	0.99%	3.08%
		y	19.83	0.37%	-0.49%	23.99	0.53%	1.65%
	G1-T1-F2	x	19.82	0.17%	-0.40%	24.83	0.14%	0.38%
		y	19.65	0.06%	0.13%	22.86	0.47%	1.40%
	G1-T1-F3	x	20.19	0.14%	0.12%	24.55	0.05%	0.05%
		y	19.48	0.38%	1.17%	21.61	0.29%	0.84%
	G1-T1-F4	x	20.77	0.21%	-0.32%	24.59	0.01%	0.00%
		y	19.40	0.60%	1.90%	21.29	0.25%	0.61%

SB2 and SB3 exhibit F_P values averaging 21.51 kN for NN and 19.84 kN for NB couplings, with cv_{Fp} averaging 2.09% for NN and 0.26% for NB, and tension loss ΔF_P averaging 3.15% for NN and 0.21% for NB. Similarly, SB1 exhibits F_P values averaging 22.03 kN for NN and 23.70 kN for NB couplings, with cv_{Fp} averaging 0.61% for NN and 0.34% for NB, and tension loss ΔF_P averaging 0.60% for NN and 1.00% for NB.

All the instrumented stud bolts exhibit a small variation of axial tension during the G1-T1 tests, however when applied to the NB configuration this variation is less remarkable, confirming the promising behaviour

of the Nb configuration.

Friction coefficient. The friction coefficient values μ_l, which are associated with the overall BRFD linear behaviour, are computed according to §6.1.1 formulations. Figure 6.13 and Table 6.7 show the average values of $\mu_{l,an}$ and $\mu_{l,EDC}$ with the standard deviation for NN and NB in both x and y directions. In NN configuration, $\mu_{l,an}$ averages 0.46 in the x direction and 0.09 in the y direction, while $\mu_{l,EDC}$ averages 0.43 in the x direction and 0.08 in the y direction. In NB configuration, $\mu_{l,an}$ averages 0.15 in the x direction and 0.03 in the y direction, while $\mu_{l,EDC}$ averages 0.14 in the x direction and 0.03 in the y direction.

TABLE 6.7: Friction coefficients associated with the overall BRFD linear behaviour of G1-T1 tests for NN and NB configurations.

Configuration	Test tag	$\mu_{l,an,x}$	$\mu_{l,EDC,x}$	$\mu_{l,an,y}$	$\mu_{l,EDC,y}$
NN	G1-T1-F1	0.49 ± 0.02	0.43 ± 0.02	0.07 ± 0.01	0.06 ± 0.01
	G1-T1-F2	0.54 ± 0.01	0.51 ± 0.01	0.08 ± 0.01	0.08 ± 0.01
	G1-T1-F3	0.43 ± 0.02	0.42 ± 0.01	0.08 ± 0.01	0.08 ± 0.01
	G1-T1-F4	0.37 ± 0.01	0.37 ± 0.01	0.11 ± 0.01	0.10 ± 0.01
NB	G1-T1-F1	0.26 ± 0.01	0.22 ± 0.01	0.03 ± 0.01	0.03 ± 0.01
	G1-T1-F2	0.16 ± 0.01	0.16 ± 0.01	0.02 ± 0.01	0.03 ± 0.01
	G1-T1-F3	0.13 ± 0.01	0.13 ± 0.01	0.03 ± 0.01	0.03 ± 0.01
	G1-T1-F4	0.15 ± 0.01	0.14 ± 0.01	0.03 ± 0.01	0.03 ± 0.01

In general, the values of the friction coefficient obtained by using the formulations derived from the analytical model of §3.2 are greater than the ones obtained by using the formulations derived from EN 15129 (CEN, 2018a), with an average percentage difference of 5% for the NN configuration and 2% for the NB configuration. Also, the values of the friction coefficient associated with the x direction are significantly greater than the ones associated with the y direction, with an average percentage difference of 81% for the NN configuration and 80% for the NB configuration. This behaviour confirms the remark of §3.2: μ_l is strictly related to the overall behaviour of the device, which differs from x to y directions.

The friction coefficient values μ_r, which are associated with the mechanical properties of the friction interfaces of the device, are computed according to §6.1.1 formulations. Figure 6.14 and Table 6.8 show the average values of $\mu_{r,an}$ and $\mu_{r,EDC}$ with the standard deviation for NN and NB configuration in both x and y directions. In NN configuration, $\mu_{r,an}$ averages 0.61 in the x direction and 0.57 in the y direction, while $\mu_{r,EDC}$ averages 0.57 in the x direction and 0.53 in the y direction. In NB configuration, $\mu_{r,an}$ averages 0.19 in the x direction and 0.18 in the y direction, while $\mu_{r,EDC}$ averages 0.19 in the x direction and 0.18 in the y direction.

Once again, the values of the friction coefficient obtained by using the formulations derived from the analytical model of §3.2 are greater than the ones obtained by using the formulations derived from EN 15129 (CEN, 2018a), with an average percentage difference of 6% for the NN configuration and 2% for the NB configuration. In addition, the values of the friction coefficient associated with the x direction are slightly greater than the ones associated with the y direction, with an average percentage difference of 7% for the NN and 4% for the NB. This behaviour confirms the remark of §3.2: μ_r is strictly related to the mechanical properties of the friction interfaces of the device, which are the same in both directions.

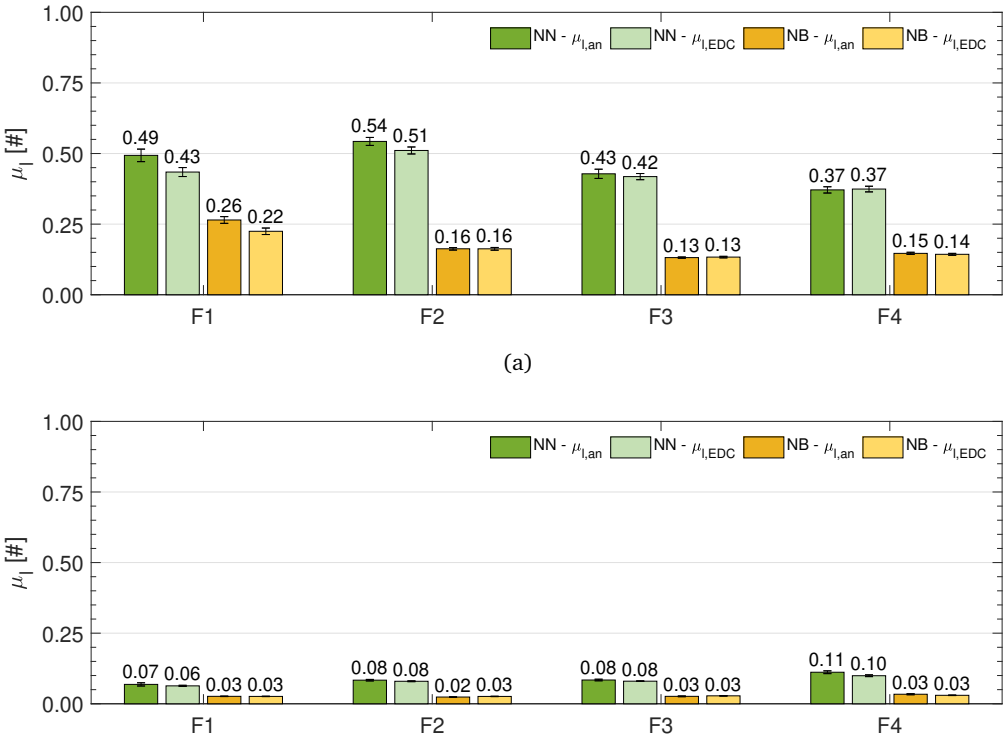

(a)

(b)

FIGURE 6.13: Friction coefficients associated with the overall BRFD linear behaviour μ_l of G1-T1 tests in a) x and b) y directions.

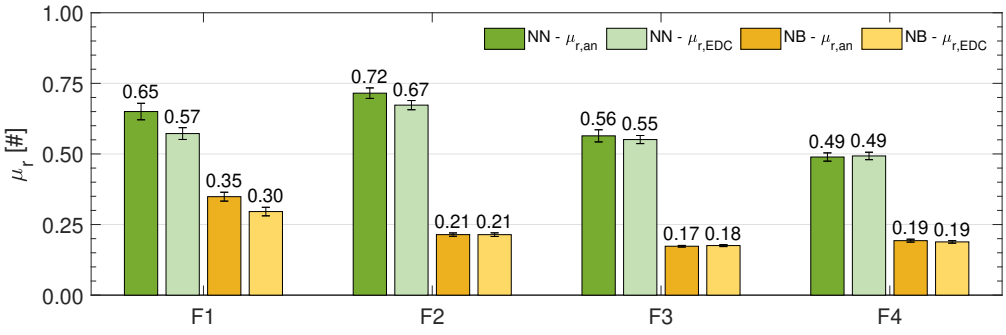

(a)

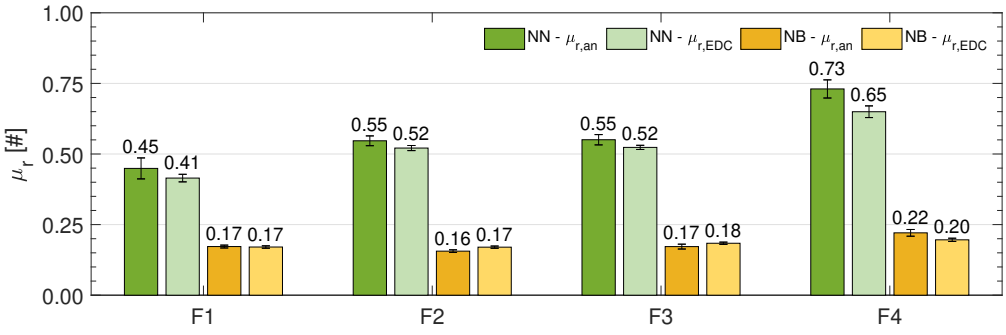

(b)

FIGURE 6.14: Friction coefficients associated with the rotational mechanism of the friction interface μ_r of G1-T1 tests in a) x and b) y directions.

TABLE 6.8: Friction coefficients associated with the rotational mechanism of the friction interface of G1-T1 tests for NN and NB configurations.

Configuration	Test tag	$\mu_{r,an,x}$	$\mu_{r,EDC,x}$	$\mu_{r,an,y}$	$\mu_{r,EDC,y}$
NN	G1-T1-F1	0.65 ± 0.03	0.57 ± 0.02	0.45 ± 0.04	0.41 ± 0.01
	G1-T1-F2	0.72 ± 0.02	0.67 ± 0.02	0.55 ± 0.02	0.52 ± 0.01
	G1-T1-F3	0.56 ± 0.02	0.55 ± 0.01	0.55 ± 0.02	0.52 ± 0.01
	G1-T1-F4	0.49 ± 0.01	0.49 ± 0.01	0.73 ± 0.03	0.65 ± 0.02
NB	G1-T1-F1	0.35 ± 0.02	0.30 ± 0.02	0.17 ± 0.01	0.17 ± 0.01
	G1-T1-F2	0.21 ± 0.01	0.21 ± 0.01	0.16 ± 0.01	0.17 ± 0.01
	G1-T1-F3	0.17 ± 0.01	0.18 ± 0.01	0.17 ± 0.01	0.18 ± 0.01
	G1-T1-F4	0.19 ± 0.01	0.19 ± 0.01	0.22 ± 0.01	0.2 ± 0.01

Temperature. Table 6.9 lists the average values of the temperature increment ΔT in correspondence of DA1, DA2 and DA3 for NN and NB configuration in both x and y directions. As previously observed during the RI tests, DA2 and DA3 exhibit a higher ΔT increment during the tests performed in the x direction than during the ones performed in the y direction. On the contrary, DA1 exhibits a higher ΔT increment during the tests performed in the y direction than during the ones performed in the x direction. Moreover, ΔT decrements as the total duration of tests decrements. DA2 and DA3 during the tests in the x directions exhibit ΔT values averaging 8.5°C and 1.5°C for the NN and NB configurations respectively, while during the tests in the y directions exhibit ΔT values averaging 1.8°C and 0.1°C for the NN and NB configurations respectively. On the contrary, DA1 during the tests in the x directions exhibits ΔT values averaging 0.1°C and 0.2°C for the NN and NB configurations respectively, while during the tests in the y directions exhibits ΔT values averaging 2.0°C and 0.8°C for the NN and NB. NB registers the smaller difference between ΔT values in both x and y directions, exhibiting once again a more stable overall behaviour than the NN configuration.

TABLE 6.9: G1-T1 test temperature variation.

Test tag	Direction	NN		NB	
		$\Delta T_{DA2\&DA3}$ [°C]	ΔT_{DA1}[°C]	$\Delta T_{DA2\&DA3}$ [°C]	ΔT_{DA1}[°C]
G1-T1-F1	x	7.2	0.3	1.1	0.7
	y	-7.7	3.6	-0.2	0.9
G1-T1-F2	x	9.7	0.1	2.1	0.1
	y	-0.1	2.4	-0.1	1.0
G1-T1-F3	x	9.0	0.2	1.5	0.1
	y	0.4	1.3	0.0	0.8
G1-T1-F4	x	8.0	0.1	1.2	0.0
	y	0.3	0.6	-0.1	0.6

The evaluation of the parameters for the selection of the better-performing configuration highlights that NB exhibits a steadier and more efficient behaviour than the NN configuration. Moreover, the computed values of μ_r, especially the ones associated with the x direction, are aligned with the ones obtained from the tribological investigation of Chapter 4. For these reasons, the NB configuration is selected as the better-performing and is subjected to additional tests with the incremented torque level T2 (75 Nm).

6.2.3.2 T2 test results

Hysteresis cycles. Figure 6.15 shows G1 test results for the NB configuration in terms of hysteresis cycles as a force-displacement relationship for F1, F2, F3 and F4 sliding frequencies. The hysteresis cycle shapes in the x direction (blue lines) are mainly rectangular with a slight hardening effect caused by a stick-slip mechanism in correspondence with the reverse motion point, especially for more significant displacements. The hysteresis cycle shapes in the y direction (orange lines) exhibits a similar behaviour, but with a stick-slip mechanism slightly more evident.

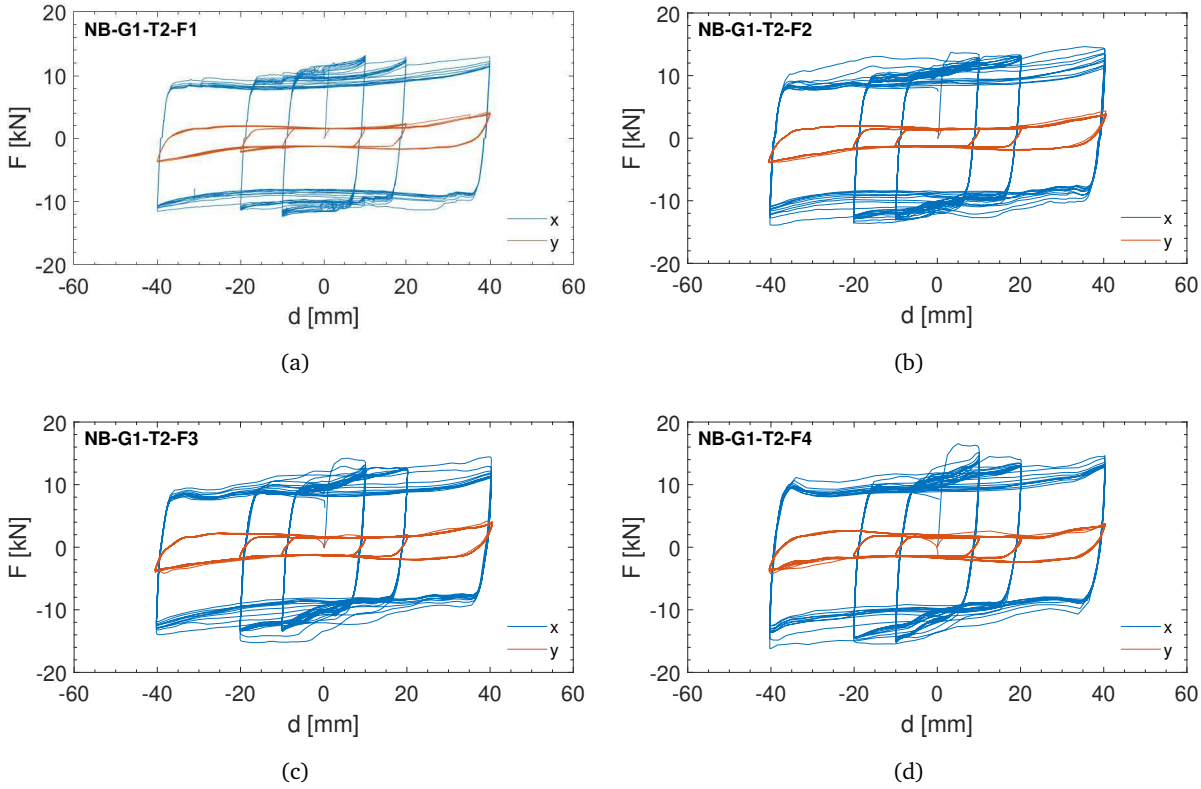

FIGURE 6.15: NB-T2-G1 test hysteresis cycles in x and y directions: a) F1, b) F2, c) F3 and d) F4 test protocols.

Despite the increment of torque level, the hysteresis cycle shape of the NB configurations still does not differ when incrementing the amplitude and frequency of the signal. As emphasised before, this is a promising behaviour because it ensures that the device's response during an earthquake remains consistent, regardless of the wave frequency content. Moreover, the recorded hysteresis cycles of NB configuration with T2 are similar to the ones obtained for NN with T1. However, NB exhibits a more rectangular and steadier shape, unaltering its damping capability.

Activation and maximum forces. The activation forces F_{act} and the maximum forces F_{max} are computed according to §6.1.1, and Table 6.10 lists the average values with the standard deviation for the NB configuration for the x and y directions. When the NB configuration is subjected to T2 torque level, F_{act} values average 10.03 kN in the x direction and 1.51 kN in the y direction, while F_{max} values average 12.84 kN in the x direction and 2.41 kN in the y direction.

TABLE 6.10: G1-T2 test activation and maximum forces.

Test tag	$F_{act,st,x}$ [kN]	$F_{act,st,y}$ [kN]	$F_{max,st,x}$ [kN]	$F_{max,st,y}$ [kN]	ΔF_x	ΔF_y
G1-T2-F1	9.95 ± 1.08	1.54 ± 0.03	11.92 ± 0.5	2.55 ± 0.91	20%	66%
G1-T2-F2	10.31 ± 0.88	1.37 ± 0.05	12.67 ± 0.68	2.35 ± 1.07	23%	71%
G1-T2-F3	9.76 ± 0.9	1.41 ± 0.08	12.76 ± 0.62	2.38 ± 1.03	31%	69%
G1-T2-F4	10.09 ± 0.69	1.72 ± 0.19	13.99 ± 0.71	2.35 ± 0.96	39%	37%

The components in both x and y directions exhibit a significant force increment from the T1 to T2 torque level, averaging 185% and 145% for the x and y directions, respectively. However, the percentage difference between F_{act} and F_{max} (ΔF) exhibits an increment from the T1 to T2 torque level, with average ΔF values of 28% and 59% for the x and y directions, respectively. This increment is particularly evident in the x direction.

The evaluation of activation and maximum forces highlights that when NB is subjected to T2 torque level, it behaves more similarly to the NN configuration subjected to T1 torque. However, the NB configuration still behaves better than the NN one, registering steadier force values.

Equivalent damping coefficient. The equivalent damping coefficient $\xi_{eq,hyst}$ is computed according to §6.1.1, and Figure 6.16 shows the average values with the standard deviation bar for the NB configuration in both x and y directions. $\xi_{eq,hyst}$ values are higher in the x direction, as a result of a hysteresis cycle with a more evident rectangular shape, with $\xi_{eq,hyst}$ values averaging 48%, which is slightly smaller to the one computed for T1 torque. On the contrary, the slightly more evident stick-slip mechanism in the y direction is responsible for the slightly smaller $\xi_{eq,hyst}$ values, which average 43%, which is similar to the one computed for T1 torque.

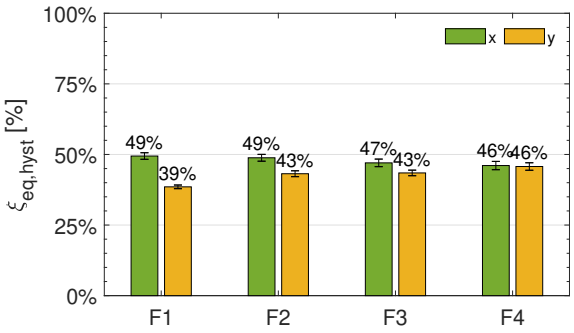

FIGURE 6.16: Equivalent damping values $\xi_{eq,hyst}$ of G1-T2 tests in x and y directions.

The evaluation of the equivalent damping coefficient highlights that the increment of torque mainly influences the x direction. In fact, the hysteresis cycles in the longitudinal direction with T2 exhibit a less rectangular loop shape than the ones with T1, and this difference is reflected in the lower $\xi_{eq,hyst}$ values.

Stud bolts axial load. The stud bolts axial load F_P is computed by using the relationship of §6.2.1, while the stud bolts axial load loss ΔF_P by using the relationship of §6.1.1. Table 6.11 lists the average values of F_P and ΔF_P with the coefficient of variation cv_{F_P} of SB1, SB2 and SB3 for the NB configuration in both x

and y directions. Similarly to the previous tests, SB2 and SB3 exhibit a higher axial tension variation during the tests performed in the x direction than during the ones performed in the y direction. On the contrary, SB1 exhibits a higher axial tension variation during the tests performed in the y direction than during the ones performed in the x direction. This difference is caused by the different dissipative areas activated during the BRFD motion (see Figure 3.2(a)); during the tests performed in the x direction the working areas are DA2 and DA3 (associated with SB2 and SB3 respectively), while during the tests performed in the y direction the working area are DA1 (associated with SB1).

TABLE 6.11: G1-T2 test stud bolts axial tension and axial tension loss.

Test tag	Direction	SB2&SB3			SB1		
		F_P [kN]	cv_{Fp}	Δ_{Fp}	F_P [kN]	cv_{Fp}	Δ_{Fp}
G1-T2-F1	x	33.27	0.50%	1.32%	42.64	0.24%	0.81%
	y	29.13	1.75%	5.62%	40.37	0.23%	0.68%
G1-T2-F2	x	33.28	0.26%	0.70%	42.99	0.20%	-0.43%
	y	28.89	1.56%	4.99%	39.94	0.22%	0.50%
G1-T2-F3	x	33.52	0.27%	0.70%	43.14	0.29%	0.45%
	y	28.89	1.64%	5.26%	39.86	0.20%	0.55%
G1-T2-F4	x	33.82	0.30%	0.95%	42.21	0.55%	1.56%
	y	28.90	1.83%	5.82%	39.84	0.20%	0.50%

SB2 and SB3 exhibit F_P values averaging 31.24 kN, with cv_{F_P} averaging 1.01% and tension loss ΔF_P averaging 3.17%. Similarly, SB1 exhibits F_P values averaging 41.37 kN, with cv_{F_P} averaging 0.27% and tension loss ΔF_P averaging 0.58%.

The NB configuration registers bigger F_P values when subjected to T2 torque level, confirming the remarks of §6.2.1. Similarly, the ΔF_P values increased with respect to the T1 torque level, with an average lower than 2% in both stud bolts. As a result, the stud bolt axial force is less steadier when NB is subjected to the T2 torque level.

Friction coefficient. The friction coefficient values μ_l, which are associated with the overall BRFD linear behaviour, are computed according to §6.1.1 formulations. Figure 6.17 shows the average values of $\mu_{l,an}$ and $\mu_{l,EDC}$ with the standard deviation bar for the NB configuration in both x and y directions. When the NB configuration is subjected to T2 torque level, $\mu_{l,an}$ averages 0.30 in the x direction and 0.04 in the y direction, while $\mu_{l,EDC}$ averages 0.29 in the x direction and 0.04 in the y direction.

The friction coefficient values μ_r, which are associated with the mechanical properties of the friction interfaces of the device, are computed according to §6.1.1 formulations. Figure 6.18 shows the average values of $\mu_{r,an}$ and $\mu_{r,EDC}$ with the standard deviation bar for the NB configuration in both x and y directions. When the NB configuration is subjected to T2 torque level, $\mu_{r,an}$ averages 0.40 in the x direction and 0.25 in the y direction, while $\mu_{r,EDC}$ averages 0.38 in the x direction and 0.24 in the y direction.

Once again, the values of the friction coefficient obtained by using the formulations derived from the analytical model of §3.2 are greater than the ones obtained by using the formulations derived from EN 15129 (CEN, 2018a), with an average percentage difference of the 4% for both μ_l and μ_r. In addition, the

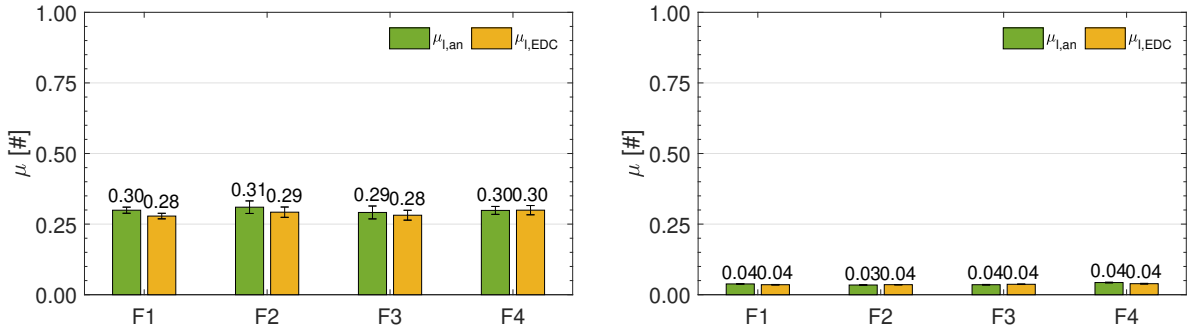

FIGURE 6.17: Friction coefficients associated with the overall BRFD linear behaviour μ_l of G1-T2 tests in a) x and b) y directions.

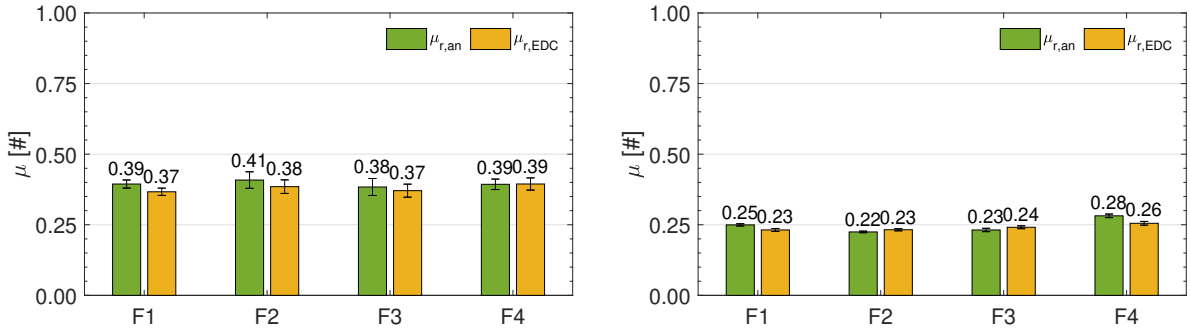

FIGURE 6.18: Friction coefficients associated with the rotational mechanism of the friction interface μ_r of G1-T2 tests in a) x and b) y directions.

values of the friction coefficient associated with the x direction are greater than the ones related to the y direction, with an average percentage difference of 87% for μ_l and of the 37% for μ_r.

The evaluation of the friction coefficients highlights that the increment of torque influences mainly the x direction. In fact, the μ_l and μ_r values exhibit an average increment of 106% in the x direction and an increment of the 37% in the y direction.

Temperature. Figure 6.19 shows the average values of the temperature increment ΔT in correspondence of DA1, DA2 and DA3 for the NB configuration in both x and y directions (Figures 6.19(a) and 6.19(b) respectively). As previously observed, DA2 and DA3 exhibit a higher ΔT increment during the tests performed in the x direction than during the ones performed in the y direction. On the contrary, DA1 exhibits a higher ΔT increment during the tests performed in the y direction than during the ones performed in the x direction. Moreover, ΔT decrements as the total duration of tests decrements. DA2 and DA3 during the tests in the x directions exhibit ΔT values averaging 2.5°C, while during the tests in the y directions exhibit ΔT values averaging 0.05°C. On the contrary, DA1 during the tests in the x directions exhibits ΔT values averaging 0.2°C, while during the tests in the y directions exhibits ΔT values averaging 1.9°C. Once again, NB registers small differences between ΔT values in both x and y directions, exhibiting once again a more stable overall behaviour than the NN configuration.

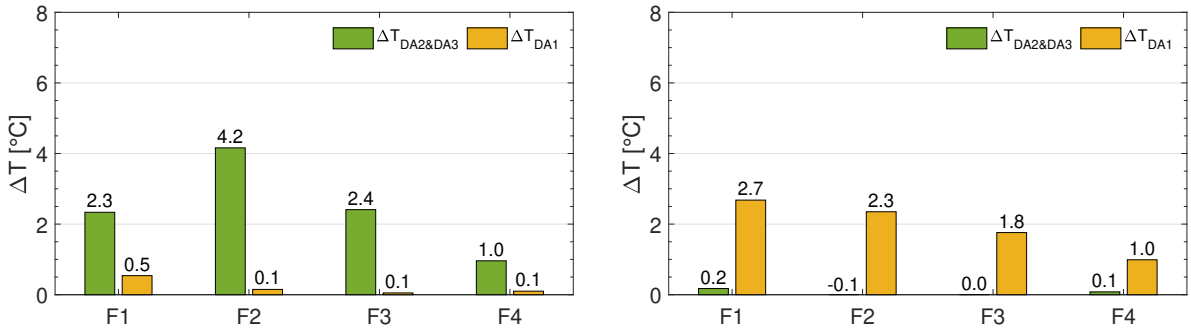

FIGURE 6.19: Temperature variation ΔT of G1-T2 tests in a) x and b) y directions.

The assessment of the torque increment on the BRFD behaviour highlights that both x and y directions components still exhibits a good performance with a significant steady and rectangular-shaped hysteresis cycle. However, the conducted tests are mono-directional and the evaluation of the BRFD behaviour when subjected to bi-directional displcements is needed to investigate eventual interactions between the x and y directions components.

6.2.4 Group 2 (G2) test results

G2 tests aim at determining the relationship between the coefficient of friction and the velocity. The findings of this section are useful to calibrate a numerical model by determining a friction constitutive model for the investigated friction interfaces.

6.2.4.1 T1 test results

Hysteresis cycles. Figure 6.20 shows the recorded hysteresis cycles of the BRFD during G2 tests for NN and NB configurations respectively, in terms of hysteresis cycles as a force-displacement relationship. When the device is subjected to displacements in the x (blue lines) and y (orange lines) directions, the hysteresis cycle shape is rectangular, with a slight hardening effect corresponding to the reverse-motion point. This behaviour slightly differs from the one observed during G1 tests, especially in the y direction. In fact, during G2 tests, the pinching effect in the y direction is less remarkable. This difference is caused by the type of displacement law, which ensures a constant sliding velocity and reduces the stick-slip mechanism.

Concerning the force values, the recorded forces decrease with sliding velocity increment when the BRFD is subjected to displacement in the x direction. On the contrary, when the BRFD is subjected to displacement in the y direction, the recorded forces remain almost constant with sliding velocity increment.

The activation forces F_{act} and the maximum forces F_{max} are computed according to §6.1.1. When NN is subjected to displacement in in the x direction, F_{act} values average 10.66 kN with a coefficient of variation of 3%, while F_{max} values average 13.37 kN with a coefficient of variation of 2%. For displacement in in the y direction, F_{act} values average 1.81 kN with a coefficient of variation of 2%, while F_{max} values average 2.89 kN with a coefficient of variation less than 1%.

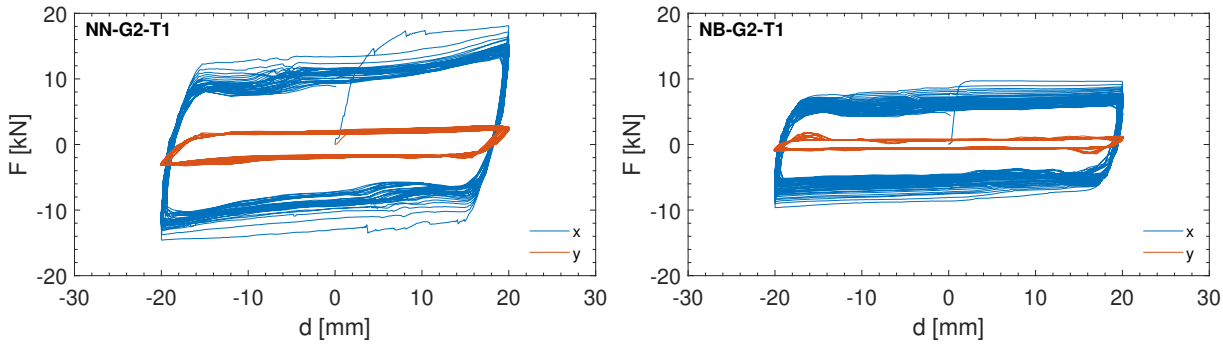

FIGURE 6.20: G2-T1 tests hysteresis cycles in x and y directions of a) NN and b) NB configurations.

When NB is subjected to displacement in in the x direction, F_{act} values average 6.40 kN with a coefficient of variation of 3%, while F_{max} values average 7.03 kN with a coefficient of variation of 2%. For displacement in in the y direction, F_{act} values average 0.71 kN with a coefficient of variation of 2%, while F_{max} values average 1.12 kN with a coefficient of variation of 2%.

Friction coefficient and velocity relationship. The friction coefficient values μ_l, which are associated with the overall BRFD linear behaviour, are computed according to §6.1.1 formulations. Figure 6.21 shows the relationship between μ_l and the sliding velocity v for the NN and NB configurations in both x (blue lines) and y (orange lines) directions. The relationships are expressed as a function of $\mu_{l,EDC}$ (triangular markers), $\mu_{l,an}$ (circular markers) and the average between them ($\mu_{l,av}$ with dashed lines). Both configurations exhibits higher μ_l at lower sliding velocity, reflecting the stick-slip mechanism, however in the NN configuration the difference between lower and higher sliding velocity is more remarkable.

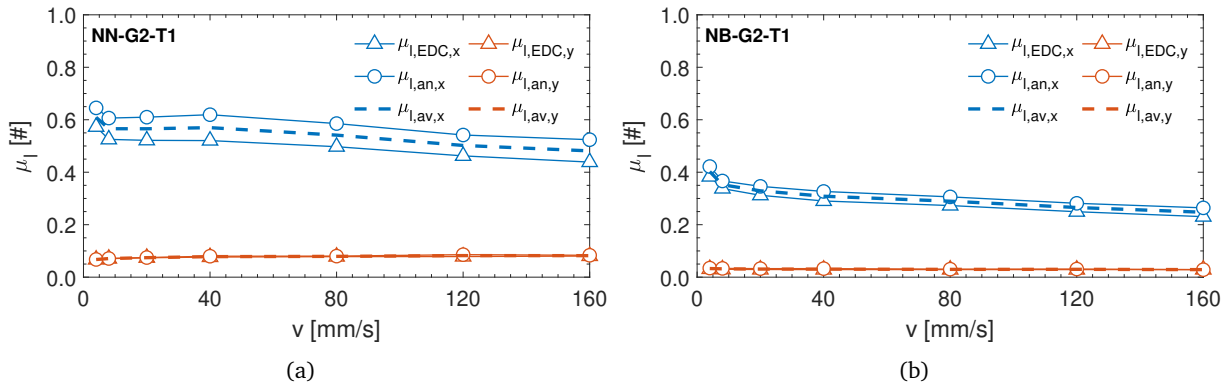

FIGURE 6.21: G2-T1 $\mu_l - v$ relationship in x and y directions of a) NN and b) NB configurations.

The NN configuration exhibits μ_l values averaging 0.55 in the x direction with a coefficient of variation of the 10% between $\mu_{l,EDC}$ and $\mu_{l,an}$, while in the y direction μ_l values averages 0.08 with a coefficient of variation of the 2% between $\mu_{l,EDC}$ and $\mu_{l,an}$. The percentage difference of μ_l values between x and y directions averages 86%, similar to the previous tests.

The NB configuration exhibits μ_l values averaging 0.31 in the x direction with a coefficient of variation of the 7% between $\mu_{l,EDC}$ and $\mu_{l,an}$, while in the y direction μ_l values averages 0.03 with a coefficient of variation of the 6% between $\mu_{l,EDC}$ and $\mu_{l,an}$. The percentage difference of μ_l values between x and y directions averages 90%, similar to the previous tests.

The friction coefficient values μ_r, which are associated with the mechanical properties of the friction interfaces of the device, are computed according to §6.1.1 formulations. Figure 6.22 shows the relationship between μ_r and the rotational sliding velocity ω for the NN and NB configurations in both x (blue lines) and y (orange lines) directions. The relationships are expressed as a function of $\mu_{r,EDC}$ (triangular markers), $\mu_{r,an}$ (circular markers) and the average between them ($\mu_{r,av}$ with dashed lines). Both configurations exhibits higher μ_r at lower sliding velocity, reflecting the stick-slip mechanism, however in the NN configuration the difference between lower and higher sliding velocity is more remarkable.

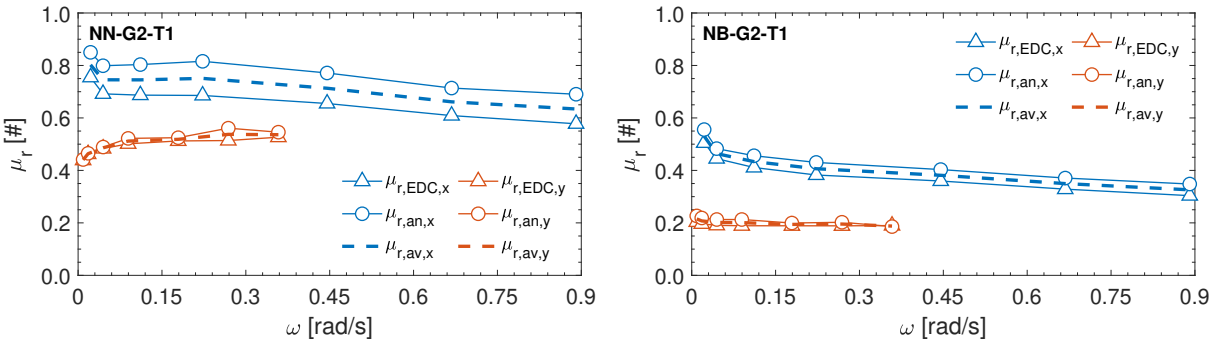

(a) (b)

FIGURE 6.22: G2-T1 $\mu_r - \omega$ relationship in x and y directions of a) NN and b) NB configurations.

The NN configuration exhibits μ_r values averaging 0.72 in the x direction with a coefficient of variation of the 11% between $\mu_{r,EDC}$ and $\mu_{r,an}$, while in the y direction μ_r values averages 0.50 with a coefficient of variation of the 2% between $\mu_{r,EDC}$ and $\mu_{r,an}$. The percentage difference of μ_r values between x and y directions averages 31%, similar to the previous tests.

The NB configuration exhibits μ_r values averaging 0.41 in the x direction with a coefficient of variation of the 8% between $\mu_{r,EDC}$ and $\mu_{r,an}$, while in the y direction μ_r values averages 0.20 with a coefficient of variation of the 6% between $\mu_{r,EDC}$ and $\mu_{r,an}$. The percentage difference of μ_r values between x and y directions averages 51%, similar to the previous tests.

Once again, the NB configuration exhibits a steadier behaviour than the NN configuration. For these reasons, the NB configuration is selected as the better-performing and is subjected to additional tests with the incremented torque level T2 (75 Nm).

6.2.4.2 T2 test results

Hysteresis cycles. Figure 6.23 shows the recorded hysteresis cycles of the BRFD during G2 tests for the NB configurations in terms of hysteresis cycles as a force-displacement relationship. When NB is subjected to T2 torque level, the hysteresis cycles in the x (blue lines) and y (orange lines) directions exhibit a rectangular shape with an almost absent hardening effect corresponding to the reverse-motion point. This

behaviour slightly differs from the one observed during G2-T1 tests, especially in the y direction. In fact, during G2-T2 tests, the hardening effect in the y direction is less remarkable. This difference is caused by the increment of torque level that stabilises the overall BRFD behaviour.

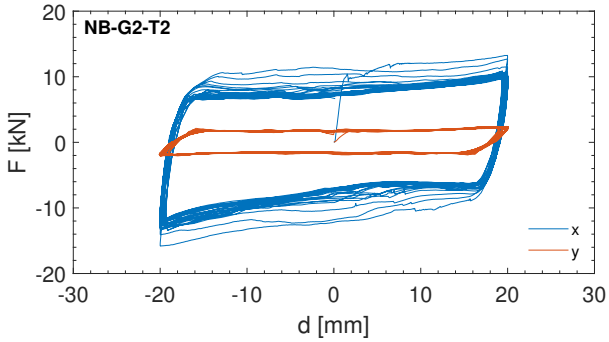

FIGURE 6.23: G2-T1 tests hysteresis cycles in x and y directions of NB configuration.

Concerning the force values, the recorded forces decrease with sliding velocity increment when the BRFD is subjected to displacement in the x direction. On the contrary, when the BRFD is subjected to displacement in the y direction, the recorded forces remain almost constant with sliding velocity increment.

When NB is subjected to displacement in in the x direction, F_{act} values average 7.71 kN with a coefficient of variation of 3%, while F_{max} values average 11.51 kN with a coefficient of variation of 3%. For displacement in in the y direction, F_{act} values average 1.67 kN with a coefficient of variation of 2%, while F_{max} values average 2.19 kN with a coefficient of variation less than 1%.

Friction coefficient and velocity relationship. The friction coefficient values μ_l and μ_r are computed according to §6.1.1 formulations. Figure 6.24 shows the relationship between μ_l and the sliding velocity v (Figure 6.24(a)) and between μ_r and the rotational sliding velocity ω (Figure 6.24(b)) for the NB configuration in both x (blue lines) and y (orange lines) directions. The relationships are expressed as a function of μ_{EDC} (triangular markers), μ_{an} (circular markers) and the average between them (μ_{av} with dashed lines). Both relationships exhibit higher μ values at lower sliding velocity, reflecting the stick-slip mechanism, however the difference between μ values computed at maximum and minimum sliding velocity decreased from T1 (percentage difference of 63%) to T2 torque levels (percentage difference of 30%).

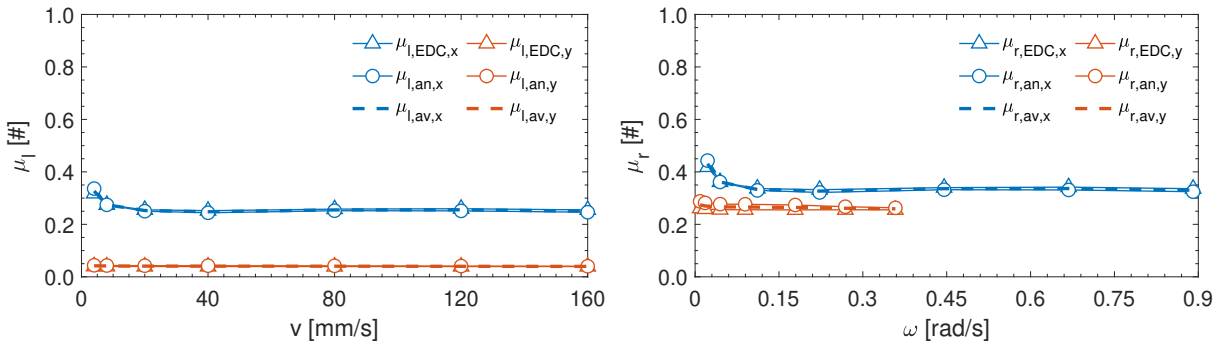

(a) (b)

FIGURE 6.24: G2-T1 a) $\mu_l - v$ and b) $\mu_r - \omega$ relationships in x and y directions of NB configuration.

When subjected to T2 torque level, the NB configuration exhibits μ_l values averaging 0.27 in the x direction with a coefficient of variation of the 2% between $\mu_{l,EDC}$ and $\mu_{l,an}$, while in the y direction μ_l values averages 0.04 with a coefficient of variation of the 5% between $\mu_{l,EDC}$ and $\mu_{l,an}$. The percentage difference of μ_l values between x and y directions averages 85%, similar to the previous tests.

When subjected to T2 torque level, the NB configuration exhibits μ_r values averaging 0.35 in the x direction with a coefficient of variation of the 2% between $\mu_{r,EDC}$ and $\mu_{r,an}$, while in the y direction μ_r values averages 0.27 with a coefficient of variation of the 5% between $\mu_{r,EDC}$ and $\mu_{r,an}$. The percentage difference of μ_r values between x and y directions averages 24%, improving the previous tests.

As a result, when subjected to T2 torque level the NB configuration behaves more similarly to the NN configuration subjected to T1 torque level but with a more significant stability. In fact, the coefficient of variation of both recorded forces and COF are lower in the NB-T2 configuration than in NN-T1 configuration.

6.2.5 Group 3 (G3) test results

G3 tests aim at assessing the BRFD behaviour in a real-use condition when subjected to bidirectional displacements. The findings of this section are useful to describe how the two components (longitudinal x-direction and transversal y-direction) of the device interacts with each other.

6.2.5.1 T1 test results

Hysteresis cycles. Figures 6.25 and 6.26 show the recorded hysteresis cycles of the NN and NB configuration when subjected to cloverleaf and spiral waveforms, respectively. The hysteresis loop shape does not change for all cases when the signal frequency is increased. The hysteresis cycle shapes in the x direction (blue lines) are mainly rectangular, with an evident hardening effect caused by a stick-slip mechanism corresponding with the reverse motion point, especially for more significant displacements. The hysteresis cycle shapes in the y direction (orange lines) significantly differ for cloverleaf (Figures 6.25(a-d), 6.26(a-d)) and spiral orbits (Figures 6.25(e-h), 6.26(e-h)). For the cloverleaf case, the hysteresis shapes are rectangular with rounded corners corresponding with the reverse motion point. In contrast, in the spiral waveform, the hysteresis shapes are rectangular but have a V shape.

The fact that the hysteresis cycle for NN and NB configurations does not differ with signal frequency is a promising behaviour because it ensures that the device's behaviour during an earthquake remains consistent, regardless of the ground motion frequency content. Regarding the different behaviour exhibited for both NN and NB in the x and y directions, this can be explained by considering a combination of the device geometrical layout and the configuration of the experimental setup, as described at the end of §6.1. However, the recorded hysteresis cycles of NB configuration exhibit a more rectangular and steadier shape, usually associated with a more effective damping capability, despite the lower values of recorded forces.

Activation and maximum forces. The activation forces F_{act} and the maximum forces F_{max} are computed according to §6.1.1; Table 6.12 lists the average values with the standard deviation for NN and NB configuration for the x and y directions. For NN, F_{act} values average 8.88 kN in the x direction and 0.96 kN in the y direction, while F_{max} values average 10.80 kN in the x direction and 2.02 kN in the y direction.

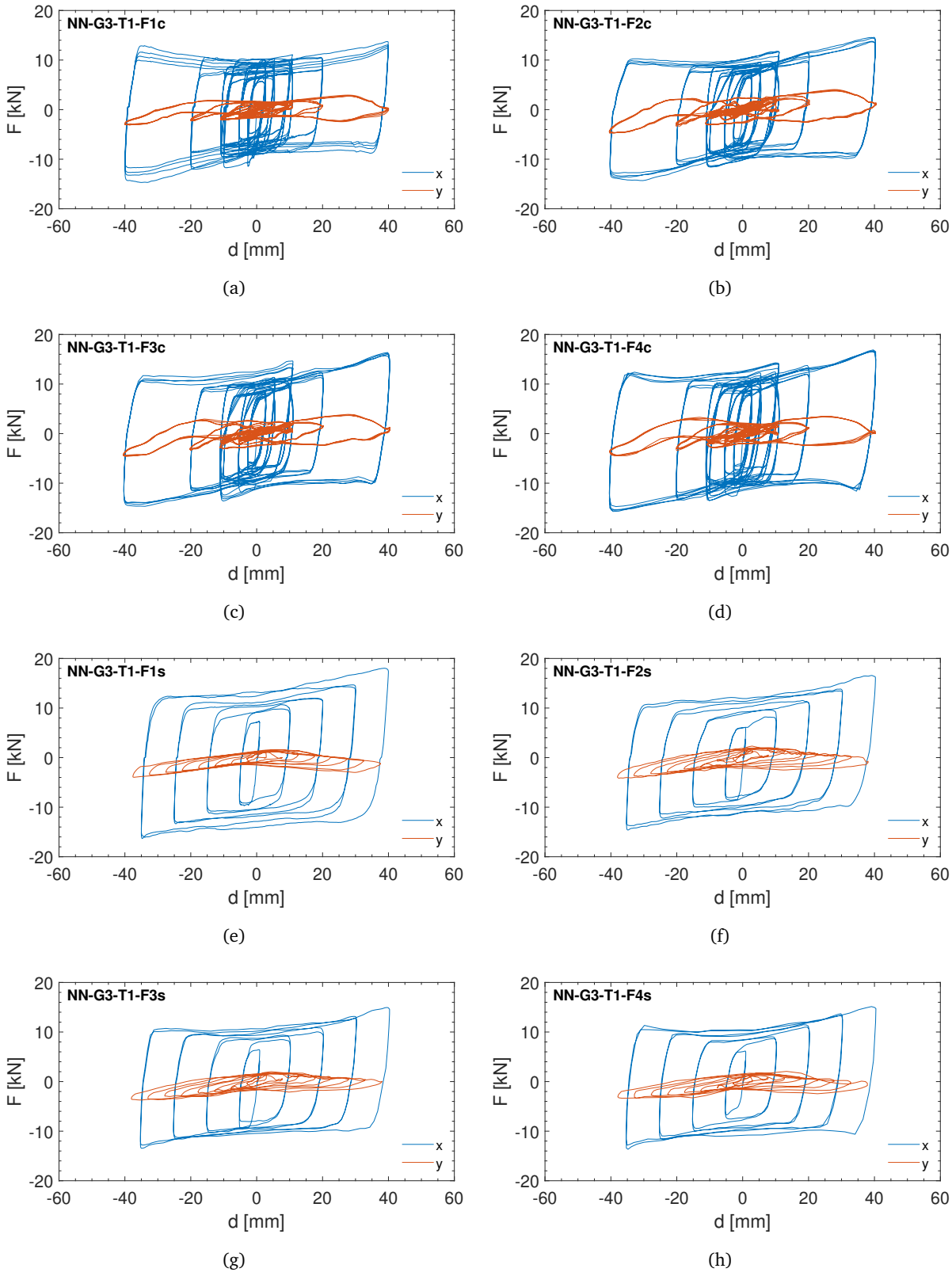

FIGURE 6.25: NN-T1-G3 test hysteresis cycles in x and y directions: a) F1c, b) F2c, c) F3c, d) F4c, e) F1s, f) F2s, g) F3s and h) F4s test protocols.

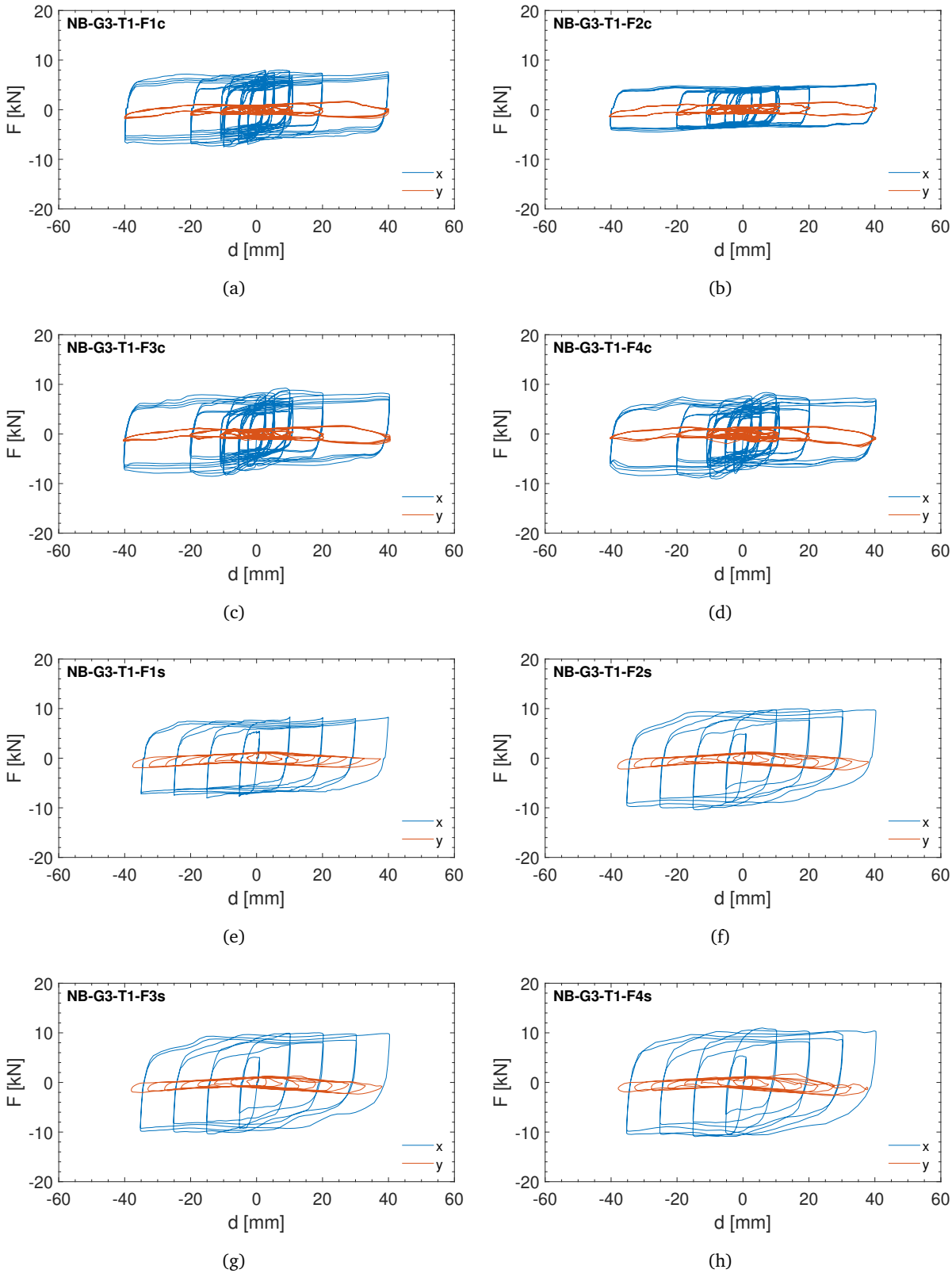

FIGURE 6.26: NB-T1-G3 test hysteresis cycles in x and y directions: a) F1c, b) F2c, c) F3c, d) F4c, e) F1s, f) F2s, g) F3s and h) F4s test protocols.

For NB, F_{act} values average 6.11 kN in the x direction and 0.82 kN in the y direction, while F_{max} values average 7.13 kN in the x direction and 1.25 kN in the y direction.

TABLE 6.12: G3-T1 test activation and maximum forces.

Configuration	Test tag	$F_{act,st,x}$ [kN]	$F_{act,st,y}$ [kN]	$F_{max,st,x}$ [kN]	$F_{max,st,y}$ [kN]
NN	G3-T1-F1c	9.08 ± 1.49	7.42 ± 1.24	1.66 ± 0.34	0.75 ± 0.26
	G3-T1-F2c	9.41 ± 1.56	7.57 ± 1.29	1.95 ± 0.68	0.66 ± 0.36
	G3-T1-F3c	10.37 ± 1.95	8.42 ± 1.52	2.04 ± 0.61	0.78 ± 0.24
	G3-T1-F4c	11.36 ± 1.58	9.07 ± 1.20	2.03 ± 0.50	0.79 ± 0.14
	G3-T1-F1s	12.65 ± 1.35	10.87 ± 0.87	2.04 ± 0.41	1.06 ± 0.11
	G3-T1-F2s	11.41 ± 1.35	9.52 ± 0.87	2.27 ± 0.33	1.34 ± 0.24
	G3-T1-F3s	11.10 ± 0.99	9.22 ± 0.46	2.15 ± 0.26	1.21 ± 0.19
	G3-T1-F4s	10.99 ± 1.35	8.92 ± 0.61	2.00 ± 0.30	1.12 ± 0.19
NB	G3-T1-F1c	5.82 ± 1.02	4.79 ± 0.92	0.99 ± 0.16	0.69 ± 0.19
	G3-T1-F2c	3.98 ± 0.3	3.22 ± 0.23	0.92 ± 0.13	0.57 ± 0.16
	G3-T1-F3c	6.04 ± 1.22	4.86 ± 0.91	1.04 ± 0.16	0.68 ± 0.15
	G3-T1-F4c	5.93 ± 1.20	4.83 ± 0.89	1.16 ± 0.28	0.75 ± 0.13
	G3-T1-F1s	7.36 ± 0.60	6.51 ± 0.59	1.38 ± 0.18	1.00 ± 0.06
	G3-T1-F2s	8.97 ± 0.92	7.85 ± 1.04	1.51 ± 0.27	0.98 ± 0.08
	G3-T1-F3s	9.15 ± 0.83	8.00 ± 0.94	1.46 ± 0.24	0.94 ± 0.08
	G3-T1-F4s	9.79 ± 1.04	8.80 ± 1.22	1.55 ± 0.27	0.96 ± 0.09

Both configurations exhibit differences between x and y directions, with a percentage difference that averages 89% for NN and 87% for NB configurations. This difference is higher (almost twice as large as expected) than the ideal 42% predicted by the analytical model of §3.2, and it is caused by the experimental setup configuration, which limits the transversal component activation, and the non-ideal behaviour of the friction interface, which usually differs from the theoretical one. However, the NB configuration exhibits steadier values, with a coefficient of variation of F_{act} that averages 14% against the 17% of NN, confirming what was observed from the hysteresis cycles.

In the selection of the better-performing configuration, the evaluation of the difference between F_{act} and F_{max} is a key parameter. Figure 6.27 shows the percentage difference between F_{act} and F_{max} (ΔF) for NN and NB configuration in both x and y directions (Figures 6.27(a) and 6.27(b), respectively). Both configurations exhibit smaller ΔF values in the in the x direction thanks to a more rectangular loop shape of the recorded hysteresis cycles, with ΔF values averaging 22% and 18% for NN and NB respectively. On the contrary, the peculiar hysteresis loop shape in the y direction is responsible for the greater ΔF values, especially for the tests conducted with cloverleaf orbit, with ΔF values averaging 120% and 52% for NN and NB respectively. Once again, the NB configuration exhibits a better-performing behaviour than the NN one, as it is associated with lower ΔF values. This is because the NB hysteresis is more rectangular than NN hysteresis cycles.

Equivalent damping coefficient. The equivalent damping coefficient $\xi_{eq,hyst}$ is computed according to §6.1.1, and reported in Figure 6.28 in terms of average values with the standard deviation bar for NN and NB configuration in the x and y directions (Figures 6.28(a) and 6.28(b), respectively). Both configurations exhibit greater $\xi_{eq,hyst}$ values in the x direction, as a result of a hysteresis cycle with a more evident rectangular and wider loop shape, with $\xi_{eq,hyst}$ values averaging 50% and 51% for NN and NB respectively.

On the contrary, the peculiar hysteresis cycle shape in the y direction is responsible for the smaller $\xi_{eq,hyst}$ values, which average 25% and 39% for NN and NB respectively.

Despite the different damping capacities between x and y directions, the NB configuration exhibits a smaller difference between $\xi_{eq,hyst}$ values computed in the x and y directions. Again, This smaller difference can be justified by the more rectangular hysteresis cycles recorded for the NB configuration, especially in the transversal direction. In fact, the more rectangular the hysteresis cycle shape is, the higher the $\xi_{eq,hyst}$ value.

Stud bolts axial load. The stud bolts axial load F_P is computed by using the relationship of §6.2.1, while the stud bolts axial load loss ΔF_P by using the relationship of §6.1.1. Table 6.13 lists the average values of F_P and ΔF_P with the coefficient of variation cv_{F_P} of SB1, SB2 and SB3 for NN and NB configuration in both x and y directions. SB2 and SB3 exhibit F_P values averaging 16.16 kN for NN and 19.90 kN for NB couplings, with cv_{F_P} averaging 12.37% for NN and 2.44% for NB, and tension loss ΔF_P averaging 7.69% for NN and 0.44% for NB. Similarly, SB1 exhibits F_P values averaging 16.25 kN for NN and 20.48 kN for NB couplings, with cv_{F_P} averaging 1.96% for NN and 1.02% for NB, and tension loss ΔF_P averaging 10.84% for NN and 3.83% for NB.

TABLE 6.13: G3-T1 test stud bolts axial tension and axial tension loss.

Configuration	Test tag	SB2&SB3			SB1		
		F_P [kN]	cv_{Fp}	ΔF_P	F_P [kN]	cv_{Fp}	ΔF_P
NN	G3-T1-F1c	14.49	21.41%	8.65%	15.67	1.80%	34.71%
	G3-T1-F2c	16.68	15.58%	10.25%	20.15	0.97%	4.94%
	G3-T1-F3c	19.53	11.17%	7.73%	19.20	1.03%	-1.81%
	G3-T1-F4c	19.39	14.65%	3.02%	20.00	1.11%	7.84%
	G3-T1-F1s	16.01	9.52%	12.08%	15.40	2.02%	13.02%
	G3-T1-F2s	15.33	9.18%	6.47%	14.17	2.95%	11.06%
	G3-T1-F3s	14.01	9.24%	8.01%	13.08	2.79%	16.34%
	G3-T1-F4s	13.83	8.19%	5.28%	12.30	2.99%	0.64%
NB	G3-T1-F1c	19.33	1.79%	0.11%	21.46	0.44%	6.33%
	G3-T1-F2c	19.44	2.29%	-0.70%	20.81	0.41%	0.00%
	G3-T1-F3c	19.75	2.36%	0.04%	20.52	0.81%	9.73%
	G3-T1-F4c	19.97	2.23%	-0.11%	18.98	1.06%	14.95%
	G3-T1-F1s	20.16	2.64%	0.89%	22.17	0.91%	6.32%
	G3-T1-F2s	20.13	2.79%	-0.26%	21.47	1.67%	4.83%
	G3-T1-F3s	20.15	2.69%	-0.72%	20.70	1.55%	4.95%
	G3-T1-F4s	20.24	2.68%	0.71%	22.36	1.27%	10.65%

All the instrumented stud bolts exhibit a small variation of axial tension during the G3-T1 tests, however when applied to the NB configuration this variation is less remarkable, confirming the promising behaviour of the NB configuration.

Friction coefficient. The friction coefficient values μ_l, which are associated with the overall BRFD linear behaviour, are computed according to §6.1.1 formulations. Table 6.14 lists the average values of $\mu_{l,an}$ and $\mu_{l,EDC}$ with the standard deviation for NN and NB in both x and y directions. In NN configuration, $\mu_{l,an}$ averages 0.56 in the x direction and 0.06 in the y direction, while $\mu_{l,EDC}$ averages 0.53 in the x direction

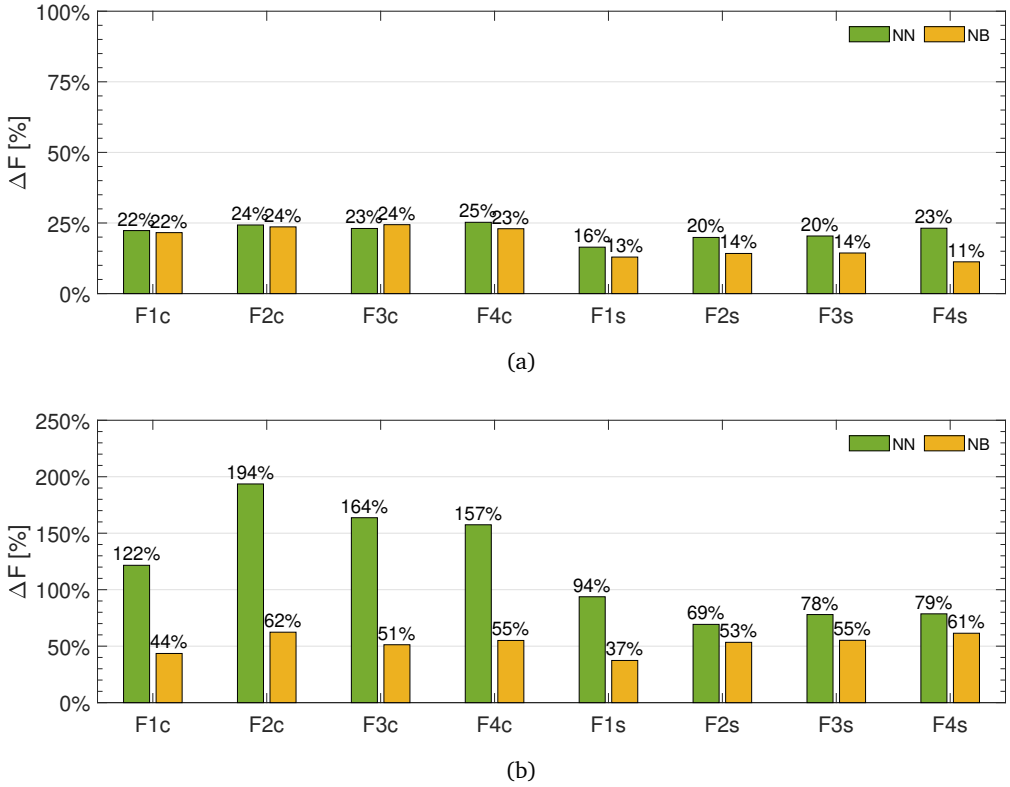

FIGURE 6.27: Difference between F_{max} and F_{act} values of G3-T1 tests in a) x and b) y directions.

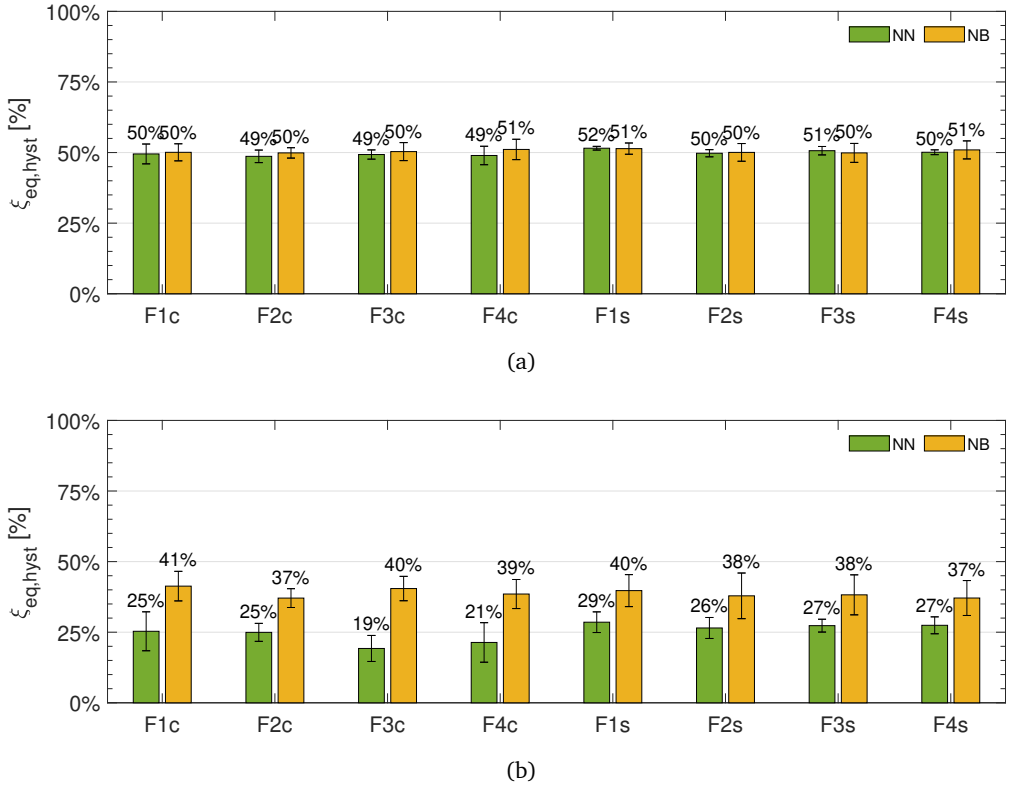

FIGURE 6.28: Equivalent damping values $\xi_{eq,hyst}$ of G3-T1 tests in a) x and b) y directions.

and 0.06 in the y direction. In NB configuration, $\mu_{l,an}$ averages 0.31 in the x direction and 0.04 in the y direction, while $\mu_{l,EDC}$ averages 0.28 in the x direction and 0.04 in the y direction.

TABLE 6.14: Friction coefficients associated with the overall BRFD linear behaviour of G3-T1 tests for NN and NB configurations.

Configuration	Test tag	$\mu_{l,an,x}$	$\mu_{l,EDC,x}$	$\mu_{l,an,y}$	$\mu_{l,EDC,y}$
NN	G3-T1-F1c	0.51 ± 0.08	0.48 ± 0.08	0.05 ± 0.02	0.05 ± 0.02
	G3-T1-F2c	0.45 ± 0.06	0.43 ± 0.07	0.03 ± 0.02	0.04 ± 0.02
	G3-T1-F3c	0.43 ± 0.06	0.41 ± 0.07	0.04 ± 0.01	0.04 ± 0.02
	G3-T1-F4c	0.47 ± 0.04	0.45 ± 0.06	0.04 ± 0.01	0.04 ± 0.02
	G3-T1-F1s	0.69 ± 0.05	0.64 ± 0.08	0.07 ± 0.01	0.06 ± 0.01
	G3-T1-F2s	0.63 ± 0.05	0.58 ± 0.08	0.1 ± 0.02	0.07 ± 0.02
	G3-T1-F3s	0.67 ± 0.01	0.63 ± 0.05	0.09 ± 0.02	0.07 ± 0.02
	G3-T1-F4s	0.65 ± 0.02	0.62 ± 0.07	0.09 ± 0.02	0.07 ± 0.02
NB	G3-T1-F1c	0.25 ± 0.05	0.24 ± 0.05	0.03 ± 0.01	0.03 ± 0.01
	G3-T1-F2c	0.17 ± 0.01	0.16 ± 0.02	0.03 ± 0.01	0.03 ± 0.01
	G3-T1-F3c	0.25 ± 0.05	0.24 ± 0.05	0.03 ± 0.01	0.03 ± 0.01
	G3-T1-F4c	0.24 ± 0.05	0.24 ± 0.05	0.04 ± 0.01	0.04 ± 0.01
	G3-T1-F1s	0.32 ± 0.03	0.29 ± 0.02	0.05 ± 0.01	0.04 ± 0.01
	G3-T1-F2s	0.39 ± 0.06	0.35 ± 0.04	0.05 ± 0.01	0.04 ± 0.01
	G3-T1-F3s	0.40 ± 0.06	0.35 ± 0.04	0.05 ± 0.01	0.04 ± 0.01
	G3-T1-F4s	0.44 ± 0.07	0.38 ± 0.05	0.04 ± 0.01	0.04 ± 0.01

In general, the values of the friction coefficient obtained by using the formulations derived from the analytical model of §3.2 are greater than the ones obtained by using the formulations derived from EN 15129 (CEN, 2018a), with an average percentage difference of 9% for the NN configuration and 7% for the NB configuration. Also, the values of the friction coefficient associated with the x direction are significantly greater than the ones associated with the y direction, with an average percentage difference of 89% for the NN configuration and 87% for the NB configuration (almost twice as much was expected, consistently with what observed in §3.2). This behaviour confirms the remark of §6.1.1: μ_l is strictly related to the overall behaviour of the device, which differs from x to y directions.

The friction coefficient values μ_r, which are associated with the mechanical properties of the friction interfaces of the device, are computed according to §6.1.1 formulations. Table 6.8 lists the average values of $\mu_{r,an}$ and $\mu_{r,EDC}$ with the standard deviation for NN and NB configuration in both x and y directions. In NN configuration, $\mu_{r,an}$ averages 0.74 in the x direction and 0.42 in the y direction, while $\mu_{r,EDC}$ averages 0.67 in the x direction and 0.36 in the y direction. In NB configuration, $\mu_{r,an}$ averages 0.40 in the x direction and 0.26 in the y direction, while $\mu_{r,EDC}$ averages 0.35 in the x direction and 0.24 in the y direction.

Once again, the values of the friction coefficient obtained by using the formulations derived from the analytical model of §3.2 are greater than the ones obtained by using the formulations derived from EN 15129 (CEN, 2018a), with an average percentage difference of 11% for the NN configuration and 9% for the NB configuration. In addition, the values of the friction coefficient associated with the x direction are moderately greater than the ones associated with the y direction, with an average percentage difference of 45% for the NN and 35% for the NB. This behaviour confirms the remark of §6.1.1: μ_r is strictly related to the mechanical properties of the friction interfaces of the device, which are the same in both directions. However, it is worth noting that the difference between longitudinal and transversal components is still evident because of the non-ideal behaviour of the friction interface, which usually differs from the theoretical one.

TABLE 6.15: Friction coefficients associated with the rotational mechanism of the friction interface of G3-T2 tests for NN and NB configurations.

Configuration	Test tag	$\mu_{r,an,x}$	$\mu_{r,EDC,x}$	$\mu_{r,an,y}$	$\mu_{r,EDC,y}$
NN	G3-T1-F1c	0.67 ± 0.1	0.62 ± 0.1	0.31 ± 0.11	0.31 ± 0.13
	G3-T1-F2c	0.59 ± 0.07	0.55 ± 0.08	0.21 ± 0.12	0.28 ± 0.13
	G3-T1-F3c	0.56 ± 0.08	0.53 ± 0.08	0.26 ± 0.08	0.26 ± 0.13
	G3-T1-F4c	0.61 ± 0.06	0.58 ± 0.07	0.25 ± 0.05	0.27 ± 0.13
	G3-T1-F1s	0.9 ± 0.06	0.79 ± 0.06	0.45 ± 0.07	0.38 ± 0.09
	G3-T1-F2s	0.83 ± 0.06	0.72 ± 0.07	0.63 ± 0.16	0.45 ± 0.15
	G3-T1-F3s	0.88 ± 0.01	0.78 ± 0.04	0.61 ± 0.15	0.48 ± 0.13
	G3-T1-F4s	0.86 ± 0.03	0.77 ± 0.06	0.6 ± 0.12	0.47 ± 0.15
NB	G3-T1-F1c	0.33 ± 0.06	0.31 ± 0.06	0.21 ± 0.06	0.2 ± 0.04
	G3-T1-F2c	0.22 ± 0.02	0.21 ± 0.02	0.18 ± 0.05	0.18 ± 0.04
	G3-T1-F3c	0.32 ± 0.06	0.31 ± 0.06	0.22 ± 0.05	0.22 ± 0.04
	G3-T1-F4c	0.32 ± 0.06	0.31 ± 0.06	0.26 ± 0.04	0.25 ± 0.05
	G3-T1-F1s	0.43 ± 0.04	0.36 ± 0.02	0.3 ± 0.02	0.26 ± 0.06
	G3-T1-F2s	0.52 ± 0.08	0.43 ± 0.04	0.3 ± 0.02	0.27 ± 0.07
	G3-T1-F3s	0.53 ± 0.07	0.44 ± 0.04	0.3 ± 0.02	0.27 ± 0.07
	G3-T1-F4s	0.58 ± 0.09	0.48 ± 0.05	0.28 ± 0.02	0.26 ± 0.07

It is worth noting that μ_r values and the differences between longitudinal and transversal components here computed using 2D wafeforms are comparable with the one derived from the mono-directional tests of §6.2.3. This result allows to neglect any eventual interaction effect between longitudinal and transversal forces.

Temperature. Figure 6.29 reports the temperature increment ΔT recorded during the tests for NN and NB configuration in the dissipative areas DA2&DA3 and DA1 (Figures 6.29(a) and 6.29(b), respectively). Both configurations exhibited greater ΔT values in the dissipative areas DA2&DA3, as a result of higher force values and a hysteresis cycle with a more evident rectangular and wider loop shape in the x direction. Moreover, ΔT decrements as the total duration of tests decrements. DA2&DA3 exhibit ΔT values averaging 1.6°C and 0.4°C for the NN and NB configurations respectively. Similarly, DA1 exhibits ΔT values averaging 0.4°C and 0.3°C for the NN and NB configurations respectively. NB registers the smaller difference between ΔT values in both x and y directions (percentage difference of 28%), exhibiting once again a more stable overall behaviour than the NN configuration (percentage difference of 76%).

NB registers the smaller difference between ΔT values in the x direction, which is associated with a more stable behaviour.

The evaluation of the parameters for the selection of the better-performing configuration highlights that NB exhibits a steadier and more efficient behaviour than the NN configuration. Moreover, the computed values of μ_r, especially the ones associated with the x direction, are aligned with the ones obtained from the tribological investigation of Chapter 4. For these reasons, the NB configuration is selected as the better-performing and is subjected to additional tests with the incremented torque level T2 (75 Nm).

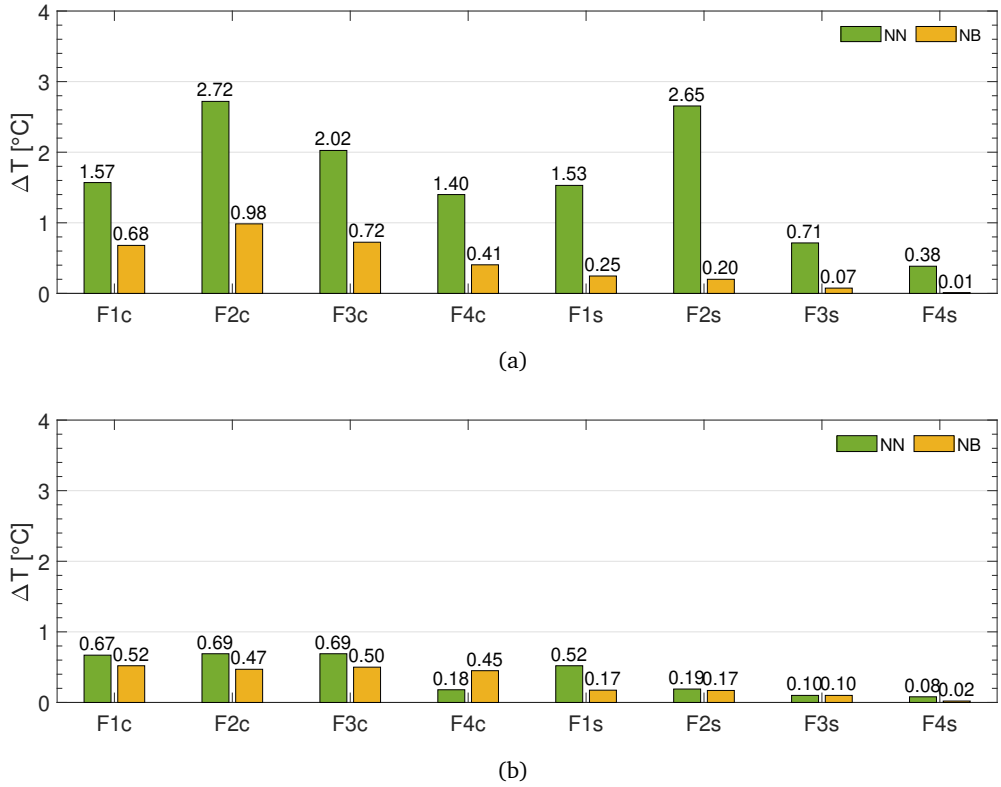

FIGURE 6.29: Temperature increment ΔT in dissipative areas (a) DA2&DA3 and (b) DA1 of G3-T1 tests. Comparison between NN and NB.

6.2.5.2 T2 test results

Hysteresis cycles. Figure 6.30 shows the recorded hysteresis cycles for NB when subjected to cloverleaf and spiral waveforms, respectively. As before, the hysteresis cycle shape does not change with the input frequency. The hysteresis cycle shapes in the x direction (blue lines) are mainly rectangular, with a moderate hardening effect caused by a stick-slip mechanism in correspondence with the reverse-motion point, especially for large displacements. The hysteresis shapes in the y direction (orange lines) significantly differ for cloverleaf (Figures 6.30(a-d)) and spiral (Figures 6.30(e-h)) cases. The hysteresis shapes are rectangular with rounded corners corresponding with the reverse-motion point for the cloverleaf input. In contrast, in the spiral case, the hysteresis cycle are rectangular but with a slight V shape.

Despite the increment of torque level, the hysteresis loop shape of the NB configurations still does not differ when incrementing the amplitude and frequency of the signal. As emphasised before, this is a promising behaviour because it ensures that the device's response during an earthquake remains consistent, regardless of the wave frequency content. Again, the NB configuration shows a difference between the x and y direction hysteresis cycle: this can be explained by considering a combination of the device geometrical layout and the configuration of the experimental setup. Moreover, the recorded hysteresis cycles of NB configuration with T2 are similar to the ones obtained for NN with T1. However, NB exhibits a more rectangular and steadier shape, unaltering its damping capability.

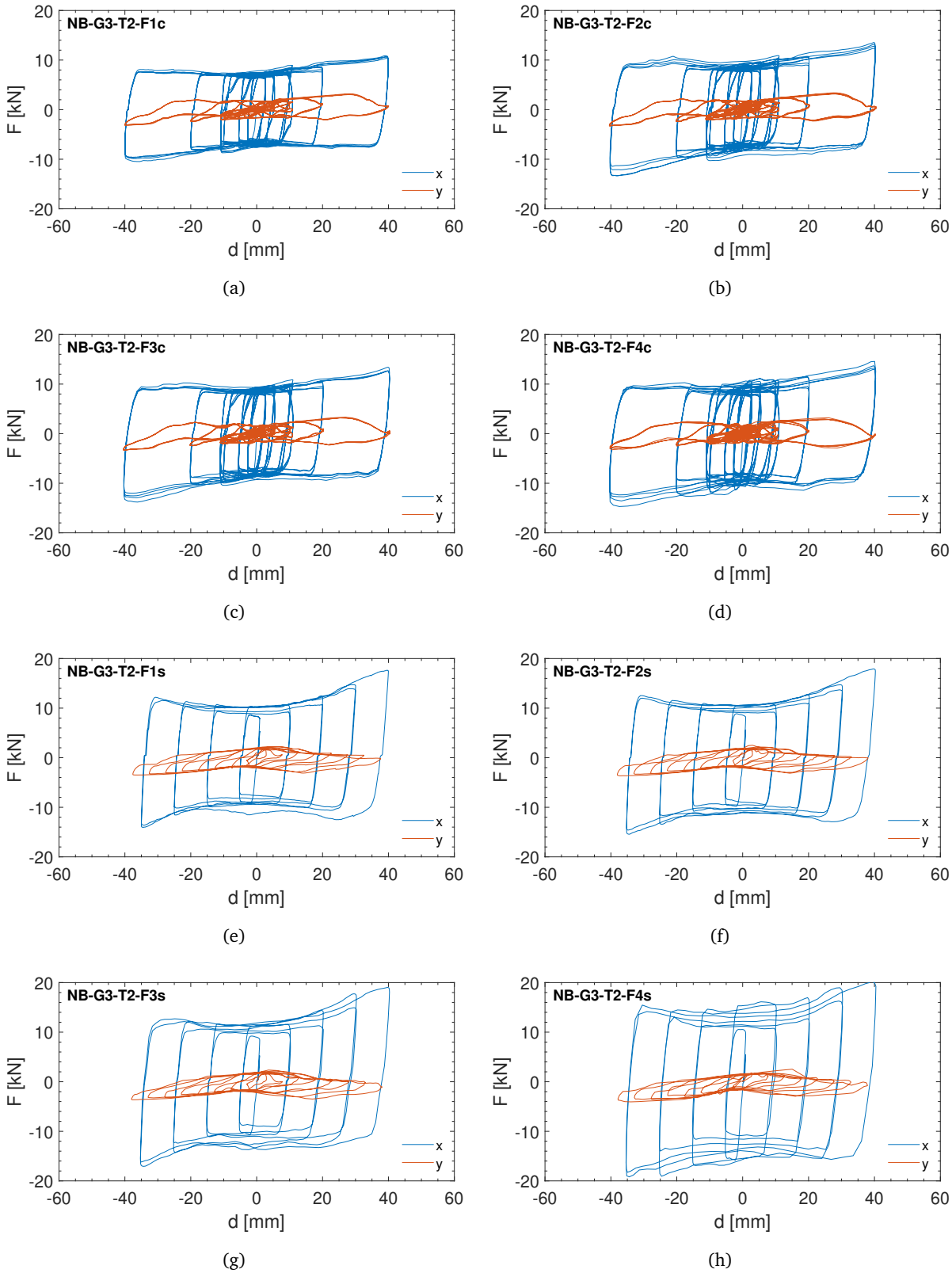

FIGURE 6.30: NB-T2-G3 test hysteresis cycles in x and y directions: a) F1c, b) F2c, c) F3c, d) F4c, e) F1s, f) F2s, g) F3s and h) F4s test protocols.

Activation and maximum forces. The activation forces F_{act} and the maximum forces F_{max} are computed according to §6.1.1; Table 6.16 lists the average values with the standard deviation for the NB configuration in the x and y directions. When the NB configuration is subjected to T2 torque level, F_{act} values average 9.40 kN in the x direction and 0.94 kN in the y direction, while F_{max} values average 11.19 kN in the x direction and 1.67 kN in the y direction.

TABLE 6.16: G3-T1 test activation and maximum forces.

Test tag	$F_{act,st,x}$ [kN]	$F_{act,st,y}$ [kN]	$F_{max,st,x}$ [kN]	$F_{max,st,y}$ [kN]	ΔF_x	ΔF_y
G3-T1-F1c	6.71 ± 0.4	0.56 ± 0.26	7.59 ± 0.77	1.71 ± 0.39	13%	206%
G3-T1-F2c	7.75 ± 0.49	0.71 ± 0.25	9.09 ± 0.97	1.78 ± 0.38	17%	153%
G3-T1-F3c	8.15 ± 0.58	0.73 ± 0.26	9.37 ± 0.89	1.77 ± 0.39	15%	142%
G3-T1-F4c	8.72 ± 0.71	0.78 ± 0.26	10.15 ± 1.07	1.77 ± 0.34	16%	127%
G3-T1-F1s	9.41 ± 0.87	1.06 ± 0.11	11.79 ± 0.57	1.67 ± 0.19	25%	59%
G3-T1-F2s	10.11 ± 0.87	1.34 ± 0.24	12.26 ± 0.53	1.69 ± 0.15	21%	26%
G3-T1-F3s	11.11 ± 0.46	1.21 ± 0.19	13.34 ± 0.84	1.71 ± 0.13	20%	41%
G3-T1-F4s	13.2 ± 0.61	1.12 ± 0.19	15.9 ± 1.57	1.27 ± 0.22	20%	13%

The components in both x and y directions exhibit a significant force increment from the T1 to T2 torque level, averaging 55% and 24% for the x and y directions, respectively. However, the percentage difference between F_{act} and F_{max} (ΔF) exhibits an increment from the T1 to T2 torque level, with average values of 19% and 96% for the x and y directions, respectively. This increment is particularly evident in the y direction and the tests performed with the cloverleaf input waveform.

The evaluation of activation and maximum forces highlights that when NB is subjected to T2 torque level, it behaves more similarly to the NN configuration subjected to T1 torque. This highlights that the combination of the device geometrical layout and the configuration of the experimental setup is more evident when the BRFD develops higher force values. However, the NB configuration still behaves better than the NN one, registering steadier force values.

Equivalent damping coefficient. The equivalent damping coefficient $\xi_{eq,hyst}$ is computed according to §6.1.1, and Figure 6.31 shows the average values with the standard deviation bar in both x and y directions. $\xi_{eq,hyst}$ values are higher in the x direction, as a result of a hysteresis cycle with a more evident rectangular shape, with $\xi_{eq,hyst}$ values averaging 51%, which is similar to the one computed for T1 torque. On the contrary, the peculiar hysteresis cycle shape of the y direction is responsible for the smaller $\xi_{eq,hyst}$ values, which average 31%, which is smaller than the one computed for T1 torque.

The evaluation of the equivalent damping coefficient highlights that the increment of torque influences the y direction. In fact, the hysteresis cycles in the transversal direction with T2 exhibit a less rectangular loop shape than the ones with T1, and this difference is reflected in the lower $\xi_{eq,hyst}$ values.

Stud bolts axial load. The stud bolts axial load F_P is computed by using the relationship of §6.2.1, while the stud bolts axial load loss ΔF_P by using the relationship of §6.1.1. Table 6.17 lists the average values of F_P and ΔF_P with the coefficient of variation cv_{F_P} of SB1, SB2 and SB3 for the NB configuration in both x and y directions. SB2 and SB3 exhibit F_P values averaging 30.29 kN, with cv_{F_P} averaging 11.21%

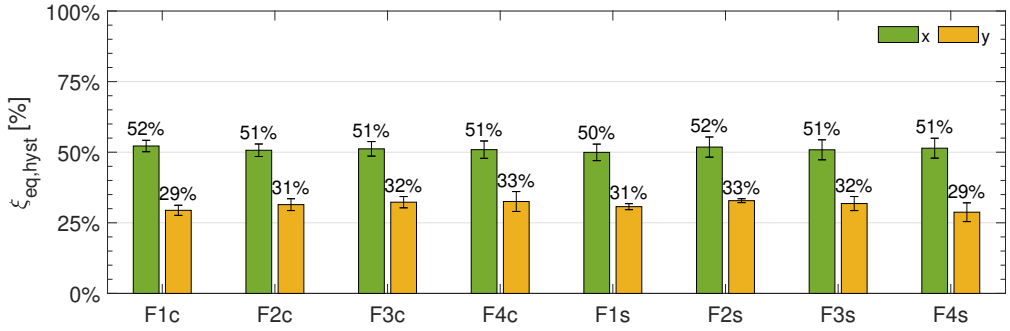

FIGURE 6.31: Equivalent damping values $\xi_{eq,hyst}$ of G3-T2 tests in x and y directions.

and a tension loss ΔF_P averaging 1.54%. Similarly, SB1 exhibits F_P values averaging 38.85 kN, with cv_{Fp} averaging 0.71%, and tension loss ΔF_P averaging 1.18%.

TABLE 6.17: G3-T1 test stud bolts axial tension and axial tension loss.

Test tag	SB2&SB3			SB1		
	F_P [kN]	cv_{Fp}	ΔF_P	F_P [kN]	cv_{Fp}	ΔF_P
G3-T1-F1c	29.91	9.92%	-1.11%	38.18	0.48%	0.84%
G3-T1-F2c	30.18	10.04%	-1.89%	38.57	0.51%	-0.61%
G3-T1-F3c	30.82	10.98%	-1.33%	38.68	0.53%	-0.38%
G3-T1-F4c	30.40	10.80%	5.88%	38.92	0.50%	4.15%
G3-T1-F1s	30.44	11.71%	1.07%	39.44	0.61%	1.38%
G3-T1-F2s	30.38	11.84%	-0.22%	39.02	0.62%	0.08%
G3-T1-F3s	30.43	12.07%	0.12%	39.08	0.98%	0.08%
G3-T1-F4s	29.72	12.36%	0.68%	38.87	1.46%	3.94%

The NB configuration registers smaller F_P values in the x direction also when subjected to T2 torque level, confirming the remarks of §6.2.1. However, the ΔF_P values decreased with respect to an average lower than 2% in both directions. As a result, the stud bolt axial force is steadier when NB is subjected to the T2 torque level.

Friction coefficient. The friction coefficient values μ_l, which are associated with the overall BRFD linear behaviour, are computed according to §6.1.1 formulations. Figure 6.17 shows the average values of $\mu_{l,an}$ and $\mu_{l,EDC}$ with the standard deviation bar for the NB configuration in both x and y directions. When the NB configuration is subjected to T2 torque level, $\mu_{l,an}$ averages 0.31 in the x direction and 0.03 in the y direction, while $\mu_{l,EDC}$ averages 0.29 in the x direction and 0.03 in the y direction.

The friction coefficient values μ_r, which are associated with the mechanical properties of the friction interfaces of the device, are computed according to §6.1.1 formulations. Figure 6.18 shows the average values of $\mu_{r,an}$ and $\mu_{r,EDC}$ with the standard deviation bar for the NB configuration in both x and y directions. When the NB configuration is subjected to T2 torque level, $\mu_{r,an}$ averages 0.41 in the x direction and 0.19 in the y direction, while $\mu_{r,EDC}$ averages 0.37 in the x direction and 0.17 in the y direction.

Once again, the values of the friction coefficient obtained by using the formulations derived from the analytical model of §3.2 are greater than the ones obtained by using the formulations derived from EN 15129 (CEN, 2018a), with an average percentage difference of the 6% for both μ_l and μ_r. In addition, the

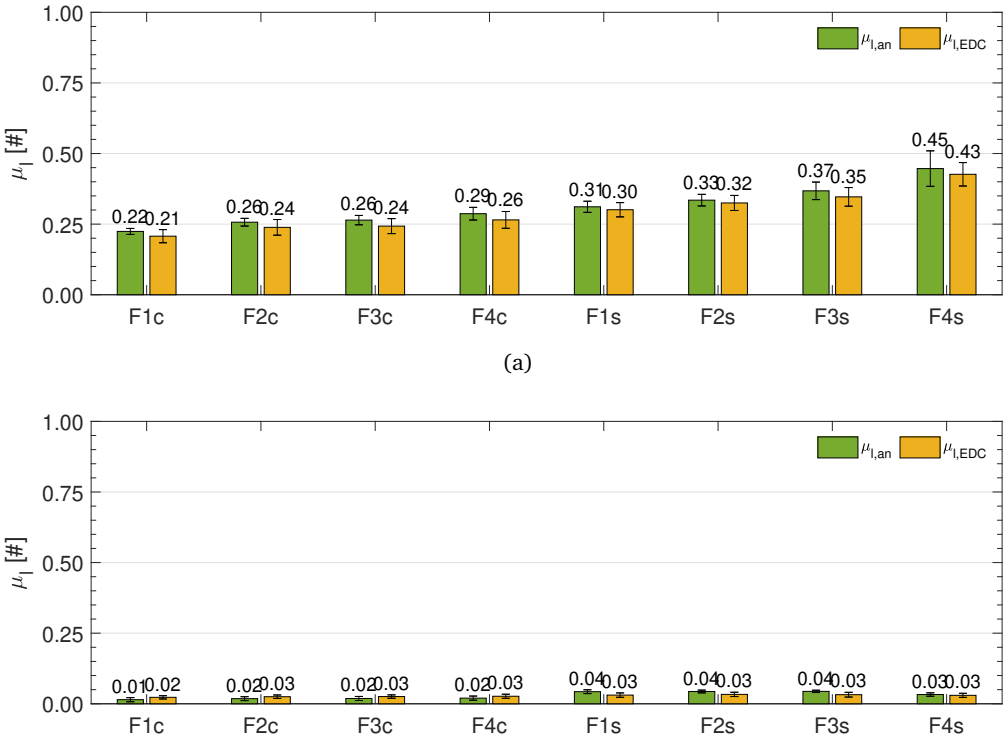

FIGURE 6.32: Friction coefficients associated with the overall BRFD linear behaviour μ_l of G3-T2 tests in a) x and b) y directions.

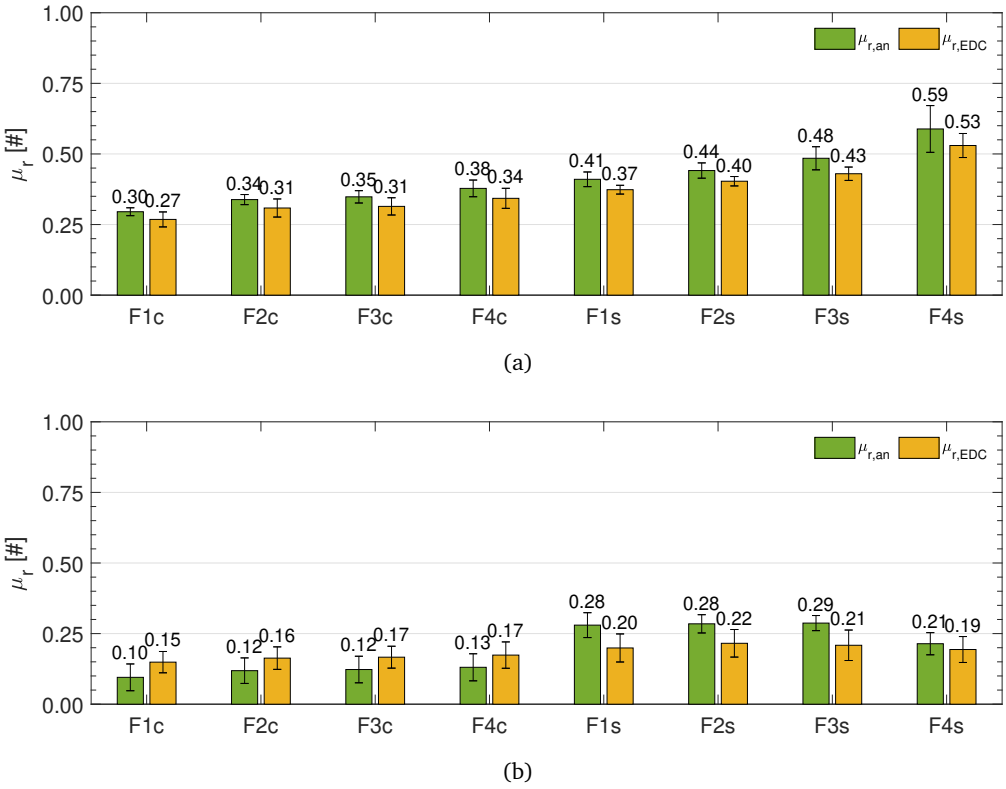

FIGURE 6.33: Friction coefficients associated with the rotational mechanism of the friction interface μ_r of G3-T2 tests in a) x and b) y directions.

values of the friction coefficient associated with the x direction are greater than the ones related to the y direction, with an average percentage difference of 90% for μ_l and of the 52% for μ_r.

The evaluation of the friction coefficients highlights that the increment of torque influences mainly the y direction. In fact, the μ_l and μ_r values exhibit a decrement of 24% in the y direction and an increment of 3% in the x direction.

Temperature. Figure 6.34 reports the temperature increment ΔT recorded during the tests in both x and y directions. Similarly to the previous tests, ΔT exhibits greater values in the x direction, as a result of higher force values and a hysteresis cycle with a more evident rectangular and wider loop shape. Moreover, ΔT decrements as the total duration of tests decrements. NB exhibits ΔT values averaging 0.7°C and 0.5°C in x and y directions, respectively, with a percentage difference of 38%.

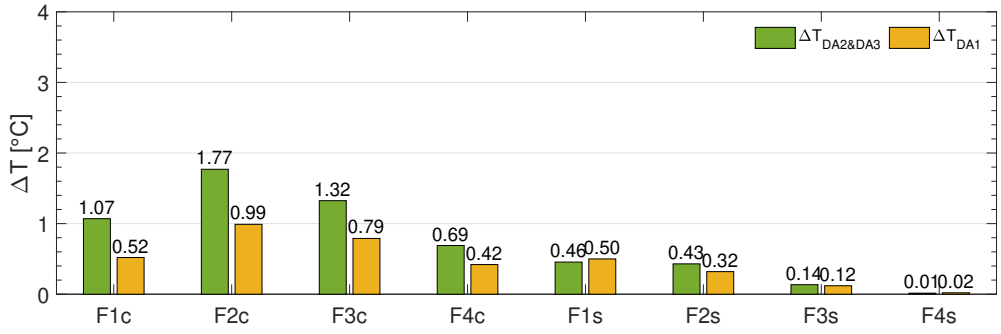

FIGURE 6.34: Temperature increment ΔT in dissipative areas DA2&DA3 and DA1 of G3-T2 tests.

The assessment of the torque increment on the BRFD behaviour highlights that, while the component in the x direction still exhibits a good performance with a significant steady and rectangular-shaped hysteresis cycle, the performance of the component in the y direction slightly decreases. This highlights the need for a further study of the BRFD elements majorly involved in developing the the component in the y direction.

6.3 Conclusive remarks

The present Chapter shows the results of bidirectional experimental tests performed on a novel bidirectional rotational friction damper (BRFD). These tests were performed by tuning two orthogonal actuators and imposing sinusoidal and triangular monodimensional input paths, and two bidimensional orbital input paths, a cloverleaf and a spiral one, with crescent amplitude and different frequencies. In addition, the stud bolts of the device were instrumented to measure and monitor the axial force of the bolts during the tests. Two different configurations of the BRFD were manufactured and tested: NN with nickelled steel vs. nickelled steel friction pads coupling and NB with nickelled steel vs. bronze friction pads coupling. Three test groups were defined: Group 1 (G1) tests aimed at assessing the BRFD behaviour in a monodirectional real-use condition; Group 2 (G2) tests aimed at determining the relationship between the coefficient of friction and the velocity to calibrate a numerical friction model; a final Group 3 (G3) aimed at assessing

the BRFD behaviour in a bidirectional real-use condition. Firstly, NN and NB were subjected to the monodimensional and bidimensional orbits with 50 Nm torque (T1), and then the better-performing coupling was subjected to 75 Nm torque (T2). The main findings and remarks are summarised below:

- The calibration of the instrumented stud bolts highlights that, while the relationship between the axial force (F_P) and the strain (ε) is similar for all the stud bolts, the relationship between the axial force (F_P) and the applied torque (T) differ for different coupling materials, i.e. NN to NB configuration. More precisely, NN exhibits higher k_{eq} values than NB, and as a result NN reaches lower F_P values than NB when applying the same torque T. This can be explained by the higher deformability of the bronze in respect to the steel. As a result, surfaces coupling with different materials can significantly affect the k_{eq} values.

- RI test results highlight a significant steadiness increment of the BRFD behaviour in both NN and NB configurations. More precisely, the coefficient of variations decreases from around 9% to 6% for the NN configuration and from around 13% to 4% for the NB configuration. Despite the overall BRFD improvement after the running-in, the NB configuration exhibits a better-performing behaviour than the NN configuration, with overall steadier hysteresis cycles, lower influence of stud bolts axial tension loss and variation, and temperature increment.

- G1 test results highlight that the hysteresis cycles for NN and NB configurations are mainly rectangular with a slight hardening effect caused by a stick-slip mechanism in correspondence with the reverse motion point in both x and y direction, and do not differ with signal frequency. This is a promising behaviour because it ensures that the device's performance during an earthquake remains consistent, regardless of the ground motion frequency content. Moreover, the similar behaviour exhibited for both NN and NB in the x and y directions highlights the stability of the BRFD. Concerning the comparison between the investigated configurations, NB exhibits a more rectangular and steadier shape despite the lower values of recorded forces. This behaviour is usually associated with a more effective damping capability, and it is confirmed by the equivalent damping coefficient values that average 47%. Again, the NB configuration exhibits a better-performing behaviour than the NN configuration, with overall steadier hysteresis cycles (7% of variation), lower influence of stud bolts axial tension loss (1.24%) and variation (0.47%), and temperature increment (0.6 °C).

- G2 test results highlight that the relationship between friction coefficient and sliding velocity decreases when the velocity increases. This behaviour is responsible for the stick-slip mechanism observed during the G1 tests, and it is less remarkable for the NB configuration. Moreover, it is worth noting that the μ_r values computed for both NN and NB configurations resemble the ones obtained during the tribological tests of Chapter 4. In fact, μ_r is strictly related to the mechanical properties of the friction interfaces of the device. Again, the NB configuration exhibits a steadier behaviour than the NN configuration both in terms of values variation, and difference between values computed with formulations derived from the analytical model of §3.2 and from EN 15129 (CEN, 2018a).

- G3 test results highlight that the hysteresis cycles for NN and NB configurations in the x direction are mainly rectangular with a hardening effect caused by a stick-slip mechanism corresponding with the reverse motion point, while in the y direction are rectangular with rounded corners for the cloverleaf signal, and have a V shape for the spiral signal. Regardless of the shape, the obtained hysteresis

cycles do not differ with signal frequency. This is a promising behaviour because it ensures that the device's performance during an earthquake remains consistent, regardless of the ground motion frequency content. Regarding the different behaviour exhibited for both NN and NB in the x and y directions, this can be explained by considering a combination of the device geometrical layout and the configuration of the experimental setup, as described at the end of §6.1. However, NB exhibits a more rectangular and steadier shape despite the lower values of recorded forces. This behaviour is usually associated with a more effective damping capability, and it is confirmed by the equivalent damping coefficient values that average 43%. Again, the NB configuration exhibits a better-performing behaviour than the NN configuration, with overall steadier hysteresis cycles (15% of variation), lower influence of stud bolts axial tension loss (3%) and variation (4%), and temperature increment (0.5°C).

- The application of T2 torque level mainly influences the force values and steadiness of the BRFD, especially in the x direction.
- The experimental setup allowed us to reproduce the longitudinal behaviour (x direction) fully and partially the transversal one (y direction). Therefore, the BFRD's damping capacity in y direction was partially exploited.

The findings of the present Chapter highlight the promising bidirectional behaviour of the BRFD, both in terms of hysteresis cycle steadiness and good damping capacity, especially the NB configuration, considered by the authors to be better performing.

Despite the good results, further research is needed to update the experimental setup configuration to allow the full BRFD damping capacity exploitation. Moreover, a numerical study is required to reproduce the behaviour of the BRFD by investigating different friction constitutive models. This last part is the focus of the followingg Chapter.

References

CEN (2018a). *Anti-seismic devices (UNI EN 15129:2018)*.

CEN (2018b). *Execution of steel structures and aluminium structures - Part 2: Technical requirements for steel structures (UNI EN 1090-2:2018)*.

Furinghetti, Marco, Alberto Pavese, Virginio Quaglini, and Paolo Dubini (2019). "Experimental investigation of the cyclic response of double curved surface sliders subjected to radial and bidirectional sliding motions". In: *Soil Dynamics and Earthquake Engineering* 117, pp. 190–202. DOI: 10.1016/j.soildyn.2018.11.020.

Jacobsen, Lydik S. (1965). "Damping in composite structures". In: Science Council of Japan, pp. 1029–1044.

MathWorks (2022). *MATLAB*.

Pavese, Alberto, Marco Furinghetti, and Chiara Casarotti (2018). "Experimental assessment of the cyclic response of friction-based isolators under bidirectional motions". In: *Soil Dynamics and Earthquake Engineering* 114, pp. 1–11. DOI: 10.1016/j.soildyn.2018.06.031.

7
Numerical BRFD models

7.1 Opensees elements for the BRFD numerical implementation

As mentioned in Chapter 3's conceptualization study and demonstrated in Chapters 5 and 6's experimental tests, the BRFD is comprised of moveable plates and its behaviour is strictly related to the friction interface generated by the friction pads. Therefore, to accurately simulate the BRFD, the numerical implementation must replicate the behaviour of its movable system and take into account a friction constitutive law to properly simulate the friction interface.

The bearing elements available inside Opensees (McKenna, 2011) are extremely adaptable and can be associated to a previous defined friction model. Among the available bearing models, the Flat Slider Bearing Element (FSB element) was selected because of its resemblance with the BRFD. In fact, both the FSB element and the BRFD are bidirectional and characterized by a flat friction interface whose behaviour is function of the applied vertical load.

The numerical implementation aimed at the definition of two different friction based numerical models that help the validation of the experimental test results: a simple model for an easy implementation inside a frame structure, and a more refined model of the BRFD itself to be used as a Virtual Lab tool. The following sections define the selected bearing elements and friction models.

7.1.1 Flat Slider Bearing Element

The Flat Slider Bearing Element (FSB element) was originally implemented to describe bearings with a flat friction interface. The FSB is an element object defined by two nodes as showed in Figure 7.1. The *iNode* represents the lower sliding surface while the *jNode* represents the upper sliders; the two nodes can have a distance equal to zero (*zero length*) or equal to an appropriate value (*non-zero length*). In a three-dimensional problem, the bearing has coupled friction properties for the shear deformations (local y and z axis of Figure 7.1) and force-displacement behaviour defined by an *UniaxialMaterial* in the remaining four directions.

The syntax of the command is the following:

```
element flatSliderBearing $eleTag $iNode $jNode $frnMdlTag $kInit -P $matTag ...
... -T $matTag -My $matTag -Mz $matTag -orient $x1 $x2 $x3 $y1 $y2 $y3 ...
... -shearDist $sDratio -doRayleigh -mass $m -iter $maxIter $tol
```

where:

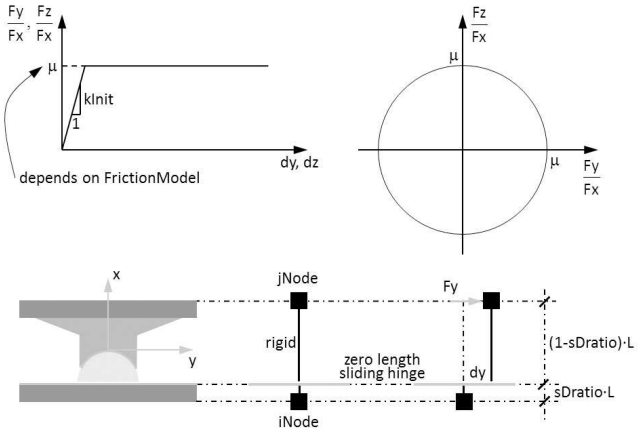

FIGURE 7.1: Flat Slider Bearing Element scheme and friction relationship (McKenna, 2011).

- `$eleTag` is the unique tag associated with the element object
- `$iNode $jNode` are the tags associated with *iNode* and *jNode* respectively
- `$frnMdlTag` is the tag associated with a previously defined *Friction Model*
- `$kInit` is the initial elastic stiffness in the local shear directions (see Figure 7.1)
- `-P $matTag` is the tag associated with a previously defined *UniaxialMaterial* in local axial direction
- `-T $matTag` is the tag associated with a previously defined *UniaxialMaterial* in local torsional direction
- `-My $matTag` is the tag associated with a previously defined *UniaxialMaterial* in moment direction around local *y*-direction
- `-Mz $matTag` is the tag associated with a previously defined *UniaxialMaterial* in moment direction around local *y*-direction
- `-orient $x1 $x2 $x3 $y1 $y2 $y3` is an optional command that defines the orientation of the local *x*-axis (`$x1 $x2 $x3`) and *y*-axis (`$y1 $y2 $y3`) in global coordinates (if not indicated, the local *x-y* axis coincides with the global *X-Y* axis if the element is *zero length*, and with the global *Z-Y* axis if the element is *non-zero length*)
- `-shearDist $sDratio` is an optional command that defines the shear distance between *iNode* and *jNode* (see Fig. 7.1)
- `-doRayleigh` is an optional command that includes the Rayleigh damping (by default is set equal to zero to avoid additional artificial viscus damping in the isolation system)
- `-mass $m` is an optional command that includes the mass of the element (by default is set equal to zero)
- `-iter $maxIter $tol` is an optional command that defines the maximum iterations (by default is set equal to 20) and the convergence tolerance (by default is set equal to 10^{-08}) to satisfy the element equilibrium

It is worth noting that, since friction forces can be affected by axial load and velocity, the FSB element can be numerically sensitive. Consequently, when performing a dynamic analysis the required convergence time-steps might be smaller than the ones used for a static analysis.

7.1.2 Friction models

The Opensees framework allows the association of one of the following friction models to the FSB element:

- *Coulomb Friction*, in which the COF is assumed to be constant
- *Velocity Dependent Friction*, in which the COF is assumed to reach different values between higher-lower velocities
- *Velocity and Normal Force Dependent Friction*, in which the COF is assumed to reach different values between higher-lower velocities and decreases when the axial load increments
- *Velocity and Pressure Dependent Friction*, in which the COF is assumed to reach different values between higher-lower velocities and decreases when the vertical pressure increments
- *Multi-Linear Velocity Dependent Friction*, in which the COF is assumed to reach different values between higher-lower velocities but the user can impose a friction-velocity relationship

In the present study only three of the listed models were selected for the numerical implementation of the BRFD; more precisely, the Coulomb Friction (CF), Velocity Dependent Friction (VDF) and Multi-Linear Velocity Dependant Friction (MLVDF) models were considered. In fact, the experimental test results of Chapter 6 highlighted that the COF was unaffected by the increment of the stud bolts tension load. On the contrary, the investigated configurations registered a COF variation when incrementing the sliding velocity.

7.1.2.1 Coulomb Friction model

The Coulomb Friction model was selected to be used mainly as a reference and, thanks to its numerical stability, to easily calibrate the FSB element in Opensees (McKenna, 2011). According to Coulomb Friction law, the friction coefficient is not affected by the sliding velocity increment, as showed in Figure 7.2, resulting in a constant friction force.

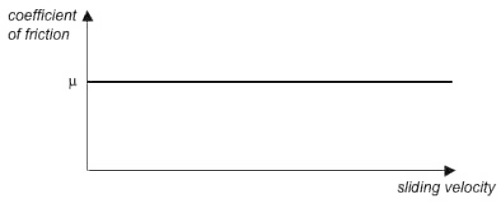

FIGURE 7.2: Relationship between friction and sliding velocity according to Coulomb's Friction law (McKenna, 2011).

The syntax of the command is the following:

```
frictionModel Coulomb $frnTag $mu
```

where:

- `$frnTag` is the unique tag associated with the friction model object
- `$mu` is the friction coefficient

7.1.2.2 Velocity Dependent Friction model

The Velocity Dependant Friction model was selected to reproduce the dependency of the friction coefficient of the investigated BRFD configurations with the sliding velocity. However, the selected model was originally implemented for PTFE and PTFE-like materials sliding on stainless steel interfaces (Constantinou et al., 1999), in which at lower sliding velocities are associated lower COF values, as showed in Figure 7.3, consequently the model might not be adequate to reproduce the friction interface properties of the investigated BRFD configurations.

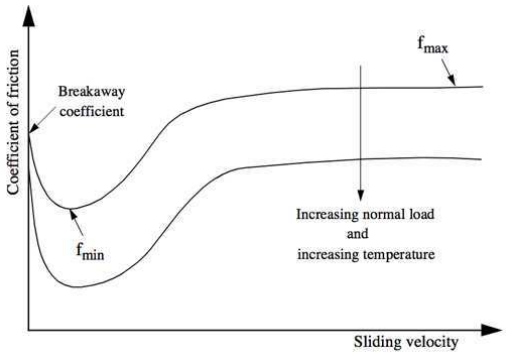

FIGURE 7.3: Relationship between friction and sliding velocity for PTFE and PTFE-like materials on stainless steel interfaces (Constantinou et al., 1999).

The syntax of the command is the following:

```
frictionModel VelDependent $frnTag $muSlow $muFast $transRate
```

where:

- `$frnTag` is the unique tag associated to the friction model object
- `$muSlow` is the friction coefficient for low velocities
- `$muFast` is the friction coefficient for high velocities
- `$transRate` is the transition rate to control the COF's transition from low to high velocity

The friction-velocity relationship for this friction model is defined as follows:

$$\mu = \mu_{fast} - \left(\mu_{fast} - \mu_{slow}\right) e^{-av} \tag{7.1}$$

where μ_{fast} is the COF at high velocity, μ_{slow} is the COF at low velocity, a is the transition rate and v the sliding velocity (Constantinou et al., 1999).

7.1.2.3 Multi-Linear Velocity Dependent Friction model

The Multi-Linear Velocity Dependant Friction model was selected to reproduce the dependency of the friction coefficient of the investigated BRFD configurations with the sliding velocity by defining a friction-velocity relationship using the test results of §6.2.4. The syntax of the command is the following:

```
frictionModel VelDepMultiLinear $frnTag -vel $velocityPoints -frn $frictionPoints
```

where:

- `$frnTag` is the unique tag associated to the friction model object
- `-vel $velocityPoints` is an array of velocity points
- `-frn $frictionPoints` is an array of COF points

In defining the array points for the friction-velocity relationship, no negative points are allowed and both arrays must have the same dimensions. Moreover, to properly define the transition between low and high velocities, a higher number of points is needed at the lower velocities in respect to the higher ones.

7.1.3 Numerical implementation of the BRFD

As stated above, the numerical implementation aimed at the definition of two different friction-based numerical models. The first one is a simplified numerical model that can be easily implemented in a structural frame and that simulates the overall BRFD behaviour. The second one is a refined numerical model that resembles the real geometry of the BRFD and simulates the real behavior and interactions of the main elements of the BRFD.

The simplified numerical model is obtained by using a single FSB element with a calibrated friction model: adopting this approach, the overall BRFD behaviour coincides with the shear behaviour of the FSB element.

The refined numerical model is obtained firstly by combining two single FSB element to reproduce the rotational behaviour of the friction interface: this modelling approach allows the simulation of the sliding moment of each friction interface of the BRFD. Finally, *elasticbeam* elements, which reproduce the core and connection plates of the BRFD, connect each friction interface: this modelling approach allows the simulation of the entire BRFD and a detailed reproduction of all its elements' movements.

The following §7.2 and §7.3 show a complete discussion of the simplified and refined BRFD numerical models, respectively.

7.2 BRFD simplified numerical model

7.2.1 Numerical implementation scheme

The simplified numerical model of the BRFD aims at reproducing its overall behaviour by computing both longitudinal and transversal components (x and y directions, respectively). To numerically obtain that, a single FSB element is considered following the scheme of Figure 7.4. Nodes 1 and 2 represent the connection points of the BRFD and at a distance t_{eq} from each other, resembling the overall thickness of

the BRFD friction interface. A vertical force F_P simulates the presence of the stud bolts axial tension and an FSB element connects Node 1 to Node 2.

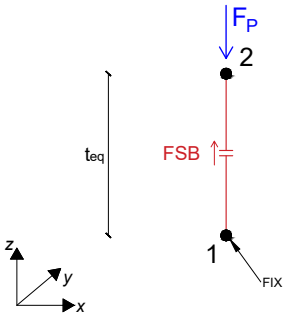

FIGURE 7.4: Scheme of the simplified BRFD numerical model implementation.

It is worth noting that, because of the definition of the FSB element itself, the obtained forces along the x direction equal the ones along the y direction, differing from the overall behaviour of the BRFD. In fact, according to the analytical model of §3.2, the components of the BRFD in the x and y directions differ by 42%. However, when considering that the BRFD has an inclination angle of 45° from the existing beam, as reported in the installation scheme of Figure 3.1(b), this difference decreases. As a result, in the BRFD horizontal projection on the global XY plane, the transversal component remains unaltered, while the longitudinal one is reduced by cos(45°). Thus, when considering the global structural behaviour, the forces provided by the BRFDs in the global X and Y directions are comparable. For these reasons, it is correct to affirm that the simplified numerical model reproduces the horizontal projection of the overall BRFD behaviour.

7.2.2 Calibration using different friction models

The calibration of the investigated friction constitutive models to be implemented inside the simplified numerical model considers the friction coefficient values μ_l of §6.2.4, which are associated with the overall behaviour of the BRFD. The experimental relationships of Figure 6.21 between μ_l and the sliding velocity v are used as to identify the friction values to insert in the constitutive models. More precisely, for the CF model, the value for `$mu` is computed as the average μ_l values along the x and y directions, respectively. For the VDF model, the value for `$muFast`, `$muSlow` and `$transRate` are computed by fitting Eq. 7.1 to the experimental relationships of Figure 6.21. For the MLVDF model, the values for `$velocityPoints` and `$frictionPoints` are computed by interpolating the experimental curve of Figure 6.21.

Figure 7.5 shows the calibration results for the VDF and MLVDF models by comparing the experimental results (continues lines) with the numerical fittings for the VDF and MLVDF models (dashed and dotted-dashed lines, respectively), while Table 7.1 lists the values adopted for the investigated friction models. In the CF model the `$mu` ($\mu_{l,x}$ and $\mu_{l,y}$) equals the average μ_l values of Figure 7.5 computed in in x and y directions. In the VDF model, `$muFast` ($\mu_{l,x,fast}$ and $\mu_{l,y,fast}$) and `$muSlow` ($\mu_{l,x,slow}$ and $\mu_{l,y,slow}$) equal the minimum and maximum μ_l values of Figure 7.5, respectively, computed in in x and y directions, while `$transRate` ($a_{l,x}$ and $a_{l,t}$) are computed by fitting the formulation of Eq. 7.1 with the experimental $\mu_l - v$ relationship. In MLVDF model, `$velocityPoints` (v_x and v_y) is a vector of sliding velocity comprised

between 0 mm/s and the maximum recorded sliding velocity 160 mm/s, while `$frictionPoints` is a vector that represent the curve of Figure 7.5.

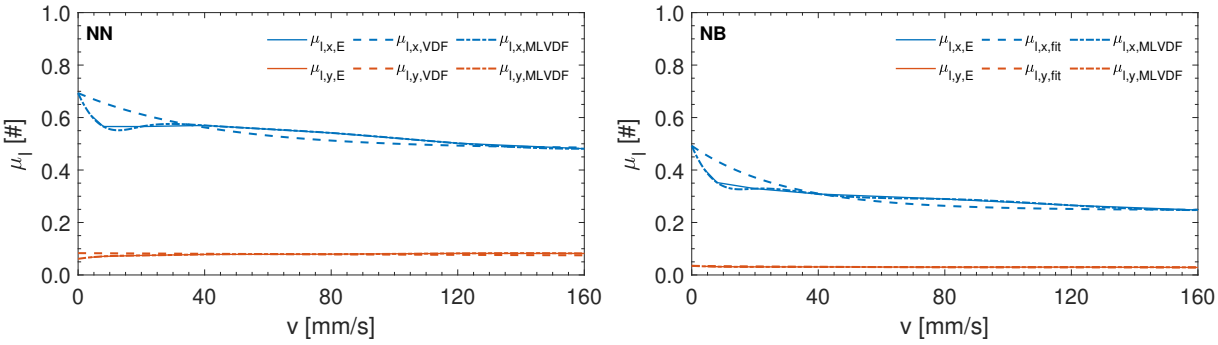

(a) (b)

FIGURE 7.5: Adopted $\mu_l - v$ relationship for the simplified numerical model in x and y directions of a) NN and b) NB configurations.

TABLE 7.1: $\mu_l - v$ calibration results for NN and NB.

Friction model	Parameters	NN	NB
CF	$\mu_{l,x}$	0.55	0.31
	$\mu_{l,y}$	0.08	0.03
VDF	$\mu_{l,x,fast}$	0.48	0.25
	$\mu_{l,x,slow}$	0.69	0.49
	$a_{l,x}$ [s/mm]	0.024	0.036
	$\mu_{l,y,fast}$	0.07	0.03
	$\mu_{l,y,slow}$	0.08	0.03
	$a_{l,y}$ [s/mm]	0.003	0.025
MLVDF	v_x [mm/s]	[0 40 80 120 160]	[0 40 80 120 160]
	$\mu_{l,x}$	[0.69 0.57 0.54 0.50 0.48]	[0.49 0.31 0.29 0.27 0.25]
	v_y [mm/s]	[0 40 80 120 160]	[0 40 80 120 160]
	$\mu_{l,y}$	[0.06 0.08 0.08 0.08 0.08]	[0.03 0.03 0.03 0.03 0.03]

To assess the accuracy in the representation of the BRFD behaviour, the simplified numerical model is subjected to G1-T1-F2, G3-T1-F2c and G3-T1-F2s test protocols of the bidirectional experimental tests (see Table 6.1). More precisely, G1-T1-F2 is a mono-directional test with a sinusoidal input waveform at a frequency of 0.50 Hz, G3-T1-F2c is a bi-directional test with a cloverleaf input 2D waveform at a frequency of 0.25 Hz and G3-T1-F2s is a bi-directional test with a spiral input 2D waveform at a frequency of 0.125 Hz. In all the mentioned test F_P value averages 22 kN. To compare the experimental results with the numerical simulation, the hysteresis cycles components are projected on a 45° plane, to simulate the installation angle inside a frame, and the transversal components are halved, to reproduce the experimental setup limits along the transversal (y) direction.

The comparison between experimental (E-curves) and simplified numerical model (N-curves) results are represented in Figures 7.6, 7.7 and 7.8 for G1-T1-F2, G3-T1-F2c and G3-T1-F2s tests respectively of NN configuration, and in Figures 7.9, 7.10 and 7.8 for G1-T1-F2, G3-T1-F2c and G3-T1-F2s tests respectively of NB configuration. All the figures compare CF, VDF and MLVDF models.

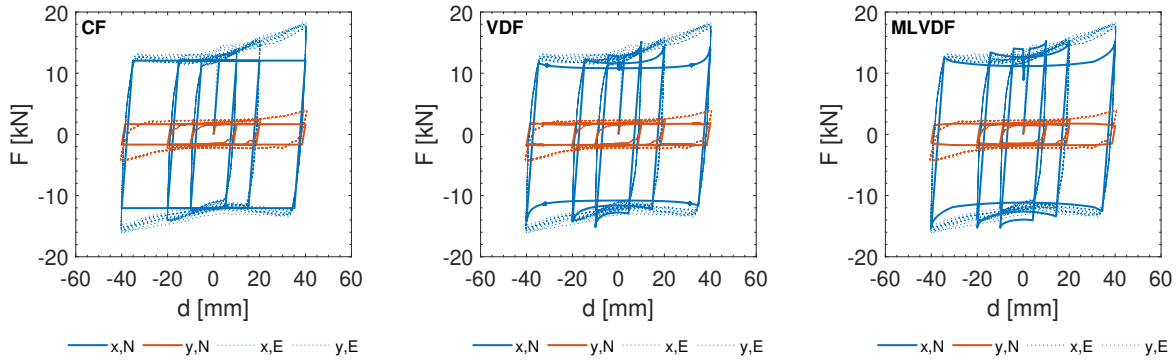

(a) (b) (c)

FIGURE 7.6: Comparison between experimental and simplified numerical model of NN sinusoidal G1-T1-F2 tests using a) CF, b) VDF and c) MLVDF models.

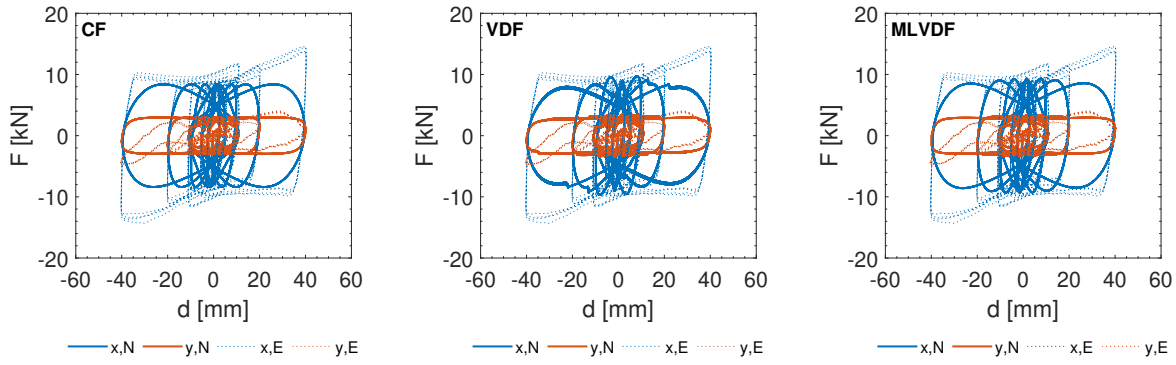

(a) (b) (c)

FIGURE 7.7: Comparison between experimental and simplified numerical model of NN cloverleaf G1-T1-F2 G1-T1-F2c tests using a) CF, b) VDF and c) MLVDF models.

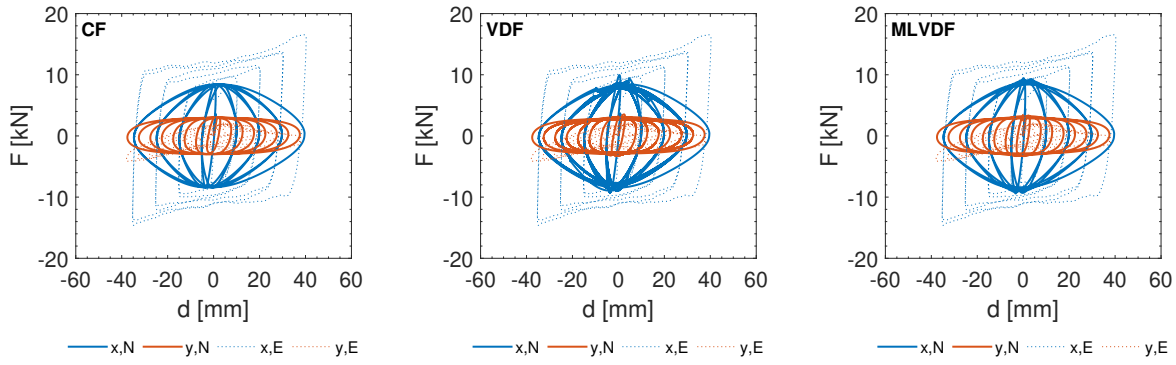

(a) (b) (c)

FIGURE 7.8: Comparison between experimental and simplified numerical model of NN spiral G1-T1-F2s tests using a) CF, b) VDF and c) MLVDF models.

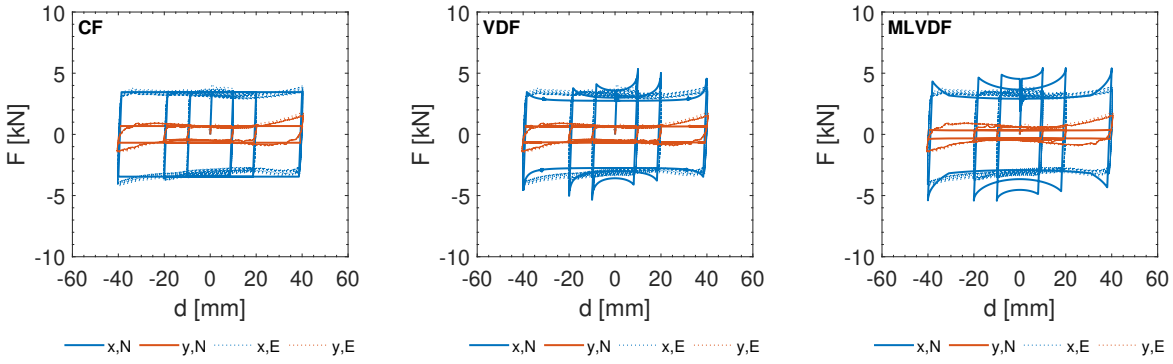

(a) (b) (c)

FIGURE 7.9: Comparison between experimental and simplified numerical model of NB sinusoidal G1-T1-F2 tests using a) CF, b) VDF and c) MLVDF models.

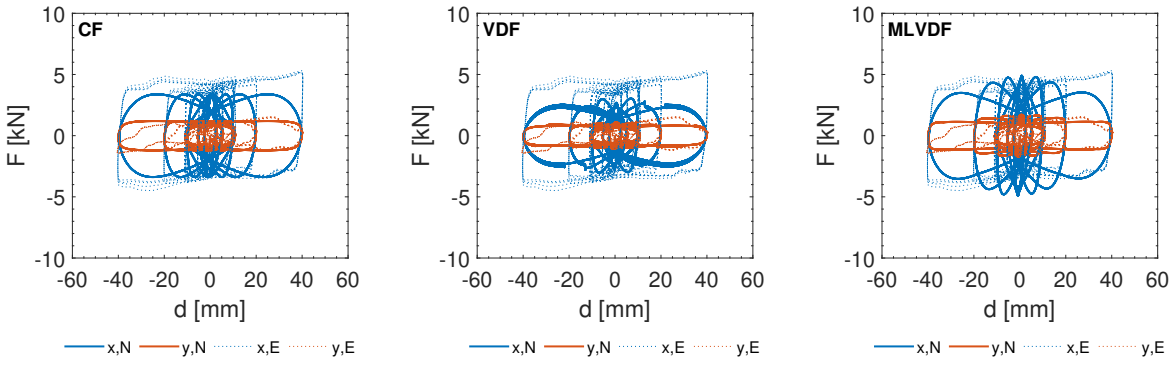

(a) (b) (c)

FIGURE 7.10: Comparison between experimental and simplified numerical model of NB cloverleaf G1-T1-F2c tests using a) CF, b) VDF and c) MLVDF models.

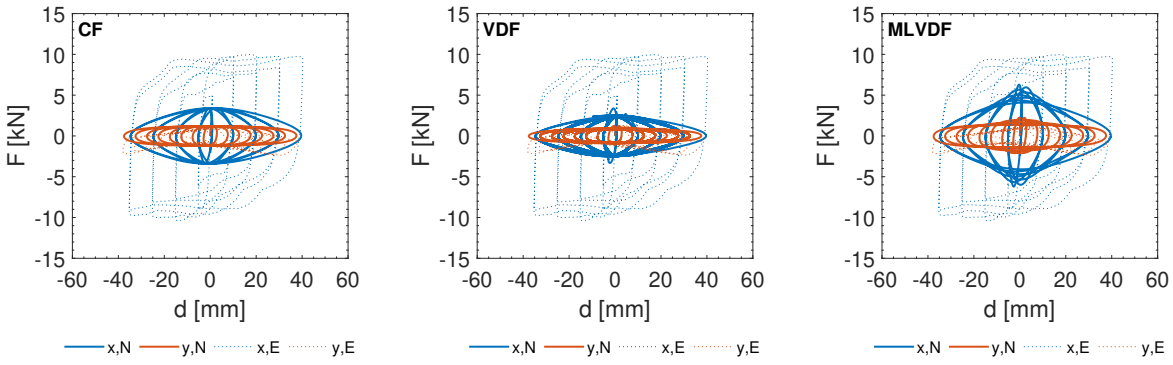

(a) (b) (c)

FIGURE 7.11: Comparison between experimental and simplified numerical model of NB spiral G1-T1-F2s tests using a) CF, b) VDF and c) MLVDF models.

For both NN and NB configurations, the adopted friction models well reproduce the activations forces in both x and y directions, especially for the mono-directional sinusoidal tests of Figures 7.6 and 7.9, but the maximum forces are well reproduced only for the NB configuration, especially when adopting the VDF and MLVDF models. However, the selected friction models do not properly reproduce the hardening effect produced by the stick-slip mechanism of the NN configuration in correspondence of the reverse motion point.

Concerning the cloverleaf 2D waveform results, the adopted friction models sufficiently reproduce the hysteresis cycle shapes of the NB configuration (see Figure 7.10) especially when adopting the CF and MLVDF model. On the contray, the selected friction models sufficiently reproduce the hysteresis cycle shapes of the NN configuration (see Figure 7.7) both in terms of activation and maximum forces only in the y direction.

Concerning the spiral 2D waveform results, the selected friction models sufficiently reproduce the hysteresis cycle shapes of both NN and NB configuration (see Figures 7.8 and 7.11) both in terms of activation and maximum forces only in the y direction, while the x direction is poorly reproduced.

As a summary, the simplified numerical model adequately reproduce the BRFD overall behaviour of NN and NB configurations when performing mono-directional tests, while the interaction between longitudinal (x) and transversal (y) components is insufficiently reproduced. This improper reproduction is to input on the FSB element itself and on how to combine the longitudinal and transversal component to reproduce the BRFD constraints according to the experimental setup configuration of Chapter 6. However, it is worth to investigate how this improper correlation between longitudinal and transversal component affect the interaction between the BRFD and a reference precast RC structure during a dynamic analysis.

Concerning the investigate friction constitutive laws, the VDF model represents a good compromise for both NN and NB configurations, being able to reproduce the hardening effect in correspondence of the reverse motion points in both x and y directions without loosing numerical stability.

7.3 BRFD refined numerical model

7.3.1 Numerical implementation scheme

The refined numerical model of the BRFD aims at reproducing the movement of all the BRFD elements and at defining a Virtual Lab tool to assess the experimental results of Chapter 6. To achieve that, the model of the rotational friction interfaces is paramount.

Considering the results of the simplified analytical formulations of §3.2 and §6.1.1, a circular dissipative area can be represented by using the scheme of Figure 7.12(a), where R_e and R_i are the outer and inner dissipative area radii and r_{eq} is the equivalent radius that takes into account the geometrical ratio between R_e and R_i. According to Eq. 6.2, a circular friction interface, with a friction coefficient μ_r and F_P stud bolt axial tension, rotate when the moment $M_{s,i}$, defined as the sliding moment of a single rotational friction interface, is reached. The friction interface can be schematically reproduced by rigidly connecting two nodes at a distance r_{eq} from the centre of rotation; the interface rotates by applying two sliding force $F_{s,i}$ with opposite direction to the two nodes. As a result, the two nodes rigidly rotate around the centre of

rotation point by following the circular path (dashed line) of Figure 7.12(a). If the two nodes have a friction coefficient μ_r and are subjected to a vertical force $F_P/2$, the sliding moment $M_{s,i}$ is reached according to Eq. 7.2.

$$M_{s,i} = 2r_{eq}F_{s,i} = 2r_{eq}\mu_r \frac{F_P}{2} = r_{eq}\mu_r F_P \tag{7.2}$$

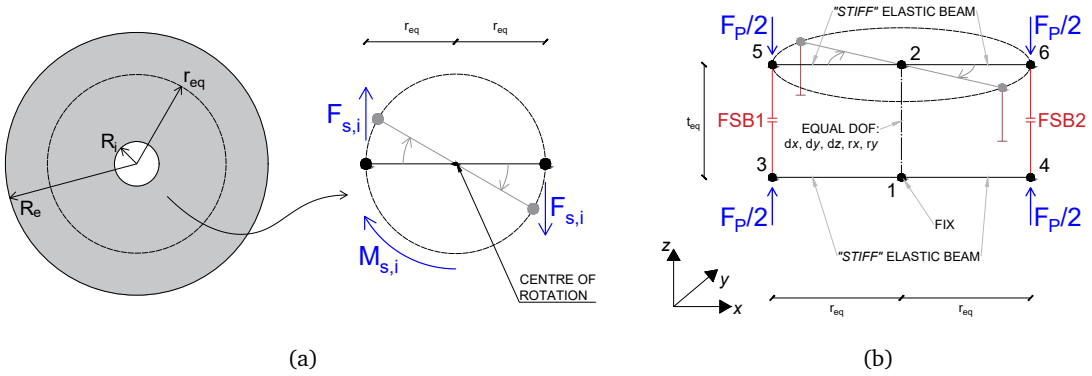

(a) (b)

FIGURE 7.12: Rotational friction interface a) scheme and b) implementation scheme of the refined numerical model.

The behaviour of the rotational friction interface can be numerically reproduced by doubling the scheme of Figure 7.12(a), obtaining the model of Figure 7.12(b). Nodes 1 and 2 represent the center of rotation of the friction interface and are positioned at a distance t_{eq} from each other, resembling the thickness of the friction interface. Nodes 1 and 2 are connected at a distance r_{eq} to, respectively, nodes 3-4 and 5-6 by adopting *Elastic Beam Column* elements with very stiff material properties and a *Corotational* geometric transformation law, which is preferred to *Linear* geometric transformation law when large displacements are involved. The adoption of very stiff material properties was employed to simulate the rigid rotation of element 5-2-6 while computing the internal force in element 3-1-4. Node 1 is fixed and node 2 is constrained to node 1 with and *EqualDOF* interaction that prevents the displacements along x, y and z directions and the rotations around x and y directions. As a result, node 2 can rotate around z direction and transmits the displacements to nodes 5 and 6, which move following the circular path (dashed line) of Figure 7.12(b), while nodes 3 and 4 stay unaltered.

To reproduce the rigid rotation of element 5-2-6 around node 2 while considering the friction properties of the interface, two FSB elements connect nodes 3-5 and 4-6, as represented by the red lines of Figure 7.12(b). FSB elements, developed to reproduce flat sliders, have coupled friction properties for their sher deformations, which allow them to deform along x and y directions independently but with the same force-displacement relationship. To simulate the compression of the friction interface arised by the stud bolts axial load, nodes 3, 4, 5 and 6 are subjected to a vertical force $F_P/2$, as shown in Figure 7.12(b), ensuring the compression of the FSB elements. The rotational friction interface rotates when FSB element develop a shear force equal to $F_{s,i}$.

The numerical model of Figure 7.12(b) reproduces the rotational movements of a circular friction interface and it is adopted to numerically implement the BRFD friction interfaces. Figure 7.13 shows the BRFD configuration (resembling the axonometric view of Figure 3.1(a)) with the core and connection plates

and the alignment guides highlighted with different colours, and the eight friction interfaces, which are associated with the four dissipative areas DA1, DA2, DA3 and DA4, highlighted with the dotted lines.

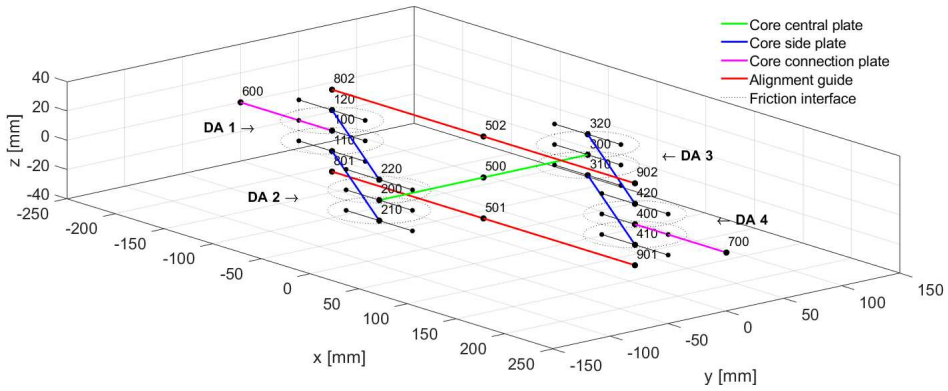

FIGURE 7.13: Scheme of the refined BRFD numerical model implementation.

The BRFD core and connection elements are implemented using a total of six *Elastic Beam Column* elements: nodes 110-210,120-220, 310-410, and 320-420 define the four core side plates (blue lines), nodes 200-500-300 represent the core central plate (green line), and nodes 600-100 and 700-400 specify the connection plates (purple lines). Nodes 801-501-901 and 802-502-902 define the lower and upper alignment guides (red lines), implemented using four *Elastic Beam Column* elements. To simulate the real behaviour of the guides in keeping aligned nodes 100-500-400 when the BRFD is subjected to a generic displacement, nodes 100-500-400 are connected to nodes 801-501-901 and 802-502-902 with ZLL elements that allows deformations only along x direction and rotations around z direction.

The four dissipative areas, DA1, DA2, DA3 and DA4, are modelled using the nodes whose numbers start with 1, 2, 3 and 4. All the areas have a node that acts as a centre of rotation (100, 200, 300 and 400, respectively) connected to two additional nodes acting as a fixed base for the FSB element using *Elastic Beam Column* elements with stiff properties. Each dissipative area has two rotational friction interfaces, and they are implemented according to the scheme of Figure 7.12.

The refined numerical model reported in Figure 7.13 can replicate the deformation of each BRFD element while reproducing the the rotational behaviour of each friction interface.

7.3.2 Calibration using different friction models

The calibration of the investigated friction constitutive models to be implemented inside the refined numerical model considers the friction coefficient values μ_r of §6.2.4, which are associated with the rotational mechanism of the BRFD friction interfaces. The experimental relationships of Figure 6.22 between μ_r and the rotational sliding velocity ω are used as to identify the friction values to insert in the constitutive models. More precisely, for the CF model, the value for `$mu` is computed as the average μ_r values along the x and y directions. For the VDF model, the value for `$muFast`, `$muSlow` and `$transRate` are computed by fitting Eq. 7.1 to the experimental relationships of Figure 6.22. For the MLVDF model, the values for `$velocityPoints` and `$frictionPoints` are computed by interpolating the experimental curve of Figure 6.22. It is to highlight that, in the following, the rotational sliding velocity ω is converted into the tangential sliding velocity v_t.

Figure 7.14 shows the calibration results for the VDF and MLVDF models by comparing the experimental results (continues lines) with the numerical fittings for the VDF and MLVDF models (dashed and dotted-dashed lines, respectively), while Table 7.2 lists the values adopted for the investigated friction models. In the CF model, the `$mu` ($\mu_{r,x}$ and $\mu_{r,y}$) equals the average μ_r values of Figure 7.5 computed in in x and y directions. In the VDF model, `$muFast` ($\mu_{r,x,fast}$ and $\mu_{r,y,fast}$) and `$muSlow` ($\mu_{r,x,slow}$ and $\mu_{r,y,slow}$) equal the minimum and maximum μ_r values of Figure 7.5, respectively, computed in in x and y directions, while `$transRate` ($a_{r,x}$ and $a_{r,t}$) are computed by fitting the formulation of Eq. 7.1 with the experimental $\mu_r - v_t$ relationship. In MLVDF model, `$velocityPoints` ($v_{t,x}$ and $v_{t,y}$) is a vector of the tangential sliding velocity comprised between 0 mm/s and the maximum recorded sliding velocity 30 mm/s, while `$frictionPoints` is a vector that represent the curve of Figure 7.5.

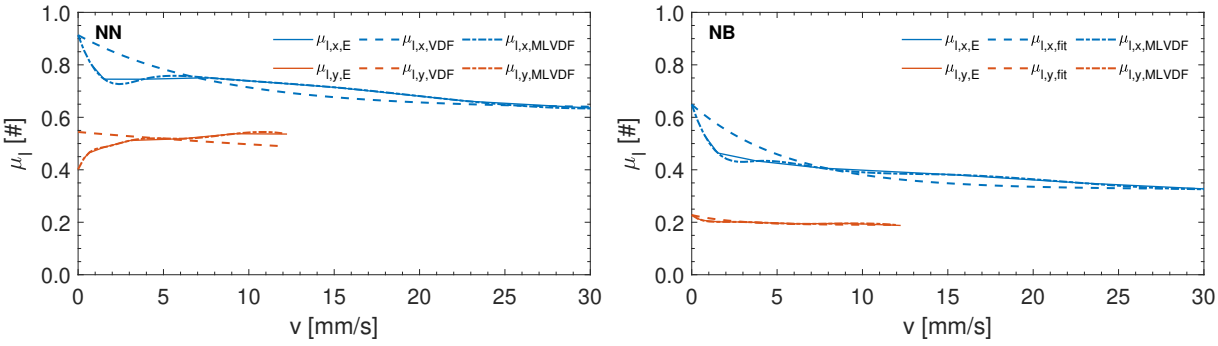

(a) (b)

FIGURE 7.14: Adopted $\mu_l - v$ relationship for the refined numerical model in x and y directions of a) NN and b) NB configurations.

TABLE 7.2: $\mu_r - v_t$ calibration results for NN and NB.

Friction model	Parameters	NN	NB
CF	$\mu_{r,x}$	0.72	0.41
	$\mu_{r,y}$	0.50	0.20
VDF	$\mu_{r,x,fast}$	0.63	0.33
	$\mu_{r,x,slow}$	0.91	0.65
	$a_{r,x}$ [s/mm]	0.125	0.040
	$\mu_{r,y,fast}$	0.44	0.19
	$\mu_{r,y,slow}$	0.54	0.23
	$a_{r,y}$ [s/mm]	0.177	0.383
MLVDF	$v_{t,x}$ [mm/s]	[0 6 12 18 24 30]	[0 6 12 18 24 30]
	$\mu_{r,x}$	[0.91 0.76 0.73 0.70 0.65 0.63]	[0.65 0.42 0.39 0.37 0.34 0.33]
	$v_{t,y}$ [mm/s]	[0 2 4 6 8 10 12]	[0 2 4 6 8 10 12]
	$\mu_{r,y}$	[0.40 0.49 0.52 0.52 0.53 0.54 0.54]	[0.23 0.20 0.20 0.19 0.19 0.20 0.19]

To assess the accuracy in the representation of the BRFD behaviour, the refined numerical model is subjected to G1-T1-F2, G3-T1-F2c and G3-T1-F2s test protocols of the bidirectional experimental tests (see Table 6.1). More precisely, G1-T1-F2 is a mono-directional test with a sinusoidal input waveform at a frequency of 0.50 Hz, G3-T1-F2c is a bi-directional test with a cloverleaf input 2D waveform at a frequency of 0.25 Hz and G3-T1-F2s is a bi-directional test with a spiral input 2D waveform at a frequency of 0.125

Hz. In all the mentioned test F_P value averages 22 kN. To compare the experimental results with the numerical simulation, the ends of the numerical BRFD model of Figure 7.13 are constrained according to the experimental setup configuration. More precisely, node 600 is fixed, and node 700 is free and subjected to the applied displacement history.

The comparison between experimental (E-curves) and refined numerical model (N-curves) results are represented in Figures 7.15, 7.16 and 7.17 for G1-T1-F2, G3-T1-F2c and G3-T1-F2s tests respectively of NN configuration, and in Figures 7.18, 7.19 and 7.17 for G1-T1-F2, G3-T1-F2c and G3-T1-F2s tests respectively of NB configuration. All the figures compare CF, VDF and MLVDF models.

For both NN and NB configurations, the adopted friction models well reproduce the activations forces in both x and y directions, especially for the mono-directional sinusoidal tests of Figures 7.15 and 7.18, but the maximum forces are well reproduced only for the NB configuration and the NN configuration in the y direction, especially when adopting the VDF and MLVDF models. The selected friction models do not properly reproduce the hardening effect produced by the stick-slip mechanism of the NN configuration in correspondence of the reverse motion point along the x direction.

Concerning the cloverleaf 2D waveform results, the adopted friction models well reproduce the hysteresis cycle shapes of both NN and NB configurations in both x and y directions (see Figures 7.19 and 7.16) especially when adopting the CF and MLVDF model.

Concerning the spiral 2D waveform results, the selected friction models sufficiently reproduce the hysteresis cycle shapes of both NN and NB configuration (see Figures 7.8 and 7.11) both in terms of activation and maximum forces only in the y direction, while the x direction is sufficiently reproduced.

As a summary, the refined numerical model adequately reproduce the BRFD overall behaviour of NN and NB configurations when performing both mono-directional and bi-directional tests, well simulating the interaction between longitudinal (x) and transversal (y) components. Moreover, the refined numerical model well reproduces the transversal hysteresis cycles shapes (y direction), confirming that their aspect is caused by a combination of the device's geometrical layout and the 2D waveform of the selected orbits.

Concerning the investigate friction constitutive laws, the VDF model represents a good compromise for both NN and NB configurations, being able to reproduce the hardening effect in correspondence of the reverse motion points in both x and y directions without loosing numerical stability.

7.4 Blind prediction of the BRFD under real use condition constrains

The developed friction-based numerical models describe the overall behaviour of the BRFD well, especially the refined numerical model. For this reason, a blind prediction has been performed to assess the hysteresis cycles of the BRFD prototype when constrained according to the actual use condition. More precisely, the simplified numerical model considers the full transversal component, while in the refined numerical model both nodes 600 and 700 of Figure 7.13 are fixed. Given the optimal calibration results of the VDF model, it is adopted as friction constitutive law by both friction-based numerical models.

Figures 7.21 and 7.22 show the comparison between the simplified analytical model (AM- lines) and simplified and refined friction-based numerical models (SNM- adn RNM- lines, respectively) when subjected

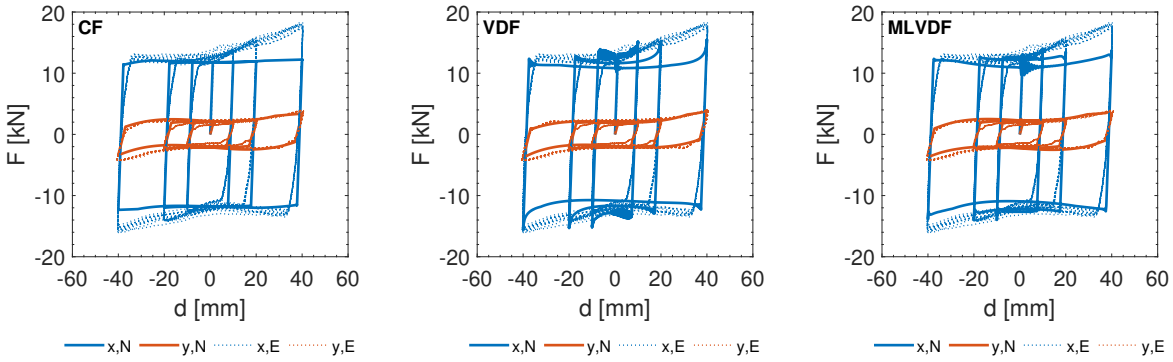

(a) (b) (c)

FIGURE 7.15: Comparison between experimental and refined numerical model of NN sinusoidal G1-T1-F2 tests using a) CF, b) VDF and c) MLVDF models.

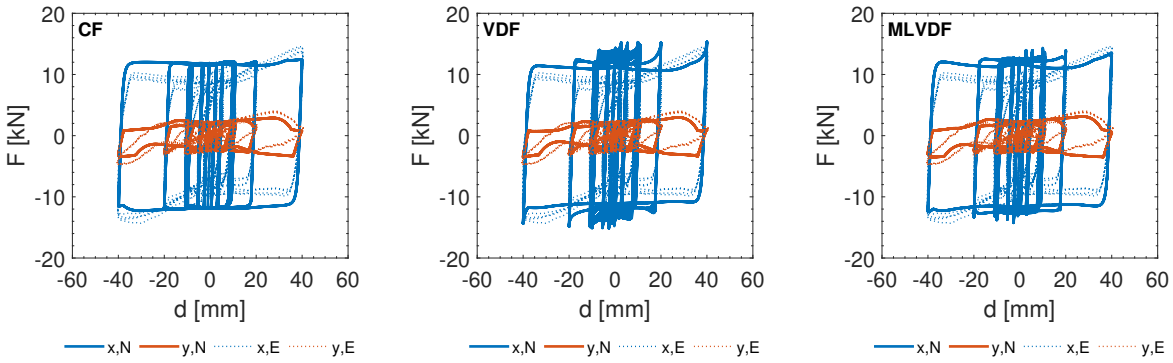

(a) (b) (c)

FIGURE 7.16: Comparison between experimental and refined numerical model of NN cloverleaf G1-T1-F2c tests using a) CF, b) VDF and c) MLVDF models.

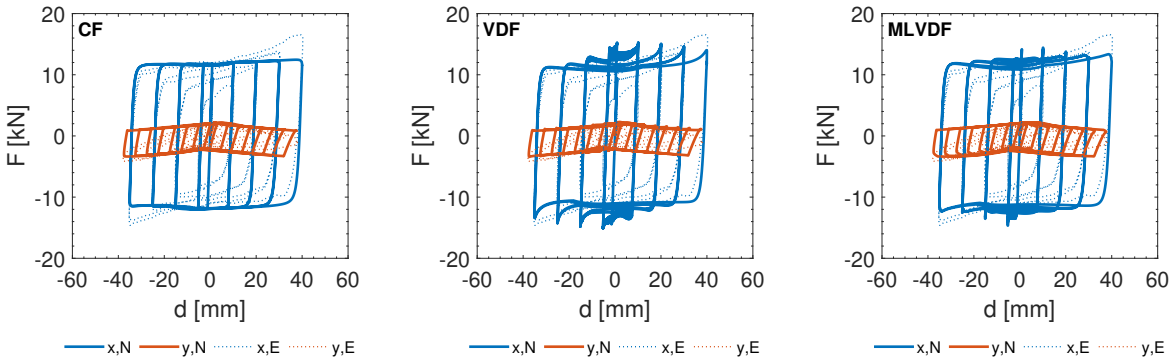

(a) (b) (c)

FIGURE 7.17: Comparison between experimental and refined numerical model of NN spiral G1-T1-F2s tests using a) CF, b) VDF and c) MLVDF models.

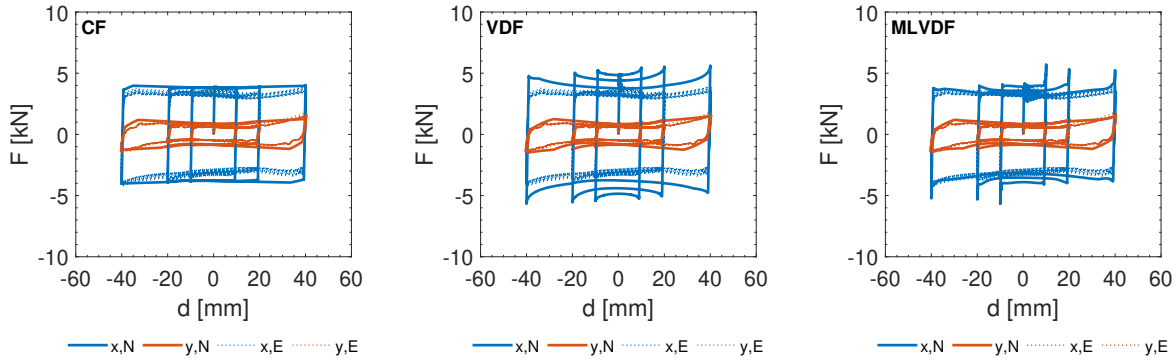

(a) (b) (c)

FIGURE 7.18: Comparison between experimental and refined numerical model of NB sinusoidal G1-T1-F2 tests using a) CF, b) VDF and c) MLVDF models.

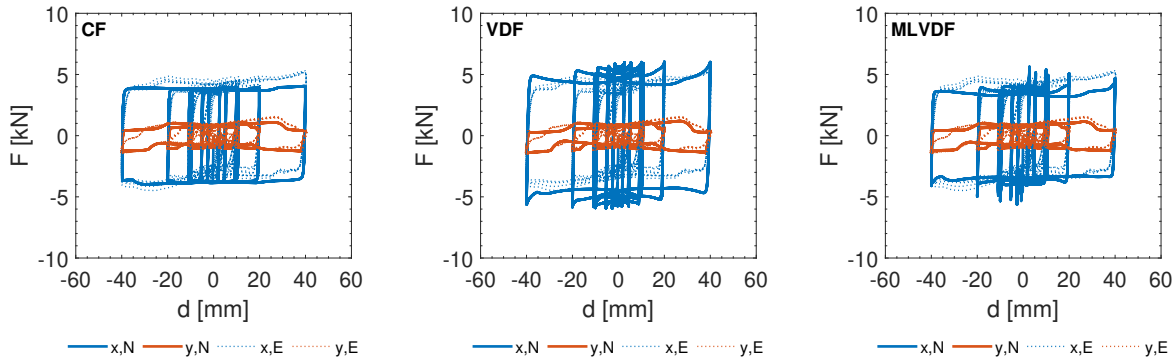

(a) (b) (c)

FIGURE 7.19: Comparison between experimental and refined numerical model of NB cloverleaf G1-T1-F2c tests using a) CF, b) VDF and c) MLVDF models.

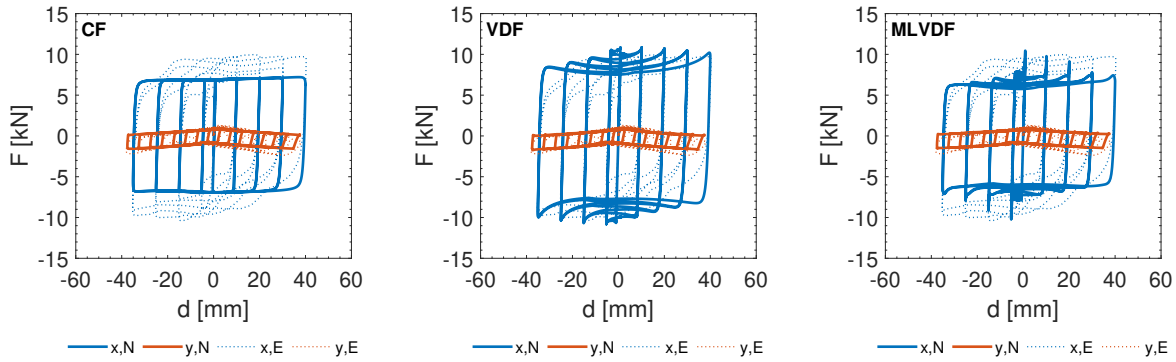

(a) (b) (c)

FIGURE 7.20: Comparison between experimental and refined numerical model of NB spiral G1-T1-F2s tests using a) CF, b) VDF and c) MLVDF models.

to the mono-directional sinusoidal displacements of G1-T1-F2 tests for the NN and NB configuration, respectively. The analytical model well describes the overall forces and stiffness, also confirming the full activation of the transversal component (y direction). However, in the NN configuration, the transversal component of the simplified numerical model (see Figure 7.21(a)) doesn't match the analytical one. On the contrary, in the NB configuration both simplified and refined numerical models (see Figures 7.22(a) and 7.22(b), respectively) well match the analytical one in both x and y directions.

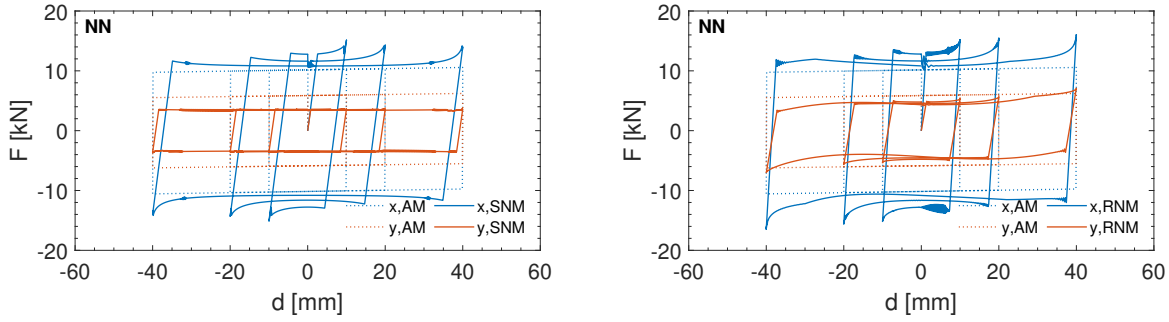

(a) (b)

FIGURE 7.21: Blind prediction for the NN configuration under real use condition constrains for G1-T1-F2: comparison between analytical and a) simplified and b) refined friction-based numerical models.

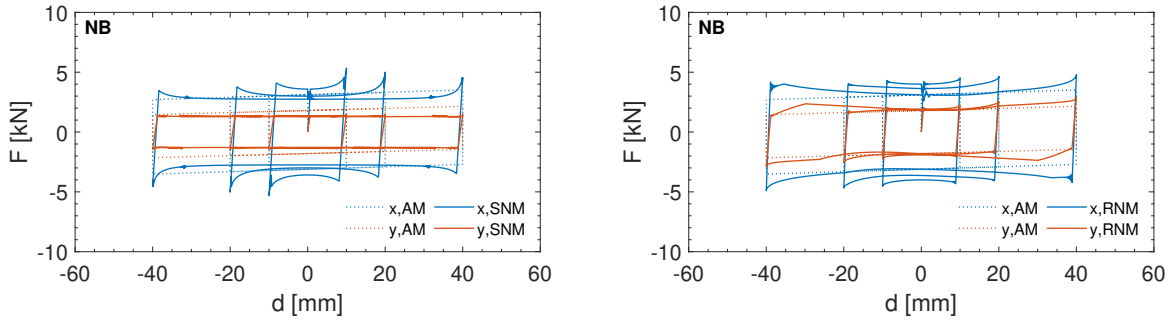

(a) (b)

FIGURE 7.22: Blind prediction for the NB configuration under real use condition constrains for G1-T1-F2: comparison between analytical and a) simplified and b) refined friction-based numerical models.

Figures 7.23 and 7.24 show the blind prediction of the refined friction-based numerical model when subjected to the bi-directional displacements of G1-T1-F2c and G1-T1-F2s tests for the NN and NB configuration, respectively. As previously observed, the refined friction-based numerical model well reproduces the interaction between x and y directions. Moreover, the transversal component (y direction) doubles the one observed during the experimental tests. This confirms that the partial activation of the BRFD components in the y direction registered during the experimental campaign is caused by the limits of the experimental setup configuration, which reduces the full BRFD damping capability. Concerning the differences between the NN and NB configurations, it is to highlight that NN exhibits a slightly smaller numerical stability.

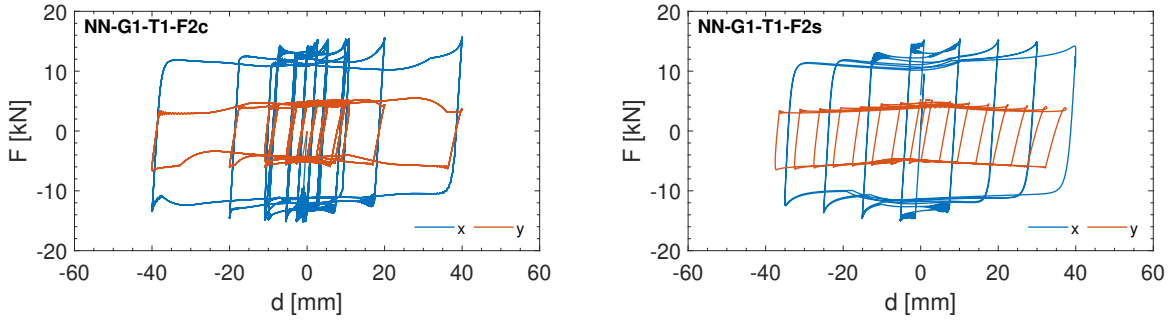

(a) (b)

FIGURE 7.23: Blind prediction for the NN configuration under real use condition constrains for a) G1-T1-F2c and b) G1-T1-F2s tests.

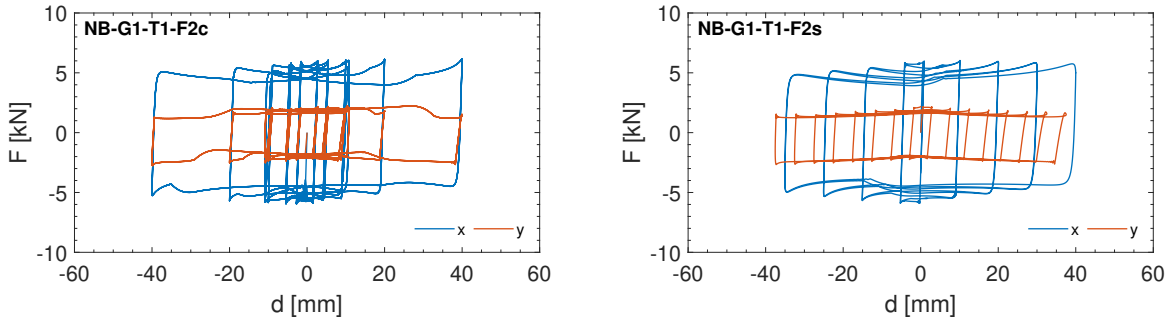

(a) (b)

FIGURE 7.24: Blind prediction for the NB configuration under real use condition constrains for a) G1-T1-F2c and b) G1-T1-F2s tests.

The NB exhibits steadier behaviour in experimental and numerical tests than the NN configuration. Moreover, in the NB configuration, the x and y components have a more similar behaviour, making it easier to reproduce numerically. For these reasons, future studies and applications will consider only the BRFD configuration with the NB friction interface.

7.5 Conclusive remarks

The present Chapter defines two friction-based numerical models that simulate the BRFD behaviour. The first one is a simplified numerical model that simulates the overall BRFD behaviour and can be easily implemented inside a frame. The second one is a refined numerical model that resembles the real geometry of the BRFD and simulates the behaviour and interactions of the main elements of the BRFD. Both numerical models are implemented in Opensees framework using *Flat Slider Bearing* elements, which have coupled friction properties for the shear deformations (local y and z axis of Figure 7.1) following a circular interaction domain. These friction properties are defined by associating a friction model to the *Flat Slider Bearing* element, and the present work investigates three different friction models. The first one is the *Coulomb Friction* (CF) model, which considers the coefficient of friction as a constant entity uninfluenced by the sliding velocity. The second one is the *Velocity Dependant Friction* (VDF) model, which considers the

coefficient of friction as an entity influenced by the sliding velocity and follows the analytical formulation of Eq. 7.1. The third one is the *Multi-Linear Velocity Dependant Friction* (MLVDF) model, which considers the coefficient of friction as an entity influenced by the sliding velocity and follows a relationship directly implemented by the user.

Both simplified and refined numerical models are implemented, and the results of the bi-directional mechanical tests of Chapter 6 are used to calibrate the friction models and validate the numerical solution. The validated models are then compared with the analytical model to assess numerical reproduction of the BRFD behaviour when constrained according to the real use conditions. The main findings and remarks are summarised below:

- The simplified numerical model reproduces well the overall behaviour of the BRFD when subjected to a mono-directional sinusoidal displacement law but reproduces well only the transversal component (y direction) when subjected to a 2D waveform orbit. This improper reproduction is imputed to the interaction domain of the friction properties of the *Flat Slider Bearing* element, which is circular and, consequently, cannot reproduce well the interaction between the longitudinal (x) and transversal (y) components of the BRFD.
- The refined numerical model reproduces well the overall behaviour of the BRFD when subjected to both mono-directional displacement law and 2D waveform orbit. Moreover, the hysteresis cycle shapes match well the ones recorded during the tests of Chapter 6, confirming that their aspect is caused by a combination of the device's geometrical layout and the 2D waveform of the selected orbits.
- The CF model reproduces well the activation forces but not the maximum forces, especially when implemented in the simplified numerical model. On the contrary, it reproduces well the maximum forces of the transversal component (y direction) when implemented in the refined numerical model. This good resemblance confirms that the hardening effect of the transversal component is caused by a geometrical layout of the BRFD when installed inside the experimental setup.
- The VDF model reproduces well the activation and maximum forces, especially when implemented in the refined numerical model. On the contrary, it reproduces badly the maximum forces of the transversal component (y direction) when implemented in the simplified numerical model. However, in the NB configuration, the resemblance between experimental and numerical results is still remarkable.
- The MLVDF model reproduces well the activation and maximum forces, especially when implemented in the refined numerical model. On the contrary, it reproduces badly the maximum forces of the transversal component (y direction) when implemented in the simplified numerical model. However, in the NB configuration, the resemblance between experimental and numerical results is still remarkable, behaving similarly to the VDF model but with more numerical instabilities.
- The comparison between analytical and friction-based numerical models shows that the numerical models well resemble the analytical one when constrained according to real-use conditions, especially for the NB configuration.

The findings of the present Chapter highlight the promising behaviour of the refined numerical model in reproducing the overall behaviour of the BRFD and the interaction between its longitudinal and transversal components. Moreover, the adoption of the VDF model reproduces well activation and maximum forces while maintaining optimal numerical stability, especially for the NB configuration.

The good results highlight the possibility of using the refined friction-based numerical model as a Virtual Lab to reproduce the real behaviour of the BRFD inside an experimental setup and the real interaction between the device and a structural system.

References

Constantinou, Michael C, Panos Tsopelas, Amarnath Kasalanati, and Eric D Wolff (1999). *Property Modification Factors for Seismic Isolation Bearings*. Report MCEER-99-0012, Multidisciplinary Center for Earthquake Engineering Research, State University of New York.

McKenna, Frank (2011). "OpenSees: A Framework for Earthquake Engineering Simulation". In: *Computing in Science & Engineering* 13 (4), pp. 58–66. DOI: 10.1109/MCSE.2011.66.

8
Conclusions and future outlooks

8.1 Conclusions

The need for structural connection improvement and minimally invasive energy dissipation devices in precast Reinforced Concrete (RC) buildings brings to the concept of dissipative beam-to-column joints, meeting both requirements in one device. The objectives of this thesis are the conceptualization, prototyping, mechanical and numerical definition of an innovative Friction Damper (FD) installed as a beam-to-column joint in precast RC structures and able to develop bidirectional damping. The damping principle of the developed device is based on friction because the energy dissipation leaves intact the device itself, which is an aspect that reflects the circular economy principles and it should be considered when designing new solutions.

The main findings of the conceptualization, prototyping, mechanical and numerical studies are summarised below:

- The conceptualization study of Chapter 3 develops a simplified analytical model that highlights how the developed Bidirectional Rotational Friction Damper (BRFD) can be described as a combination of two components, a longitudinal (local x direction) and a transversal (local y direction) one, identifying an activation force ($F_{act,x}$ and $F_{act,y}$) and an initial stiffness (K_x and K_y) for each one. The hysteresis cycles can be described using a bilinear hysteretic laws, and the uncoupled behaviour simplifies the numerical implementation of the BRFD, as it can be defined as a link with two separated hysteresis laws, one for each component. To evaluate the influence of the BRFD on a structure's behaviour during a seismic event, a case study is conducted on a single-story, single-bay precast RC structure that lacks secondary frames, allowing the implementation of BRFD inside the main frames only. The performance of a quasi-static analysis shows that the BRFDs application positively influence the case study's structural behaviour, unaltering the top displacement associated with the column yielding and slightly increasing the related total base shear. Moreover, when the BRFDs activate, the original static scheme of the structure is restored, allowing the columns to behave as cantilevers. To identify the optimal configuration of the BRFD for the case study, a sensitivity analysis was carried out performing an importance analysis using a multi-criteria decision-making (MCDM) approach. The introduction of the optimal BRFD's configuration positively benefits the case study's dynamic performance, significantly reducing the interstorey drift (62%) and the total base shear (28%) without altering the existing structural scheme, and avoiding structural and non-structural damage.

- The device's prototyping of Chapter 4 shows an experimental investigation performed for the development of the novel BRFD by using Pin-on-Disk (PoD) tests, and highlights the main tribological aspects useful for the full-scale tests. PoD tests are set to simulate the real use condition of the device in development under the action of subsequent earthquakes. Sliding surface's material and machining processes are selected taking into account the main body of the device, and the need of reducing the friction's abrasive component and the particle formation during sliding. More precisely, since the main body of the developed BRFD is made of steel S355JR, the testing mate surfaces have been selected based on the lower ware rate exhibited when coupled with this material, such as: steel S355JR itself, bronze CuSn12, brass OT58, shot peened steel S355JR, nickel base coating and zinc base coating. Contextually, the requirement of a low-cost process has led to the selection of machine processes traditionally used in surfaces machining, such as turning and milling, considering different roughness values. The main findings highlight that the execution of preliminary running-in stages sensibly reduce transition times necessary to guarantee a steady coefficient of friction. Moreover, the interaction between steel and softer metals, especially the interaction between nickel-treated steel and bronze, registers the overall better COF behaviour without significant surfaces damage.

- The mechanical studies of Chapters 5 and 6 assesses the device's mechanical behaviour when subjected to mono-directional and bi-directional displacements. The experimental tests are performed following EN 15129 guidelines and investigating different frequencies and displacement amplitudes. Considering the results of the PoD tests, the BRFD prototype is manufacture by considering two different friction interfaces: nickelled steel vs. nickelled steel (NN) and nickelled steel vs. bronze (NB). Three test groups are defined: Group 1 (G1) tests aimed at assessing the BRFD behaviour in a mono-directional real-use condition; Group 2 (G2) tests aimed at determining the relationship between the coefficient of friction and the velocity to calibrate a numerical friction model; a final Group 3 (G3) aimed at assessing the BRFD behaviour in a bidirectional real-use condition. To increase the steadiness of the overall BRFD behaviour, running-in (RI) have been performed in both longitudinal and transversal directions before the actual tests. Firstly, NN and NB were subjected to the mono-dimensional and bi-dimensional orbits with 50 Nm torque (T1), and then the better-performing coupling was subjected to 75 Nm torque (T2). The findings of the mechanical studies highlight the promising bidirectional behaviour of the BRFD, both in terms of hysteresis cycle steadiness and good damping capacity, especially the NB configuration, considered by the authors to be better performing. More precisely, RI test results highlight a significant steadiness increment of the BRFD behaviour in both NN and NB configurations. More precisely, the coefficient of variations decreases from around 9% to 6% for the NN configuration and from around 13% to 4% for the NB configuration. G1 and G3 test results highlight that the hysteresis cycles for NN and NB configurations are mainly rectangular with a slight hardening effect caused by a stick-slip mechanism in correspondence with the reverse motion point in both x and y direction, and do not differ with signal frequency. This is a promising behaviour because it ensures that the device's performance during an earthquake remains consistent, regardless of the ground motion frequency content. G2 test results highlight that the relationship between friction coefficient and sliding velocity decreases when the velocity increases. This behaviour is responsible for the stick-slip mechanism observed during the G1 tests, and it is less remarkable for the NB configuration.

- The numerical study of Chapter 7 focuses on the definition of numerical models implementable inside FEM softwares and that reproduces the device's behaviour. More precisely, the numerical implementation aimed at the definition of two different friction-based numerical models that help the validation of the experimental test results: a simple model for an easy implementation inside a frame structure, and a more refined model of the BRFD itself to be used as a Virtual Lab tool. Both numerical models are implemented in Opensees framework by using *Flat Slider Bearing* elements, which have coupled friction properties for the shear deformations (local y and z axis of Figure 7.1) following a circular interaction domain. These friction properties are defined by associating a friction model to the *Flat Slider Bearing* element, and the present work investigates three different friction models. The first one is the *Coulomb Friction* (CF) model, which considers the coefficient of friction as a constant entity uninfluenced by the sliding velocity. The second one is the *Velocity Dependant Friction* (VDF) model, which considers the coefficient of friction as an entity influenced by the sliding velocity and follows the analytical formulation of Eq. 7.1. The third one is the *Multi-Linear Velocity Dependant Friction* (MLVDF) model, which considers the coefficient of friction as an entity influenced by the sliding velocity and follows a relationship directly implemented by the user. The simplified numerical model reproduces well the overall behaviour of the BRFD when subjected to a mono-directional sinusoidal displacement law but reproduces well only the transversal component (y direction) when subjected to a 2D waveform orbit. This improper reproduction is imputed to the interaction domain of the friction properties of the *Flat Slider Bearing* element, which is circular and, consequently, cannot reproduce well the interaction between the longitudinal (x) and transversal (y) components of the BRFD. The refined numerical model reproduces well the overall behaviour of the BRFD when subjected to both mono-directional displacement law and 2D waveform orbit. Moreover, the hysteresis cycle shapes match well the ones recorded during the tests of Chapter 6, confirming that their aspect is caused by a combination of the device's geometrical layout and the 2D waveform of the selected orbits. Concerning the investigated friction models, the adoption of the VDF model reproduces well activation and maximum forces while maintaining optimal numerical stability, especially for the NB configuration.

As a summary, the conceptualisation analysis performed on the BRFD highlights that such a system can effectively improve a precast RC structure's behaviour during seismic events, while PoD tests highlight the main tribological aspects involving the BRFD and useful for the full-scale tests. The mechanical tests successfully highlight a very promising behaviour of the BRFD thanks to both good damping capacity and reliability of the hysteresis cycles, especially for the NB configuration, in here considered the most interesting. In fact, despite the development of lower friction coefficient values than NN, the steadiness of the hysteresis cycles is considered by the author more reliable and then preferable. The numerical study highlights the promising behaviour of the refined numerical model in reproducing the overall behaviour of the BRFD and the interaction between its longitudinal and transversal components.

The present work aims at prolonging the service life and mitigate seismic losses of precast RC structures in earthquake-prone areas, especially when those structures are designed for gravity loads only. This is a particular sensitive topic that allow the pursuit of goals 11, 12 and 13 of the UN 2030 Agenda for Sustainable Development.

8.2 Future outlooks

The present work highlights that the BRFD can significantly improve the seismic behaviour of precast RC structures while developing steady and reliable hysteresis cycles. Moreover, the refined friction-based numerical model can be used as a Virtual Lab tool to reproduce the real behaviour of the BRFD inside an experimental setup and the real interaction between the device and a structural system.

Despite the promising results, additional research is needed to validate the solution. Further research topics are listed below:

- To validate the full development of the transversal component, additional mechanical tests can be conducted using an updated experimental setup to achieve the complete damping development of the BRFD. To be more specific, the addition of external guides in the setup can help maintain the BRFD connection plates fixed, thus enabling the full development of the transversal component.
- To investigate the benefits of the BRFD when connected to existing precast RC frames, additional numerical studies can be performed by considering different structural topologies. For example, it can be investigated how the introduction of infill panels or flexible floors influence the damping capabilities of the BRFD.
- To validate the interaction between the BRFD and a structure, shaking table tests can be conducted on a scaled precast RC building prototype. This is the object of an awarded ERIES project (Horizon), and it will take place at the AZALEE shaking table at EMSI-TAMARIS of CEA in Paris Saclay Research Centre (France) in spring-summer 2025. The results can be used as a benchmark to conduct typological studies and investigate the potential of the BRFD.
- To investigate the benefits of the BRFD when connected to existing buildings, additional numerical studies can be performed by considering different structural typologies. For example, it can be investigated how the introduction of the BRFD within steel structures or within the soft floor of pilotis RC structures influences the dynamic response of those buildings.
- Life Cycle Assessment studies can be conducted to evaluate how the BRFD presence can improve the resilience and sustainability of buildings and clusters of buildings in an earthquake-prone area.

A

Complete dissertation of the simplified analytical model

A.1 Longitudinal behaviour

When the BRFD is subjected to longitudinal displacements (x direction), its static scheme can be simplified into the one of Figure A.1. A is a rigid node that can slide along x direction, while O is a hinged node. When the horizontal force F_x is applied to node A, the displacement $\Delta_x/2$ occurs and the reaction forces H_O, V_O, V_A and M_A are generated. It is to underline that, since only half of the BRFD is investigated, the registered displacement are halves in respect to the overall BRFD displacements, while, on the contrary, the registered forces are equals to the overall BRFD forces.

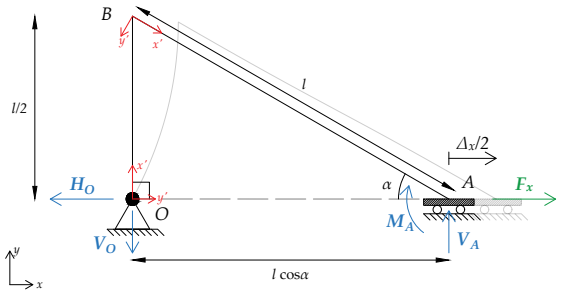

FIGURE A.1: BRFD core static scheme when subjected to longitudinal displacement.

The static scheme of Figure A.1 is one-time hyperstatic and to resolve it analytically the Principle of Virtual Work (PVW) is applied. The analytical procedure is to decrease the constrain's degree of node O allowing the vertical displacements and obtaining the so called *equivalent isostatic* or *real* system, in which the force F_x is applied to node A as showed in Figure A.2(a), and the *virtual* system, in which a unitary vertical force 1^* is applied to node O as showed in Figure A.3(a). The vertical displacement of node O in the real system (η_O) is then compered to the displacement of node O in the virtual system (η'_O) to determine the vertical force $\overline{V}$ that equals the two displacements, as given by Eq A.1, and that corresponds to the V_O reaction force of original system.

$$\eta_O + \overline{V}\eta'_O = 0 \tag{A.1}$$

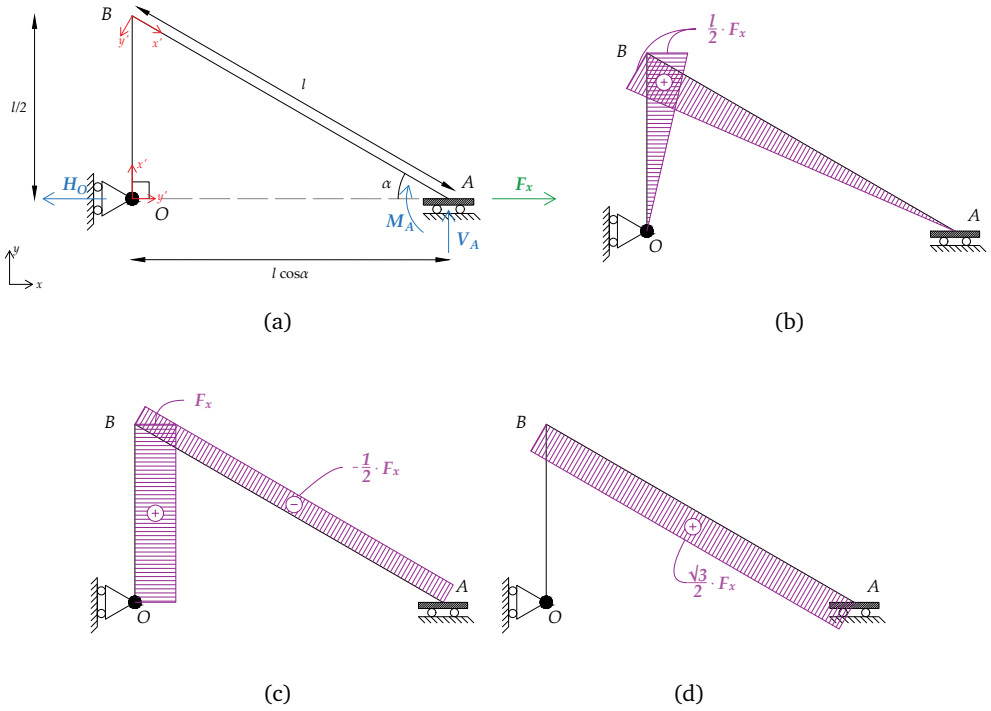

FIGURE A.2: BRFD core's real system: (a) static scheme, (b) bending moment, (c) shear and (d) axial force diagrams when longitudinal displacement (x direction) occurs.

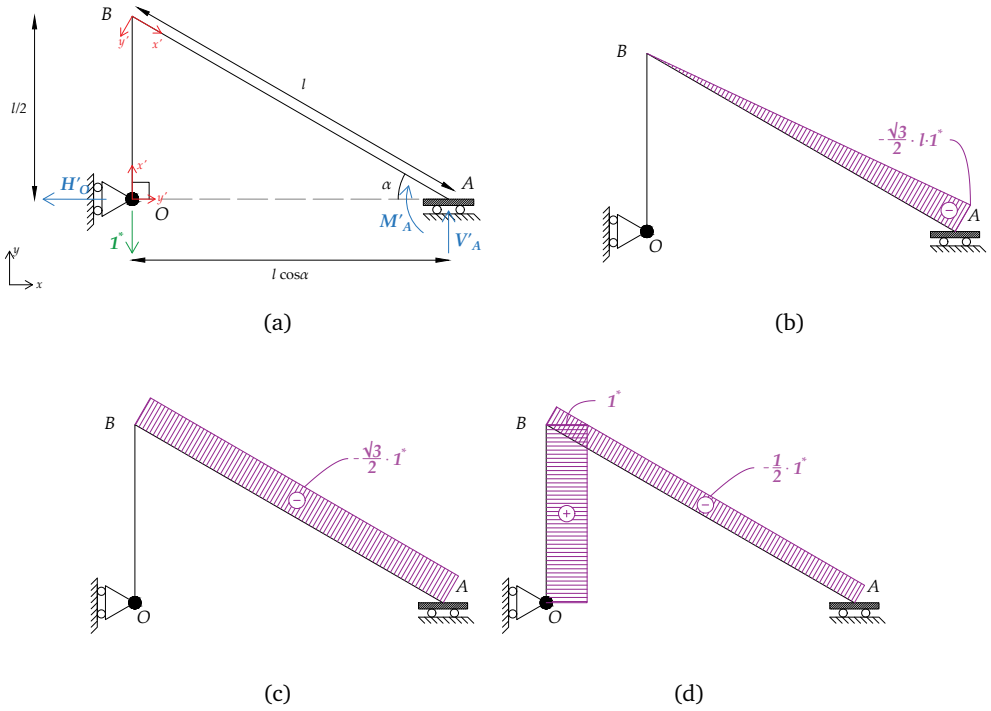

FIGURE A.3: BRFD core's virtual system: (a) static scheme, (b) bending moment, (c) shear and (d) axial force diagrams when longitudinal displacement (x direction) occurs.

The real system scheme is pictured in Figure A.2(a): in this configuration, when the horizontal force F_x is applied to node A, the reaction forces H_O, V_A and M_A are generated with the values of Eq A.2.

$$\begin{cases} H_O = F_x \\ V_A = 0 \\ M_A = 0 \end{cases} \tag{A.2}$$

According to the local reference $x'y'$, the internal loads laws of the associated real system are given by Eqs A.3 and A.4, for OB and BA segments respectively. The bending moment, shear and axial force diagrams are pictured in, respectively, Figures A.2(b), A.2(c) and A.2(d).

$$\overline{OB} : \begin{cases} N_{OB}(x') = 0 \\ V_{OB}(x') = F_x \\ M_{OB}(x') = x' \cdot F_x \end{cases} \rightarrow x' \in \left[0; \frac{l}{2}\right] \tag{A.3}$$

$$\overline{BA} : \begin{cases} N_{BA}(x') = F_x \cdot \cos(\alpha) \\ V_{BA}(x') = -F_x \cdot \sin(\alpha) \\ M_{BA}(x') = F_x \cdot \sin(\alpha)(l - x') \end{cases} \rightarrow x' \in [0; l] \tag{A.4}$$

The virtual system is pictured in Figure A.3(a): in this configuration, when the vertical force 1^* is applied to node O, the reaction forces H'_O, V'_A and M'_A are generated with the values of Eq A.5.

$$\begin{cases} H'_O = 0 \\ V'_A = 1^* \\ M'_A = 1^* \cdot l \cos(\alpha) \end{cases} \tag{A.5}$$

According to the local reference $x'y'$, the internal loads laws of the virtual system are given by Eqs A.6 and A.7, for OB and BA segments respectively. The bending moment, shear and axial force diagrams are pictured in, respectively, Figures A.3(b), A.3(c) and A.3(d).

$$\overline{OB} : \begin{cases} N'_{OB}(x') = 1^* \\ V'_{OB}(x') = 0 \\ M'_{OB}(x') = 0 \end{cases} \rightarrow x' \in \left[0; \frac{l}{2}\right] \tag{A.6}$$

$$\overline{BA} : \begin{cases} N'_{BA}(x') = -1^* \cdot \sin(\alpha) \\ V'_{BA}(x') = -1^* \cdot \cos(\alpha) \\ M'_{BA}(x') = -x' \cdot 1^* \cdot \cos(\alpha) \end{cases} \rightarrow x' \in [0; l] \tag{A.7}$$

According to the PVW, η_O and η'_O are given by Eqs A.8 and A.9, where E is the Young's modulus, I_{OB} the moment of inertia of OB segment and I_{BA} the moment of inertia of BA segment. It is to underline that, in order to maintain a generical formulation, the moment of inertia of the two segments OB and BA are kept independent to each other. $\overline{OB}$ and $\overline{BA}$ represent, respectively, the core central and lateral plates of the real device: these two elements have a different stratification and can have a different geometry, consequently

their moment of inertia can be significantly different.

$$\begin{aligned}
\eta_O &= \frac{1}{EI_{OB}}\int_0^{l/2} M'_{OB}(x')M_{OB}(x')dx' + \frac{1}{EI_{BA}}\int_0^{l} M'_{BA}(x')M_{BA}(x')dx' = \\
&= \frac{1}{EI_{OB}}\int_0^{l/2} (0)(x'F_x)dx' + \frac{1}{EI_{BA}}\int_0^{l} (-x'\cos(\alpha))\left[F_x\cdot\sin(\alpha)(l-x')\right]dx' = \\
&= \frac{F_x\sin(\alpha)\cos(\alpha)}{EI_{BA}}\int_0^{l}(-x'l+x'^2)dx = \frac{F_x\sin(\alpha)\cos(\alpha)}{EI_{BA}}\left[-\frac{x'^2}{2}l+\frac{x'^3}{3}\right]_0^l = \\
&= -\frac{1}{6}\cdot\frac{F_x l^3\sin(\alpha)\cos(\alpha)}{EI_{BA}}
\end{aligned} \tag{A.8}$$

$$\begin{aligned}
\eta'_O &= \frac{1}{EI_{OB}}\int_0^{l/2} (M'_{OB}(x'))^2dx' + \frac{1}{EI_{BA}}\int_0^{l} (M'_{BA}(x'))^2dx' = \\
&= \frac{1}{EI_{OB}}\int_0^{l/2} (0)^2dx' + \frac{1}{EI_{BA}}\int_0^{l} (-x'\cos(\alpha))^2dx' = \frac{\cos(\alpha)^2}{EI_{BA}}\left[\frac{x'^3}{3}\right]_0^l = \\
&= \frac{1}{3}\cdot\frac{l^3\cos(\alpha)^2}{EI_{BA}}
\end{aligned} \tag{A.9}$$

Applying Eq A.1, the vertical force $\overline{V}$ is calculated as given by Eq A.10 applying the hypothesis of $\alpha = 30°$. This hypothesis is related to the BRFD design requirement of core central and lateral plates ($A'B'$, $B'B$ and BA segments of Figure 3.2(b)) of the same length. As a consequence, for sake of conciseness, this hypothesis is adopted in the analytical formulations that follow.

$$\overline{V} = -\frac{\eta_O}{\eta'_O} = -\left(-\frac{1}{6}\cdot\frac{F_x l^3\sin(\alpha)\cos(\alpha)}{EI_{BA}}\right)\cdot\left(3\frac{EI_{BA}}{l^3\cos(\alpha)^2}\right) = \frac{1}{2}F_x\tan(\alpha) \overset{(\alpha=30°)}{=} \frac{\sqrt{3}}{6}F_x \tag{A.10}$$

As previously stated, the vertical force $\overline{V}$ corresponds to the V_O reaction force of original system (Figure A.1): in this configuration, when the horizontal force F_x is applied to node A, the reaction forces H_O, V_O, V_A, H_A and M_A are generated with the values of Eq A.11.

$$\begin{cases}
H_O = F_x \\
V_O = \overline{V} = \frac{\sqrt{3}}{6}F_x \\
V_A = \overline{V} = \frac{\sqrt{3}}{6}F_x \\
M_A = \overline{V}\cdot l\cdot\cos(\alpha) = \frac{1}{4}F_x l
\end{cases} \tag{A.11}$$

According to the local reference $x'y'$, the internal loads laws of the original system are given by Eqs A.12 and A.13, for OB and BA segments respectively. The bending moment, shear and axial force diagrams are

pictured in, respectively, Figures A.4(a), A.4(b) and A.4(c).

$$\overline{OB}: \begin{cases} N_{OB}(x') = \frac{\sqrt{3}}{6}F_x \\ V_{OB}(x') = F_x \\ M_{OB}(x') = x' \cdot F_x \end{cases} \rightarrow x' \in \left[0; \frac{l}{2}\right] \tag{A.12}$$

$$\overline{BA}: \begin{cases} N_{BA}(x') = F_x \cdot \cos(\alpha) - \overline{V} \cdot \sin(\alpha) = \frac{5\sqrt{3}}{12}F_x \\ V_{BA}(x') = -F_x \cdot \sin(\alpha) + \overline{V} \cdot \cos(\alpha) = -\frac{3}{4}F_x \\ M_{BA}(x') = F_x \cdot \sin(\alpha)(l - x') - x' \cdot \overline{V} \cdot \cos(\alpha) = \left(\frac{1}{2}l - \frac{3}{4}x'\right)F_x \end{cases} \rightarrow x' \in [0; l] \tag{A.13}$$

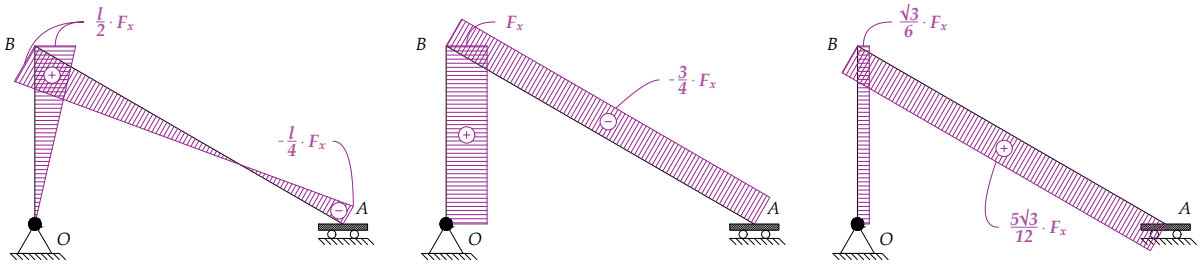

(a) (b) (c)

FIGURE A.4: BRFD core: (a) bending moment, (b) shear and (c) axial force diagrams when longitudinal displacement (x direction) occurs.

Node B reaches the higher value of bending moment (see Figure A.4(a)), consequently, when longitudinal displacement (x direction) occurs, the BRFD activates when $M_B = M_s$. As a result, the relationship between M_s and the horizontal activation force $F_{act,x}$ is described as follows:

$$F_{act,x} = \frac{M_s}{\frac{1}{2}l} = \frac{2M_s}{l} \tag{A.14}$$

Once determined the analytical formulations of the internal loads laws (Eqs A.12 and A.13), the displacement $\Delta_x/2$ of Figure A.1 is calculated applying the PVW and the BRFD's initial stiffness K_x is obtained from the ratio between F_x and Δ_x. The procedure is to use the BRFD core static scheme to obtain the real system, in which the force F_x is applied to node A as showed in Figure A.1, and the virtual system, in which a unitary horizontal force 1^* is applied to node A as showed in Figure A.5. The analytical formulation of the internal loads of real and virtual systems allows to calculate the displacement $\Delta_x/2$ applying the PVW. It is to highlight that, since the virtual system is identical to the real system in which F_x has been substituted by 1^*, the virtual system's analytical formulation of the internal load are automatically obtained substituting F_x with 1^* in the Eqs A.12 and A.13. The horizontal displacement $\Delta_x/2$ is given by Eq A.15 where $M_{OB}(x')$ and $M_{BA}(x')$ are the internal loads law of the real system (Figure A.1) and $M'_{OB}(x')$ and

$M'_{BA}(x')$ are the internal loads law of the virtual system (Figure A.5).

$$\begin{aligned}
\frac{\Delta_x}{2} &= \frac{1}{EI_{OB}}\int_0^{l/2} M'_{OB}(x')M_{OB}(x')dx' + \frac{1}{EI_{BA}}\int_0^{l} M'_{BA}(x')M_{BA}(x')dx' = \\
&= \frac{1}{EI_{OB}}\int_0^{l/2} (x')(x'F_x)dx' + \frac{1}{EI_{BA}}\int_0^{l} \left(\frac{1}{2}l-\frac{3}{4}x'\right)\left(\frac{1}{2}l-\frac{3}{4}x'\right)F_x dx' = \\
&= \frac{F_{x'}}{EI_{OB}}\int_0^{l/2} (x'^2)dx' + \frac{F_x}{EI_{BA}}\int_0^{l} \left(\frac{1}{2}l-\frac{3}{4}x'\right)^2 dx' = \frac{F_x}{EI_{OB}}\left[\frac{x'^3}{3}\right]_0^{l/2} + \frac{F_x}{EI_{BA}}\left[\frac{l}{4}x' + \frac{9}{16}\frac{x'^3}{3} - \frac{3}{4}\frac{x'^2}{2}l\right]_0^{l/2} = \\
&= F_x l^3\left(\frac{1}{24EI_{OB}} + \frac{1}{16EI_{BA}}\right) \qquad \text{(A.15)}
\end{aligned}$$

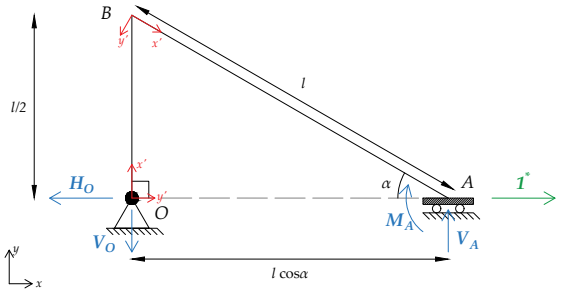

FIGURE A.5: BRFD core's static scheme when subjected to longitudinal displacement: virtual system.

The BRFD's initial longitudinal stiffness is calculated as follows:

$$K_x = \frac{F_x}{\Delta_x} = \frac{E}{l^3}\left(\frac{1}{12I_{OB}} + \frac{1}{8I_{BA}}\right)^{-1} \qquad \text{(A.16)}$$

As previously stated, to maintain a generical analytical model, the moment of inertia of the two segments *OB* and *BA* have been kept independent to each other. The real device's core central and lateral plates have a different stratification and can have a different geometry, which affect their inertia. However, for a better comprehension of the BRFD's mechanical behavior, several simplifying assumption can be adopted to study how the relationship between I_{OB} and I_{BA} affects K_x:

- if core central and lateral plates have same geometry and same stratification (1 plate each), substituting $I_{OB} = I_{BA} = I$ in Eq A.16, K_x results:

$$K_x = \frac{24}{5}\frac{EI}{l^3} \qquad \text{(A.17)}$$

- if core central and lateral plates have same geometry but the stratification is 1 and 2 plates respectively, substituting $I_{OB} = I$ and $I_{BA} = 2I$ in Eq A.16, K_x results:

$$K_x = \frac{48}{7}\frac{EI}{l^3} \qquad \text{(A.18)}$$

- if core central and lateral plates have same geometry but the stratification is 2 and 3 plates respectively, substituting $I_{OB} = 2I$ and $I_{BA} = 3I$ in Eq A.16, K_x results:

$$K_x = 12\frac{EI}{l^3} \tag{A.19}$$

From Eqs A.17, A.18 and A.19 it is observed that increasing the stratification of the BRFD, the initial stiffness K_x increases as well.

A.2 Transversal displacements

When the BRFD is subjected to transversal displacements (y direction), its static scheme can be simplified into the one of Figure A.6. A is a rigid node that can slide along y direction, while O is a hinged node. When the vertical force F_y is applied to node A, the displacement $\Delta_y/2$ occurs and the reaction forces H_O, V_O, H_A and M_A are generated. It is to underline that, since only half of the BRFD is investigated, the registered displacement are halves in respect to the overall BRFD displacements, while, on the contrary, the registered forces are equals to the overall BRFD forces.

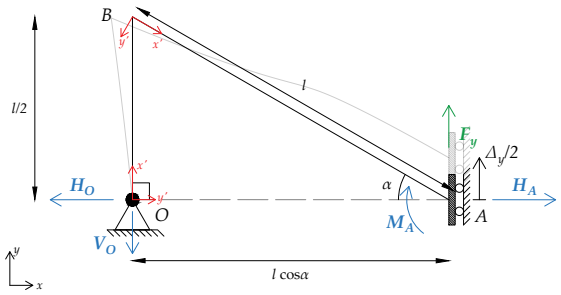

FIGURE A.6: BRFD core static scheme when subjected to transversal displacement.

The static scheme of Figure A.6 is one-time hyperstatic and to resolve it analytically the Principle of Virtual Work (PVW) is applied. The analytical procedure is to decrease the constrain's degree of node O allowing the horizontal displacements and obtaining the so called *equivalent isostatic* or *real* system, in which the force F_y is applied to node A as showed in Figure A.7(a), and the *virtual* system, in which a unitary horizontal force 1^* is applied to node O as showed in Figure A.8(a). The horizontal displacement of node O in the real system (ξ_O) is then compered to the displacement of node O in the virtual system (ξ'_O) to determine the horizontal force $\overline{H}$ that equals the two displacements, as given by Eq A.20, and that corresponds to the H_O reaction force of original system.

$$\xi_O + \overline{H}\xi'_O = 0 \tag{A.20}$$

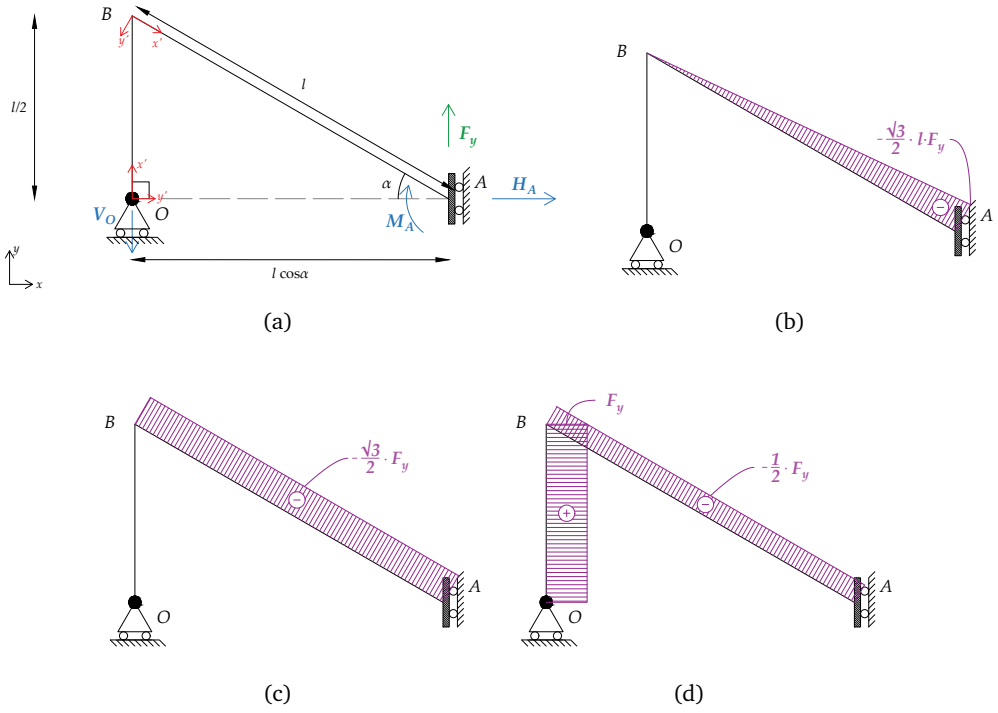

FIGURE A.7: BRFD core's real system: (a) static scheme, (b) bending moment, (c) shear and (d) axial force diagrams when transversal displacement (y direction) occurs.

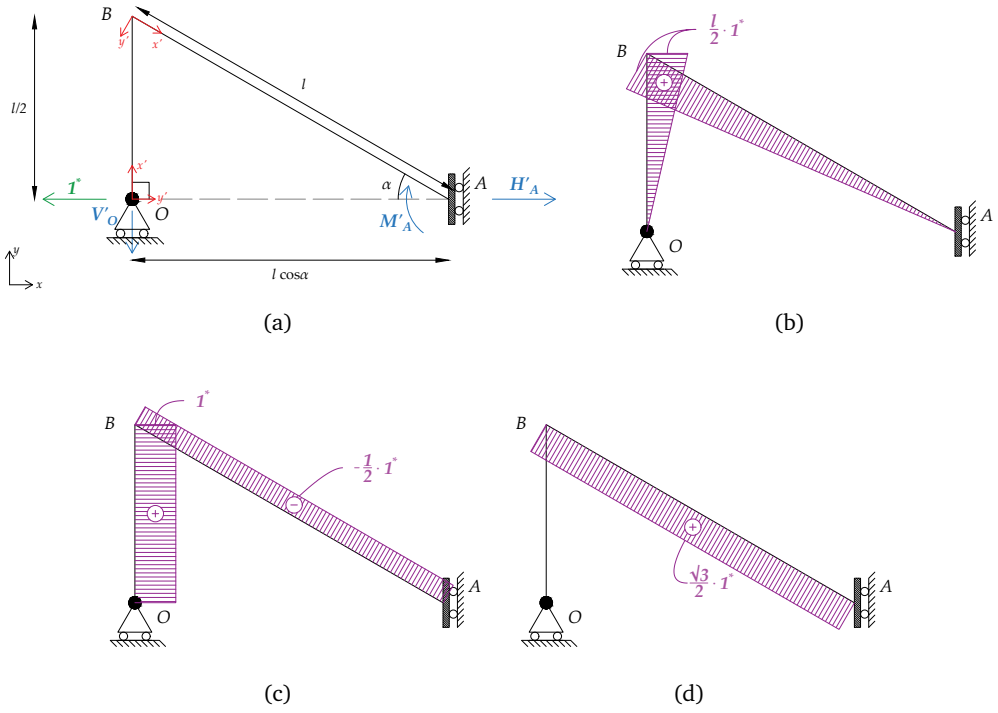

FIGURE A.8: BRFD core's virtual system: (a) static scheme, (b) bending moment, (c) shear and (d) axial force diagrams when transversal displacement (y direction) occurs.

The real system scheme is pictured in Figure A.7(a): in this configuration, when the vertical force F_y is applied to node A, the reaction forces V_O, H_A and M_A are generated with the values of Eq A.21.

$$\begin{cases} V_O = F_y \\ H_A = 0 \\ M_A = F_y \cdot l\cos(\alpha) \end{cases} \tag{A.21}$$

According to the local reference $x'y'$, the internal loads laws of the associated real system are given by Eqs A.22 and A.23, for OB and BA segments respectively. The bending moment, shear and axial force diagrams are pictured in, respectively, Figures A.7(b), A.7(c) and A.7(d).

$$\overline{OB}: \begin{cases} N_{OB}(x') = F_y \\ V_{OB}(x') = 0 \\ M_{OB}(x') = 0 \end{cases} \rightarrow x' \in \left[0; \frac{l}{2}\right] \tag{A.22}$$

$$\overline{BA}: \begin{cases} N_{BA}(x') = -F_y \cdot \sin(\alpha) \\ V_{BA}(x') = -F_y \cdot \cos(\alpha) \\ M_{BA}(x') = -F_y \cdot x' \cos(\alpha) \end{cases} \rightarrow x' \in [0; l] \tag{A.23}$$

The virtual system is pictured in Figure A.8(a): in this configuration, when the horizontal force 1^* is applied to node O, the reaction forces V'_O, H'_A and M'_A are generated with the values of Eq A.24.

$$\begin{cases} V'_O = 0 \\ H'_A = 1^* \\ M'_A = 0 \end{cases} \tag{A.24}$$

According to the local reference $x'y'$, the internal loads laws of the virtual system are given by Eqs A.25 and A.26, for OB and BA segments respectively. The bending moment, shear and axial force diagrams are pictured in, respectively, Figures A.8(b), A.8(c) and A.8(d).

$$\overline{OB}: \begin{cases} N'_{OB}(x') = 0 \\ V'_{OB}(x') = 1^* \\ M'_{OB}(x') = 1^* \cdot x' \end{cases} \rightarrow x' \in \left[0; \frac{l}{2}\right] \tag{A.25}$$

$$\overline{BA}: \begin{cases} N'_{BA}(x') = 1^* \cdot \cos(\alpha) \\ V'_{BA}(x') = -1^* \cdot \sin(\alpha) \\ M'_{BA}(x') = -1^* \cdot \sin(\alpha)(l - x') \end{cases} \rightarrow x' \in [0; l] \tag{A.26}$$

According to the PVW, ξ_O and ξ'_O are given by Eqs A.27 and A.28, where E is the Young's modulus, I_{OB} the moment of inertia of OB segment and I_{BA} the moment of inertia of BA segment. It is to underline that, in order to maintain a generical formulation, the moment of inertia of the two segments OB and BA are kept independent to each other. $\overline{OB}$ and $\overline{BA}$ represent, respectively, the core central and lateral plates of the real device: these two elements have a different stratification and can have a different geometry, consequently

their moment of inertia can be significantly different.

$$\begin{aligned}
\xi_O &= \frac{1}{EI_{OB}}\int_0^{l/2} M'_{OB}(x')M_{OB}(x')dx' + \frac{1}{EI_{BA}}\int_0^{l} M'_{BA}(x')M_{BA}(x')dx' = \\
&= \frac{1}{EI_{OB}}\int_0^{l/2} (x')(0)dx' + \frac{1}{EI_{BA}}\int_0^{l} [-F_y x'\cos(\alpha)][\sin(\alpha)(l-x')]dx' = \\
&= \frac{F_y\sin(\alpha)\cos(\alpha)}{EI_{BA}}\int_0^{l}(-x'l+x'^2)dx = \frac{F_y\sin(\alpha)\cos(\alpha)}{EI_{BA}}\left[-\frac{x'^2}{2}l+\frac{x^3}{3}\right]_0^l \\
&= -\frac{1}{6}\cdot\frac{F_y l^3\sin(\alpha)\cos(\alpha)}{EI_{BA}}
\end{aligned} \tag{A.27}$$

$$\begin{aligned}
\xi'_O &= \frac{1}{EI_{OB}}\int_0^{l/2} (M'_{OB}(x'))^2dx' + \frac{1}{EI_{BA}}\int_0^{l} (M'_{BA}(x'))^2dx' = \\
&= \frac{1}{EI_{OB}}\int_0^{l/2} (x')^2dx' + \frac{1}{EI_{BA}}\int_0^{l} \sin(\alpha)^2(l-x')^2dx' = \\
&= \frac{1}{EI_{OB}}\left[\frac{x'^3}{3}\right]_0^{l/2} + \frac{\sin(\alpha)^2}{EI_{BA}}\left[x'l^2+\frac{x'^3}{3}-2l\frac{x'^2}{2}\right]_0^l = \frac{l^3}{24EI_{OB}} + \frac{l^3\sin(\alpha)^2}{EI_{BA}}
\end{aligned} \tag{A.28}$$

Applying Eq A.20, the horizontal force $\overline{H}$ is calculated as given by Eq A.29 applying the hypothesis of $\alpha = 30°$. This hypothesis is related to the BRFD design requirement of core central and lateral plates ($A'B'$, $B'B$ and BA segments of Figure 3.2(b)) of the same length. As a consequence, for sake of conciseness, this hypothesis is adopted in the analytical formulations that follow.

$$\begin{aligned}
\overline{H} &= -\frac{\xi_O}{\xi'_O} = -\left(-\frac{1}{6}\cdot\frac{F_y l^3\sin(\alpha)\cos(\alpha)}{EI_{BA}}\right)\left(\frac{1}{\frac{l^3}{24EI_{OB}}+\frac{l^3\sin(\alpha)^2}{EI_{BA}}}\right) = \\
&\overset{(\alpha=30°)}{=} \frac{\sqrt{3}}{24}\frac{F_y}{I_{BA}}\left(\frac{1}{\frac{1}{24I_{OB}}+\frac{1}{12I_{BA}}}\right) = \frac{\sqrt{3}}{2}\frac{F_y}{\frac{I_{BA}}{2I_{OB}}+1}
\end{aligned} \tag{A.29}$$

To compact the formulation, in the following it is inserted a parameter k that take in account of the relationship between I_{OB} and I_{BA} ad is defined as follows:

$$k = \frac{I_{BA}}{2I_{OB}} + 1 \tag{A.30}$$

Substituting Eq A.30 in Eq A.29, the new formulation for the horizontal force $\overline{H}$ is:

$$\overline{H} = \frac{\sqrt{3}}{2}\frac{F_y}{k} \tag{A.31}$$

As previously stated, the horizontal force $\overline{H}$ corresponds to the H_O reaction force of original system (Figure A.6): in this configuration, when the vertical force F_y is applied to node A, the reaction forces H_O, V_O, V_A, H_A and M_A are generated with the values of Eq A.32.

$$\begin{cases} H_O = \overline{V} = \frac{\sqrt{3}}{2}\frac{F_y}{k} \\ V_O = F_y \\ V_A = F_y \\ M_A = F_y \cdot l \cdot \cos(\alpha) = \frac{\sqrt{3}}{2}F_2 l \end{cases} \tag{A.32}$$

According to the local reference $x'y'$, the internal loads laws of the original system are given by Eqs A.33 and A.34, for *OB* and *BA* segments respectively. The bending moment, shear and axial force diagrams are pictured in, respectively, Figures A.9(a), A.9(b) and A.9(c).

$$\overline{OB}: \begin{cases} N_{OB}(x') = F_y \\ V_{OB}(x') = \frac{\sqrt{3}}{2}\frac{F_y}{k} \\ M_{OB}(x') = \frac{\sqrt{3}}{2}\frac{F_y}{k}x' \end{cases} \rightarrow x' \in \left[0; \frac{l}{2}\right] \tag{A.33}$$

$$\overline{BA}: \begin{cases} N_{BA}(x') = \overline{H} \cdot \cos(\alpha) - F_y \cdot \sin(\alpha) = \left(\frac{3}{4k} - \frac{1}{2}\right)F_y \\ V_{BA}(x') = -\overline{H} \cdot \sin(\alpha) - F_y \cdot \cos(\alpha) = -\left(\frac{\sqrt{3}}{4k} + \frac{\sqrt{3}}{2}\right)F_y \\ M_{BA}(x') = \overline{H} \cdot \sin(\alpha)(l-x) - x' \cdot F_y \cdot \cos(\alpha) = \frac{\sqrt{3}}{4}\frac{F_y l}{k} - \left(\frac{\sqrt{3}}{4k} + \frac{\sqrt{3}}{2}\right)x'F_y \end{cases} \rightarrow x' \in [0; l] \tag{A.34}$$

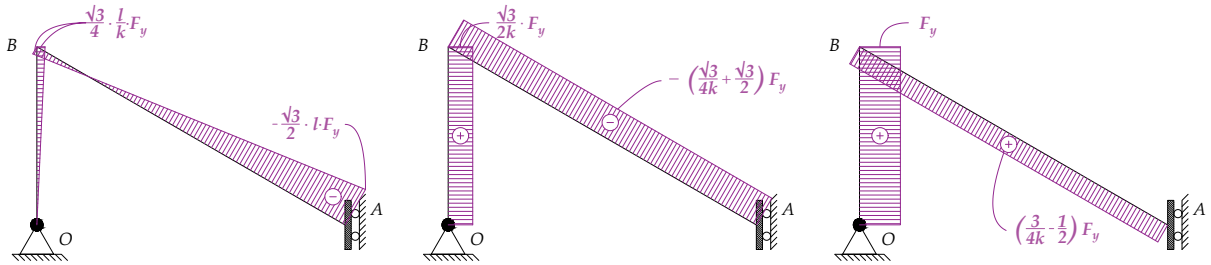

(a) (b) (c)

FIGURE A.9: BRFD core: (a) bending moment, (b) shear and (c) axial force diagrams when transversal displacement (Y direction) occurs.

Node A reaches the higher value of bending moment (see Figure A.9(a)), consequently, when transversal displacement (y direction) occurs, the BRFD activates when $M_A = M_s$. As a result, the relationship between M_s and the vertical activation force $F_{act,y}$ is described as follows:

$$F_{act,y} = \frac{M_s}{\frac{\sqrt{3}}{2}l} = \frac{2\sqrt{3}}{3}\frac{M_s}{l} \tag{A.35}$$

Once determined the analytical formulations of the internal loads laws (Eqs A.33 and A.34), the displacement $\Delta_y/2$ of Figure A.6 is calculated applying the PVW and the BRFD's initial stiffness K_y is obtained from the ratio between F_y and Δ_y. The procedure is to use the BRFD core static scheme to obtain the real system, in which the force F_y is applied to node A as showed in Figure A.6, and the virtual system, in which a unitary vertical force 1^* is applied to node A as showed in Figure A.10. The analytical formulation of the internal loads of real and virtual systems allows to calculate the displacement $\Delta_y/2$ applying the PVW. It is to highlight that, since the virtual system is identical to the real system in which F_y has been substituted by 1^*, the virtual system's analytical formulation of the internal load are automatically obtained substituting F_y with 1^* in the Eqs A.33 and A.34. The horizontal displacement $\Delta_y/2$ is given by Eq A.36 where $M_{OB}(x')$ and $M_{BA}(x')$ are the internal loads law of the real system (Figure A.6) and $M'_{OB}(x')$ and $M'_{BA}(x')$ are the internal loads law of the virtual system (Figure A.10).

$$
\begin{aligned}
\frac{\Delta_y}{2} &= \frac{1}{EI_{OB}}\int_0^{l/2} M'_{OB}(x')M_{OB}(x')dx' + \frac{1}{EI_{BA}}\int_0^{l} M'_{BA}(x')M_{BA}(x')dx' = \\
&= \frac{1}{EI_{OB}}\int_0^{l/2}\left(\frac{\sqrt{3}}{2k}x'\right)^2 F_y dx' + \frac{1}{EI_{BA}}\int_0^{l}\left[\frac{\sqrt{3}}{4k}l-\left(\frac{\sqrt{3}}{4k}+\frac{\sqrt{3}}{2}\right)x'\right]^2 F_y dx' = \\
&= \frac{F_y}{EI_{OB}}\int_0^{l/2}\left(\frac{3}{4k^2}x'^2\right)dx' + \frac{F_y}{EI_{BA}}\int_0^{l}\left[\frac{3}{16k^2}l+\left(\frac{3}{16k^2}+\frac{3}{4}+\frac{3}{4k}\right)x'^2-\frac{3}{2k}\left(\frac{1}{4k}+\frac{1}{2}\right)lx'\right]dx' = \\
&= \frac{F_y}{EI_{OB}}\left[\frac{3}{4k^2}\frac{x'^3}{3}\right]_0^{l/2} + \frac{F_y}{EI_{BA}}\left[\frac{3}{16k^2}lx'+\left(\frac{3}{16k^2}+\frac{3}{4}+\frac{3}{4k}\right)\frac{x'^3}{3}-\frac{3}{2k}\left(\frac{1}{4k}+\frac{1}{2}\right)\frac{lx'^2}{2}\right]_0^{l/2} = \\
&= F_y l^3\left[\frac{1}{32k^2EI_{OB}}+\frac{1}{EI_{BA}}\left(\frac{1}{4k}-\frac{1}{2}\right)^2\right]
\end{aligned}
\tag{A.36}
$$

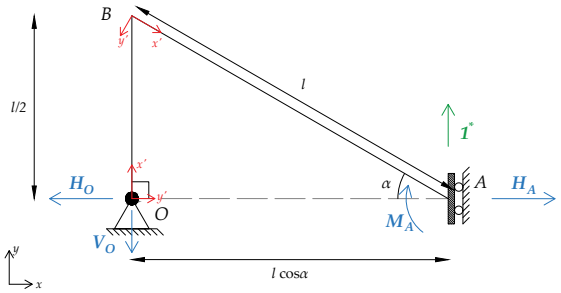

FIGURE A.10: BRFD core's static scheme when subjected to transversal displacement: virtual system.

The DD's initial transversal stiffness is calculated as follows:

$$
K_y = \frac{F_y}{\Delta_y} = \frac{E}{l^3}\left[\frac{1}{16k^2I_{OB}}+\frac{2}{I_{BA}}\left(\frac{1}{4k}-\frac{1}{2}\right)^2\right]^{-1} \tag{A.37}
$$

As previously stated, to maintain a generical analytical model, the moment of inertia of the two segments OB and BA have been kept independent to each other. The real device's core central and lateral plates

have a different stratification and can have a different geometry, which affect their inertia. However, for a better comprehension of the BRFD's mechanical behavior, several simplifying assumption can be adopted to study how the relationship between I_{OB} and I_{BA} affects K_y:

- if core central and lateral plates have same geometry and same stratification (1 plate each), substituting $I_{OB} = I_{BA} = I$ and $k = 3/2$ in Eq A.37, K_y results:

$$K_y = 4\frac{EI}{l^3} \tag{A.38}$$

- if core central and lateral plates have same geometry but the stratification is 1 and 2 plates respectively, substituting $I_{OB} = I$ and $I_{BA} = 2I$ and $k = 2$ in Eq A.37, K_y results:

$$K_y = \frac{32}{5}\frac{EI}{l^3} \tag{A.39}$$

- if core central and lateral plates have same geometry but the stratification is 2 and 3 plates respectively, substituting $I_{OB} = 2I$ and $I_{BA} = 3I$ and $k = 7/4$ in Eq A.37, K_y results:

$$K_y = \frac{21}{2}\frac{EI}{l^3} \tag{A.40}$$

From Eqs A.38, A.39 and A.40 it is observed that increasing the stratification of the BRFD, the initial stiffness K_y increases as well.

B

The design of the BRFD elements

B.1 The design forces

One of the main conditions in the DD design is that, during the seismic event, the elements of the device cannot enter the plastic domain. Consequently, when the BRFD is subjected to a generic displacement $\vec{\Delta} = \vec{\Delta_x} + \vec{\Delta y}$, all the elements cannot yield. At the same time, one of the main hypothesis of the simplified analytical model is that, once the device is activated, in the dissipative areas (nodes *B-B'* and *A-A'* of Figure 3.2(b) when Δ_x and Δ_y are applied respectively) the bending moment cannot exceed M_s. Consequently, when the BRFD is subjected to a generic displacement Δ the expected maximum internal forces can be assumed equal to the sum of Eqs. A.12, A.13, A.33 and A.34 in which F_x and F_y are substituted with $F_{act,x}$ and $F_{act,y}$ respectively. Associating the tags C and S to core central and side plates respectively, the designed internal forces are deducted as follows:

$$\begin{aligned} N_{Ed,C} &= \left(\frac{\sqrt{3}}{6}F_{act,x} + F_{act,y}\right)\gamma_{ov} \\ V_{Ed,C} &= \left(F_{act,x} + \frac{\sqrt{3}}{2}\frac{F_{act,y}}{k}\right)\gamma_{ov} \\ M_{Ed,C} &= M_s\gamma_{ov} \end{aligned} \tag{B.1}$$

$$\begin{aligned} N_{Ed,S} &= \left[\frac{5\sqrt{3}}{12}F_{act,x} + \left(\frac{3}{4k} - \frac{1}{2}\right)F_{act,y}\right]\gamma_{ov} \\ V_{Ed,S} &= \left[\frac{3}{4}F_{act,x} + \left(\frac{\sqrt{3}}{4k} + \frac{\sqrt{3}}{2}\right)F_{act,y}\right]\gamma_{ov} \\ M_{Ed,S} &= M_s\gamma_{ov} \end{aligned} \tag{B.2}$$

where γ_{ov} is an overstrength factor set equal to 1.25 according to Eurocode 8:1 (EC8:1). Table B.1 collects the safety factors that will be adopted in the following design relationships according to Eurocode 3:1-1 (EC3:1-1), Eurocode 3:1-8 (EC3:1-8) and EC8:1.

TABLE B.1: Safety factors adopted during the design according to EC3:1-8 and EC8:1.

Definition	Symbol	Value
Resistance of members (EC3:1-1))	γ_{M0}	1.05
Resistance of cross-sections (EC3:1-1)	γ_{M1}	1.05
Resistance of bolts (EC3:1-8)	γ_{M2}	1.25
Preload of high strength bolts (EC3:1-8)	γ_{M7}	1.10
Overstrength factor (EC8:1)	γ_{ov}	1.25

In the following, the design procedure is focused firstly on the BRFD elements, secondly on the jointed union and bolts.

B.2 The design of the elements

The design of the BRFD's elements follows the relationships of EC3:1-1 (CEN, 2014) focusing on:

- bending moment
- shear
- tension
- compression
- buckling

taking in account that the cross-sections are rectangular shaped and elastic field is required. In addition, further considerations are developed for pads and elements cavity for their correct interlocking.

The design bending moment resistance M_{Rd} is set equal to:

$$M_{Rd} = \frac{W_{el} f_{yk}}{\gamma_{M0}} \tag{B.3}$$

where f_{yk} is the steel yielding tension and W_{el} is the cross-section's elastic modulus, which for a rectangular section of width b and thickness t is set equal to:

$$W_{el} = \frac{bt^2}{6} \tag{B.4}$$

The design shear resistance V_{Rd} is set equal to:

$$V_{Rd} = \frac{A_v f_{yk}}{\sqrt{3}\gamma_{M0}} \tag{B.5}$$

where f_{yk} is the steel yielding tension and A_v is the cross-section's shear area, which for a rectangular section of width b and thickness t is set equal to:

$$A_v = bt \tag{B.6}$$

The design tension resistance $N_{t,Rd}$ is set as the smaller between:

- the gross cross-section resistance $N_{pl,Rd}$

$$N_{pl,Rd} = \frac{A f_{yk}}{\gamma_{M0}} \tag{B.7}$$

- the net cross-section resistance $N_{u,Rd}$ (in case of hollowed sections)

$$N_{pl,Rd} = \frac{0.9 A_{net} f_{yk}}{\gamma_{M2}} \tag{B.8}$$

where A is the cross-section area and A_{net} is the net cross-section area taking in account the eventual holes.

The design compression resistance $N_{c,Rd}$ is set equal to:

$$N_{c,Rd} = \frac{Af_{yk}}{\gamma_{M0}} \tag{B.9}$$

The design buckling resistance for a compression member $N_{b,Rd}$ is set equal to:

$$N_{b,Rd} = \frac{\chi Af_{yk}}{\gamma_{M1}} \tag{B.10}$$

where χ is a reduction factor for the relevant buckling mode calculated as follows:

$$\chi = \frac{1}{\Phi + \sqrt{\Phi^2 - \overline{\lambda}^2}} \leq 1 \tag{B.11}$$

with:

- $\overline{\lambda}$ non-dimensional slenderness calculated as:

$$\overline{\lambda} = \sqrt{\frac{Af_{yk}}{N_{cr}}} \tag{B.12}$$

  with N_{cr} elastic critical buckling force, which for a rectangular cross section with l_0 as the appropriate buckling length is calculated as follows:

$$N_{cr} = \frac{\pi EI}{l_0^2} \tag{B.13}$$

- Φ factor calculated as

$$\Phi = 0.5[1 + \alpha(\overline{\lambda} - 0.2) + \overline{\lambda}^2] \tag{B.14}$$

  with α imperfection that can be assumed equal to 0.49 for rectangular cross-sections.

BRFD's friction pads and core elements have a particular geometry that allows their interlocking. This design choice has been adopted to substitute the friction pads during the mechanical investigation, allowing the study of more pads coupling and, for future applications, to substitute the eventual damaged friction pads keeping unaltered the main body.

Friction pads are designed with two different types of holes (see Figure B.1(a)): the circular one is for the stud bolt that keeps the stratification coupled, the slotted one is for the teeth present on the surface of the core elements. These slotted holes and teeth are designed according to shear failure.

In the configuration of Figure B.1(b), the design force $F_{t,Ed}$ is set equal to:

$$F_{t,Ed} = \frac{M_{s,i}}{n_t R_m} \tag{B.15}$$

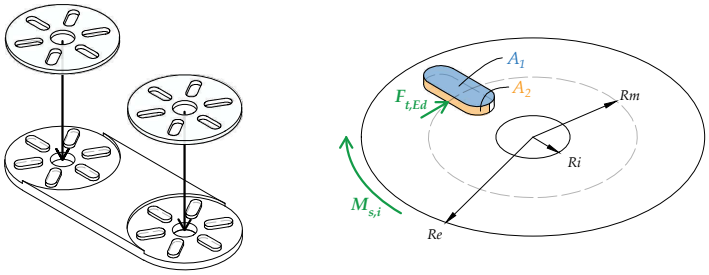

(a) (b)

FIGURE B.1: BRFD a) interlocking between friction pads and core elements, and b) detail of elements' teeth.

where $M_{s,i}$ id defined by Eq 3.1, n_t is the total number of teeth/slotted holes and $R_m = (R_e + R_i)/2$ the medium radius.

The design teeth shear resistance (see Figure B.1(b)) is the smaller between:

- shear resistance of area A_1

$$F_{t,Rd1} = \frac{A_1 f_{yd}}{\sqrt{3}} \tag{B.16}$$

- compression resistance of A_2

$$F_{t,Rd2} = A_2 f_{yd} \tag{B.17}$$

where $f_{yd} = f_{yk}/\gamma_{ov}$ is the design steel yielding tension. The design slotted holes shear resistance is defined by Eq B.17.

The design criteria for the elements is assumed in Eq B.18, where Ed is the general design force and Rd its associated design resistance.

$$\rho = \frac{Ed}{Rd} < 1 \tag{B.18}$$

B.3 The design of the jointed union

In the BRFD, the jointed union of the core elements (points *A'*, *B'*, *B* and *A* of Figure 3.2(b)) is responsible of the correct functioning of the device: in these points the tension produced by nuts and bolts generate the preload F_P and, consequently, the sliding moment M_s. Once the BRFD is activated, the elastic field is required for all the elements of the jointed union.

According to EC3:1-1, the bolt preload F_P is given by Eq B.19, however, since BRFD's bolts are subjected to fatigue cycles, in the following the Eq B.20 is assumed in order to reduce bolts stresses. In these formulations, f_{ub} is the ultimate tensile strength and A_s is the tensile strength area of the bolts and stud bolts.

$$F_P = \frac{0.7 f_{ub} A_s}{\gamma_{M7}} \quad \text{(EC3:1-1)} \tag{B.19}$$

$$F_P = \frac{0.35 f_{ub} A_s}{\gamma_{M7}} \tag{B.20}$$

The design resistance of bolts is set smaller between:

- design shear resistance $F_{v,Rd}$ for 8.8 bolt class set as:

$$F_{v,Rd} = \frac{0.6 f_{ub} A_s}{\gamma_{M2}} \tag{B.21}$$

- design tension resistance $F_{t,Rd}$ for 8.8 bolt class set as:

$$F_{t,Rd} = \frac{0.9 f_{ub} A_s}{\gamma_{M2}} \tag{B.22}$$

In addition to Eqs B.21 and B.22, the interaction effect of Eq B.23 must be checked, where $F_{v,Ed}$ and $F_{t,Ed}$ are, respectively, design shear and tension jointed union forces.

$$\frac{F_{v,Ed}}{F_{v,Rd}} + \frac{F_{t,Ed}}{1.4 F_{t,Rd}} \leq 1 \tag{B.23}$$

Jointed union plates are verified considering:

- bearing resistance $F_{b,Rd}$, set equal to:

$$F_{b,Rd} = \frac{k_1 \alpha_b f_u d t}{\gamma_{M2}} \tag{B.24}$$

  where, f_u is the plate ultimate tension d is the bolt nominal diameter, t the plate thickness, $\alpha_b = \min\{e_1/3d_0; f_{ub}/f_u; 1\}$ and $k_1 = \min\{2.8e_2/d_0 - 1.7; 2.5\}$

- punching shear resistance $B_{p,Rd}$, set equal to:

$$B_{p,Rd} = \frac{0.6\pi d_m t_p f_u}{\gamma_{M2}} \tag{B.25}$$

  where t_p is the plate thickness and d_m is the smaller between nut and bolt head diameter.

The design criteria for the bolts and union plates is assumed in Eq B.18, where Ed is the general design force and Rd its associated design resistance.